

Dissertation
submitted to the
Combined Faculties for the Natural Sciences and for
Mathematics
of the Ruperto-Carola University of Heidelberg, Germany
for the degree of
Doctor of Natural Sciences

presented by
M.Sc. Physics Jonathan Michael Blake Downing
born in Halifax, Nova Scotia, Canada
Oral examination: 18 November, 2009

Compact Binary Populations in Globular Clusters and Prospects for Gravitational Wave Detection

Referees: Prof. Dr. Rainer Spurzem
Prof. Dr. Ralf Klessen

Abstract

The inspiral and merger of compact binary stars will be major detection events for interferometric gravitational wave observatories. These observatories operate most effectively by comparing their output to template waveforms. In order to make these templates the physical parameters of the source population must be understood. Compact binaries in the galactic field have been investigated using population synthesis models but in dense stellar environments interactions can alter the binary population and may enhance the merger rate.

I study compact binaries in star clusters using a Monte Carlo model for the dynamics. I find that the black hole population interacts strongly, leading to an enhancement in both the number of black hole binaries and the black hole binary merger rate. Due to the high interaction rate the majority of black hole binaries are ejected and thus the mergers occur in the galactic field. I find a promising rate of 1 – 100 detections per year for the next generation of ground-based gravitational wave detectors and two possible sources for space-based detectors, both highly eccentric. I conclude that star clusters must be taken into account in order to predict accurate event rates for gravitational wave detectors.

Zusammenfassung

Als wichtigste Zielobjekte für interferometrische Gravitationswellen-Detektoren werden umeinander spiralande und verschmelzende kompakte Doppelsternsysteme angesehen. Die Detektoren arbeiten am effektivsten durch Vergleichen der Beobachtung mit einer Schablone aus der erwarteten Wellenform. Um die Schablonen zu erstellen müssen die physikalischen Parameter der Quellenpopulationen verstanden werden. In der Galaxie können kompakte Doppelsternsysteme mithilfe von Populationssynthese-Modellen untersucht werden, wohingegen in dichten Sterngebieten stellare Wechselwirkungen die Verteilung der Doppel-Systeme beeinflussen und die Kollisionsrate anheben können.

Ich erforsche kompakte Doppelsternsysteme in Kugelsternhaufen unter der Verwendung eines Monte-Carlo-Modells für die Dynamik. Diese Studien zeigen, dass die Population der schwarzen Löcher stark interagiert, wodurch sich sowohl die Anzahl der Paare von schwarzen Löchern als auch deren Verschmelzungsrate erhöht. Die Mehrheit dieser Doppel-systeme wird aus dem Kugelsternhaufen geschleudert, um endgültig im galaktischen Feld zu verschmelzen. Für die erdgebundenen Gravitationswellen-Detektoren der nächsten Generation erwarte ich eine vielversprechende Rate von 1 – 100 detektierten Ereignissen pro Jahr sowie zwei mögliche Quellen für weltraum-basierte Messungen, jeweils mit Bahnen hoher Exzentrizität. Daher schließe ich, dass Sternhaufen mit in Betracht gezogen werden müssen, um genaue Ereignisraten für Gravitationswellen-Detektoren vorherzusagen.

Dedication

To my mother with many thanks for her unconditional love and support over so many years. She has had confidence in me as a person and not just as an academic when I have had none in myself. Without her I would never have made it this far.

WE LIVE LIFE FORWARDS BUT UNDERSTAND IT BACKWARDS.
SØREN KIERKEGAARD

Contents

1	Introduction	1
1.1	Interferometric Gravitational Wave Detectors	2
1.2	Compact Binaries as Gravitational Wave Sources	4
1.3	Basic Concepts in Star Cluster Dynamics	5
1.3.1	Evolution of the Phase Space Distribution	5
1.3.2	The Relaxation Time	6
1.3.3	Mass Segregation	7
1.3.4	The Gravothermal Catastrophe	8
1.3.5	Few-Body Interactions	9
1.3.6	Escape Processes	9
1.4	Overview	10
2	The Formation of Compact Binaries	11
2.1	The Evolution of Isolated Binaries	12
2.2	The Formation of Compact Binaries in Star Clusters	18
2.2.1	Single-Single Interactions	18
2.2.2	Binary-Single Interactions	19
2.2.3	Binary-Binary Interactions	21
2.3	Current Results for Compact Binaries	22
2.3.1	Population Synthesis in the Galactic Field	22
2.3.2	Binaries in Clusters	22
3	The Relativistic Evolution of Compact Binaries	25
3.1	The Linearised Field Equations	25
3.2	Power Generation by Gravitational Waves	27
3.3	Radiated Power as a Function of Harmonic	32
4	The Monte Carlo Code	35
4.1	The Monte Carlo Approximation	35
4.2	The Structure of a Monte Carlo Timestep	36
4.2.1	The Potential	37
4.2.2	The Timestep	38
4.2.3	Additional Physics	38
4.2.4	Relaxation Processes	38
4.2.5	New Positions and New Potential	41
4.2.6	New Velocities in the New Potential	41
4.3	Few Body Interactions	42

4.3.1	3-Body Binary Formation	43
4.3.2	Binary-Single Interactions	44
4.3.3	Binary-Binary Interactions	46
4.4	Stellar Evolution	47
4.5	Tidal Escape	48
4.6	Limitations	49
5	Initial Conditions	51
6	Compact Binaries Within Star Clusters	55
7	The Escapers	69
7.1	Escaper Statistics	69
7.2	Mergers due to Gravitational Radiation	75
7.3	Other Species	79
8	Prospects for Gravitational Wave Detection	81
8.1	Ground-Based Detectors	81
8.2	Space-Based Detectors	86
9	Million-Body Simulations	89
9.1	Initial Conditions	89
9.2	Population Statistics Within the Clusters	90
9.3	Escapers	99
9.4	Detection Rates	102
10	Discussion and Outlook	111
10.1	Discussion	111
10.2	Future Directions	114
10.2.1	Direct Integration of Few-Body Encounters	114
10.2.2	Relativistic Interactions	114
10.2.3	Direct N-Body Simulations	118
10.2.4	Further Analysis of the Simulations	121
10.3	Conclusions	122
	Bibliography	125

List of Tables

3.1	Gravitational Wave Inspiral Timescales	30
5.1	Initial Conditions for the 500k Simulations	53
6.1	Number of BHs	56
6.2	Number of BH-BH binaries	57
7.1	Number of BH-BH Escapers	71
7.2	Number of NS-NS and BH-NS Escapers and Mergers	79
7.3	Properties of NS-NS and BH-NS Escapers	79
8.1	Celestial coordinates and distances for the 16 globular clusters within 5 pc of Earth	87
8.2	Properties of the LISA Sources	88
9.1	Initial Conditions for the Million-Body Simulations	90
9.2	Number of BHs	91
9.3	Number of BH-BH Binaries	92
9.4	BH-BH Mergers Parameters within Cluster	96
9.5	Number of Escaping and Merging Compact Binaries	99

List of Figures

1.1	Polarisation states of Gravitational Waves	2
1.2	Configurations of Gravitational Wave Detectors	3
2.1	The Roche Potential	12
3.1	GW Power Enhancement due to Eccentricity	29
3.2	Gravitational Wave Inspirals	31
3.3	GW Power as a Function of Harmonic	33
6.1	BH-BH Number per 500 Myr	58
6.2	r_h of BH system	59
6.3	BH-BH Chirp Masses	60
6.4	BH-BH Chirp Masses at $9t_{rh}$	61
6.5	Binding Energy of BH-BH Binaries	62
6.6	Periods of BH-BH Binaries	63
6.7	Eccentricity vs. Period for BH-BH Binaries	64
6.8	Gravitational Wave Inspiral Timescales	65
6.9	Dynamical Disruption Timescale	66
7.1	Binding Energy of BH-BH Escapers	70
7.2	Number of BH-BH Binary Escapes per Gyr	72
7.3	Period of Escaping BH-BH Binaries	73
7.4	Period vs. Eccentricity of BH-BH Binaries at Escape	74
7.5	Number of BH-BH Binary Mergers per Gyr	76
7.6	Gravitational Wave Inspiral Timescale in the Galactic Field	77
7.7	Chirp Mass Distribution of Ejected BH-BH Mergers	78
8.1	Merger Detection Rate with $S/N > 2$	82
8.2	Merger Detection Rate with $S/N > 8$	83
8.3	Detection Rate over all Cluster Types	84
9.1	Number of BH-BHs per 500 Myrs	93
9.2	Half-mass Radii of the BH system	94
9.3	BH-BH Binding Energy Distribution	95
9.4	BH-BH Period Distribution	96
9.5	BH-BH GW Inspiral Timescales	97
9.6	Disruption Timescales for BH-BH Binaries	98
9.7	Number of BH-BH Escapers per Gyr	100
9.8	Number of BH-BH Merges per Gyr	101

9.9	Period Distribution for Escaping BH-BH Binaries	102
9.10	Period vs. Eccentricity for Escaping BH-BH Binaries	103
9.11	Inspiral Timescales for Escaping BH-BH Binaries	104
9.12	Ground-Based Detection Rates by Cluster Type: $S/N > 2$	105
9.13	Ground-Based Detection Rates by Cluster Type: $S/N > 8$	106
9.14	The Detection Rate per Year for Ground-Based Detectors	107
9.15	Ground-Based Detection Rates as a Function of z for the Current Generation of Detectors	108
9.16	Ground-Based Detection Rates as a Function of z for advanced LIGO	109
10.1	Scattering in a Central Potential	116
10.2	Relativistic Scattering Angles	117
10.3	Relativistic Two-body Orbits	118
10.4	PN Energy Error in Direct N-Body Simulations	120

Chapter 1

Introduction

Gravitational waves open up an exciting new way of observing the universe. Almost all present observations of the universe are limited to the electromagnetic spectrum. Thus gravitational waves provide completely new kinds of information about astrophysical processes and allow us to observe objects such as neutron stars (NSs) and black holes (BHs) that do not emit electromagnetic radiation. Gravitational waves produce perturbations in space-time that interact with gravitational wave detectors. There are several detectors currently in operation. These include the LIGO (Laser Interferometer Gravitational Wave Observatory) detectors in Livingstone, Louisiana and Hanford, Washington USA (Abramovici et al. 1992); the Virgo gravitational wave detector in Cascina, Italy (Bradaschia et al. 1990); the GEO 600 detector near Hannover, Germany (Danzmann et al. 1992); and the TAMA 300 detector in Tokyo, Japan (Tsubono 1995). These detectors use laser interferometry and are described further in Section 1.1. There have been no detections of gravitational waves so far but advanced versions of the LIGO and Virgo detectors (planned for 2014) will significantly improve their sensitivity and increase the probability of a detection.

In addition to these ground-based detectors, there are plans for a much larger space-based gravitational wave detector, LISA (Laser Interferometer Space Antenna), that will be sensitive to gravitational waves at lower frequencies than its ground-based counterparts (Hughes 2006). A pathfinder mission to test the feasibility of LISA technology is planned for 2014 and if successful LISA itself should be launched between 2018 and 2020.

To be used to their full advantage gravitational wave detectors require predictions of event rates and the expected waveforms. There are several physical sources for ground-based detectors including supernovae, rotation of asymmetric compact objects, star quakes in white dwarfs and neutron stars, and the merger and coalescence of double-degenerate binary stars. Of these sources, the mergers of binaries where the members are neutron stars or black holes are considered to be the most promising for early detection (e.g. Thorne 1987) because they are relatively massive and can be detected out to large distances. Due to its lower frequency range LISA will be more sensitive to the inspiral of super-massive black holes (SMBHs) in galactic centres and cosmological sources such as topological defects or cosmic strings. LISA may also be able to detect stellar mass black hole-black hole (BH-BH) binaries in the galactic disk at larger orbital separations than the ground based detectors. Although the compact merger population in the galactic field has been subject to much investigation (see Section 1.2 and Chapter 2) the situation for star clusters where binaries can interact with other objects is less well-known. The focus of my work is to understand the binaries in star clusters that generate gravitational waves. For the remainder of the

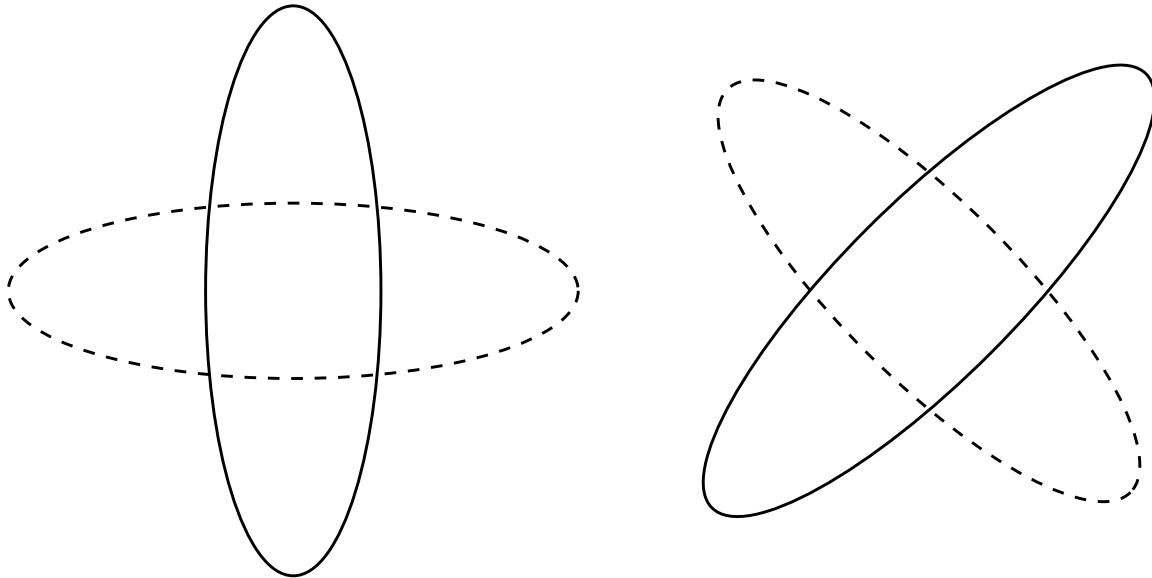


Figure 1.1: The two polarisation states for gravitational waves. On the left is the h_+ polarisation and on the right is the h_\times polarisation. A circle of test masses interacting with a gravitational wave travelling out of the page with a pure h_+ or h_\times polarisation will oscillate between the configurations shown in the solid and dotted lines.

introduction I give a brief description of gravitational wave detectors, explain why dense stellar systems are expected to be important for gravitational wave detection rates, and describe the basics of star cluster dynamics.

1.1 Interferometric Gravitational Wave Detectors

Gravitational waves are always transverse (at least in standard general relativity) and come in two polarisations, h_+ and h_\times , that are rotated 45° to each other (I will describe the reason for this further in Chapter 3). Figure 1.1 shows the reaction of a circle of test masses to a gravitational wave of either polarisation travelling out of the page. As the gravitational wave moves through the masses the distance between individual masses changes but, because gravitational waves are a metric perturbation rather than a force, the masses are not accelerated and only their separation is affected. By monitoring the distance between isolated test masses it is possible to detect the passage of a gravitational wave.

The current generation of gravitational wave detectors use laser interferometry to detect changes in distance between mirrors acting as isolated test masses. On the left of Figure 1.2 is the set-up for a typical ground-based detector (LIGO or Virgo). They are, in essence, large Michelson interferometers with Fabry-Perot interferometers embedded into the arms for additional sensitivity (Maggiore 2008). As a gravitational wave passes the interferometer, the relative arm lengths change as a function of time and the change can be measured with very high precision. The change that needs to be detected is $\Delta L = h_0 L/2$ where L is the length of the detector arm and h_0 is the amplitude of the gravitational wave at the detector. h_0 is very small, on the order of 10^{-21} , and thus ΔL is also very small. For a standard ground-based detector with ~ 4 km arms $\Delta L \sim 10^{-18}$ m (Maggiore 2008), smaller than the size of an atomic nucleus. The construction of such detectors and isolating and modelling

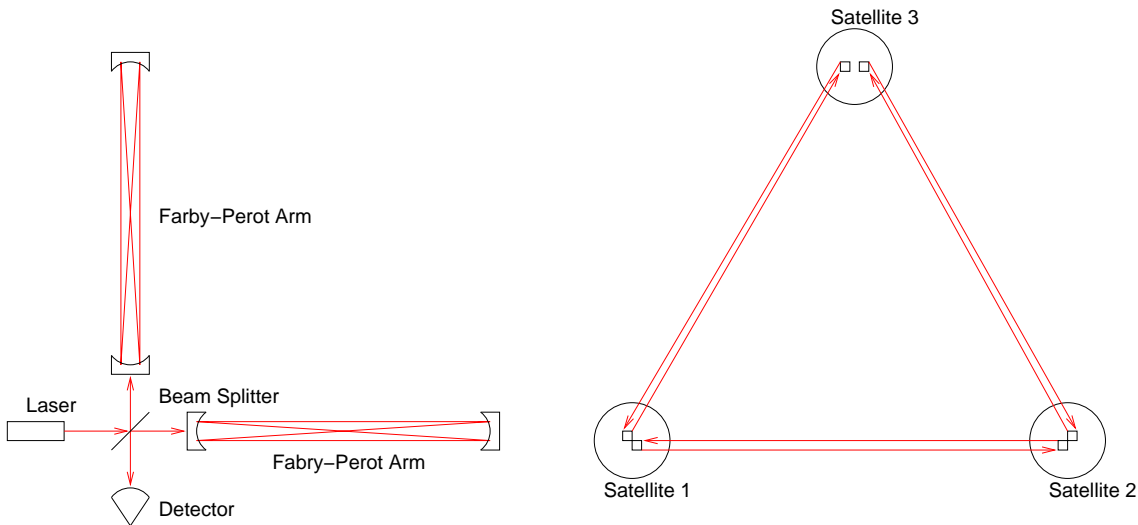


Figure 1.2: The interferometer configurations for ground-based gravitational wave detectors (left) and the space-based gravitational wave detector LISA (right).

noise sources is very complicated. Some information on the orientation of the gravitational wave with respect to the detector can be derived by considering the relative change in length of the arms and an array of gravitational wave detectors can give some idea of the sky position by comparing relative orientations and time delays between detection. LISA uses a slightly different configuration as shown on the left of Figure 1.2. It is a triangular configuration of three satellites, each with two test masses in free-fall. Each satellite uses a laser to measure the distance between one of the test masses in each of the other satellites. The underlying principle is, however, the same. The distance between the satellites is measured as a function of time and the change in separation can be used to detect the passage of a gravitational wave. The orientation of the wave relative to the observatory and the sky position of the source can be determined by combining information on the relative separations between the arms and how this changes as the observatory orbits around the sun.

A gravitational wave detector produces a time series of separations that are a convolution of noise (noise sources include seismic noise for ground-based detectors, thermal noise, shot noise, and even radiation pressure from the lasers on the mirrors) and (hopefully) gravitational wave signals. In order to detect a gravitational wave the noise must be removed. This is done by modelling the known noise sources and correcting for them. The simplest way to find gravitational waves is then to search the data for anomalous signals using band-pass filtering. In such searches a detection threshold is set in the time domain and a signal exceeding this threshold is counted as a detection. This method is useful for finding gravitational wave bursts of unknown form. The signal-to-noise ratio can be significantly improved by using matched filtering searches (Flanagan & Hughes 1998; Thorne 1987). Here template gravitational waveforms are generated by modelling physical sources and then the detector output is searched for matching signals. Gravitational wave templates for a binary require orbital parameters, source distances, orientation with respect to the observer, and sky location in order to be compared to the detector signal. A description of how this is done is given for double neutron star binaries in Abbott et al. (2005) and for BH-BH binaries in Abbott et al. (2006). It is obviously useful to have as complete a bank of

templates as possible to increase the sensitivity of the detectors. It is also helpful to know which sources are most likely to exist in nature in order to limit the necessary number of templates as far as possible and limit the number of free parameters in the fit.

1.2 Compact Binaries as Gravitational Wave Sources

For my purposes I define compact binaries to be binaries where both members are degenerate objects (white dwarfs (WDs), neutron stars (NSs), or black holes (BHs)). The late phase of compact binary evolution is governed by the emission of gravitational radiation. The power radiated by a binary in gravitational waves in the orbit-averaged approximation is $P = -32G\mu^2m_t^3/(5c^5a^5)f(e)$ where μ is the mass ratio, m_t the total mass of the binary, a the semi-major axis, and $f(e)$ a function dependent on the eccentricity of the binary (Peters 1964, this will be discussed further in Chapter 3). Thus compact binaries must be very close ($P < 1$ day) for gravitational wave radiation to strongly affect the orbital evolution. Some empirical estimates of event rates for gravitational wave detectors can be derived from observations of WD and NS binaries (Kalogera et al. 2001; Lorimer 2005; Narayan, Piran & Shemi 1991). Such methods are limited both by low-number statistics and because many gravitational wave sources, such as BH-BH binaries, are not visible in the electromagnetic spectrum. The event rates for un-observed objects must be constrained through population synthesis models where the evolution of a large number of binaries with a realistic distribution of initial conditions is calculated. Population synthesis in the galactic field (the population of stars in the galaxy not in star clusters), where binaries evolve, inspiral, and merge in isolation has been the focus of several studies (Belczynski, Benacquista & Bulik 2008; Belczynski, Kalogera & Bulik 2002; Belczynski et al. 2007; Fryer, Woolsey & Hartmann 1999; Portegies Zwart & Yungelson 1998). In general these studies have found that NS-NS mergers should be the most plentiful in the local universe. This is partly because they are produced in greater numbers due to the shape of the initial mass function (IMF). The IMF is the number of stars per unit mass and is normally taken to be a power-law (Kroupa, Tout & Gilmore 1993; Salpeter 1955) with a slope at the high-mass end of ~ -2.3 . Thus high-mass stars are less common than low mass stars, and since NSs have lower mass progenitors, they will be more plentiful than BHs. NS-NS binary progenitors also have a better chance of survival to the double-degenerate stage due to the details of mass transfer. BH-BH binaries may, however, make a significant contribution to the detection rate because they are significantly more massive and can be detected at greater distances. This will be discussed in Section 2.3.1.

In star clusters, where binaries can interact with both single stars and other binaries and where new binaries can be formed by dynamical interactions the situation becomes more complicated. Sigurdsson & Phinney (1993) predicted that dynamical interactions in dense stellar environments could enhance the number of BH-BH binaries. This view has been confirmed by further numerical simulations but none involving a self-consistent treatment of both stellar dynamics and stellar evolution. Gültekin, Miller & Hamilton (2004) and O’Leary et al. (2006) investigated the behaviour of BHs in clusters using simulations without stellar evolution and where the BHs were assumed to form a dynamically decoupled subsystem in the cluster centre. Sadowski et al. (2008) performed simulations with stellar evolution but assuming that BHs stay in equilibrium with the cluster stars (the opposite dynamical assumption). Both find differing degrees of enhancement in the number of BH-BH binaries. I will perform simulations with fully-self consistent stellar dynamics and a

treatment of stellar evolution to better constrain the compact binary population in star clusters. I will concentrate in this study on binaries containing neutron stars and black holes. White dwarfs populations in star clusters have been studied both as “loaded guns” for type Ia supernovae (Shara & Hurley 2002) and as noise sources for LISA (Ivanova et al. 2006; Ruiter et al. 2007; Willems et al. 2007). They are, however, weaker sources of gravitational wave radiation than the more massive NS and BH binaries and, due to their lower masses, will not be as strongly affected by dynamical processes in star clusters. Therefore, while my simulations do produce data on the white dwarf population, I will not consider white dwarfs in this work but save them for future study.

1.3 Basic Concepts in Star Cluster Dynamics

I now describe some of the basic dynamical processes that drive the evolution of star clusters. These processes govern the phase-space evolution of stars, relaxation times, mass-segregation, escape processes, and the gravothermal catastrophe. I will save a more detailed description of the few-body encounters affecting binaries for Chapters 2 and 4. The description in this section is condensed from Spitzer (1987) and Binney & Tremaine (1987). Both explore the subjects summarised here in much deeper and more quantitative detail.

1.3.1 Evolution of the Phase Space Distribution

Consider a cluster consisting of N gravitationally bound stars. The state of the system at a given time, t , is described by a distribution function, $f(\vec{x}, \vec{v}, t)$, in a $6N$ dimensional phase space of positions and velocities. The time-evolution of $f(\vec{x}, \vec{v}, t)$ can be described using the Boltzmann equation (Binney & Tremaine 1987):

$$\frac{\partial f}{\partial t} + \vec{v} \cdot \vec{\nabla} f - \vec{\nabla} \phi \cdot \frac{\partial f}{\partial \vec{v}} = \Gamma[f] \quad (1.1)$$

where ϕ is the overall gravitational potential of the system and $\Gamma[f]$ is called the collision term and represents the effect of close encounters between the stars. For $\Gamma = 0$ Equation 1.1 reduces to the classical collisionless Boltzmann equation.

If the term $\Gamma[f]$ can be determined then Equation 1.1 can be used to describe the evolution of the star system. There are several methods for solving $\Gamma[f]$. The simplest conceptually is direct N -body integration where each stellar orbit is integrated explicitly using Newton’s equation:

$$\ddot{\vec{r}}_i = -G \sum_{i \neq j}^N \frac{m_j (\vec{r}_j - \vec{r}_i)}{|\vec{r}_j - \vec{r}_i|^3} \quad (1.2)$$

and Equation 1.1 is never directly solved. This treatment is, in principle, the most accurate way to model a star cluster since it reproduces all of the micro physics exactly. The method suffers from poor scaling with system size ($\mathcal{O}(N^4)$ in the worst case) and requires high accuracy integration because of the exponential non-linear instabilities and deterministic chaos introduced by close encounters (Miller 1964). Another method is to use the Fokker-Planck equation where $\Gamma[f]$ is approximated in the weak scattering limit by an expansion

in powers of the phase space coordinates ($\vec{x}, \vec{v} \in \vec{w}$). Thus (Binney & Tremaine 1987):

$$\Gamma[f] = - \sum_{i=1}^6 \frac{\partial}{\partial w_i} [f(\vec{w}) \langle \Delta w_i \rangle] + \frac{1}{2} \sum_{i,j=1}^6 \frac{\partial^2}{\partial w_i \partial w_j} [f(\vec{w}) \langle \Delta w_i \Delta w_j \rangle] \quad (1.3)$$

where $\langle \Delta X \rangle$ is the expectation value of the phase space location over some Δt . Yet another method of approximating $\Gamma[f]$ that is mathematically equivalent to Equation 1.3 but very different in implementation is the Monte Carlo method. Here each star is represented individually, much as in the direct N-body method, and the effect of interactions with other stars is simulated by choosing a random scattering angle for each star during each time step by Monte Carlo sampling. This is the method I have chosen and I describe it in more detail in Chapter 4.

1.3.2 The Relaxation Time

There are two basic timescales used to describe star cluster evolution: the crossing time, t_{cross} , and the relaxation time, t_{rlx} . $t_{\text{cross}} = R/v$ is simply the time it takes a star with the average velocity in the system, v , to cross a cluster of diameter, R , and is roughly the same as the orbital timescale. The relaxation time is the time it takes for the velocity of a star in the cluster to change by the order of itself (Binney & Tremaine 1987). This can be thought of as the time necessary for a cluster to lose the memory of its initial conditions, or, more exactly, the time necessary for a random initial velocity distribution to approximate a Maxwellian (Spitzer 1987). It is shown in both Spitzer (1987) and Binney & Tremaine (1987) that:

$$t_{\text{rlx}} \propto \frac{0.1N}{\ln N} t_{\text{cross}} \quad (1.4)$$

A cluster older than t_{rlx} has lost the memory of its initial conditions and is said to be relaxed. t_{rlx} depends on the local density in the cluster, since a higher density leads to more interactions, and the local crossing time. For this reason t_{rlx} can vary throughout a cluster. In practise the dense core of a cluster is often fully relaxed while the less dense outer region (called the halo) is un relaxed. A typical global estimate for t_{rlx} is the relaxation time at the radius containing half the mass of the cluster, r_h . This is called the half-mass relaxation time, t_{rh} , and is given by Spitzer (1987) as:

$$t_{rh} = \frac{0.138}{\ln(\gamma N)} \sqrt{\frac{N r_h^3}{\langle m \rangle G}} \quad (1.5)$$

where $\ln \gamma N$ is called the Coulomb logarithm and γ is an empirically determined constant. t_{rh} is normally on the order of $10^7 - 10^9$ yrs for globular clusters. Since most galactic globular clusters are ~ 10 Gyr old they are dynamically relaxed objects. t_{rh} is normally assumed to be the dynamical timescale for star cluster evolution and two clusters that have evolved for the same number of half-mass relaxation times are said to have the same dynamical age, regardless of their physical age. Note that there are also other measures of the half-mass relaxation time, particularly that of Larson (1970):

$$t_{rxL} = \frac{9}{16G^2 \sqrt{\pi}} \frac{\sigma^3}{m_{\text{ave}} \rho \ln(\gamma N)} \quad (1.6)$$

where ρ is the local mass density, m_{ave} the average mass, and σ the average velocity dispersion. For consistency I will use the Spitzer (1987) definition for the rest of this work.

1.3.3 Mass Segregation

In self-gravitating systems encounters tend to equalise the kinetic energy between objects in order to achieve energy equipartition in phase space (Binney & Tremaine 1987). For initial conditions where the mass, position, and initial velocities of particles are uncorrelated the more massive particles will tend to have higher kinetic energies. It follows that during encounters massive stars will tend to lose kinetic energy to their less massive neighbours and as a result sink to the centre of the system. The mass stratification this produces is called mass segregation. The timescale for mass segregation in a two mass system is (Spitzer 1969):

$$t_{ms} \propto \frac{m_1}{m_2} t_{rh} \quad (1.7)$$

where $m_1 < m_2$. This has been confirmed using both Monte Carlo methods (Watters, Joshi & Rasio 2000) and direct N -body simulations (Khalisi, Amaro-Seoane & Spurzem 2007). Mass segregation has an important role in my work. The stars that leave massive compact remnants evolve very quickly and most neutron stars and black holes are produced in the first 100 Myr of a cluster's life. Compact remnants no longer suffer stellar mass loss and thus, due to continued mass-loss by the lower-mass stars, they rapidly become the most massive objects in the system. This means compact objects are strongly affected by mass segregation and rapidly move to the core of the cluster. This is the highest density region and has the shortest relaxation time. Thus the compact objects will experience a disproportionately large number of interactions.

Spitzer (1969) defines a quantity χ for the two-mass system such that:

$$\chi \equiv \frac{M_2}{M_1} \left(\frac{m_2}{m_1} \right)^{3/2} \quad (1.8)$$

where $M_{1,2}$ is the total mass in the cluster of stars with individual masses $m_{1,2}$. Spitzer (1969) goes on to show analytically that if $\chi > 0.16$ then it is impossible to achieve equipartition and the massive stars will continue to donate kinetic energy to the lighter stars, fall towards the centre, gain more kinetic energy, and further increase their departure from equipartition. This is called the equipartition or ‘‘Spitzer’’ instability. Equation 1.8 has been further investigated by numerical methods. The Monte-Carlo study by Watters, Joshi & Rasio (2000) suggested that equipartition is possible only when:

$$\Lambda \equiv \frac{M_2}{M_1} \left(\frac{m_2}{m_1} \right)^{2.4} < 0.32, \quad (1.9)$$

a slight modification of the analytical criterion. Khalisi, Amaro-Seoane & Spurzem (2007) define the equipartition parameter:

$$\eta = \frac{m_2 \sigma^2}{m_1 \sigma_1^2} \quad (1.10)$$

where $\sigma_{1,2}$ are the velocity dispersions of the two components. Equipartition is only attained when $\eta = 1$ and Khalisi, Amaro-Seoane & Spurzem (2007) use direct N -body simulations to show that this cannot occur for all choices of cluster initial conditions. Thus the Spitzer

instability can occur in realistic star clusters. In reality the massive objects form a small, dynamically decoupled subsystem in the centre of the cluster, that interacts only with itself. Since BHs are quite massive they should be particularly subject to this effect and this is the justification for the assumptions made in the models of Gültekin, Miller & Hamilton (2004) and O’Leary et al. (2006).

1.3.4 The Gravothermal Catastrophe

It is possible to define a dynamical temperature for a star cluster using the average velocity in the system (Binney & Tremaine 1987):

$$\frac{1}{2}mv_{\text{ave}}^2 = \frac{3}{2}k_B T \quad (1.11)$$

where v_{ave} is the average velocity over the entire cluster. The temperature can also be defined locally by taking a local velocity average if desired. By taking the average dynamical temperature per star and multiplying by the size of the system this can be related to the total kinetic energy:

$$E_K = \frac{3}{2}Nk_B T \quad (1.12)$$

Using the virial theorem ($E = -E_K$) this can then be related to the total energy of the system:

$$E = -\frac{3}{2}Nk_B T \quad (1.13)$$

and thus it is possible to calculate the heat capacity of a self gravitating system:

$$C = \frac{dE}{dT} = -\frac{3}{2}Nk_B \quad (1.14)$$

Because all the terms on the RHS of Equation 1.14 are positive the heat capacity for a self-gravitating system is negative and the loss of energy from the system actually causes its temperature to increase. This seemingly paradoxical result means that, in the absence of a heat source, there is no stable equilibrium solution for a self gravitating system.

Consider a star cluster with a high-density core surrounded by a low-density halo. The halo is not strongly self-gravitating and acts as a heat bath for the strongly self gravitating core. During any perturbation where the core becomes dynamically hotter than the halo, energy will flow from the core to the halo. Due to its negative heat capacity, this heats the core faster than the halo and the flow of energy cannot be shut off. The core will contract in response and continue to heat in a runaway process. This instability is known as the gravothermal catastrophe and was first noted in the context of star clusters by Antonov (1962). It has been further investigated analytically in the context of general isothermal spheres by Lynden-Bell & Wood (1968), and numerically in the context of star clusters by Hachisu et al. (1978) and Lynden-Bell & Eggleton (1980).

This effect manifests in star cluster simulations in a process known as core collapse where the core of the star cluster becomes very dense. This process does not proceed all the way to a singularity but is halted by the formation of an energy source in the core (Hénon 1971a, 1975) which has been found to be binary stars (Bettwieser & Sugimoto 1984; Goodman 1987; Hénon 1971a; Hut 1985). In their interactions with other stars these binaries act as a heat source and provide the system with energy. This process is analogous to the nuclear burning that preserves hydrodynamic equilibrium in stars and is thus christened

“binary burning”. Binary burning can bring the core back into equilibrium and even cause it to re-expand again (Bettwieser & Sugimoto 1984; Goodman 1987). The timescale for core collapse to occur is $12 - 20t_{rh}$ (Spitzer 1987), less than the lifetime of many galactic globular clusters. It is possible that some clusters in our galaxy may have undergone core collapse (Harris 1996).

1.3.5 Few-Body Interactions

In the galactic field stellar densities are sufficiently low that stars rarely interact. In star clusters however stellar densities can reach 10^5 pc^{-3} (Harris 1996) and thus interactions between stars are very likely. This is particularly true for binaries because their interaction cross-section depends on the semi-major axis of their orbit rather than their stellar radii. Important interactions include formation of binaries by tidal capture, formation of binaries by 3-body interactions, and binary-single and binary-binary interactions that can both increase and decrease the binary binding energy and change binary membership. Due to these interactions the binary population in a star cluster can be significantly different than that in the galactic field. All of these processes will be discussed in more detail in Chapters 2 and 4. Direct stellar collisions are also possible and are speculated to be the source of some anomalous types of stars (Freitag & Benz 2002; Portegies Zwart et al. 1999; Sills, Karakas & Lattanzio 2009). These objects will not emit gravitational waves and thus I do not investigate them in this work.

1.3.6 Escape Processes

A star can be removed from the system if its velocity exceeds the escape velocity of the cluster, $v_e^2 = -2U/m$ where m is the mass of the individual star and U is the potential energy of the cluster. Using the virial theorem v_e can be related to the average velocity in the cluster (Binney & Tremaine 1987):

$$\langle v_e^2 \rangle = -\frac{4U}{M} = 4\langle v^2 \rangle \quad (1.15)$$

where M is the total mass of the cluster and $E_K = 1/2M\langle v \rangle^2$ is the total kinetic energy of the cluster. There are two means by which a star can be accelerated beyond v_e : ejection and evaporation. In ejection the star is accelerated due to a single encounter with another star. Such interactions tend to be violent ($\Delta E/m \gg v_e$) and occur most often in binary-single and binary-binary interactions. This is due both to the large interaction cross-section for binaries compared to single stars and to the fact that binding energy from the binary can be liberated during the interaction and added to the kinetic energy of the centres of mass. Evaporation occurs when a star reaches escape velocity due to repeated weak encounters (relaxation). Relaxation tends to maintain a local Maxwellian velocity distribution. Because a fraction of 7.38×10^{-3} of the total number objects in such a distribution have a velocity greater than four times the square of the mean velocity (Binney & Tremaine 1987), there are always stars with $v > v_e$ in the system. Thus there are two types of escapers from a star system: those ejected rapidly by close encounters with $\Delta E/m \gg v_e$ and those that escape slowly due to repeated small-angle scattering events and with $\Delta E/m \approx v_e$ (e.g. Spurzem & Aarseth 1996) and which may populate the region $v > v_e$ for some time before they escape. Both of these processes ensure that the cluster can always produce stars with $v > V_e$ and the eventual fate of all star clusters is to dissolve due to escape processes.

There is also the possibility of tidal escape. In this case some external potential is applied to represent the galactic field and can strip stars away from the outer regions of the cluster. The simplest implementation of this is a tidal cutoff radius, r_t , calculated in an effective co-rotating galactic potential and beyond which stars are removed. There are two criterion that can be used for escape, the energy criterion and the apocenter criterion. With the energy criterion stars are removed if their energy exceeds the potential energy at the tidal radius, the so-called tidal energy. This is simple to implement but produces an escape rate that is too high (Ernst et al. 2007; Takahashi & Portegies Zwart 1998) because stars with energy equal to or exceeding the tidal energy can still remain in the cluster if they are on the correct orbits. A star with an energy equal to the tidal energy, for instance, will remain in the cluster if it is on anything other than a purely radial orbit. The more accurate apocenter criterion, proposed by Takahashi & Portegies Zwart (1998), takes the angular momentum, \vec{J} , of the star into account. Using this criterion, only stars with an orbital apocenter beyond the tidal radius will be removed. It is also worth noting that tidal escape is not an instantaneous process but stars will only escape once they have had time to move outside the cluster (on average after a crossing time). For this reason the tidal escape of a star from a star cluster simulation is often delayed for a crossing time crossing time using the formalism of Lee & Ostriker (1987). More complex treatments are needed in regions with strong tidal fields (see for example Ernst, Just & Spurzem (2009) for a treatment of tidal disruption near galactic centres) but tidal cut-offs are sufficient in the halo where I will be carrying out my simulations. Most of the escapers of interest to me will be massive compact binaries and these will be the result of violent ejection from the cluster core. These escapers will have velocities well above v_e and are thus unlikely to be affected by the details of the tidal field.

1.4 Overview

I consider the population statistics of compact binaries in star clusters and analyse them as gravitational wave sources. In Chapter 2 I discuss the properties of compact binaries in general both in star clusters and in the galactic field. In Chapter 3 I consider the relativistic effects that govern the evolution of double degenerate binaries and how these binaries generate gravitational waves. In Chapter 4 I describe the Monte Carlo code I use to model the evolution of star clusters. In Chapter 5 I describe the initial conditions used in my simulations. In Chapters 6 and 7 I describe the binary population that remains in the clusters and the binaries that escape from the cluster respectively. In Chapter 8 I describe the prospects for detecting these binaries with both ground- and space-based detectors. In Chapter 9 I briefly describe new results for a set of million body simulations. Finally Chapter 10 I discuss my results and give some prospects for future directions.

Chapter 2

The Formation of Compact Binaries

Several types of binaries with different observational signatures contain compact objects. Cataclysmic variables (CVs) consist of white dwarfs accreting matter from either a dwarf star or another white dwarf. CVs demonstrate complex and time-variable optical properties and may produce dwarf novae if the receiving white dwarf accretes a sufficient amount of material. High- and low-mass X-ray binaries (HMXBs and LMXBs) contain a neutron star or black hole accreting from a high-mass main sequence star (a star still burning hydrogen in its core) (HMXBs), a low-mass main sequence star, or a white dwarf (LMXBs). HMXBs and LMXBs are observed primarily in X-rays emitted from the accretion disk around the compact object. Pulsar binaries contain at least one pulsar (a rapidly rotating neutron star with a strong radio jet) with a compact companion. The companion is usually a white dwarf or neutron star although a black hole companion is possible. These binaries are observed due to their radio pulses. Finally black hole-black hole binaries are possible but they are non-luminous and cannot be observed without gravitational wave observatories. A list of binary types and their observational signatures is given in Hilditch (2001). Each of these binaries is a potential source of gravitational wave radiation.

There are several mechanisms that can lead to the formation binaries containing compact objects. The final configuration of an isolated binary depends on the details of the various stages of mass transfer that are in turn determined by the initial masses and separation of the binary components. In the dense stellar environments found in the cores of star clusters, binaries can interact with the surrounding stars and the evolution can be supplemented by changes the binding energy of the binary or even changes in membership due to the exchange of one of the original binary members for another star. Therefore a dense stellar environment can have a major effect on its binary population.

In this section I will discuss the processes that lead to the formation of compact binaries both in isolation and in star clusters. In Section 2.1, I will discuss the evolution of binaries in isolation. In Section 2.2, I will discuss how a dense stellar environment can affect the evolution of a binary. Finally, in Section 2.3, I will discuss current results regarding the population of compact binaries both in the galactic field and in star clusters.

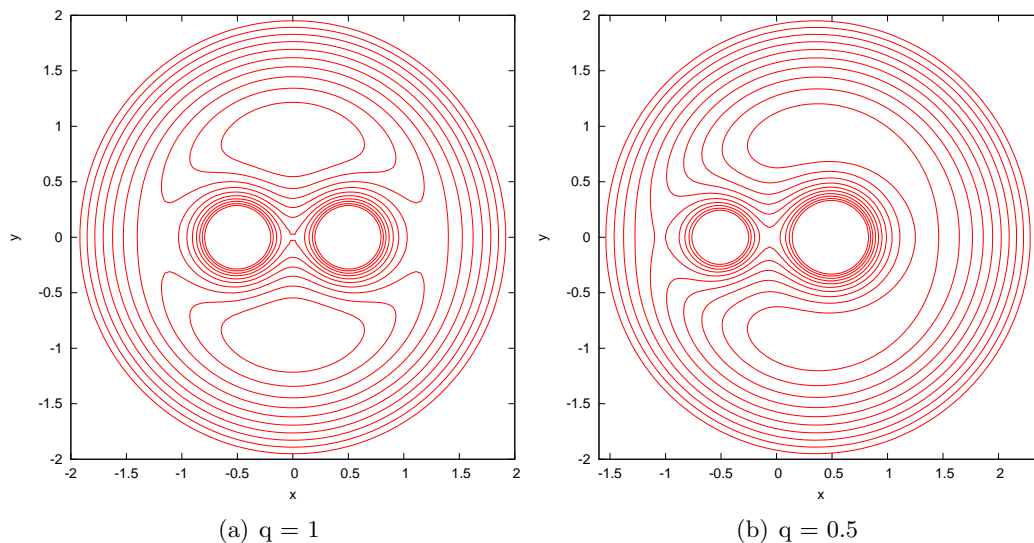


Figure 2.1: The equipotential surfaces of the Roche model for a circular orbit for a binary with a mass ratio of 1 (left) and 0.5 (right). Units are normalised to a separation of $a = 1$.

2.1 The Evolution of Isolated Binaries

In this section I consider the evolution of an isolated primordial binary, that is, a binary where both stars are formed in a bound orbit around a common centre of mass and that remains unaffected by interactions with other objects. In this case the evolution of the binary is completely determined by the mass of the binary members, m_1 and m_2 , the mass ratio, $q = m_2/m_1$, the initial separation between the centres of the stars, a , and possibly the eccentricity of the orbit, e . The more massive star is called the primary and the less massive the secondary. This section is based on the description of mass transfer in Hilditch (2001) and the review of relativistic binaries in star clusters by Benacquista (2006).

The Roche model, named for the 19th century mathematician Edouard Roche who studied the restricted three-body problem (Hilditch 2001), governs the evolution of binary stars. In this model each star is surrounded by an ellipsoidal region, called its Roche lobe, where its own gravity is dominant. Any particle inside a star's Roche lobe is gravitationally bound to the star and belongs to it alone. Outside the Roche lobe of either star the total gravitational potential of the binary is dominant and any matter here belongs to the binary as a whole but neither star individually. Choosing a rotating, non-inertial coordinate system where the primary is located at the origin and the x -axis points towards the secondary then, for a circular orbit with the mass normalised to the total mass of the binary and $a \equiv 1$, the potential of the Roche lobe model is (Hilditch 2001):

$$\Phi_N = \frac{2}{(1+q)r_1} + \frac{2q}{(1+q)r_2} + \left(x - \frac{q}{1+q}\right)^2 + y^2 + \mathcal{O}(x^3, y^3) \quad (2.1)$$

where r_1 is the distance from the primary and r_2 is the distance from the secondary. An example of the equipotential surfaces of the Roche potential is given in Figure 2.1.

The Roche lobes meet at the inner Lagrangian point. As long as the radius of each star remains smaller than its Roche lobe, its evolution is not strongly affected by the presence of the other member. If, however, the radius of one of the stars expands beyond its Roche

lobe (either due to the orbit shrinking or the star expanding) then its outer layers no longer remain bound and mass transfer to the other star can occur in a process called Roche lobe overflow (RLOF).

There are three relevant timescales for mass transfer: dynamical, thermal, and nuclear. Furthermore mass transfer can be either conservative (all mass lost by the donor is accreted by the receiver) or non-conservative (not all mass is accreted and some is lost from the system). The dynamical timescale is the time the a star takes to re-establish hydrostatic equilibrium after a perturbation (Hilditch 2001):

$$t_{dyn} = \left(\frac{2R^3}{Gm}\right)^{1/2} \approx 40 \left[\left(\frac{R}{R_\odot}\right)^3 \frac{M_\odot}{m} \right]^{1/2} \text{ min} \quad (2.2)$$

where R is the radius of the star and m is its mass. t_{dyn} is on the order of minutes for solar mass stars. The thermal timescale is the time it takes the star to re-establish thermal equilibrium after a perturbation (Hilditch 2001):

$$t_{th} = \frac{Gm^2}{RL} \approx 3.0 \times 10^7 \left(\frac{m}{M_\odot}\right)^2 \left(\frac{R_\odot}{R}\right) \left(\frac{L_\odot}{L}\right) \text{ yrs} \quad (2.3)$$

where L is the luminosity of the star. t_{th} is on the order of Myrs for solar mass stars. Finally the nuclear timescale is essentially the main-sequence (core hydrogen-burning) lifetime of the star (Hilditch 2001):

$$t_{nuc} = (7 \times 10^9) \frac{m}{M_\odot} \frac{L_\odot}{L} \text{ yrs} \quad (2.4)$$

t_{nuc} is on the order of Gyrs for solar mass stars.

The type of mass transfer occurring is determined by the rate of change in stellar radius as a response to a change in mass compared to the rate of change in the size of the Roche lobe of the star. This comparison can be made by computing the logarithmic derivatives of the mass-radius relationships that characterises the dependence of an object's radius on its mass:

$$\zeta = \frac{d \ln R}{d \ln M} \quad (2.5)$$

for each kind of mass transfer to the exponent for the Roche lobe. ζ can be calculated for mass changes occurring on each timescale for specific stars using stellar evolution models and for the Roche lobe by using the approximation to the Roche lobe radius in terms of the mass ratio of Eggleton (1983):

$$r_L = \frac{0.49q^{2/3}}{0.69a^{2/3} + \ln(1 + q^{1/3})} \quad (2.6)$$

Hjellming & Webbink (1987) describe how the exponents for each timescale ζ_{dyn} , ζ_{th} , and ζ_{nuc} , can be compared to the exponent for the Roche lobe, ζ_L . If $\zeta_L > \zeta_{dyn}$ then the mass transfer occurs faster than the dynamical timescale of the donor and the mass transfer rate is limited only by the sound speed at the inner Lagrange point. In such a situation mass transfer is said to be dynamically unstable. If $\zeta_{dyn} < \zeta_L < \zeta_{th}$ then the donor can maintain hydrostatic equilibrium but the Roche lobe shrinks faster than t_{th} and mass transfer takes place across the inner Lagrangian point on a thermal timescale. Finally if $\zeta_{th} < \zeta_L$ then

the star can also restore thermal equilibrium and mass transfer can only occur due to slow stellar-evolutionary processes such as main sequence expansion or magnetic breaking.

Conservative mass transfer occurs when all material lost from the donor is accreted by the receiver. The condition for conservative mass transfer is a transfer rate slower than the dynamical timescale of the receiver. Only then can the receiver adjust its state fast enough to absorb all the donated mass. Conservative mass transfer is usually a result of either slow stellar expansion on the main sequence or a slowly decreasing separation due to magnetic breaking or gravitational radiation. No mass is lost from the system so, assuming a negligible contribution from the spin angular momentum of the individual stars, the total angular momentum of the system remains constant:

$$J_{orb} = \left[\frac{Gm_1^2 m_2^2 a (1 - e^2)}{M_{tot}} \right]^{1/2} \quad (2.7)$$

and assuming e remains constant the separation can be written $a = \text{constant}/(m_1 m_2)^2$. Thus, although the angular momentum remains constant, the separation of the orbit, and hence its period, can change due to conservative mass transfer. By Kepler's third law the period of a binary, P , is related to the semi-major axis by:

$$P^2 = \frac{4\pi^2 a^3}{G(m_1 + m_2)} \quad (2.8)$$

Recalling the relation for a , the ratio of the periods before (P_i) and after a mass exchange process is:

$$\frac{P}{P_i} = \left[\frac{m_{1i} m_{2i}}{m_1 m_2} \right]^3 \quad (2.9)$$

where m_{1i} and m_{2i} are the masses before the mass exchange. Differentiating Equation 2.9 with respect to time yields:

$$\frac{\dot{P}}{P_i} = 3 \left[\frac{m_{1i} m_{2i}}{m_1 m_2} \right]^2 \left[-\frac{\dot{m}_1}{m_1^2 m_2} - \frac{\dot{m}_2}{m_1 m_2^2} \right] m_{1i} m_{2i} \quad (2.10)$$

For conservative mass transfer $\dot{m}_1 = -\dot{m}_2$ so, with some manipulation, Equation 2.10 can be re-written:

$$\frac{\dot{P}}{P} = \frac{3\dot{m}_1(m_1 - m_2)}{m_1 m_2} \quad (2.11)$$

If the more massive star, m_1 , loses mass then $\dot{m}_1 < 0$. Thus, since $m_1 - m_2 > 0$, $\dot{P} < 0$ and the orbit shrinks. If, however, the less massive star, m_2 , loses mass then $\dot{m}_1 > 0$ but $m_1 - m_2 < 0$. Thus $\dot{P} > 0$ and the orbit expands. In general the more massive star evolves more quickly on the main sequence and is the first to overflow its Roche lobe and initiate mass transfer. Therefore conservative mass transfer, at least initially, tends to causes binary orbits to shrink. When $m_1 = m_2$, however, a minimum separation is reached and if m_1 continues to donate mass the process is reversed and the orbit re-expands until m_1 no longer overflows its Roche lobe. m_2 can now expand and overflow its Roche lobe, initiating a second phase of mass transfer and orbital shrinking. Depending on the masses and separations of the stars, there can be multiple phases of conservative mass transfer in a binary.

Non-conservative mass transfer takes place when the receiving star cannot accrete all of the mass lost by the donor star and some of the mass is lost from the binary system. There are three types of non-conservative mass transfer: mass loss due to stellar winds, Roche lobe overflow on timescales shorter than the dynamical timescale of the receiver, and supernova explosions.

Mass loss due to stellar winds always leads to an increase in the orbital period. Assuming a spherically symmetric wind that does not interact with the second star, the linear velocity of the star losing mass remains constant and the angular momentum changes only due to mass-loss. Differentiation of Equation 2.8 yields:

$$\frac{\dot{P}}{P} = \frac{1}{2(m_1 + m_2)} \left[3(m_1 + m_2) \frac{\dot{a}}{a} - \dot{m}_1 \right] \quad (2.12)$$

Assuming a circular orbit the requirement for constant linear velocity of the losing star can be written $a_1 2\pi/P = \text{constant}$ (where m_1 is the star assumed to be losing mass), and by recalling from the transformation to centre of mass coordinates that $a_1 = am_1/(m_1 + m_2)$, then:

$$\frac{\dot{a}}{a} = -\frac{\dot{m}_1}{m_1 + m_2} \quad (2.13)$$

and thus the period evolution is given by:

$$\frac{\dot{P}}{P} = -\frac{2\dot{m}_1}{m_1 + m_2} \quad (2.14)$$

Since stellar winds always remove mass from a star $\dot{m}_1 < 0$ and $\dot{P} > 0$. This mechanism is not of interest for the formation of relativistic compact binaries since it will increase the separation of the binary and move it away from the relativistic regime.

During RLOF on timescales shorter than the dynamical timescale of the receiver the radius of the receiver cannot adjust quickly enough to absorb all of the donated matter and some must be lost from the system. This most commonly occurs when the primary expands very quickly (often as it is moving up the giant branch) and completely engulfs the secondary in a process known as common envelope (CE) evolution. In this situation the orbital energy of the binary is used to eject the envelope of the donor from the system, normally through the outer Lagrange point. The efficiency of the ejection process is given by the parameter (Benacquista 2006):

$$\alpha_{CE} = \frac{\Delta E_{bind}}{\Delta E_{orb}} \quad (2.15)$$

where ΔE_{bind} is the binding energy of the mass stripped from the the envelope of the donor and ΔE_{orb} is the change in orbital energy of the binary. If $\Delta E_{bind} > \Delta E_{orb}$ the binary cannot eject all of the envelope and will merge due to viscous friction. If $\Delta E_{bind} < \Delta E_{orb}$ the binary will be able to eject the envelope of the donor and the result will be a tight binary with the former secondary (now usually the most massive member) orbiting the stripped core of the former primary. This process results in a shorter period since the most massive member is the donor, because of the orbital angular momentum carried away by the ejecta, and due to the large amount of viscous friction in the common envelope. If the former secondary is still on the main sequence this process can happen a second

time as the secondary moves onto the giant branch. This can lead either to a merger or a double-degenerate binary (usually WD-WD).

In the case of a supernova, mass-loss is instantaneous and often disrupts a binary. It can, however, lead to a binary with an NS or BH and a high eccentricity. To describe the basic processes involved, I follow Padmanabhan (2000) as presented in Benacquista (2006) and consider the case of a circular binary, neglecting the effect of the expanding shell on the secondary, and assuming the velocity of the remnant does not change in response to the supernova (there is no natal kick). The binding energy before the supernova is given by:

$$E_i = \frac{1}{2} \left(\frac{m_1 m_2}{m_1 + m_2} \right) v^2 - \frac{G m_1 m_2}{r} \quad (2.16)$$

where v is the relative velocity between the two components and r is their separation. Following the supernova event and the passage of the shell of matter beyond the orbit of the secondary the energy is:

$$E_f = \frac{1}{2} \left(\frac{m_r m_2}{m_r + m_2} \right) v^2 - \frac{G m_r m_2}{r} \quad (2.17)$$

Where m_r is the mass of the compact remnant left by the supernova. Since I have assumed that the secondary is unaffected by the passage of the matter shell, that the remnant receives no natal kick, and assuming a circular orbit, the instantaneous velocity of each member is unaffected and is given by:

$$v^2 = \frac{G(m_1 + m_2)}{r} \quad (2.18)$$

and Equation 2.17 can be re-written as:

$$E_f = \frac{G m_r m_2}{2r} \left(\frac{m_1 + m_2}{m_r + m_2} - 2 \right) \quad (2.19)$$

E_f will be positive and the binary disrupted if $m_r < (m_1 + m_2)/2$. Therefore a binary will be disrupted after a supernova event if:

$$\Delta m > \frac{m_1 + m_2}{2} \quad (2.20)$$

where Δm is the change in mass of the exploding star. If the binary survives it will gain a new orbital separation of (Hilditch 2001):

$$r_f = r \left(\frac{m_1 + m_2 - \Delta m}{m_1 + m_2 - 2\Delta m} \right) \quad (2.21)$$

a new period of:

$$P_f = P_i \left(\frac{r_f}{r} \right)^{3/2} \left(\frac{2r_f - r}{r_f} \right)^{1/2} \quad (2.22)$$

and an induced eccentricity of:

$$e_f = \frac{\Delta m}{m_1 + m_2 - \Delta m} \quad (2.23)$$

The remnant can also receive a velocity boost in a random direction (called a natal kick) due to a non-spherical supernova explosion. Such kicks are thought to be ubiquitous and can significantly reduce the chances of a binary surviving the supernova event (Lyne & Lorimer 1994; Pfahl, Rappaport & Podsiadlowski 2002). The distribution of velocity kicks is thought to be Maxwellian with a dispersion of $\sim 190 \text{ km s}^{-1}$ (Hansen & Phinney 1997). Such kicks will also impart higher eccentricities in the surviving binaries. In practise, few binaries will survive the supernova of both their members and NS-NS, NS-BH, and BH-BH binaries should be fairly rare outcomes of isolated binary evolution.

The final outcome of compact binary evolution depends both on the nature of mass transfer and when it takes place. Classically mass transfer has been divided into four epochs based on when the primary initiates RLOF (Kippenhahn & Weigert 1967):

Case A: Mass transfer while the donor is still on the main sequence in the hydrogen core burning phase. A very short initial period, normally less than a few days, is necessary in order for RLOF to be initiated this early.

Case B: Mass transfer while the donor is expanding to the red giant phase with a helium core and hydrogen burning shell. This occurs for binaries with initial periods of less than 100 days but longer than for Case A mass transfer.

Case C: Mass transfer while the donor is in the red super-giant phase with a degenerate core and hydrogen and helium shell burning. This usually takes place in binaries with an initial period of more than 100 days.

Case D: Initial separation so large that mass transfer never occurs. The binary members evolve as isolated stars.

Binaries that experience Case D mass transfer will have separations too large to be interesting for gravitational wave detection and will be so weakly bound that they are unlikely to survive any kind of supernova event.

Case A mass transfer tends to be a result of Roche lobe overflow that occurs on nuclear timescales and as such is usually conservative. The normal outcome for Case A mass transfer is a stellar merger since it usually leads to common envelope evolution brought on by mutual Roche lobe overflow by both members. As such, Case A mass transfer will produce few compact binaries (Hilditch 2001).

Case B mass transfer can be either dynamically stable or unstable. During Case B mass transfer the primary normally donates enough mass to the secondary to reverse their roles but not enough for the primary to avoid a supernova. Due to this role-reversal it is the less massive star that first experiences a supernova and the chances of the binary surviving the event are increased. Most HMXBs are thought to result from Case B mass transfer (Hilditch 2001).

Finally Case C mass transfer is normally dynamically unstable and non-conservative. Like Case B mass transfer the primary and secondary usually exchange roles but also undergo common envelope evolution. It is possible for the primary to retain enough mass to undergo a supernova explosion and produce an LMXB but it is more likely that either the envelope of the primary is completely stripped, leaving a degenerate core or for the binary to merge. Binaries with a stripped degenerate core normally become CVs (Hilditch 2001).

In principle compact binaries can be produced by any of these processes depending on the mass of the secondary and the details of later stages of mass transfer. WD-WD binaries

will be by far the most common both because WDs are lower mass and due to the shape of the IMF are more plentiful than NSs and BHs and because they do not have to survive a supernova. As will be shown in Section 2.3, however, some binaries containing NSs and BHs do exist.

2.2 The Formation of Compact Binaries in Star Clusters

Binaries in dense environments have the evolution described in Section 2.1 supplemented by interactions. These can be classified into three types: interactions between two or more single stars that can form new binaries, interactions between binaries and single stars that can increase or decrease the orbital separation and can exchange stars between the field and the binary, and interactions between binaries that provide the same opportunities as binary-single interactions but for both binaries. This section is based on the review of Benacquista (2006), Spitzer’s book on the dynamical evolution of star clusters (Spitzer 1987), and the paper by Heggie (1975) giving the original description of binary-single interactions.

2.2.1 Single-Single Interactions

The interactions between single stars can form new binaries through tidal capture or 3-body interactions. Tidal capture was first proposed as a mechanism for the formation of X-ray sources in star clusters by Fabian, Pringle & Rees (1975). In tidal capture two stars encounter each other on an elongated relative orbit. The close passage at pericenter excites non-radial tidal oscillations within the stars and, if enough kinetic energy is dissipated in these oscillations, the orbit becomes bound. The exact nature of the oscillations is not important for the final nature of the orbit, only the amount of energy dissipated. Even though the kinetic energy at pericenter is very high, it is only necessary to reduce the total energy at *apocenter* to less than zero in order to obtain a bound orbit. The condition for tidal capture is:

$$\Delta E_{T1} + \Delta E_{T2} \geq \frac{1}{2} m_r v^2 \quad (2.24)$$

where $\Delta E_{T1,T2}$ is the amount of energy associated with the tidal oscillations in each star, m_r is the reduced mass of the pair, and v is the relative velocity at apocenter (or infinity). Thus only $\sim (v/v_p)^2$ where v_p is the velocity at pericenter needs to be converted to tidal energy in order for capture to occur. The typical velocity dispersion in a globular cluster is of the order 10 km s^{-1} whereas the relative velocity of the pair at closest approach can be on the order of 100 km s^{-1} or more (Fabian, Pringle & Rees 1975). Thus the actual fraction of kinetic energy dissipated in tidal oscillations can be very small. Since this process forms binaries from stars on nearly hyperbolic orbits the eccentricity of the orbit of the new binary will be very high initially. The binary will circularise over time due to further tidal dissipation at pericenter.

The periastron distance for tidal capture must be small, normally on the order of a few stellar radii with some dependence on the equation of state of the star, in order to excite strong enough tidal oscillations for tidal capture to occur (Fabian, Pringle & Rees 1975; Lee & Ostriker 1986; Press & Teukolsky 1977) so this process tends to form very close binaries. Tidal capture is, however, unlikely to form close binaries from single compact objects because of their very small radii and the difficulty of exciting tidal oscillations in degenerate matter. Gravitational radiation may enhance the capture rate of compact objects by providing a mechanism other than tidal oscillations to dissipate energy during

close encounters. This possibility will be briefly discussed in Chapter 10. Furthermore, tidal capture is no longer thought to be a major formation channel for binaries in star clusters because the most likely outcome of such encounters is in fact a merger between the two stars involved (Benz & Hills 1987; Lee & Ostriker 1986; McMillan, McDermott & Taam 1987; Ray, Kembhavi & Antia 1987). Thus it is unlikely that tidal capture binaries are present in large numbers in star clusters.

Three-body capture is another way to remove the relative kinetic energy between two stars and leave them on a bound orbit. In this process three stars come close together and interact. One star gains kinetic energy at the expense of the others and is ejected. If enough kinetic energy is removed the remaining stars are left on a bound orbit. In general the least massive star is the one ejected since it is the easiest to accelerate to the escape velocity of the three-body system. Heggie (1975) shows that if x is the binding energy of the new binary the rate of three-body binary formation is $\propto x^{-7/2}$ and in contrast to tidal capture, three-body formation strongly favours the creation of binaries with low binding energy and large separation. Therefore a merger is a much less likely outcome than for tidal capture. Most of these binaries will be quickly disrupted by further interactions but some fraction will actually have their binding energy increased by these interactions and their periods will shrink. A binary with a binding energy $x/k_B T \approx 1$ where $k_B T$ is the thermal energy of the cluster will have a 10% chance of surviving and increasing its binding energy until $x/k_B T \approx 10$ at which point its survival probability in interactions is almost unity (Goodman & Hut 1993; Spitzer 1987). For a system of equal-mass stars, all of solar mass and radius, and with a velocity dispersion of 10 km s^{-1} the rate of production of such long-lived binaries due to three-body encounters is $\approx 1.91 \times 10^{-13} (n/10^4 \text{ pc}^{-3})^3 \text{ pc}^{-3} \text{ yr}^{-1}$ (Goodman & Hut 1993; Hut 1985; Spitzer 1987) whereas the rate of production of binaries due to tidal capture is $\approx 1.52 \times 10^{-8} (n/10^4 \text{ pc}^{-3})^2 \text{ pc}^{-3} \text{ yr}^{-1}$ for a stellar equation of state of polytropic index 3. From this it is apparent that the rate of binary formation should be dominated by tidal capture for $n < 7.96 \times 10^8 \text{ pc}^{-3}$ after which three-body capture should dominate. Due to the large number of mergers that result from tidal capture when the finite size of stars is taken into account (Lee & Ostriker 1986; McMillan, McDermott & Taam 1987; Ray, Kembhavi & Antia 1987), however, three-body capture can actually be important at lower stellar densities. It is worth noting, however, that neither of these mechanisms will produce very many binaries. Maintaining the assumption of equal-mass, solar-type stars and choosing $n = 10^5 \text{ pc}^{-3}$, three-body capture will produce only 2 – 3 binaries over a Hubble time and tidal capture will produce only 1.4×10^4 (not taking into account the merges which can be the outcome of more than 50% of tidal capture events (Benz & Hills 1987; Lee & Ostriker 1986)). Therefore most binaries in star clusters must trace their history back to a binary formed as part of the star formation process, a so-called primordial binary. Binaries can, however, have stars exchanged into them as will be described next and thus not all individual stars in binary systems need to have been formed there.

2.2.2 Binary-Single Interactions

Binary-single interactions are complicated, especially in the multi-mass case, but in the equal mass case the generic outcomes can be understood based on the change in energy during the interaction. Considering a three-body system where all stars are of equal mass m , two of which start bound and one that approaches from infinity then x is the initial binding energy of the binary, y is the change in binding energy of the binary and can be

either positive or negative, V_0 is the initial velocity of the approaching star with respect to the centre of mass of the three-body system, and V_1 is the velocity at infinity with respect to the centre of mass for the departing star after the interaction. Working in the rest frame of the centre of mass and noting that the reduced mass for the relative motion of a single star with respect to the binary is $\mu_{3b} = m_3(m_1 + m_2)/(m_1 + m_2 + m_3) = 2m/3$ then by conservation of energy $(1/3)mV_1^2 = (1/3)mV_0^2 + y$ and the following outcomes are possible (Heggie 1975):

- If $y > 0$ then the single star is accelerated at the expense of the orbital energy of the binary and the binding energy of the binary increases.
- If $-(1/3)mV_0^2 < y < 0$ the single star still escapes to infinity but there are two possible outcomes.
 - If $-x < y$ the binary survives but has its binding energy decreased.
 - If $-(1/3)mV_0^2 < y < -x$ the binary is disrupted. If $y < -x$ and $y < -(1/3)mV_0^2$ then the third body can in fact be captured in a process similar to three-body capture and one of the original binary members escapes.
- If $-x < y < -(1/3)mV_0^2$ no particle escapes and a resonant interaction occurs. A semi-stable three-body system is formed and its evolution is governed by further interactions with other stars.

For the multi-mass case the interaction can be broadly characterised by V_c , the critical velocity where the kinetic energy of the single star is equal to x . For binary masses m_1 and m_2 and a single star mass of m_3 (Hut & Bahcall 1983):

$$V_c^2 = \frac{m_1 + m_2 + m_3}{m_3(m_1 + m_2)} \quad (2.25)$$

If $V > V_c$ where V is the velocity of the star encountering the binary, then the binary can not capture the single star and the single star can disrupt the binary. If $V < V_c$ then the binary can capture the single star and cannot be disrupted by the process. This introduces an important way of classifying binaries: those where $x < k_B T$, where $k_B T$ is the thermal energy of the cluster per unit mass defined in Section 1.3.4, are called soft binaries and those where $x > k_B T$ are called hard binaries. Normally stars encountering a soft binary have $V > V_c$ and thus soft binaries tend to lose binding energy and/or be disrupted in their interactions with single stars. Soft binaries can also experience exchange interactions where a member of the binary is swapped for the encountering star. This process functions in a very similar way to three-body capture. It is of course possible for soft binaries to encounter stars with $V < V_c$ and thus increase their binding energy (harden). The soft binaries that form due to three-body capture and survive do so because they harden in this way. Normally stars that encounter hard binaries have $V < V_c$ and thus hard binaries are seldom disrupted by interactions with single stars. The binding energy of a hard binary increases on average by $\langle y \rangle = 0.4x$ due to an encounter with a single star assuming a Maxwellian velocity distribution (Heggie 1975) although this is only fully valid for very hard binaries (Hut 1985). Thus the binding energy of hard binaries tend to increase due to interactions and the period gets shorter. Hard binaries can also capture passing stars and form stable three-body systems. These three-body systems can be disrupted during later encounters or, depending on the exact dynamics of the interaction, eject one of the

original binary stars in favour of the third body. The behaviour of soft vs. hard binaries is summarised in Heggie’s law “Hard binaries tend to get harder and soft binaries tend to get softer” (Heggie 1975).

Through the exchange interactions, binary-single encounters provide a method for introducing field stars into binaries. As in the case of three-body capture, it tends to be the lightest star that gains the most kinetic energy and is removed. Thus binary-single interactions tend to introduce massive objects, such as black holes, into pre-existing binaries. It has been shown (Hills & Fullerton 1980; Spitzer 1987) that for $m_3 \gg m_1$ or m_2 that the probability for the massive star to be exchanged into the binary during the encounter is ~ 1 .

2.2.3 Binary-Binary Interactions

There are more possible outcomes for binary-binary interactions than for binary-single interaction and they depend sensitively on the details of the encounter. Therefore there is no detailed, quantitative theory for the outcomes of binary-binary encounters. One possibility is that the two binaries are sufficiently distant that they appear to each other as single stars. In this case a hardening or softening interaction will occur for both binaries depending on their relative velocities and binding energies. There are also general results for close encounters between two hard binaries, A and B, where all stars have equal mass. If A is assumed to be much harder than B then A can be treated as a single star with a mass twice that of B. This means that an exchange where one of the stars in B escapes and is replaced by binary A is the most likely outcome. This leaves a triple configuration with the remaining member of B bound to A. If the remaining member of B comes close enough to A it will either be ejected or exchanged into A. If the remaining member does not come close enough, a semi-stable triple system is formed that can be disrupted by further interactions with other stars. It is also possible, although unlikely, that both binaries survive and can even exchange members with each other. The only way to determine the relative probability of different outcomes is to perform numerical experiments with many different initial parameters. Results from Mikkola (1983), Mikkola (1984a) and Mikkola (1984b) for equal mass binaries show that in 88% of cases the softer binary is disrupted and the harder binary hardens. In the other 12% of cases both binaries survive on a hyperbolic orbit relative to each other. Similar prescriptions, partially based on Mikkola’s work have been provided by Gao et al. (1991) and have also been used in Fokker-Planck and Monte-Carlo codes. Ultimately binary-binary interactions provide a mechanism to change binary membership and can harden compact binaries but often lead to the destruction of at least one of the binaries involved in the interaction.

A dense stellar environment generally increases the population of compact binaries. New compact binaries can be created by three-body encounters and existing binaries can have compact objects from the field exchanged into them. Binaries that are already compact can also be brought closer to the gravitational radiation regime by hardening interactions. In Section 2.3 I briefly review the current work addressing the importance of dense stellar environments for compact binaries.

2.3 Current Results for Compact Binaries

There have been several population synthesis studies of NS-NS, NS-BH, and BH-BH binaries in both the galactic field and in star clusters. I here consider the current results and what my work has to build upon.

2.3.1 Population Synthesis in the Galactic Field

There have been several studies of the neutron star and black hole binary population in the galactic field (Belczynski, Benacquista & Bulik 2008; Belczynski, Kalogera & Bulik 2002; Belczynski et al. 2007; Fryer, Woolsey & Hartmann 1999; Portegies Zwart & Yungelson 1998). In these studies the evolution of a large number of isolated binaries is calculated assuming various star formation rates and using analytic stellar and binary evolution tracks. In general these authors find that the majority of mergers in the galactic field will be NS-NS binaries. In particular Belczynski, Kalogera & Bulik (2002) find that in the galactic field 61% of mergers involve NS-NS binaries, 30% involve BH-BH binaries and only 9% NS-BH binaries. This is because neutron stars are more plentiful due to the steep power-law drop-off in the IMF at high masses and because NS-NS binaries are more likely to survive the various mass transfer phases and become double-degenerate. This result is dependent on the treatment of common envelope evolution and in particular Belczynski et al. (2007) show that for a donor star in the Hertzsprung gap (a phase where the star does not have a clear boundary between its outer envelope and its inner, nuclear burning core) a merger is a very likely outcome of the mass transfer event. This affects all binaries but particularly the progenitors of BH-BH binaries and the number of BH-BH merges is sharply reduced. Assuming a space density of 0.01 Milky Way type galaxies per Mpc Belczynski et al. (2007) predicts an NS-NS detection rate of $\sim 20 \text{ yr}^{-1}$ for advanced LIGO, a BH-BH detection rate of $\sim 2 \text{ yr}^{-1}$ and only $\sim 1 \text{ detection yr}^{-1}$ for NS-BH binaries. Thus there is a good chance for the next generation of ground-based detectors to observe relativistic mergers from galactic field populations and this rate should be dominated by NS-NS binary inspirals.

Belczynski, Benacquista & Bulik (2008) perform a similar analysis for Milky Way stellar-mass binaries in the LISA band. They find that there is a rather small formation efficiency for LISA sources with only a few thousand detections for all types of binaries. These results also depend strongly on the treatment of common envelope evolution and in particular if common envelope evolution is allowed during the Hertzsprung gap phase there will be a negligible signal from BH-BH binaries. Therefore NS-NS inspirals will dominate the field population signal for both ground-based and space-based detectors.

2.3.2 Binaries in Clusters

Several studies have examined the compact binary population in star clusters. Sigurdsson & Phinney (1993) proposed that capture and exchange interactions in the cores of star clusters should efficiently move massive stars into binaries. This work was taken up by Gültekin, Miller & Hamilton (2004) using scattering experiments with a rough treatment of gravitational radiation to determine if intermediate mass black holes (IMBHs) can be formed through interactions and merger between stellar mass black holes in star clusters. Gültekin, Miller & Hamilton (2004) found that interactions and mergers between black holes are common, particularly in young clusters, but the chance of IMBH formation was low because most binaries are ejected from the core by the scattering events or the GW

recoil produced at the merger. They found that BH-BH binaries that will pass through the LISA band with maximum eccentricities of $0.8 - 0.9$ are formed in young clusters and will later merge and be visible in the LIGO band. O’Leary et al. (2006) performed an analysis assuming that the BH population is forms a decoupled subsystem in the core due to mass segregation, that is, the BHs are Spitzer unstable (see Section 1.3.3). They simulated only the BH subsystem explicitly and embedded it inside a cluster potential. They used Monte Carlo sampling to chose interactions between BHs and/or BH-BH binaries and directly integrating the few-body encounters. They confirmed that mergers of compact binaries occurred with some frequency in young dense clusters but that BH-BH binaries are efficiently ejected from the cluster either during interactions or due to gravitational wave recoil after mergers. Thus most BH-BH binaries are gone from the cluster in less than 1 Gyr. Using a standard cosmological model and assuming one cluster per Mpc^3 O’Leary et al. (2006) calculated a detection rate for the advanced version of the LIGO detector and found $\sim 1 - 10$ detections per year, depending on the initial cluster model, for clusters that formed at $z = 7.8$ (approximately 13 Gyr ago). They also find that 30-70% of mergers occur outside the cluster after the binary has been ejected. Neither Gültekin, Miller & Hamilton (2004) nor O’Leary et al. (2006) include a treatment of stellar evolution in their simulations.

Ivanova et al. (2006, 2008) have considered simplified two-zone (core-halo) models of globular clusters with stellar evolution prescriptions and direct few-body integration of encounters. They have analysed these simulation for binaries containing white dwarfs and neutron stars but not black holes. They find the X-ray fluxes of CVs (WD binaries) are increased and posit that this is due to more massive WDs being exchanged into these binaries. They also find that most binaries containing a neutron star gain it by an exchange interaction. In general however they find very few NS-NS binaries and conclude that they are not efficiently formed in star clusters.

The Ivanova et al. (2008) models been extended to black holes by Sadowski et al. (2008) who find that unlike NS-NSs, BH-BH binaries are efficiently produced by cluster dynamics. These two-zone models assume that the BHs always remain in dynamical equilibrium with the other stars in the cluster and thus cannot experience the Spitzer instability. This is the opposite dynamical assumption to that made by O’Leary et al. (2006). Unlike O’Leary et al. (2006) Sadowski et al. (2008) observe a fairly constant rate of BH-BH mergers, most due to dynamically formed binaries, at rates of $\sim 2.5 \text{ Gyr}^{-1}$. They analyse this merger rate for detection by current and advanced LIGO, finding only $\sim 0.01 - 1$ detection per year for current LIGO but $\sim 25 - 3000$ mergers per year for advanced LIGO. This fraction depends both on the cluster model and the fraction of stars in the universe assumed to be in star clusters. This is a far larger detection rate than reported by O’Leary et al. (2006) and emphasises the effect different treatments of cluster dynamics can have. Including stellar evolution allows them to determine that there are no neutron star binaries and thus the detection rate from star clusters will be dominated by BH-BH mergers. They find systematically higher masses for their BH-BH binaries than for the field population but all of their simulations use low metallicity ($Z = 0.001$) and this is most likely a metallicity effect.

Finally Portegies Zwart & McMillan (2000) have performed small ($N \sim 10^3$) direct N-body simulations with full stellar evolution to understand the behaviour of compact objects in star clusters. They find results consistent with O’Leary et al. (2006), namely that black holes and BH-BH binaries are quickly ejected from clusters and that old clusters should have at most one black hole or BH-BH binary in their core. This implies that the constant

merger rate of Sadowski et al. (2008) is unlikely to be seen in reality but the simulations are too small to give conclusive results.

My primary goal is to use fully self-consistent dynamical models with realistic particle numbers to investigate the behaviour of compact binaries in star clusters. Specifically I will be able to determine if and how quickly the BHs mass-segregate and whether objects other than BHs can take part in dynamical binary formation if full cluster dynamics are included. The Monte Carlo code I use contains full stellar evolution prescriptions so that I can determine the relative importance of different merger species in star clusters. The stellar evolution prescriptions are valid for a variety of metallicities so I will be able to explore the metallicity dependence of compact binary production and determine if the mass enhancement reported by Sadowski et al. (2008) has a stellar dynamical or stellar evolutionary origin. I will be able to determine the number of binaries that escape from the cluster and determine if any of the escapers can merge in the galactic field. I will also be able to use my results of my simulations to produce detection rates for both ground- and space-based detectors. By comparing my results to theirs, I will also be able to determine whether the O'Leary et al. (2006) or Sadowski et al. (2008) approximation more accurately matches the full dynamical result and thus which is more likely to produce an accurate estimate of the gravitational wave detection rate.

Chapter 3

The Relativistic Evolution of Compact Binaries

Once a binary becomes double-degenerate its evolution is governed by emission of gravitational wave radiation. Gravitational waves are metric perturbations that carry both energy and angular momentum. For compact binaries the energy used to generate gravitational waves is taken from the orbital energy and thus separation between the stars decreases. If the binaries are close enough they will be able to merge and the gravitational waves produced by this merger will be detectable by ground-based gravitational wave detectors such as Virgo and LIGO. At larger separations and lower frequencies the waves can be detected by the space-based LISA mission. Much of this chapter is based on the texts of Cheng (2005) and Maggiore (2008) as well as the review by Hughes (2009).

3.1 The Linearised Field Equations

The Einstein field equations for the response of spacetime to a mass-energy distribution are:

$$G_{\mu\nu} = R_{\mu\nu} - \frac{1}{2}g_{\mu\nu}R = -\frac{8\pi G}{c^4}T_{\mu\nu} \quad (3.1)$$

where $R_{\mu\nu}$ is the reduced Riemann curvature tensor (the Ricci curvature tensor) and $R = \text{tr}[R_{\mu\nu}]$ is the Ricci scalar. $g_{\mu\nu}$ is the metric tensor describing the background curvature of spacetime. $T_{\mu\nu}$ describes that mass-energy distribution producing the spacetime curvature on the LHS of Equation 3.1. G and c are the Newtonian gravitational constant and the speed of light respectively.

Far from the gravitational wave source Equation 3.1 can be linearised by writing the metric tensor as:

$$g_{\mu\nu} = \eta_{\mu\nu} + h_{\mu\nu} \equiv g_{\mu\nu}^{(1)} \quad , \quad |h_{\mu\nu}| \ll 1 \quad (3.2)$$

where $\eta_{\mu\nu}$ is the flat Minkowski metric and $h_{\mu\nu}$ is the perturbation due to a gravitational wave. $g_{\mu\nu}^{(1)}$ indicates that, because $h_{\mu\nu}$ is small, only first-order terms in $h_{\mu\nu}$ are kept. Inserting Equation 3.2 into $G_{\mu\nu}$ and keeping only first order terms yields (Hughes 2009):

$$G_{\mu\nu} = \frac{1}{2} \left(\partial_\mu \partial^\alpha h_{\alpha\nu} - \partial_\nu \partial^\alpha h_{\alpha\mu} - \partial_\mu \partial_\nu h - \square h_{\mu\nu} + \eta_{\mu\nu} \square h - \eta_{\mu\nu} \partial^\alpha \partial^\beta h_{\alpha\beta} \right) \quad (3.3)$$

where $h = \text{tr}[h_{\mu\nu}]$. Equation 3.3 can be greatly simplified both by using the trace-reversed metric:

$$\bar{h}_{\mu\nu} = h_{\mu\nu} - \frac{1}{2}\eta_{\mu\nu}h \quad (3.4)$$

where $\text{tr}[\bar{h}_{\mu\nu}] = -h$ and working in the Lorentz (or harmonic) gauge where:

$$\partial^\mu \bar{h}_{\mu\nu} = 0 \quad (3.5)$$

In this case Equation 3.3 takes on a particularly simple form:

$$G_{\mu\nu} = -\frac{1}{2}\square\bar{h}_{\mu\nu} \quad (3.6)$$

and the linearised field equation becomes:

$$\square\bar{h}_{\mu\nu} = -\frac{16\pi G}{c^4}T_{\mu\nu} \quad (3.7)$$

This is a wave equation and in analogy to classical electrodynamics the solution is a radiative Green's function (Hughes 2009) of the form:

$$\bar{h}_{\mu\nu}(\vec{x}, t) = \frac{4G}{c^4} \int d^3\vec{x}' \frac{T_{\mu\nu}(\vec{x}', t - |\vec{x} - \vec{x}'|)}{|\vec{x} - \vec{x}'|} \quad (3.8)$$

The radiative solutions to Equation 3.8 represent gravitational waves.

Although it appears from Equation 3.8 that all components of $\bar{h}_{\mu\nu}$ are radiative this is not actually the case. to gain some insight into the nature of gravitational waves consider a gravitational wave propagating in a vacuum where:

$$\square\bar{h}_{\mu\nu} = 0 \quad \Rightarrow \quad \square h_{\mu\nu} = 0 \quad (3.9)$$

The solution to these equations are plane waves of the form (Cheng 2005):

$$h_{\mu\nu}(\vec{x}, t) = \varepsilon_{\mu\nu} e^{ik_\alpha x^\alpha} \quad (3.10)$$

where $\varepsilon_{\mu\nu}$ and k_α are the polarisation and wave vectors respectively. Equation 3.5 still leaves some residual gauge freedom (Cheng 2005) and gravitational waves can always be represented using the transverse-traceless (TT) gauge where:

$$k^\mu \varepsilon_{\mu\nu} = 0 \quad (3.11)$$

and:

$$\varepsilon^\mu{}_\mu = 0 \quad (3.12)$$

Therefore only the transverse and traceless elements of $h_{\mu\nu}$ are non-zero. A gravitational wave propagating in the z direction can be written explicitly as:

$$h_{\mu\nu}(z, t) = \begin{pmatrix} 0 & 0 & 0 & 0 \\ 0 & h_+ & h_\times & 0 \\ 0 & h_\times & -h_+ & 0 \\ 0 & 0 & 0 & 0 \end{pmatrix} e^{i\omega(z-ct)/c} \quad (3.13)$$

with the two polarisation states:

$$\varepsilon_{(+)}^{\mu\nu} = h_+ \begin{pmatrix} 0 & 0 & 0 & 0 \\ 0 & 1 & 0 & 0 \\ 0 & 0 & -1 & 0 \\ 0 & 0 & 0 & 0 \end{pmatrix}, \quad \varepsilon_{(\times)}^{\mu\nu} = h_\times \begin{pmatrix} 0 & 0 & 0 & 0 \\ 0 & 0 & 1 & 0 \\ 0 & 1 & 0 & 0 \\ 0 & 0 & 0 & 0 \end{pmatrix} \quad (3.14)$$

These are the h_+ and h_\times in Figure 1.1.

3.2 Power Generation by Gravitational Waves

Gravitational waves carry energy and angular momentum away from the binary (Peters & Mathews 1963). To calculate the energy flux carried by a gravitational wave it is necessary to calculate the perturbation the gravitational wave induces in the background metric. To do so the metric tensor can be written (Cheng 2005; Maggiore 2008):

$$g_{\mu\nu} = g_{\mu\nu}^{(b)} + h_{\mu\nu} \quad (3.15)$$

where in contrast to Equation 3.2 the background metric, $g_{\mu\nu}$, is allowed to have a small curvature introduced by $h_{\mu\nu}$ and $g_{\mu\nu}^{(b)} = \eta_{\mu\nu} + \mathcal{O}(h^2)$. Such a decomposition is only possible by assuming that variations in the background metric have much longer frequencies than the variations in $h_{\mu\nu}$ and thus the scales are well-separated. The Ricci tensor (and hence the Ricci scalar) can be decomposed in a similar fashion:

$$R_{\mu\nu} = R_{\mu\nu}^{(b)} + R_{\mu\nu}^{(1)} + R_{\mu\nu}^{(2)} + \dots \quad (3.16)$$

where $R_{\mu\nu}^{(n)}$ is $\mathcal{O}(h^n)$. The background term $R_{\mu\nu}^{(b)}$ depends only on $g_{\mu\nu}^{(b)}$ by construction and thus contains only low-frequency modes. By contrast $R_{\mu\nu}^{(1)}$ is the only term linear in $h_{\mu\nu}$ and thus contains only high-frequency modes. The term $R_{\mu\nu}^{(2)}$ is quadratic in $h_{\mu\nu}$ and Maggiore (2008) show that it can contain both high- and low-frequency modes. Ignoring terms of more than quadratic order in $h_{\mu\nu}$ this means that the Einstein field equations can be decomposed into high- and low-frequency parts (Maggiore 2008):

$$R_{\mu\nu}^{(1)} = -[R_{\mu\nu}^{(2)}]_{\text{high}} + \frac{8\pi G}{c^4} \left(T_{\mu\nu} - \frac{1}{2} g_{\mu\nu} T \right)_{\text{high}} \quad (3.17)$$

$$R_{\mu\nu}^{(b)} = -[R_{\mu\nu}^{(2)}]_{\text{low}} + \frac{8\pi G}{c^4} \left(T_{\mu\nu} - \frac{1}{2} g_{\mu\nu} T \right)_{\text{low}} \quad (3.18)$$

where $t = \text{tr}(T_{\mu\nu})$. In free-space Equation 3.17 reduced to Equation 3.7 while Equation 3.18 describes the response of the background metric to the presence of a gravitational wave. Since the frequency scales are assumed to be well-separated, it is possible to average away the high-frequency fluctuations over the low-frequency timescale. This averaging procedure is well-defined for tensors up to $\mathcal{O}(\lambda^2/L^2)$ where λ is the gravitational wavelength and L is the fluctuation scale in the background metric (Hughes 2009). Thus Equation 3.18 can be re-written (Maggiore 2008):

$$R_{\mu\nu}^{(b)} = -\langle R_{\mu\nu}^{(2)} \rangle + \frac{8\pi G}{c^4} \left\langle T_{\mu\nu} - \frac{1}{2} g_{\mu\nu} T \right\rangle \quad (3.19)$$

Now in free-space $T_{\mu\nu} = 0$ and thus Equation 3.19 reduces to:

$$R_{\mu\nu}^{(b)} = \langle R_{\mu\nu}^{(2)} \rangle \quad (3.20)$$

The gravitational wave itself has an associated mass-energy tensor, $t_{\mu\nu}$ that is responsible for the curvature in the background metric and $R_{\mu\nu}^{(b)}$ must satisfy Equation 3.1:

$$R_{\mu\nu}^{(b)} + \frac{1}{2}\eta_{\mu\nu}R^{(b)} = -\frac{8\pi G}{c^4}t_{\mu\nu} \quad (3.21)$$

Inserting Equation 3.20 into Equation 3.21 gives a condition for the mass-energy tensor of the gravitational wave in terms of $\langle R_{\mu\nu}^{(2)} \rangle$ only (Cheng 2005):

$$t_{\mu\nu} = \frac{c^4}{8\pi G} \left[\langle R_{\mu\nu}^{(2)} \rangle - \frac{1}{2}\eta_{\mu\nu}\langle R^{(2)} \rangle \right] \quad (3.22)$$

Maggiore (2008) calculates the terms in the Ricci tensor that are second-order in $h_{\mu\nu}$ and, inserting them into Equation 3.22, finds a mass-energy tensor:

$$t_{\mu\nu} = \frac{c^4}{32\pi G} \langle \partial_\mu h_{\alpha\beta} \partial_\nu h^{\alpha\beta} \rangle \quad (3.23)$$

The gauge invariant energy density is given by the term t^{00} (Cheng 2005). In the TT gauge only the spatial coordinates are non-zero and t_{00} can be written (Maggiore 2008):

$$t_{00} = \frac{c^4}{32\pi G} \langle \dot{h}_{ij}^{TT} \dot{h}_{ij}^{TT} \rangle \quad (3.24)$$

The energy flux for a wave travelling at a speed of c is simply ct^{00} , thus after noting the tensor transformation:

$$\frac{dE}{dAdt} = \frac{c^3}{32\pi G} \langle \dot{h}_{ij}^{TT} \dot{h}_{ij}^{TT} \rangle \quad (3.25)$$

The energy flux can be related to the physical properties of the binary by calculating h_{ij} as a multipole expansion of Equation 3.8 in the far-zone, long wavelength limit. If D is the orbital separation of the binary, r the distance to the observer, and λ the gravitational wavelength then in the regime where $r \gg D$ and $\lambda \gg D$ then Equation 3.8 can be re-written:

$$\bar{h}_{ij} \approx \frac{1}{r} \frac{4G}{c^4} \int d^3\vec{x}' T_{ij}(\vec{x}', t - r/c) \quad (3.26)$$

In the Lorentz gauge the continuity equations are (Hughes 2009):

$$\partial^t T_{tt} + \partial^j T_{jt} = 0 \quad \text{and} \quad \partial^t T_{tj} + \partial^i T_{ij} = 0 \quad (3.27)$$

Equation 3.26 can then be integrated by parts and Equation 3.27 and Gauss's theorem can be used to discard the surface terms. The first two terms vanish meaning that gravitational wave sources emit neither monopole (as in classical electrodynamics) nor dipole radiation. Thus the leading order radiation term is quadrupole:

$$\frac{1}{r} \frac{4G}{c^4} \int d^3\vec{x}' T_{ij}(\vec{x}', t - r/c) \quad \rightarrow \quad \frac{1}{2} \frac{d^2}{dt^2} \int d^3\vec{x}' x^i x^j T_{tt}(\vec{x}', t - r/c) \quad (3.28)$$

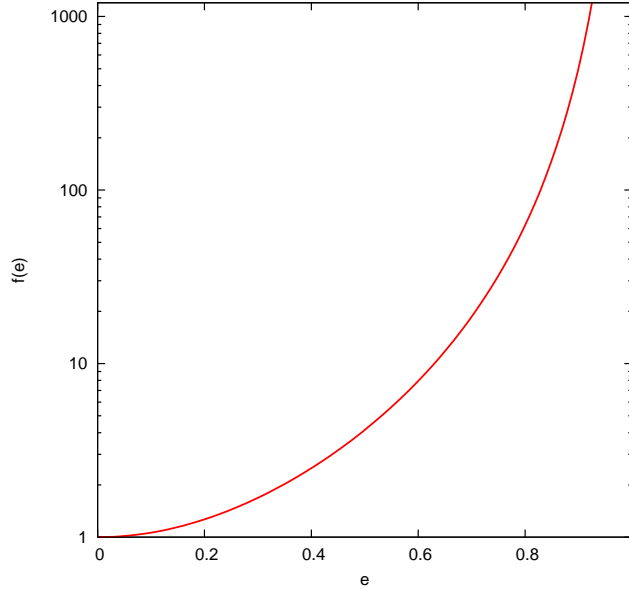


Figure 3.1: The gravitational wave power enhancement due to eccentricity, $f(e) = (1 - e^2)^{-7/2} (1 + 73/24e^2 + 37/96e^4)$

where $T_{tt} = \text{tr}[T_{ij}]$ is simply the local energy density $\rho(x)c^2$. Thus the integral in Equation 3.28 can be re-written in terms of the second mass moment:

$$I_{ij} = \int d^3\vec{x} \rho(\vec{x}) x_i x_j \quad (3.29)$$

and to quadrupole order:

$$\bar{h}_{ij} = \frac{1}{r} \frac{2G}{c^4} \frac{d^2}{dt^2} I_{ij}(t - r/c) \quad (3.30)$$

This is called the quadrupole formula for gravitational radiation and can be easily converted into the TT gauge with the transformation (Hughes 2009):

$$h_{ij}^{TT} = \bar{h}_{ij} (P_{ki} P_{lj} - \frac{1}{2} P_{kl} P_{ij}) \quad (3.31)$$

where for a gravitational wave traveling in the direction \vec{n} , P_{ij} is the matrix that projects spatial coordinates orthogonal to \vec{n} and is given by:

$$P_{ij} = \delta_{ij} - n_i n_j \quad (3.32)$$

Therefore in the TT gauge the quadrupole formula for gravitational waves is (Hughes 2009):

$$h_{ij}^{TT} = \frac{i}{r} \frac{2G}{c^4} \ddot{I}_{ij} (P_{ki} P_{lj} - \frac{1}{2} P_{kl} P_{ij}) \quad (3.33)$$

Integrating Equation 3.25 over all angles and then inserting Equation 3.33 we get:

$$\dot{E} = \frac{dE}{dt} = \int d\Omega r^2 \frac{dE}{dAdT} = \frac{G}{5c^5} \langle \ddot{I}_{ij} \ddot{I}_{ij} \rangle \quad (3.34)$$

Thus the power radiated by a rotating body due to gravitational wave radiation is, related to the third time derivative of its quadrupole moment. For a binary in a Kepler orbit with a semi-major axis a , eccentricity e , and masses m_1 and m_2 , I_{ij} can be written explicitly. The non-zero terms are (Peters & Mathews 1963):

$$\begin{aligned} I_{11} &= \mu d^2 \cos^2 \psi \\ I_{22} &= \mu d^2 \sin^2 \psi \\ I_{12} &= I_{21} = \mu d^2 \cos \psi \sin \psi \end{aligned} \quad (3.35)$$

where $\mu = m_1 m_2 / (m_1 + m_2)$ is the reduced mass,

$$d = \frac{a(1 - e^2)}{1 + e \cos \psi} \quad (3.36)$$

and

$$\psi = \frac{\sqrt{G(m_1 + m_2)a(1 - e^2)}}{d^2} \quad (3.37)$$

These can be inserted into Equation 3.34 and averaged over an orbital period to find the classical formula of Peters & Mathews (1963) relating the gravitational radiation from a Keplerian binary to its orbital parameters:

$$\langle \dot{E} \rangle = \frac{32}{5} \frac{G^4}{c^5} \frac{m_1^2 m_2^2 (m_1 + m_2)}{a^5 (1 - e^2)^{7/2}} \left(1 + \frac{73}{24} e^2 + \frac{37}{96} e^4 \right) \quad (3.38)$$

It is worth noting that the radiated power is very strongly enhanced at high eccentricities due to the close passages at periastron. For a binary of eccentricity > 0.9 the power radiated in gravitational waves can be enhanced by a factor of 10^3 or more over a binary with the same parameters but with a circular orbit. The shape of the enhancement function is plotted in Figure 3.1.

Inspirational Timescales [Myr]			
e	$q = 1$	$q = 0.5$	$q = 0.1$
0.0	5113	9290	41888
0.1	4790	8764	39245
0.2	3949	7176	32355
0.3	2878	5230	23582
0.4	1859	3372	15205
0.5	1047	1902	8576
0.6	500	908	4095
0.7	168	340	1536
0.8	46	83	378
0.9	4	7	33

Table 3.1: The inspiral timescale for energy loss due to the emission of gravitational radiation in Myrs. Note that the inspiral timescale decreases with both increasing eccentricity and increasing stellar mass. The initial period is always one day and the mass of the primary is $10 M_\odot$.

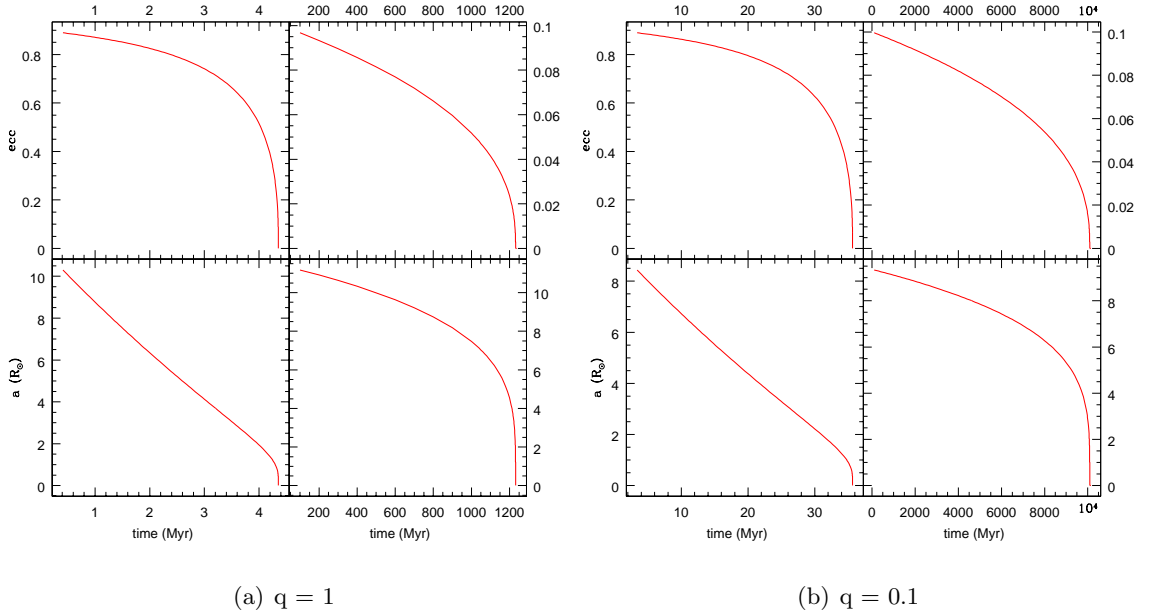


Figure 3.2: The gravitational wave inspiral for compact binaries. On the left $m_1 = m_2 = 10M_\odot$ and on the right $m_1 = 10M_\odot$ and $m_2 = 1M_\odot$. For both plots the top panels are the eccentricity and the bottom the semi-major axis. On the left of both plots is for an initial eccentricity of 0.9 and on the right an eccentricity of 0.1. Both higher mass and higher initial eccentricity leads to significantly faster inspiral. Note that the left and right scales on the y-axis are not the same for the different eccentricities..

It is possible to perform a similar calculation for the radiated angular momentum. However, the details are significantly more difficult because the mass-current moment as well as the mass-moment of the source must be invoked. The calculation was performed in Peters (1964) and I merely quote the result:

$$\langle \dot{L} \rangle = -\frac{32}{5} \frac{G^{7/2}}{c^5} \frac{m_1^2 m_2^2 \sqrt{m_1 + m_2}}{a^{7/2} (1 - e^2)^2} \left(1 + \frac{7}{8} e^2 \right) \quad (3.39)$$

By combining Equation 3.38 with Equation 3.39 the evolution of the semi-major axis and eccentricity can be calculated in the quadrupole approximation (Peters 1964):

$$\langle \dot{a} \rangle = -\frac{64}{5} \frac{G^3}{c^5} \frac{m_1 m_2 (m_1 + m_2)}{a^3 (1 - e^2)^{7/2}} \left(1 + \frac{73}{24} e^2 + \frac{37}{96} e^4 \right) \quad (3.40)$$

$$\langle \dot{e} \rangle = -\frac{304}{15} e \frac{G^3}{c^5} \frac{m_1 m_2 (m_1 + m_2)}{a^4 (1 - e^2)^{5/2}} \left(1 + \frac{121}{304} e^2 \right) \quad (3.41)$$

Using the Equations 3.40 and 3.41 the gravitational wave inspiral timescale for binaries can be estimated simply by taking a/\dot{a} and e/\dot{e} . Table 3.1 shows the results for various initial eccentricities and mass ratios. It is also possible to solve Equations 3.40 and 3.41 using a simple numerical integrator and calculate the the evolution a and e under the influence of gravitational radiation. The results of such a calculation using a simple Runge-Kutta 4th-order integrator I have written are shown in Figure 3.2.

3.3 Radiated Power as a Function of Harmonic

The radiated power is a strong function of eccentricity. As well as the total power, it is interesting to look at the power radiated at each harmonic of the orbital frequency. Following Pierro et al. (2001) the mass moments in Equation 3.35 can be re-written:

$$\begin{aligned} I_{11} &= \mu a^2 \xi^2 \\ I_{22} &= \mu a^2 \zeta^2 \\ I_{12} &= I_{21} = \mu a^2 \xi \zeta \end{aligned} \quad (3.42)$$

where:

$$\xi = \left(\frac{d \cos \psi}{a} \right) \quad \text{and} \quad \zeta = \left(\frac{d \sin \psi}{a} \right) \quad (3.43)$$

According to Kepler equations for the eccentric and mean anomaly, E and M :

$$\frac{d \cos \psi}{a} = \cos E - e \quad \frac{d \sin \psi}{a} = (1 - e^2)^{1/2} \sin E \quad (3.44)$$

$$M = \frac{2\pi t}{T} = \omega t = E - e \sin E \quad (3.45)$$

where T is the orbital period and ω is the orbital frequency. The quantities defined in Equation 3.42 do not represent harmonic motion for anything other than a circular orbit. Thus ξ and ζ must be expanded in a Fourier series:

$$\begin{aligned} \xi^2 &= \frac{\gamma_0}{2} + \sum_{n=1}^{\infty} \xi_n \cos nM \\ \zeta^2 &= \frac{\delta_0}{2} + \sum_{n=1}^{\infty} \zeta_n \sin nM \\ \xi \zeta &= \sum_{n=1}^{\infty} (\xi \zeta)_n \sin nM \end{aligned} \quad (3.46)$$

The Fourier coefficients, ξ_n , ζ_n , and $(\xi \zeta)_n$ are calculated in Pierro et al. (2001) and are found to be combinations of Bessel functions of the eccentricity and harmonic order (n), $J_n(ne)$:

$$\begin{aligned} \xi_n &= \frac{1}{n} [J_{n-2}(ne) - J_{n+2}(ne)] - \frac{2e}{n} [J_{n-1}(ne) - J_{n+1}(ne)] \\ \zeta_n &= -\frac{1}{n} [J_{n-2}(ne) - J_{n+2}(ne)] \\ (\xi \zeta)_n &= \frac{1}{n} (1 - e^2)^{1/2} [J_{n-2}(ne) + J_{n+2}(ne) - 2J_n(ne)] \end{aligned} \quad (3.47)$$

I_{ij} can now be represented in terms of a Fourier series and Equation 3.34 used to find the power radiated at each harmonic of the orbital frequency:

$$\langle \dot{E}_n \rangle = \frac{32 G^4 m_1^2 m_2^2 (m_1 + m_2)}{5 c^5 a^5} g(n, e) \quad (3.48)$$

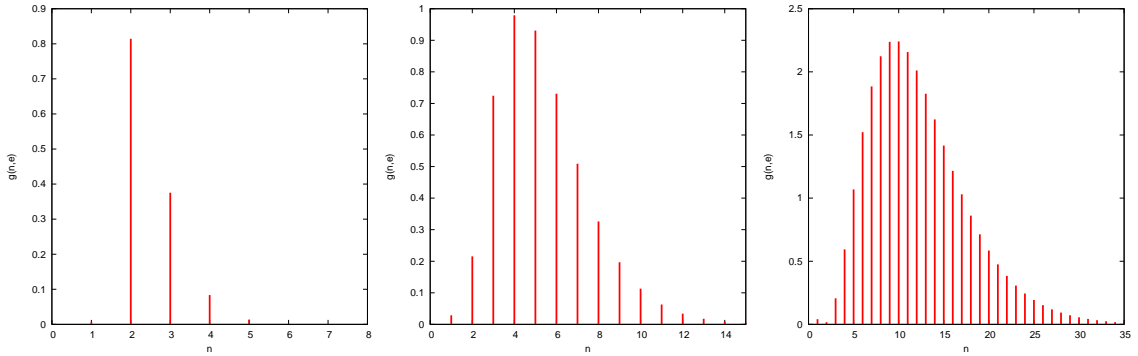


Figure 3.3: The power generated in gravitational waves as a function of harmonic for eccentricities 0.2 (left), 0.5 (middle), and 0.7 (right). Power is normalised to the power radiated by a circular orbit. Note the different x and y scales.

where (Peters & Mathews 1963):

$$g(n, e) = \frac{n^4}{32} \left(\left[J_{n-2}(ne) - 2eJ_{n-1}(ne) + \frac{2}{n}J_n(ne) + 2eJ_{n+1}(ne) - J_{n+2}(ne) \right]^2 \right. \\ \left. + (1 - e^2) [J_{n-2}(ne) - 2J_n(ne) + J_{n+2}(ne)]^2 + \frac{4}{3n^2} [J_n(ne)]^2 \right) \quad (3.49)$$

In order for this to be consistent with Equation 3.38 the condition:

$$\dot{E} = \sum_{n=1}^{\infty} \dot{E}_n \quad \Rightarrow \quad \sum_{n=1}^{\infty} g(n, e) = \frac{1 + (73/24)e^2 + (37/96)e^4}{(1 - e^2)^{7/2}} \quad (3.50)$$

must be satisfied. This is verified in Peters & Mathews (1963).

I plot $g(n, e)$ up to $n = 35$ for three eccentricities in Figure 3.3. For increasing eccentricity more power is radiated at higher harmonics. Therefore eccentric binaries emit gravitational waves at higher frequencies than their circular counterparts. Since all detectors have a minimum frequency for which they are effective, eccentric binaries are detectable at much longer periods than circular binaries. Therefore it is important to take the eccentricity of binaries into account when calculating their population statistics.

It is possible, by combining Equations 3.13, 3.33, 3.42, 3.46 and 3.47 to derive expressions for h_+ and h_\times as a function of the orbital parameters of the binary. In the formulation of Pierro et al. (2001):

$$h_\times = \frac{\cos \vartheta}{\sqrt{2}} [2h_{xy} \cos 2\varphi - (h_{xx} - h_{yy}) \sin 2\varphi] \quad (3.51)$$

$$h_+ = \frac{1}{\sqrt{2}} \left(\frac{3 + \cos 2\vartheta}{4} [2h_{xy} \sin 2\varphi + (h_{xx} - h_{yy}) \cos 2\varphi] - \frac{1 - \cos 2\vartheta}{4} (h_{xx} + h_{yy}) \right) \quad (3.52)$$

where φ and ϑ specify the direction of the observer in a spherical coordinate system with the centre of mass at the origin and the orbit of the binary in the equatorial plane. The

metric components h_{xy} and $h_{x\pm y} = h_{xx} \pm h_{yy}$ are given by the the Fourier expansions:

$$h_{xy} = \sum_{n=1}^{\infty} h_{xy}^{(n)} \sin n\omega t \quad (3.53)$$

$$h_{x\pm y} = \sum_{n=1}^{\infty} h_{x\pm y}^{(n)} \cos n\omega t \quad (3.54)$$

and the Fourier coefficients $h_{xy}^{(n)}$ and $h_{x\pm y}^{(n)}$ are:

$$h_{xy}^{(n)} = h_0 n (1 - e^2)^{1/2} [J_{n-2}(ne) + J_{n+2}(ne) - 2J_n(ne)] \quad (3.55)$$

$$h_{x-y}^{(n)} = 2h_0 n \left(J_{n-2}(ne) - J_{n+2}(ne) - 2e [J_{n-1}(ne) - J_{n+1}(ne)] + \frac{2}{n} J_n(ne) \right) \quad (3.56)$$

$$h_{x+y}^{(n)} = -4h_0 J_n(ne) \quad (3.57)$$

$$(3.58)$$

with the scale factor

$$h_0 = \frac{2G^{5/3} \omega^{2/3} M_{\text{chirp}}^{5/3}}{rc^4} \quad (3.59)$$

where:

$$M_{\text{chirp}} = (m_1 m_2)^{3/5} / (m_1 + m_2)^{1/5} \quad , \quad M_{\text{chirp}}^5 = \mu^3 M_{\text{tot}}^2 = \mu m_1^2 n_2^2 \quad (3.60)$$

where μ is the reduced mass of the binary and M_{tot} is the total mass. M_{chirp} is an important quantity in gravitational wave detection because this, rather than total mass, determines the amplitude of gravitational waves. It is also interesting to note that gravitational wave amplitude is proportional to r^{-1} rather than r^{-2} . Thus gravitational waves should be able to travel farther and be detected at greater distances than electromagnetic radiation. Pierro et al. (2001) have made extensive numerical experiments to determine to which order Equations 3.51 and 3.52 must be taken in order to produce accurate templates. They find that for the error to be $< 1\%$ then for $e = 0.1$ only four terms need to be calculated whereas for $e = 0.9$ 206 terms need to be calculated.

The results of this chapter can be used to estimate both the detectability of a relativistic binary at various distances and orientations as well as to calculate inspiral timescales and produce merger event rate estimates. In Chapter 8 I carry out this analysis for the compact binaries produced by my simulations.

Chapter 4

The Monte Carlo Code

Star cluster simulations must model the gravitational interactions described in Section 1.3 accurately and yet efficiently enough to be computationally tractable. Monte Carlo simulations are one answer to this problem. These simulations use two-body scattering events drawn from the theory of two-body relaxation (Chandrasekhar & von Neumann 1942) by Monte Carlo sampling and some simple physical arguments to apply the results to the whole cluster. Two different implementations of the Monte Carlo method were originally developed by Hénon (Hénon 1971a,b) and Spitzer (Spitzer 1975). I use the Giersz Monte Carlo code described in Giersz (1998) and Giersz (2001). This code is a re-working of the Monte Carlo code presented in Stodólkiewicz (1982, 1986) that was itself based on the code of Hénon (1971a). Chapter 4 is based on the papers of Giersz, Stodólkiewicz, and Hénon.

4.1 The Monte Carlo Approximation

To understand the nature of the Monte Carlo code and its advantages, it is instructive to compare it to direct N -body simulations. In direct N -body simulations Newton's gravitational force equation:

$$\ddot{\vec{r}}_i = -G \sum_{j \neq i}^N \frac{m_j (\vec{r}_i - \vec{r}_j)}{|\vec{r}_j - \vec{r}_i|^3} \quad (4.1)$$

is solved by direct integration. The natural timescale of such simulations is the orbital timescale. This method scales, at worst, with the fourth power of the number of stars in the system, N . A factor of N^2 comes from calculating the force on each particle from each other particle. As N increases the number of encounters also increases and smaller timesteps are needed in order to resolve this, adding another factor of N . Finally the natural timescale of the simulation, the orbital timescale, is related to the crossing time. The number of crossing times per relaxation time is not constant and they are related by $t_c \propto t_{rlx} \log N/N$. This adds (roughly) another factor of N in order to simulate a cluster to the same dynamical age. Therefore calculating direct N -body models quickly become intractable for large numbers of stars. By using adaptive timestepping a factor of N can be saved, reducing the scaling to N^3 . An intelligent neighbour scheme where not all force pairs have to be calculated every timestep can reduce this by another modest factor. Direct N -body simulations remain elusive for very large N and for $N > 10^5$ may take several months to run.

The Monte Carlo method improves on this by making several physically motivated assumptions about star clusters (Hénon 1971a,b):

- In the spirit of Monte Carlo, only the statistical properties of the cluster are considered.
- Star clusters are assumed to be large ($N \gg 1000$).
- Star clusters are assumed to be older than t_{rlx} .
- Star clusters are assumed to be spherically symmetrical.

Restricting the focus to statistical properties means that the details of individual orbits do not have to be reproduced. Large N means that the gravitational field can be divided into two parts: a steady mean field from the distant stars that does not change over several orbital times and a rapidly fluctuating field due to encounters with close neighbours. Considering timescales longer than t_{rlx} means that the relaxation timescale, rather than the orbital timescale, becomes the natural timescale for the system and the timestep, Δt , is chosen such that $t_c \ll \Delta t \ll t_{rlx}$. Over Δt the orbit is governed by the mean field and because the cluster is spherically symmetric the stellar orbits are plane rosettes determined solely by their energy, E_i , and angular momentum, \vec{J}_i .

To calculate the evolution of the orbit beyond Δt the effect of the fluctuating field must be included. To do so two further simplifications are introduced. First the method assumes that the fluctuating field will introduce orbital changes only through two-body interactions. Thus the encounters affecting the orbit can be drawn from a distribution given by the classical theory of two-body relaxation (Chandrasekhar & von Neumann 1942). Further, the simulations operate in the weak scattering limit where a single encounter is statistically representative of all encounters a star will undergo over Δt . Thus for each star only one encounter with one other star needs to be calculated per timestep and the scattering angle in this encounter is then multiplied by an appropriate factor (described in Section 4.2) to give the statistically correct angle for the sum over all encounters during Δt . This procedure is then repeated for all stars to get the new orbital configuration for the cluster after Δt .

The result of this process is a star-by-star representation of a cluster with statistically correct time evolution and much better scaling with N than direct N -body simulations. Two factors of N are saved by calculating only one interaction for each star with only one neighbour. A third factor is saved by using t_{rlx} rather than the orbital timescale as the evolution timescale of the system. This leaves a fixed number of operations to be performed on each star per timestep and the running time scales linearly with N rather than with N^3 or N^4 . Therefore it is possible to use Monte Carlo simulations for both large particle numbers ($N \approx 10^5 - 10^6$) and to use multiple simulations to explore the parameter space of initial conditions. Both of these tasks, are, at present, beyond the reach of direct N -body simulations. The Monte Carlo method is self-consistent if after each Monte Carlo timestep Poisson's equation is solved for the gravitational potential.

4.2 The Structure of a Monte Carlo Timestep

In order to understand how the Monte Carlo code accomplishes the tasks set out in Section 4.1 it is instructive to look at the details of how the code allows the system to evolve over the time Δt . The Giersz Monte Carlo code represents each star and each binary as a

single centre of mass (m_i) with an associated radius (r_i), tangential velocity (v_{ti}), and radial velocity (v_{ri}). Because the spatial location of each star is represented only by a radius, each star is often described as a shell with radius r_i and with the mass m_i evenly distributed over its surface. Thus a simulation can be considered as a set of concentric, interacting mass shells (Giersz 1998). The shells themselves are organised in zones, depending on the length of the local timestep, Δt_k , in zone k . The evolution of the system is governed by the equations:

$$\frac{\partial U(r, t)}{\partial t} + \left(\frac{dE}{dt} \right)_{fl} = \frac{dE}{dt} \quad (4.2)$$

$$\frac{d\vec{J}}{dt} = \left(\frac{d\vec{J}}{dt} \right)_{fl} \quad (4.3)$$

where $U(r, t)$ is the slowly varying, self-consistent gravitational potential of the system and the subscript fl describes terms associated with the rapidly fluctuating field. The task of the Monte Carlo code is to describe the evolution of Equations 4.2 and 4.3 and the response of the stellar orbits. To do this the timestep of a Monte Carlo code is organised into several parts:

1. Calculate the current potential.
2. Calculate the current timestep in each zone and re-organise the zones if necessary.
3. Incorporate additional physics such as strong few-body interactions and stellar evolution.
4. Perform the relaxation, i.e., calculate the effect of the fluctuating field on each star.
5. Calculate new positions and the new potential.
6. Calculate new velocities in the new potential.
7. Repeat.

I now describe each of these operations in greater detail.

4.2.1 The Potential

Because each star is represented as a spherical shell of radius r_i the potential is easy to calculate. For r_q , the radius of a given star, the potential between that star and the next ($r_q < r < r_{q+1}$) is simply:

$$U(r) = G \left(\frac{1}{r} \sum_{i=1}^q m_i - \sum_{i=q+1}^N \frac{m_i}{r_i} \right) \quad (4.4)$$

where N is the outermost star in the simulation and assuming the convention $U(\infty) = 0$. The ease of calculating this potential is yet another reason for assuming spherical symmetry.

4.2.2 The Timestep

In the original formulation of Hénon (1971b) the timestep for the code was the same at all radii and was chosen to be a small fraction of the relaxation time :

$$t_c = AGM^{5/2}|E|^{-3/2} \quad \text{and} \quad \frac{t_{rlx}}{t_c} = \frac{BN}{\ln N} \quad (4.5)$$

where A and B are constants of proportionality. Thus:

$$\Delta t = b \frac{N}{\ln N} f M^{5/2} |E|^{-3/2} \quad (4.6)$$

where E is the total energy of the system and $b \sim 0.005$ is an empirically determined parameter. The Giersz code uses a more careful criterion that allows individual time stepping (Giersz 1998; Stodółkiewicz 1982). I describe this as part of the relaxation step (Section 4.2.4).

4.2.3 Additional Physics

The Giersz Monte Carlo code is a star-by-star representation of the cluster and thus it is relatively straightforward to include additional stellar physics not directly related to the global dynamics. Each star simply has additional information stored that evolves over Δt according to its own physical laws. The most important processes are strong few-body interactions (Section 4.3), stellar evolution (Section 4.4), and tidal escape (Section 4.5).

4.2.4 Relaxation Processes

This step is the heart of the Monte Carlo scheme. Here the code calculates an individual scattering angle for each star, multiplies the chosen angle by an appropriate factor in order to simulate the cumulative effect of multiple encounters, and applies the final result to the velocity vector of each star. To accomplish this first note that the scattering angle, β , for a single two-body encounter in the small-angle scattering regime (Binney & Tremaine 1987; Spitzer 1987) with an impact parameter b is:

$$\beta^2 = \frac{4G^2(m_1 + m_2)^2}{b^2 w^4} \equiv \left(\frac{2b_0}{b} \right)^2 \quad (4.7)$$

where m_1 and m_2 are the masses of the two stars and w is their relative velocity. This must now be integrated over all masses, impact parameters, and relative velocities:

$$\langle \beta^2 \rangle = \int dm d^2\vec{b} d^3\vec{w} n \Delta t w f(\vec{w}) f(m) \frac{4b_0^2}{b^2} \quad (4.8)$$

where n is the local stellar number density. So far this result is exact. The method now introduces the approximation that one encounter is statistically representative of all encounters over Δt (the local approximation). Thus the integral over each distribution function is one and:

$$\langle \beta^2 \rangle = 4b_0^2 n w \Delta t \int \frac{d^2\vec{b}}{b^2} \quad (4.9)$$

Integrating over the angular part of the impact parameter integral yields:

$$\langle \beta^2 \rangle = 8\pi b_0^2 n w \Delta t \int \frac{db}{b} \quad (4.10)$$

The integral over the impact parameter has a solution of the form (Binney & Tremaine 1987; Spitzer 1987):

$$\int \frac{db}{b} = \ln \gamma N \quad (4.11)$$

where $\ln \gamma N$ is called the Coulomb logarithm. The value of the constant γ is a matter of some debate. Early authors have calculated a value of $\gamma = 0.4$ (Binney & Tremaine 1987; Spitzer 1987) based on assumptions about the maximum and minimum impact parameter. (Giersy & Heggie 1994), however, obtained a value of $\gamma = 0.11$ for equal-mass systems based on comparisons between continuum models (gas dynamical and Fokker-Planck) and direct N -body simulations. The value for more general systems is not well-known. In a comparison between Monte Carlo and direct N -body simulations Giersz, Heggie & Hurley (2008) find a best-fit value of $\gamma = 0.02$ and this is the value I will use in my simulations. The evolution of stellar systems depends only weakly on γ and thus my results will not depend strongly on this choice. The scattering angle for a single star over Δt in the Monte Carlo approximation is thus:

$$\langle \beta^2 \rangle = 8\pi b_0^2 n w \Delta t \ln \gamma N \quad (4.12)$$

where n can be computed by the number of shells within some distance of the star of interest.

Although Equation 4.12 can be used to follow the evolution of the stellar distribution by calculating β for a given Δt it is often more convenient to keep β fixed and use this to choose a local Δt . The Giersz version of the Monte Carlo method does this by noting the change in energy for star 1 due to an encounter with star 2 is:

$$m_1 \Delta v_1^2 = 4 \frac{m_1 m_2^2}{(m_1 + m_2)^2} w^2 \sin^2 \beta / 2 \quad (4.13)$$

The mean energy per encounter can be integrated over all stars over Δt in the same way and with the same assumptions as for Equations 4.7 to 4.12. The result is (Hénon 1975):

$$\langle m_1 \Delta v_1^2 \rangle = 8\pi G^2 n \Delta t \left\langle \frac{m_1 m_2^2}{w} \right\rangle \ln \gamma N \quad (4.14)$$

It is now possible to define an effective scattering angle, β_{eff} , such that the LHS of Equation 4.13 has the correct mean value for cumulative scattering over Δt . In this case Equations 4.13 and 4.14 must give the same value and:

$$4 \left\langle \frac{m_1 m_2^2}{(m_1 + m_2)^2} w^2 \sin^2 \frac{\beta_{\text{eff}}}{2} \right\rangle = 8\pi G^2 n \Delta t \left\langle \frac{m_1 m_2^2}{w} \right\rangle \ln \gamma N \quad (4.15)$$

and β_{eff} and Δt are connected by:

$$\left\langle \sin^2 \frac{\beta_{\text{eff}}}{2} \right\rangle = 2\pi G^2 \frac{(m_1 + m_2)^2}{w^3} n \Delta t \ln \gamma N \quad (4.16)$$

Equation 4.16 places a hard limit on Δt because the RHS must always be less than one. If the RHS > 1 then the system is under relaxed and evolves too slowly for the timestep. In practise, the timestep is chosen to be even shorter than this. The timestep is calculated in zones, each containing many shells. To do this Equation 4.16 is written in dimensionless form:

$$\left\langle \sin^2 \frac{\beta_{\text{eff}}}{2} \right\rangle = \langle A \rangle \Delta t_z \quad (4.17)$$

where Δt_z is the timestep in the zone of interest and:

$$\langle A \rangle = \frac{6k}{r_l^3 - r_{l-k}^3} \frac{\langle m \rangle^2}{(\langle w^2 \rangle)^{3/2}} \quad (4.18)$$

where r_l is the radius of the outermost shell in the zone of interest and k is the number of shells in the zone. The quantities $\langle m \rangle$ and $\langle w^2 \rangle$ are given by the equations:

$$\langle m \rangle = \sum_{i=l-k+1}^l \frac{m_i}{k} \quad , \quad \langle w^2 \rangle = \frac{2}{k} \sum_{i=l-k+1}^l \frac{m_i v_i^2}{\langle m \rangle} \quad (4.19)$$

Δt is then chosen according to the empirically determined limits:

$$0.025 < \left\langle \sin^2 \frac{\beta_{\text{eff}}}{2} \right\rangle < 0.05 \quad (4.20)$$

for the equal mass case and:

$$0.00625 < \left\langle \sin^2 \frac{\beta_{\text{eff}}}{2} \right\rangle < 0.0125 \quad (4.21)$$

for the unequal mass case. Δt_z is subject to the additional restriction that it must be a power-of-two multiple of some base value:

$$\Delta t_z = 2^{-s} \tau \quad , \quad s \in \mathbb{N} \quad (4.22)$$

The limiting radii of the zones are chosen to satisfy these conditions for Δt_z . For simplicity in organisation two restrictions are applied to s : s can differ by no more than one between zones and s cannot increase while moving out from the cluster centre. Thus the centre of the cluster always has the shortest timestep and the timestep increases towards the halo.

Once Δt_z has been calculated for a zone and the deflection angle β_{eff} due to the interaction of two shells defined then the new velocities for the two stars can be calculated. The code considers the interaction between a star with a velocity $v_1 = (v_{t1}, 0, v_{r1})$ and a neighbouring star (chosen some p shells away where p is a small positive number) with velocity $v_2 = (v_{t2} \cos \phi, v_{t2} \sin \phi, v_{r2})$. ϕ is the relative phase of the two orbits and is chosen to be $\phi = 2\pi X$ where X is a random number between 0 and 1. The relative velocity is:

$$\vec{w} = \vec{v}_2 - \vec{v}_1 = (v_{t2} \cos \phi - v_{t1}, v_{t2} \sin \phi, v_{r2} - v_{r1}) \quad (4.23)$$

For convenience the code defines three more quantities:

$$w_p = \sqrt{w_x^2 + w_y^2} \quad (4.24)$$

$$\vec{w}_1 = \left(\frac{w_y w}{w_p}, -\frac{w_x w}{w_p}, 0 \right) \quad \vec{w}_2 = \left(-\frac{w_x w_z}{w_p}, -\frac{w_y w_z}{w_p}, w_p \right) \quad (4.25)$$

where $w = |\vec{w}| = |\vec{w}_1| = |\vec{w}_2|$ and all three vectors are mutually perpendicular. Using conservation of energy, the relative velocity of the two stars after the encounter, w' , can then be written in terms of these three vectors as:

$$\vec{w}' = \vec{w} \cos \beta + \vec{w}_1 \sin \beta \cos \psi + \vec{w}_2 \sin \beta \sin \psi \quad (4.26)$$

where ψ is the angle of the plane of relative motion between the two particles with reference to the plane defined by (\vec{w}_1, \vec{w}_2) . Similarly to ϕ we chose $\psi = 2\pi Y$ where Y is also a random number between 0 and 1. The new velocity of each star is:

$$\vec{v}'_1 = \vec{v}_1 - \frac{m_2}{m_1 + m_2}(\vec{w}' - \vec{w}) \quad \vec{v}'_2 = \vec{v}_2 + \frac{m_1}{m_1 + m_2}(\vec{w}' - \vec{w}) \quad (4.27)$$

The new tangential and radial velocities are calculated directly from the new velocity components:

$$v'_{1,2r} = v'_{1,2z} \quad v'_{1,2t} = \sqrt{v'^2_{1,2x} + v'^2_{1,2y}} \quad (4.28)$$

Finally the new energy and angular momentum of each star can be calculated:

$$E'_{1,2} = U(r) + \frac{1}{2}(v'^2_{1,2r} + v'^2_{1,2t}) \quad J'_{1,2z} = r_{1,2} v'_{1,2t} \quad (4.29)$$

4.2.5 New Positions and New Potential

If zone q is the outermost zone with the current timestep Δt_q and r_+ is the radius of the outermost star in zone q then after the relaxation step all stars with a radius less than r_+ have new velocities, energies, and angular momenta. The orbit of each star can be found in the spherical potential calculated in step (1) and the pericenter (r_{ip}) and apocenter (r_{ia}) of each orbit can be defined. The code now updates $U(r, t)$ in response to the new orbital structure. To do so it calculates a new shell configuration by choosing a time-weighted random position for each star with a radius less than r_+ between r_{ip} and r_{imax} where r_{imax} is the lesser of either r_{ia} or r_+ . With new positions for each star the code can calculate a new $U(r, t)$ using Equation 4.4.

4.2.6 New Velocities in the New Potential

Finally the code must update the (already relaxed) velocities of each star in response to the new potential. To do so the mechanical energy of each star with a radius less than r_+ is updated and a new tangential and radial velocity calculated. For the i^{th} star the change in mechanical energy due to the new potential is:

$$\Delta E_i = \int dt \frac{\partial U(r, t)}{\partial t} \quad (4.30)$$

where the integral is taken along the trajectory of star i . In order to calculate ΔE_i the code randomly chooses two points along the trajectory of the star, r_{i1} and r_{i2} , and assumes that these are representative of the orbit. By assuming that the orbit has not changed very

much between the new and the old potential Equation 4.30 can be approximated by:

$$\Delta E_i \approx \frac{1}{2} (\Delta U(r_{i1}) + \Delta U(r_{i2})) \quad (4.31)$$

where $\Delta U(r) = U_{\text{new}}(r) - U_{\text{old}}(r)$ is the difference between the old and new potential evaluated at radius r . Equation 4.31 can then be written explicitly in terms of the old and new potential as:

$$\frac{1}{2} v_{i\text{new}}^2 + U_{\text{new}}(r_{i1}) - \frac{1}{2} v_{i\text{old}}^2 - U_{\text{old}}(r_{i1}) = \frac{1}{2} [U_{\text{new}}(r_{i1}) - U_{\text{old}}(r_{i1}) + U_{\text{new}}(r_{i2}) - U_{\text{old}}(r_{i2})] \quad (4.32)$$

where $v_{i\text{old}}$ is the velocity after relaxation in the old potential and $v_{i\text{new}}$ is the velocity after relaxation and in the new potential. Equation 4.32 can be solved for the new velocity:

$$\frac{1}{2} v_{i\text{new}}^2 = v_{i\text{old}}^2 + U_{\text{old}}(r_{i1}) + U_{\text{new}}(r_{i1}) - U_{\text{old}}(r_{i2}) - U_{\text{new}}(r_{i2}) \quad (4.33)$$

where $v_{i\text{new}}$ is now a function of $v_{i\text{old}}$ and the old and new potential (all known). The new tangential velocity is calculated by conservation of angular momentum and it and the new radial velocity are:

$$v_{t\text{new}} = v_{t\text{old}} \frac{r_{i1}}{r_{i2}} \quad v_{r\text{new}} = \sqrt{v_{i\text{new}}^2 - v_{t\text{new}}^2} \quad (4.34)$$

This procedure can be shown to formally conserve energy (Stodólkiewicz 1982) but introduces an inconsistency between the position and velocity of the particles because star positions are determined from their orbits in the old potential but the resulting velocity is calculated in the new potential. Normally this causes no difficulties. However it is possible that a position is chosen that is far outside the new orbit and this creates problems calculating the new value of v_r . In this situation the procedure outlined in Giersz (1998) is adopted. If $v_{i\text{new}}^2 < 0$ then the new radial velocity is set to zero and the tangential velocity calculated according to conservation of angular momentum. The kinetic energy lost through this process is accumulated for all stars in the current timestep. At the end of the timestep all stars up to zone q have their energy reduced by the ratio of the total kinetic energy to the total kinetic energy minus the lost kinetic energy. This ratio is close to one since the fraction of cases with this problem is $\approx 0.01\%$ and the total accumulated energy is only a few percent of the kinetic energy of the system (Giersz 1998).

Now the cluster up to the q^{th} zone has been advanced to its next state, the code can go back to the first step and repeat the calculation. This procedure is repeated until the desired evolutionary state is achieved and allows the dense inner zones, which evolve faster, to be relaxed more frequently than the less dense halo. This procedure has been shown to agree very well both with theoretical predictions and with the results of direct N -body simulations for a wide range of initial conditions (Giersz 1998, 2001, 2006).

4.3 Few Body Interactions

As described in Section 2.2, strong few body encounters in clusters can have a drastic effect on binary stars. These strong interactions are not part of the Monte Carlo approximation because they are not statistically representative of the other encounters a star will experience. It is relatively simple, in principle, to add special prescriptions for few-body encounters to the Monte Carlo scheme. Each shell represents either a single star or a binary

and thus the probability for a strong interaction is calculated between shells. If the interaction is assumed to be short compared to the timestep of the system, its outcome can be calculated in a separate routine and returned to the main code before the next relaxation step.

There are two methods for finding the outcome of few-body interactions. The first is direct integration of the encounter. This approach is used in the Fregeau & Rasio (2007) Monte Carlo code using the FEWBODY package of Fregeau et al. (2004) and in the Giersz & Spurzem (2003) hybrid gas-Monte Carlo code using the regularisation mechanism of Aarseth & Zare (1974) and Mikkola (1983). The primary advantage of using few-body integrators is accurate interaction outcomes for any initial configuration. Few-body integration can also treat long-lived hierarchical systems and mergers during the interaction. The primary disadvantage of this method is computational cost. The timestep for few-body interaction is much shorter than for cluster evolution and much simulation time is spent on integrating a very few hierarchical systems (direct N -body simulations can suffer from the same problem).

A second approach, used in the Giersz Monte Carlo code, is to use prescriptions based on analytic formulae and scattering experiments to predict the outcome of an interaction without actually calculating its orbit. This method is fast and simple to implement: an interaction occurs, an initial configuration is generated, the prescriptions consulted, and a result is found. This method is, however, only as good as the models upon which the prescriptions are based. Results are available only for some initial configurations and there are no good analytic expressions for the outcomes of binary-binary interactions. Because the prescriptions do not resolve orbits explicitly they cannot predict mergers that happen during the interaction. There are also no prescriptions for long-lived hierarchical systems. Despite these limitations the Monte Carlo code using these formulae has been shown to agree well with direct N -body simulations (Giersz 1998, 2001) as well as with observations of real star clusters (Giersz & Heggie 2008, 2009; Giersz, Heggie & Hurley 2008; Heggie & Giersz 2009). These cross-sections do not take into account binaries formed by tidal capture since this process is not thought to be important, particularly for compact binaries (see Section 2.2). Three-body binary formation, binary-single interactions, and binary-binary interactions are all treated with varying degrees of accuracy.

4.3.1 3-Body Binary Formation

As described in Section 2.2 close encounters between three stars can allow one star to carry away kinetic energy and leave the others as a bound binary. For any timezone in the Monte Carlo code with three consecutive stars, there is a possibility of three-body binary formation. For the equal mass case the probability of a binary forming in a volume dV over a time period dt was calculated by Hut (1985) as:

$$P_{3b} = \int dV dt 0.9G^5 m^5 n^3 \sigma^{-9} \quad (4.35)$$

where m is the mass of the stars, n the local number density, and σ the local velocity dispersion. For any three consecutive stars P_{3b} can be calculated and compared to a random number X . If $X < P_{3b}$ then a binary is formed out of the inner two stars and the third is allowed to escape. The binding energy for the new binary is chosen to be $3k_B T$, the minimum value for a new binary to be considered permanent and not liable to immediate disruption (Giersz 1998). The new orbits are calculated by assuming the single star and the centre of mass of the new binary are in energy equilibrium with the rest of the cluster. Note

that Equation 4.35 is the probability for permanent three-body binaries to be formed. Many more soft binaries would form but are immediately disrupted again. Since the dynamics of the cluster is dominated by hard binaries these soft binaries are not modelled. It is worth noting they can have an effect on cluster dynamics, such as catalysing four body encounters due to their high interaction cross-section and participating in hardening events, but this is likely to be small in terms of the total energetics and thus neglecting them introduces (probably) only a small error.

The unequal mass case is more difficult because the probability of formation P_{3b} is harder to calculate. The rate of 3-body binary formation between stars with masses m_1 , m_2 , and m_3 at a given location is:

$$\frac{dN_{3b}}{dt} = Bn_1n_2n_3 \quad (4.36)$$

where n_1 , n_2 , and n_3 are the local number densities for stars of mass m_1 , m_2 , and m_3 , and B is a constant that depends on the masses of the interacting stars and the local mean kinetic energy (Heggie 1975). Over some time δt and volume δV Equation 4.36 becomes:

$$N_{3b} = Bn_1n_2n_3\delta V\delta t \quad (4.37)$$

For a each Monte Carlo zone the stars are collected in groups of three as before. The probability for each group of stars to have masses m_1 , m_2 , and m_3 will be $(n_1n_2n_3)/n^3$ where n is the local number density for all stars. Then:

$$N_{3b} = \frac{N}{3} \frac{n_1n_2n_3}{n^3} P_{3b} \quad (4.38)$$

where N is the total number of stars in the zone. In order for Equations 4.37 and 4.38 to be equal:

$$P_{3b} = \frac{3Bn^3\delta v\delta t}{N} \quad (4.39)$$

Equation 4.39 depends only on the total number density, n , rather than the number density of stars of each mass. This is important because in a system with a range of masses there may be very few stars of a given mass present in any one zone and individual number densities can be difficult to define. Other than the change in the formation probability, unequal mass binary formation follows the same process as for the equal mass case, producing binaries with binding energies of $3k_B T$ and an escaper all in equilibrium with the rest of the cluster.

4.3.2 Binary-Single Interactions

Only close binary-single interactions are considered and the probability for an interaction is calculated pairwise between each binary and a single star. A distance of closest approach for all encounter is chosen to be:

$$r_{\min, sb} = 3a \quad (4.40)$$

where a is the semi-major axis of the binary. An maximum impact parameter for which a strong interaction can occur given the relative velocity of the single star and the binary, v must then be calculated. To do so gravitational focusing, the enhancement of the interaction cross-section by gravitational attraction (Binney & Tremaine 1987; Spitzer 1987) must be taken into account. The effect of gravitational focusing is given by the parameter (Spitzer

1987):

$$f_{sb} = 1 + \frac{2(m_1 + m_2 + m_3)}{r_{\min} v^2} \quad (4.41)$$

and from this the maximum impact parameter for which a significant binary-single interaction can occur is (Hut & Bahcall 1983; Spitzer 1987):

$$p_{\max, sb} = r_{\min, sb} \sqrt{f_{sb}} \quad (4.42)$$

and the probability of an interaction between the single star and the binary over the time period Δt is (Giersz & Spurzem 2000; Hut & Bahcall 1983):

$$P_{sb} = \frac{N}{2 \ln \gamma N} p_{\max, sb}^2 n v \Delta t \quad (4.43)$$

where n is the local number density of single stars around the binary. For every binary at every timestep P_{sb} is calculated between it and a single star. A random number, $X \in [0, 1]$, is chosen and if $X < P_{sb}$ an interaction occurs. A new binding energy for the binary is chosen from the distribution found in Spitzer (1987):

$$f(z) = \cos^6 z \quad z = \arctan \frac{\Delta E_b}{E_b} \quad (4.44)$$

$2\Delta E_b/3$ of the kinetic energy produced is given to the single star and $\Delta E_b/3$ is given to the centre of mass of the binary. The recoil velocity for the binary is given by the formula (Giersz 1998):

$$\Delta v^2 + 2(v_r \cos \theta + v_t \sin \theta \cos \phi) \Delta v - \frac{4\Delta E_b}{3m_b} = 0 \quad (4.45)$$

where v_r and v_t are the initial radial and tangential velocities, m_b is the mass of the binary, θ is chosen from the distribution $f(\theta) = \sin(\theta/2)$ ($\theta \in (0, \pi)$), and ϕ is chosen randomly between 0 and π . The new velocity for the single star can be calculated in a similar fashion. The new velocity components can be determined from v_r , v_t , θ , and ϕ and then new orbits can be calculated for the single star and the binary. Disruption of soft binaries is also allowed by this process.

Exchange interactions are also allowed during binary-single encounters. In this process one of the stars of the binary is exchanged for the field star. The cross-section for an exchange is based on binary-single scattering experiments performed by Heggie, Hut & McMillan (1996) and fitted by the formula:

$$\begin{aligned} \Sigma = & 1.39 \left(\frac{a}{0.1 \text{AU}} \right) \left(\frac{10 \text{kms}^{-1}}{V} \right)^2 \left(\frac{M_{123}}{M_\odot} \right) \left(\frac{m_{23}}{m_{123}} \right)^{1/6} \left(\frac{m_3}{m_{13}} \right)^{7/2} \left(\frac{m_{123}}{m_{12}} \right)^{1/3} \left(\frac{m_{13}}{m_{123}} \right) \\ & \times \exp(3.07 + 7.49\mu_1 - 1.89\mu_2 - 15.49\mu_1^2 - 2.92\mu_1\mu_2 - 2.92\mu_2^2 + 3.07\mu_1^3 \\ & + 13.15\mu_1^2\mu_2 - 5.23\mu_1\mu_2^2 + 3.12\mu_2^3) \text{AU}^2 \end{aligned} \quad (4.46)$$

where $m_{13} = m_1 + m_3$, $\mu_1 = m_1/m_{12}$, and $\mu_2 = m_3/m_{123}$. This formula tends to insert massive stars into binaries and thus BHs are likely to be exchanged into any binaries they encounter.

4.3.3 Binary-Binary Interactions

Binary-binary interactions are the most difficult to deal with because it is both difficult to define an interaction probability and because there are many possible outcomes for the interaction. The outcomes for binary-binary interactions depend sensitively on the initial conditions and detailed dynamics of the encounter, making a comprehensive analytic theory difficult. Nonetheless it is possible to treat binary-binary interactions with prescriptions, albeit in a fairly crude way.

The probability of binary-binary interactions is based on the work of Stodólkiewicz (1986) and Bacon, Sigurdsson & Davies (1996). The outcomes are based on the scattering simulations of Mikkola (1983), Mikkola (1984a), and Mikkola (1984b). To begin with it is assumed that all binary-binary interactions are strong. Stable 3-body configurations are also disallowed as an outcome. Such configurations are immediately broken up and the energy distributed among the members. The probability of an interaction is calculated in a similar way to the binary-single interactions. First two binaries and a point of closest approach are chosen. The point of closest approach is taken to be the apocenter distance of the softer binary:

$$r_{\min,bb} = a_s(1 + e_s) \quad (4.47)$$

where a_s is the semi-major axis of the softer binary and e_s is its eccentricity. The effect of gravitational focusing is calculated in a similar way as for the binary-single case:

$$f_{bb} = 1 + \frac{2(m_{b1} + m_{b2})}{r_{\min,bb}v^2} \quad (4.48)$$

where $m_{b1,b2}$ are the total masses of the two binaries and v is again the relative velocity between the two binaries. The maximum impact parameter for an interaction to occur is then:

$$p_{\max,bb} = r_{\min,bb}\sqrt{f_{bb}} \quad (4.49)$$

and the probability for an interaction to occur over time Δt is then (Bacon, Sigurdsson & Davies 1996; Giersz & Spurzem 2000):

$$P_{bb} = \frac{N}{\ln \gamma N} \pi P_{\max,bb}^2 \bar{n}_{12} v \Delta t \quad (4.50)$$

where \bar{n}_{12} is the average of the number densities of the two binaries involved in the interaction, $n_{1,2}$. Again a random number $X \in [0, 1]$ is compared to P_{bb} and if $X < P_{bb}$ an interaction occurs.

There are two allowed outcomes for binary-binary interactions based on prescriptions derived from the numerical experiments of Mikkola (1983, 1984a,b):

1. 12% of cases - Two binaries on hyperbolic orbits. The recoil energy of both binaries is taken to be $0.4E_{b1}$ where E_{b1} is the binding energy of the softer binary. Both binaries are also hardened by this amount to conserve energy.
2. 88% of cases - One bound binary and two single escaping stars. The softer binary is disrupted and the total recoil energy is taken to be $0.516(E_{b1} + E_{b2})$. This energy is distributed in such a way as to conserve total momentum. The surviving binary also has its binding energy increased by the same amount. In this case exchanges are also allowed. The most massive star has an exchange probability calculated according to

the cross-section given in Equation 4.46 and can be inserted into the surviving binary. Again the most likely outcome for a massive object is exchange into the binary.

This formulation is not accurate in all cases and the energy generated is only approximate. Nonetheless, the binding energy generated by this prescription seems to agree with results of direct N -body simulations to within 10% (Heggie & Giersz 2009). It would be preferable to include few-body integration for binary-binary encounters but this would be complicated and make the code run much slower. In addition, it would not help establish a better interaction probability for the various processes.

4.4 Stellar Evolution

A treatment of stellar evolution is vital in order to perform population synthesis models of star clusters. Analytic prescriptions are used to reproduce stellar evolution in star cluster simulations. These consist of formulae relating the star's parameters at a given age to its zero-age main sequence (ZAMS) mass, radius, and metallicity. In principle it would be possible to include live hydrodynamic calculations of stellar evolution in star cluster simulation codes but this would be prohibitively computationally expensive. Live evolution is probably only significant in the cases of mergers or unstable mass transfer in binaries.

The Giersz Monte Carlo code uses the SSE stellar evolution recipes of Hurley, Pols & Tout (2000) to calculate the evolution of single stars. SSE includes a full set of analytic stellar evolution tracks from the ZAMS to the degenerate remnant for stars over a wide range of mass and metallicity. SSE also includes a prescription for velocity kicks upon formation for neutron stars and black holes due to asymmetric supernovae (Hurley, Tout & Pols 2002). SSE takes into account that mass-loss due to stellar winds is smaller at low metallicity and the amount of fallback from a supernova explosion can be larger (see Belczynski, Kalogera & Bulik (2002) for further discussion). For my purposes this generates more massive BHs at low metallicity.

Since every star is represented individually in a Monte Carlo code, the implementation of stellar evolution recipes is fairly straightforward. Every star has a set of associated stellar properties that can be updated according to the recipes. In principle evolution updates occur:

1. Every time the code takes a dynamical timestep to a new configuration.
2. Every time the code outputs a snapshot.
3. Before and after each dynamical interaction described in Section 4.3.
4. If the timescale for stellar evolution is shorter than the time to the next dynamical update then the star should be updated on this timescale.

These update times are independent of the actual stellar evolution recipes used.

For the binary evolution described in Section 2.1 the code uses BSE, the binary stellar evolution recipes of Hurley, Tout & Pols (2002). These are an extension of SSE and contain the recipes for the evolution of each binary member in isolation supplemented by prescriptions for the various phases of mass transfer and Roche lobe overflow described in Section 2.1. Also included are formulae describing the effect of magnetic braking and a simple treatment of the gravitational wave inspiral timescale based on the quadrupole approximation and Equation 3.40. A velocity kick is applied to each NS and BH after it

forms due to a supernova explosion as described in Chapter 2. The kick is drawn from a Maxwellian velocity distribution with a dispersion of 190 km s^{-1} (Hansen & Phinney 1997).

The implementation of SSE and BSE in the Giersz Monte Carlo code is described in Giersz, Heggie & Hurley (2008). A variation of the McScatter interface, described in Heggie, Portegies Zwart & Hurley (2006), is used to communicate between the dynamical and stellar parts of the code. The implementation has been tested against both direct N -body models and observations of the old open cluster M67 in Giersz, Heggie & Hurley (2008) with excellent results. Further improvements to BSE have been included and the tests extended to observations of M4 (Giersz & Heggie 2008) and both observations and direct N -body models of NGC6397 (Giersz & Heggie 2009; Heggie & Giersz 2009). In both cases the agreement between the Monte Carlo code and other results is very good. Thus the Giersz Monte Carlo code provides a robust and reliable method for performing population synthesis studies of globular clusters and the simulations can be compared successfully to observations.

4.5 Tidal Escape

According to Spitzer (1987) a star is no longer bound to the cluster if its mechanical energy exceeds $-1.5GM/r_t$ where M is the total mass of the cluster and r_t is its tidal radius. A star with an apocenter greater than r_t is also be stripped from the cluster and lost. In practise such simple prescriptions do not work and the original models of Hénon (1971b), Stodólkiewicz (1982), and Stodólkiewicz (1986) had a higher escape rate than would be expected from direct N -body simulations. The reason for this is that while there is little ambiguity for high velocity stars ejected in strong interactions, those that escape due to weak encounters in the relaxation process often have energies only very slightly above the threshold and are only very slightly unbound. Furthermore the escape process is not instantaneous but requires the star to move beyond the boundary of the cluster. During this motion, the star has the opportunity to interact with other stars and to be scattered back into the cluster with an energy below the escape threshold. A solution to this problem, found in the theory of Baumgardt (2001) and implemented in the code in Giersz, Heggie & Hurley (2008), is to define an effective radius, $r_{\text{eff}} = r_t/\alpha$ where $\alpha = 1.5 - a [\ln(\gamma N/N)]^{1/4}$, and use this rather than r_t for determining the threshold energy for escape. Since $r_{\text{eff}} < r_t$ this means that the cluster is more concentrated compared to the tidal radius than before and the stars must have a higher energy in order to escape. Giersz, Heggie & Hurley (2008) find that $a \approx 3$ gives the best agreement to N -body models. Another tidal escape model inspired by the destruction of stars around massive black holes has been proposed by Spuzem et al. (2005) in the context of the anisotropic gas model. In this model the potential escapers are found in a region of energy-angular-momentum space called a “loss-cone”. The rate of escape from and re-population of the loss cone is characterised by two diffusion timescales, t_{in} and t_{out} . Spuzem et al. (2005) claim that this is a more accurate representation of tidal escape from star clusters but it has not yet been implemented in the Monte Carlo code.

The exact details of tidal escape will not be very important in my simulations since I use large tidal radii and because the compact binaries are both centrally concentrated and undergo many strong interactions. Thus the majority of compact objects removed from the cluster will be ejections after strong interactions and will be well above the threshold

energy for escape, thus avoiding most of the slow or ambiguous cases the detailed schemes must describe.

4.6 Limitations

Despite the Monte Carlo code's many advantages the method has limitations that must be kept in mind. There is, for instance, the assumption of spherical symmetry that is important in several places. The Monte Carlo code may not perform well in regions where the distinction between the mean and the fluctuating field breaks down. Finally the approximate treatment of few-body interactions will always be a concern in any study dealing with the binary populations of star clusters.

The assumption of spherical symmetry is not a major concern for my work. Most globular clusters are spherical to first approximation and few have significant rotation. Furthermore there is a large parameter space to study (metallicity, concentration, mass function, binary fraction, etc.) before it makes sense to study deviations from spherical symmetry.

Of more importance is the limit where the separation between the mean and fluctuating field breaks down and the Monte Carlo approximation is no longer valid. This can happen in small N systems where all encounters produce large angle scattering and direct N -body methods are needed. This could become a concern in my simulations since black holes and neutron stars will rapidly become the most massive objects in the system and as such will mass-segregate and become very centrally concentrated. If the compact objects are sufficiently more massive than the mean stellar mass they will become Spitzer unstable (Spitzer 1987) and form a decoupled subsystem in the cluster core interacting only with each other. If the number of compact objects is small enough the Monte Carlo approximation could break down. Heggie & Giersz (2009) have tested the Monte Carlo code in comparison to direct N -body simulations for a realistic cluster with a realistic mass function. They find the escape rate and energy generation in the core agree with the N -body results to within 10%, indicating the core dynamics are being treated correctly by the Monte Carlo code. Furthermore, my simulations should produce enough compact objects that any Spitzer unstable subsystem will be fairly large. Finally I will be able to compare to results from other researchers using different approximations as a sanity check for my results.

Finally the approximate nature of the few-body interactions is obviously a concern. I will not reproduce the full range of possible few-body interactions. In particular because the actual stellar orbits are not reproduced during the interactions I will not find any mergers that might happen due to close passages during the course of the interaction. I also lose the ability to form hierarchical triples that can pump up the eccentricity of the inner binary through orbital resonances (Kozai 1962) and increase both the gravitational wave signal and the inspiral rate. Finally, I cannot incorporate relativistic effects into my few body interactions and thus may miss some gravitational wave burst events occurring during close hyperbolic encounters. For these reasons my simulations will tend to under-produce gravitational wave events and the results will be lower limits.

Chapter 5

Initial Conditions

I have performed simulations of star clusters with 16 different sets of initial conditions. Each simulation has 5.0×10^5 centres of mass (single stars or binaries). All simulations use a Kroupa IMF (Kroupa, Tout & Gilmore 1993), a broken power-law with a low-mass slope of $\alpha_l = 1.3$, a high-mass slope of $\alpha_h = 2.3$, and a break mass of $M_{\text{break}} = 0.5M_\odot$. Following Sadowski et al. (2008) I choose masses between $0.1 M_\odot$ and $150 M_\odot$. All simulations are initialised as Plummer models (Plummer 1911) with a tidal cut-off of $r_t = 150$ pc. According to the formula of Spitzer (1987):

$$r_t^3 = \frac{M_C}{2M_G} R_G^3 \quad (5.1)$$

where M_C is the mass of the cluster, M_G is the mass of the galaxy, and R_G is the galactocentric radius. Stars beyond the tidal cut-off are removed from the simulation. For a galactic mass of $\approx 6 \times 10^{10} M_\odot$ and my cluster masses (Table 5.1) this yields $R_G \sim 9 - 10$ kpc, a cluster slightly outside the solar orbit. My models do not include disk shocking so these models represent halo clusters. I choose relatively isolated clusters so that the evolution is driven by the internal dynamics. The tidal cut-off is not held constant during the evolution but is re-calculated at each timestep according to the current cluster mass.

I use two different metallicities in my simulations: $Z_h = 0.02$ and $Z_l = 0.001$. Z_h corresponds roughly to solar metallicity and thus $[\text{Fe}/\text{H}]_h \sim 0.0$ and $[\text{Fe}/\text{H}]_l \sim -1.3$. Bimodal metallicity distributions are ubiquitous in globular cluster systems (Brodie & Strader 2006) and the Milky Way is no exception to this. The metallicities I have chosen are slightly higher than the galactic globular cluster metallicity distribution which has peaks at ~ -0.5 and ~ -1.6 (Harris 1996) but agree well with the results for eight brightest cluster galaxies presented by Harris et al. (2006). These systems have metallicity distributions with high metallicity peaks of $0.5 > [\text{Fe}/\text{H}] > -0.5$ and low metallicity peaks of $-1 > [\text{Fe}/\text{H}] > -2$. Thus my chosen metallicities fall in a reasonable range for general globular cluster systems. For the purpose of my study the primary difference between these metallicities is the treatment of stellar mass-loss in the Hurley, Tout & Pols (2002) stellar evolution code. Mass-loss is suppressed at low metallicity and this allows the formation of significantly more massive BHs. These high-mass BHs will mass-segregate more swiftly than their low-mass counterparts and should be stronger gravitational wave sources.

I consider two different binary fractions: $f_b = 0.1$ and $f_b = 0.5$. Thus, while they have the same number of centres of mass, simulations with $f_b = 0.1$ have 6.0×10^5 stars whereas simulations with $f_b = 0.5$ have 7.5×10^5 stars. The simulations with $f_b = 0.5$ will be more massive and produce more BHs since there are more stars present. I also expect a larger

number of BHs to be exchanged into binaries in clusters with $f_b = 0.5$ since there will be more binaries available for interaction. I follow the work of Giersz, Heggie & Hurley (2008) and take the initial binary parameters from Kroupa (1995). These prescriptions start with a thermal distribution of birth eccentricities ($f(e_b) = 2e_b$), birth mass ratios (q_b) drawn at random from the Kroupa, Tout & Gilmore (1993) IMF, and a birth period distribution of:

$$f(P_b) = 2.5 \frac{\log P_b - 1}{45 + (\log P_b - 1)^2} \quad (5.2)$$

with the limits $\log P_{b,min} = 1$ and $\log P_{b,max} = 8.43$. These birth values are then modified according to the eigenvalue and feeding algorithm to simulate the effect of pre-main sequence evolution. Initial eccentricities are calculated as:

$$\ln e_{in} = -\rho + \ln e_b \quad (5.3)$$

where

$$\rho = \int_0^{\Delta t} dt \rho' = \left(\frac{\lambda R_\odot}{R_{peri}} \right)^\chi \quad (5.4)$$

where ρ'^{-1} is the circularisation timescale, $\Delta t \approx 10^5$ yr is the pre-main-sequence evolution timescale, R_{peri} is the pericenter distance of the binary, and $\lambda = 28$ and $\chi = 0.75$ are empirically determined constants. The initial mass ratio is given by:

$$q_{in} = q_b + (1 - q_b)\rho^* \quad (5.5)$$

where

$$\rho^* = \begin{cases} \rho & \rho \leq 1 \\ 1 & \rho > 1 \end{cases} \quad (5.6)$$

where the mass of the secondary is modified according to $m_{2,in} = q_{in}m_{2,b}$ and the mass of the primary is unchanged $m_{1,in} = m_{1,b}$. Finally the period is given by:

$$P_{in} = P_b \left(\frac{m_{t,b}}{m_{t,in}} \right)^{1/2} \left(\frac{1 - e_b}{1 - e_{in}} \right)^{3/2} \quad (5.7)$$

where $m_{t,b}$ and $m_{t,in}$ are the total masses before and after the application of Equation 5.5. The main effect of the eigenvalue and feeding evolution is the depopulate the short-period, high-eccentricity area of the period-eccentricity diagram as observed in galactic binaries. The Kroupa (1995) prescriptions provide a good match to the binary parameters observed in the galactic field.

I have performed simulations with four initial concentrations. I control the initial concentration by the ratio of the initial tidal radius to the initial half-mass (r_h). I use initial ratios of $r_t/r_h = 21, 37, 75,$ and 180 , corresponding to initial number densities within r_h of $\sim 10^2$ pc $^{-3}$, 10^3 pc $^{-3}$, 10^4 pc $^{-3}$, and 10^5 pc $^{-3}$ respectively. The initial concentration primarily affects the half-mass relaxation time defined in Equation 1.5. The systems with higher initial concentrations and thus smaller values of r_h will also have shorter values of t_{rh} and will experience faster dynamical evolution than their less concentrated counterparts. Whatever effect dynamics have on the production of BH-BH binaries should be accelerated in these systems. I have chosen these densities to cover parameter space rather than to match any particular observed distribution.

Since star cluster dynamics are stochastic and chaotic, large fluctuations can occur between different realisations of the same simulation (Giersz & Heggie 2008, 2009; Giersz, Heggie & Hurley 2008). In general stochastic fluctuations decrease with $N^{-1/2}$ and thus larger N models should experience less simulation-to-simulation fluctuation. Single encounters, however, always depend sensitively on the initial conditions since star cluster dynamics experienced deterministic chaos and their effect on the system is N -independent. The typical energy fed into the system by a close three-body encounter as a fraction of the total binding energy of the cluster is, for example, independent of N . Thus for any N physically equivalent initial conditions still lead to statistically independent results. To constrain this I perform four independent realisations of each combination of initial conditions, each differing only by the initial random seed, and I have a total of 64 simulations to analyse. Table 5.1 gives the initial parameters of my 16 different simulations, averaged over the four realisations. Each simulation is run on a single processor at the HLRS supercomputer in Stuttgart. The time at this computer was provided through bwgrid as part of the German Astrogrid-D and D-Grid projects. The simulation time increases slightly with the binary fraction and strongly with the initial concentration. The shortest simulations (10sol21) take ~ 4 h to complete on this machine and the longest (50low180) take $\sim 12 - 14$ h.

Simulation	Initial conditions				
	f_b	Z	rt/r_h	$M(M_\odot)$	t_{rhi} (Myr)
10sol21	0.1	0.02	21	3.63×10^5	3.5×10^3
10sol37	0.1	0.02	37	3.64×10^5	1.5×10^3
10sol75	0.1	0.02	75	3.63×10^5	5.2×10^2
10sol180	0.1	0.02	180	3.63×10^5	1.4×10^2
10low21	0.1	0.001	21	3.60×10^5	3.5×10^3
10low37	0.1	0.001	37	3.62×10^5	1.5×10^3
10low75	0.1	0.001	75	3.65×10^5	5.2×10^2
10low180	0.1	0.001	180	3.63×10^5	1.4×10^2
50sol21	0.5	0.02	21	5.07×10^5	3.0×10^3
50sol37	0.5	0.02	37	5.07×10^5	1.3×10^3
50sol75	0.5	0.02	75	5.06×10^5	4.4×10^2
50sol180	0.5	0.02	180	5.09×10^5	1.2×10^2
50low21	0.5	0.001	21	5.08×10^5	3.0×10^3
50low37	0.5	0.001	37	5.07×10^5	1.3×10^3
50low75	0.5	0.001	75	5.06×10^5	4.4×10^2
50low180	0.5	0.001	180	5.07×10^5	1.2×10^2

Table 5.1: The initial models for my simulations. Column 1 gives the model, column 2 the initial binary fraction, column 3 the metallicity, column 4 the initial ratio of tidal to half-mass radius, column 5 the initial mass averaged over four independent realisations, and column 6 the initial half-mass relaxation time averaged over four independent realisations. The small variation in initial mass within each binary fraction is due to random sampling of the IMF.

Chapter 6

Compact Binaries Within Star Clusters

I present results for the BH-BH binary population that remains within my star cluster simulations. My simulations produce no NS-NS binaries. Binaries destined to become NS-NS either merge during one of the phases of mass transfer or are disrupted by the natal kick during one of the supernova events. This is true for the NS-BH binaries as well. The BH-BH binaries are formed dynamically, a process that, as described in Chapters 2 and 4, is most efficient for massive objects. Since the BHs are, for the most part, significantly more massive than the NSs they will be preferentially exchanged into binaries until they are depleted by dynamical ejection from the cluster. None of my simulations are completely depleted of BHs after one Hubble time and thus the NSs have little opportunity to take part in dynamical binary formation.

In Table 6.1 I show the total number of BHs formed both in isolation and in binaries in each simulation averaged over the four independent realisations. For each simulation the scatter across the independent realisations is small, merely a result of random sampling of the IMF. The number of BHs formed is not a function of concentration in any range of Z or f_b . This is not surprising since individual BHs are produced by stellar evolutionary processes that are not strongly affected by dynamics. It is possible that extra BHs could be produced by stellar interactions, particularly by mergers where a star above the threshold mass for forming a BH can be created from two stars both below the threshold. Such events would be expected to be more frequent in dense clusters but do not seem to be important in my simulations. The number of BHs formed depends on f_b because a higher binary fraction corresponds to a larger number of individual stars (each binary contains two individual stars so the $f_b = 0.1$ have 6.0×10^5 stars in total whereas the $f_b = 0.5$ simulations have 7.5×10^5 stars in total), and on Z because as described in Chapter 4 mass-loss is less efficient at low metallicity and stars with a lower zero age main sequence mass can become BHs. Again more BHs could be produced in simulations with larger f_b as a consequence of mergers but few actually occur in my simulations and thus this effect is not very important. Proportionately more BHs are formed in binaries at $f_b = 0.5$ than at $f_b = 0.1$. This is simply a consequence of the larger portion of stars found in binaries at high binary fraction. Very few binaries that form a single BH survive the BH's formation; most either merge or are disrupted at the supernova. Very few binaries where both members are black holes (BH-BH binaries) form directly from primordial binaries and of those *all* are disrupted by

Individual Black Hole Statistics				
Simulation	$N_{sBH} \pm \sigma$	$N_{bBH} \pm \sigma$	$N_{BHBH} \pm \sigma$	$N_{surv} \pm \sigma$
10sol21	1118 ± 26	210 ± 8	2 ± 1	0 ± 0
10sol37	1142 ± 38	217 ± 20	2 ± 1	0 ± 0
10sol75	1114 ± 18	204 ± 10	2 ± 1	0 ± 0
10sol180	1124 ± 27	204 ± 21	2 ± 1	0 ± 0
10low21	1243 ± 49	227 ± 21	3 ± 1	1 ± 1
10low37	1253 ± 19	242 ± 22	6 ± 2	1 ± 1
10low75	1280 ± 23	239 ± 19	4 ± 5	1 ± 1
10low180	1320 ± 45	234 ± 19	3 ± 1	1 ± 1
50sol21	1477 ± 24	966 ± 21	10 ± 3	1 ± 1
50sol37	1486 ± 24	978 ± 14	13 ± 4	0 ± 0
50sol75	1478 ± 25	964 ± 24	8 ± 2	0 ± 0
50sol180	1553 ± 53	963 ± 20	8 ± 3	0 ± 0
50low21	1718 ± 38	1090 ± 32	10 ± 2	3 ± 1
50low37	1722 ± 25	1121 ± 9	17 ± 5	2 ± 1
50low75	1711 ± 33	1111 ± 31	15 ± 2	2 ± 1
50low180	1762 ± 26	1067 ± 26	8 ± 2	5 ± 3

Table 6.1: Number of BHs formed in each model by stellar evolutionary processes. N_{sBH} is the total number of black holes formed in the cluster. N_{bBH} is the total number of black holes formed in binaries. N_{BHBH} is the total number of black hole-black hole binaries formed in the cluster due to stellar evolutionary processes. N_{surv} is the number of binaries that form a black hole and survive the formation process. Note that all black hole-black hole binaries are disrupted during the second supernova, none survive. Each quantity is averaged over the four independent realisations and includes the standard deviation.

the supernova during the formation of the second BH. Thus all BH-BH binaries produced later in the simulations are formed by dynamical processes.

In Table 6.2 I present the cumulative number of BH-BH binaries in each simulation up to a given dynamical time, shown in units of t_{rh} , and after one Hubble time ($T_H = 14$ Gyr). The ages $3t_{rh}$, $9t_{rh}$, and $25t_{rh}$ correspond to the dynamical age of the clusters with $r_t/r_h = 21$, 37 , and 75 at $\approx 1T_H$ respectively. The simulations with $r_t/r_h = 180$ have dynamical ages of $\sim 117t_{rh}$ at $1T_H$. A new BH-BH binary is counted every time a binary where both members are BHs is created. Both a binary with one BH and one main sequence (MS) star where the MS star is exchanged for a BH and a binary where both members are BHs and one of the BHs is exchanged for a new BH are counted as new BH-BH binaries. The scatter in the number of BH-BH binaries produced by different realisations of the same simulation is significantly larger than for the single BHs. This is because, unlike stellar evolution, dynamical binary formation is a stochastic process driven by chance encounters that are strongly dependent on the details of the individual system. As was shown in by Table 6.1 all BH-BH binaries in these simulations are formed dynamically and thus variations between individual realisations are to be expected.

There are some clear trends in Table 6.2. After $1T_H$ the number of BH-BH binaries increases with f_b and initial concentration and decreases with Z . The reason for the f_b correlation is clear: the larger number of both BHs and hard binaries for the BHs to be exchanged into. The correlation with initial concentration is related both to the larger

interaction rate in dense systems and to the relative dynamical ages of the clusters after $1T_H$. For the same f_b and Z simulations have roughly the same number of BH-BHs when compared at the same dynamical age. By $1T_H$, however, clusters with a higher initial concentration are dynamically older and have had more opportunity to produce BH-BH binaries than their dynamically younger counterparts. The correlation with Z is due to the higher mass BHs present at low metallicity. From Equation 1.7 I expect the more massive BHs to sink to the core more rapidly than the less massive ones. Since BH-BH binary formation is a result of interactions and since the core is the densest region of the cluster, this faster mass segregation will allow the cluster to start creating BH-BH binaries earlier than its high-metallicity counterpart. The more massive BHs are also more likely to be retained by the cluster since they will need larger kicks upon formation in order to reach escape velocity.

Figure 6.1 shows the number of BH-BH binaries in each simulation per 500 Myrs. The trends noted in Table 6.2 are apparent, particularly those associated with the initial concentration. Simulations with higher initial concentration have a peak in BH-BH binary number per unit time while young but this number drops off later. Those with a lower concentration have smaller but more constant numbers of BH-BH binaries over longer spans of physical time. Often these low concentration clusters do not reach a maximum in BH-BH binary number per unit time within a Hubble time. It is also clear that the more metal-poor simulations evolve more quickly and produce BH-BH binaries earlier than their metal-rich counterparts. This again is a consequence of faster mass segregation. Finally, f_b does not affect the location of peak BH-BH binary number for a given set of initial conditions but simulations with $f_b = 0.5$ are able to sustain production of BH-BH binaries longer, probably because the supply of BHs and hard binaries to exchange them into is larger in these clusters.

Simulation	BH-BH Binaries After xt_{rh}			
	$t = 3t_{rh}$	$t = 9t_{rh}$	$t = 25t_{rh}$	$t = 14 \text{ Gyr}$
10sol21	1 ± 1	-	-	2 ± 2
10sol37	1 ± 1	8 ± 2	-	9 ± 1
10sol75	0 ± 0	8 ± 4	50 ± 24	52 ± 25
10sol180	0 ± 0	14 ± 6	56 ± 25	128 ± 4
10low21	28 ± 10	-	-	33 ± 12
10low37	23 ± 4	44 ± 9	-	44 ± 9
10low75	22 ± 6	40 ± 13	54 ± 6	55 ± 6
10low180	27 ± 10	52 ± 4	90 ± 9	124 ± 15
50sol21	1 ± 1	-	-	2 ± 1
50sol37	4 ± 0	42 ± 7	-	57 ± 9
50sol75	1 ± 1	22 ± 7	113 ± 35	146 ± 41
50sol180	0 ± 0	9 ± 1	110 ± 21	342 ± 13
50low21	104 ± 6	-	-	126 ± 3
50low37	92 ± 15	173 ± 28	-	182 ± 26
50low75	64 ± 10	137 ± 13	173 ± 22	176 ± 23
50low180	95 ± 20	189 ± 29	276 ± 42	480 ± 127

Table 6.2: The cumulative number of BH-BH binaries after 3, 9, and 25 t_{rh} , and also after $1T_H$. Each column is averaged over the four independent realisations and includes the standard deviation.

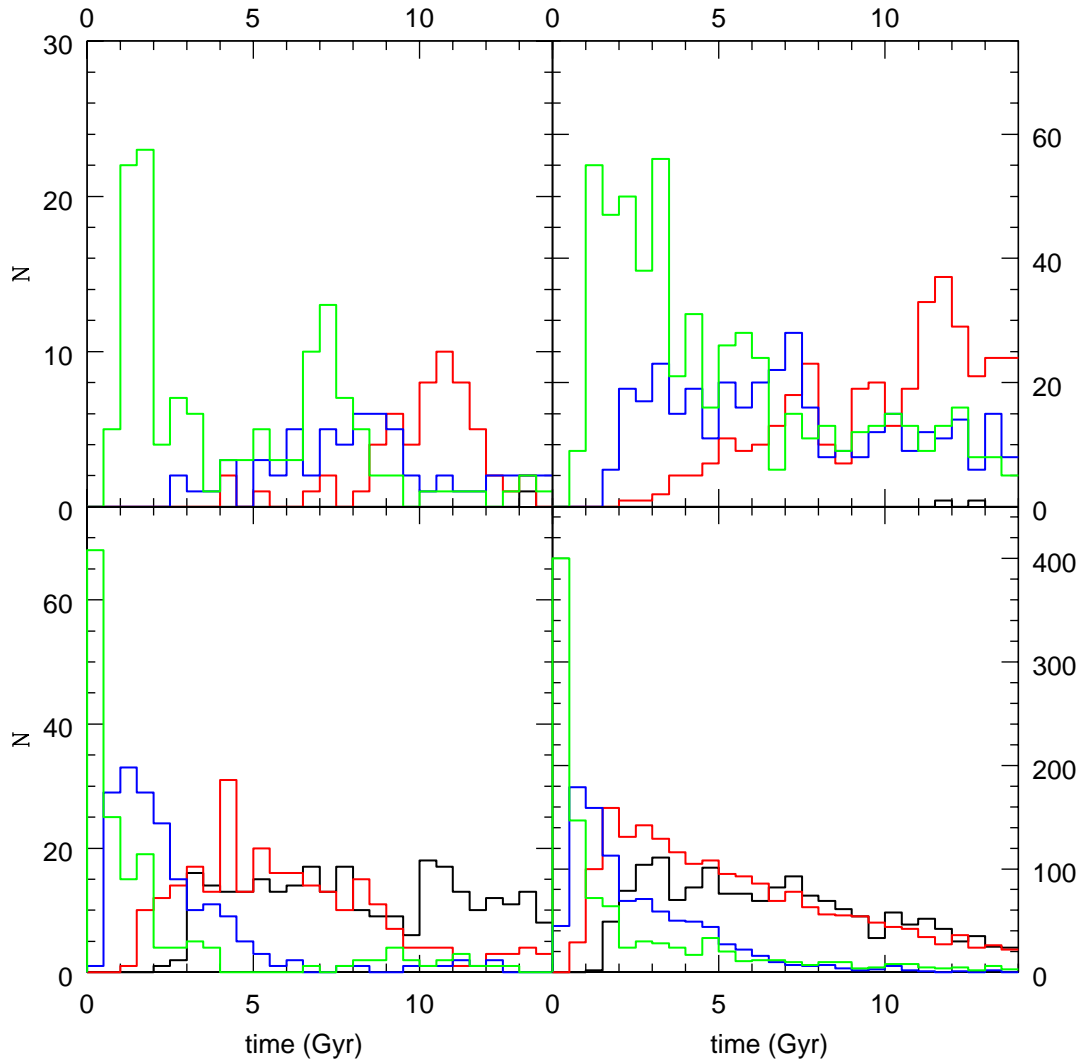


Figure 6.1: The number of BH-BH binaries per 500 Myr. Top row has $Z = 0.02$ and bottom row has $Z = 0.001$. Left column has $f_b = 0.1$ and right column has $f_b = 0.5$. Concentrations are $r_t/r_h = 21$ (black), $r_t/r_h = 37$ (red), $r_t/r_h = 75$ (blue), and $r_t/r_h = 180$ (green). Each bin is averaged over the four independent realisations.

In Figure 6.2 I present the spatial distribution of the BHs and BH-BH binaries in my simulations. In all cases BHs are centrally concentrated as a consequence of mass segregation. This shows that the BH population does not remain in dynamical equilibrium with the rest of the cluster and in terms of previous work favours the assumptions made by O’Leary et al. (2006) over those made by Sadowski et al. (2008). The varying mass segregation timescales can be seen in the length of time taken for the half-mass radius of the BH population to contract to an equilibrium state induced by binary burning. The BH population in the low metallicity, high density clusters contracts and reaches equilibrium much faster than for the high metallicity, low density simulations. The half-mass radii

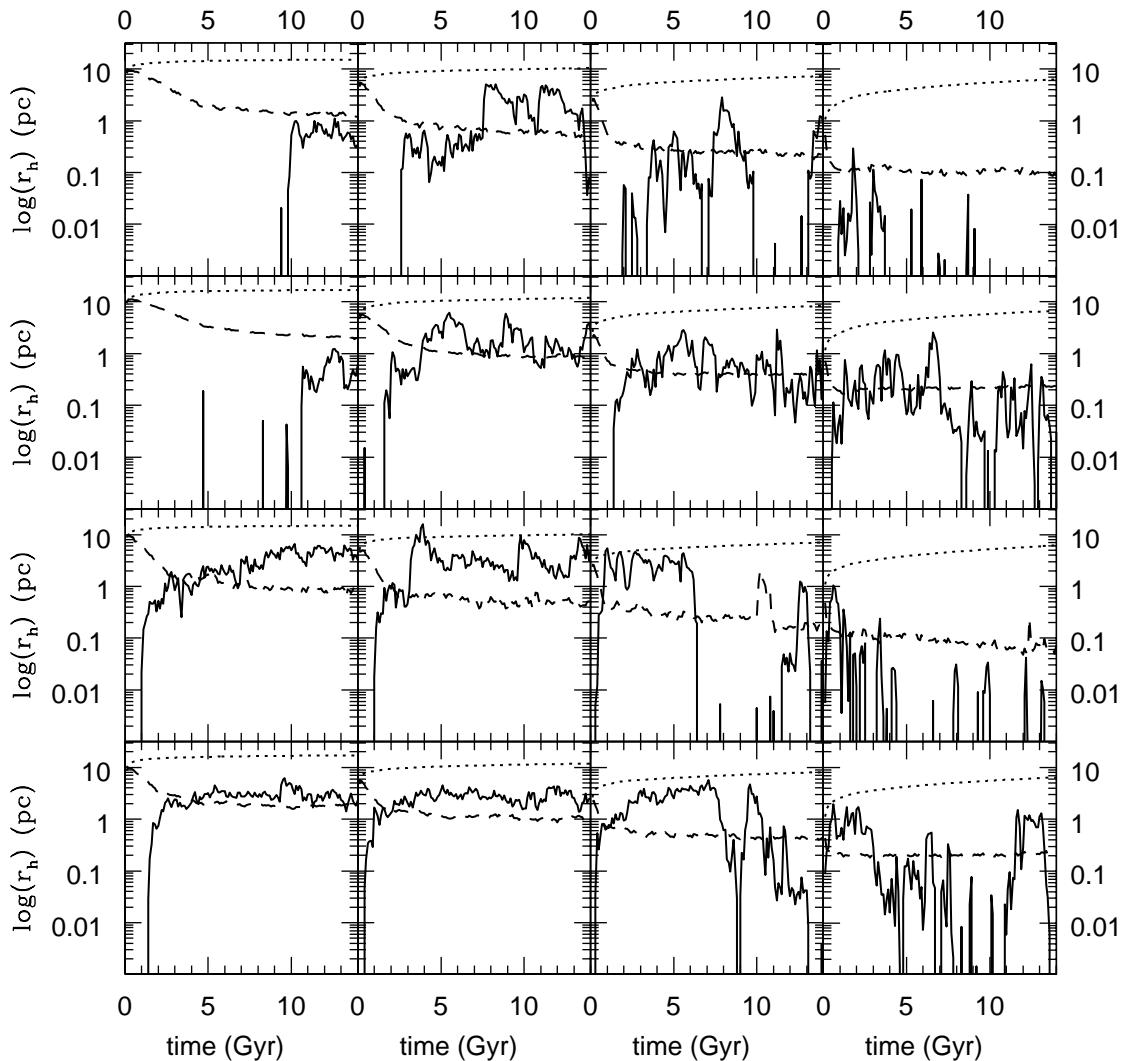


Figure 6.2: The half-mass radii for the BH system. Top to bottom: $Z = 0.02$ and $f_b = 0.1$, $Z = 0.001$ and $f_b = 0.1$, $Z = 0.02$ and $f_b = 0.5$, and $Z = 0.001$ and $f_b = 0.5$. Left to right: $r_t/r_h = 21$, $r_t/r_h = 37$, $r_t/r_h = 75$, and $r_t/r_h = 180$. Shown are r_h for all cluster stars (dotted), r_h of all BHs (dashed), and r_h of all BH-BH binaries (solid). The radial profiles have been smoothed over a 100 Myr box and then each box has been averaged across the four independent realisations.

of the BH-BH populations must be interpreted more carefully. Since BH-BH binaries are formed dynamically from BHs, the BH-BH binary population is initially very centrally concentrated. As the population evolves, however, the BH-BH binaries interact strongly and can eject each other from the core region. As is clear from Figure 6.1 there are often very few BH-BH binaries in the cluster at any given time and the half-mass radius of the BH-BH population in Figure 6.2 is often based on very few objects. Thus the location of a single massive BH-BH binary outside the core can dominate the determination of the

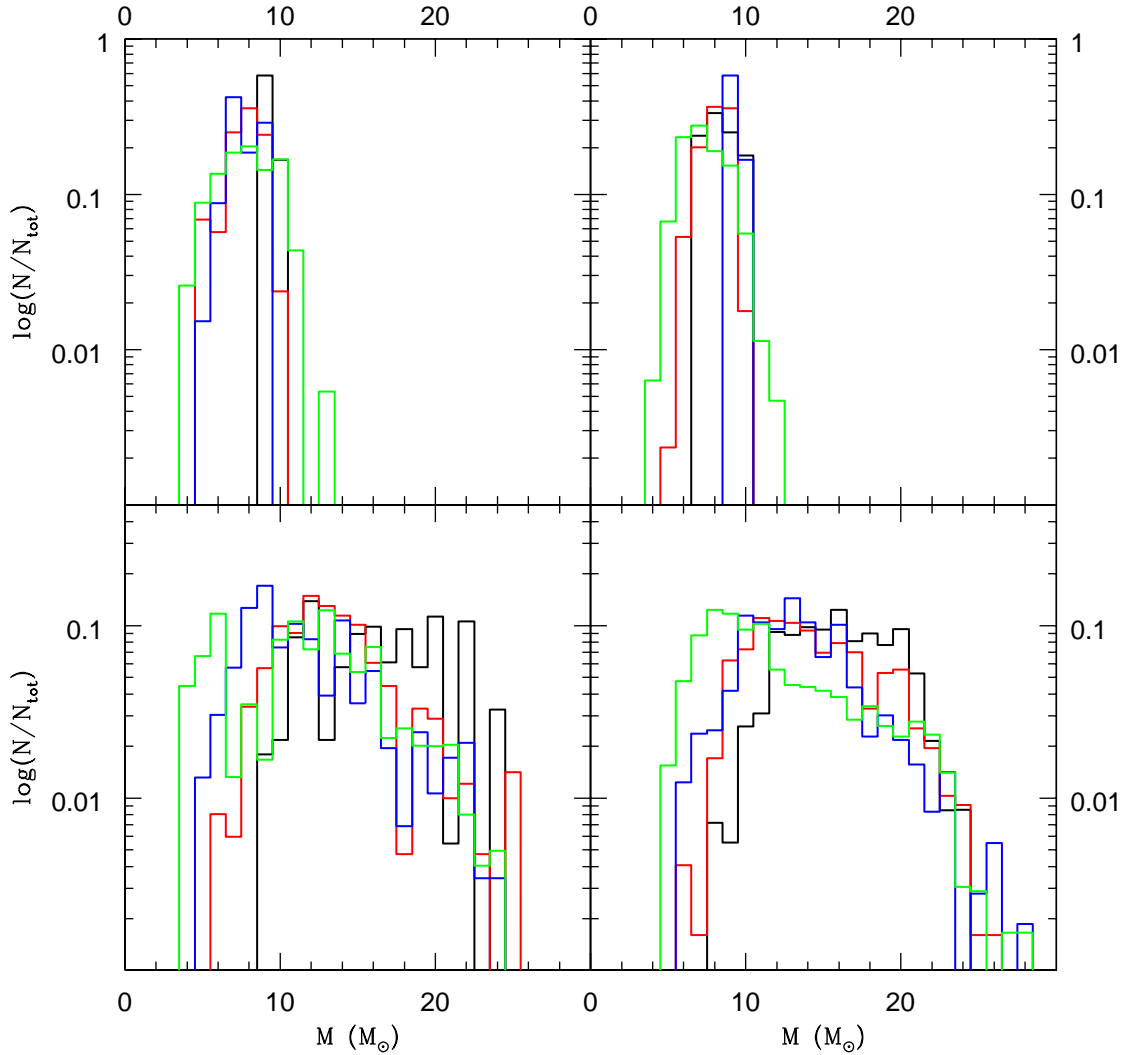


Figure 6.3: The cumulative chirp mass distribution of BH-BH binaries up to $1T_H$ binned in $1M_\odot$ bins. Top row has $Z = 0.02$ and bottom row has $Z = 0.001$. Left column has $f_b = 0.1$ and right column has $f_b = 0.5$. Concentrations are $r_t/r_h = 21$ (black), $r_t/r_h = 37$ (red), $r_t/r_h = 75$ (blue), and $r_t/r_h = 180$ (green). Each bin is averaged over the four independent realisations.

BH-BH half-mass radius. Because of this it is difficult to draw significant conclusions about the spatial distribution of BH-BH binaries other than to say that they tend to be centrally concentrated and evolve quickly. It is clear, however, that the BH population forms a mass-segregated subsystem in the cluster core where strong interactions will dominate the dynamics.

The cumulative chirp mass distribution for all BH-BH binaries the simulations after $1T_H$ are given in Figure 6.3. Note that these are cumulative profiles for all BH-BHs at all times before $1T_H$, not a snapshot at $1T_H$. I show M_{chirp} because as discussed in Chapter 3 it is

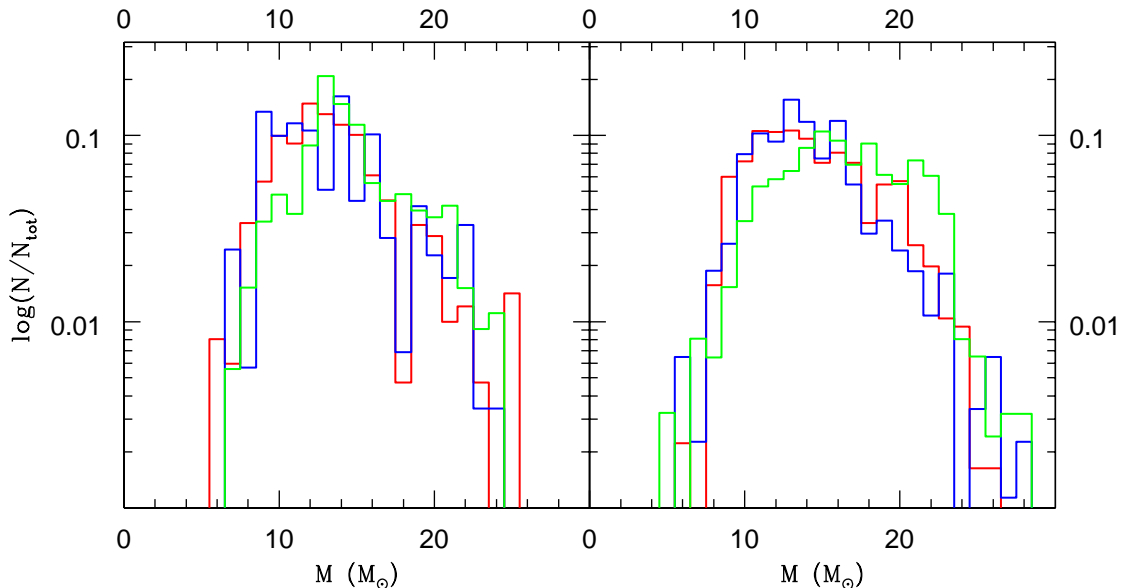


Figure 6.4: The cumulative chirp mass distribution of BH-BH binaries up to $9t_{rh}$ for six simulations binned in $1M_{\odot}$ bins. Both plots are for $Z = 0.001$ with the left plot having $f_b = 0.1$ and the right plot having $f_b = 0.5$. Concentrations are $r_t/r_h = 37$ (black), $r_t/r_h = 75$ (red), and $r_t/r_h = 180$ (blue). $9t_{rh}$ is the dynamical age of the simulation with $r_t/r_h = 37$ after one Hubble time. The simulations with $r_t/r_h = 21$ are not shown since they do not reach $9t_{rh}$ within one Hubble time and have too few BH-BHs at $3t_{rh}$ for interesting statistics. Each bin is averaged over the four independent realisations.

this and not the total mass of the binary that is the quantity of interest for gravitational wave detection. For the higher metallicity simulations the distribution is narrow with a peak around $8 - 10M_{\odot}$. The distribution is not affected by any of the other initial conditions except in overall number of BH-BH binaries produced. The low-metallicity distribution is much broader and is fairly flat between $\sim 10 - 20M_{\odot}$. This is a consequence of the more massive BHs generated at lower metallicity and agrees with the low-metallicity simulations of Sadowski et al. (2008). Here the distribution is affected by the initial concentration with the distribution peaking at lower masses for the more concentrated simulations. This is a result of the relative dynamical ages of the simulations as shown in Figure 6.4, the distribution of M_{chirp} after $9t_{rh}$. At the same dynamical age the mass distribution is unaffected by the concentration. Recalling both that the more dense clusters evolve more quickly and that the more massive BHs sink to the centre faster than the less massive BHs, the more massive BHs will interact, take part in binary formation, and be disrupted or ejected earlier than the low-mass BHs. Only after the high-mass BHs have gone will the low-mass BHs dominate the BH-BH dynamics. Since the more concentrated clusters are dynamically older, they have had more time to experience this effect, deplete their high-mass BHs and BH-BH binaries, and thus have a larger fraction of low-mass binaries after a Hubble time. The high-metallicity clusters do not have a broad enough distribution in mass for this effect to be important. Perhaps the most interesting result is that after $1T_H$ the chirp mass distributions are systematically different between clusters with different metallicities

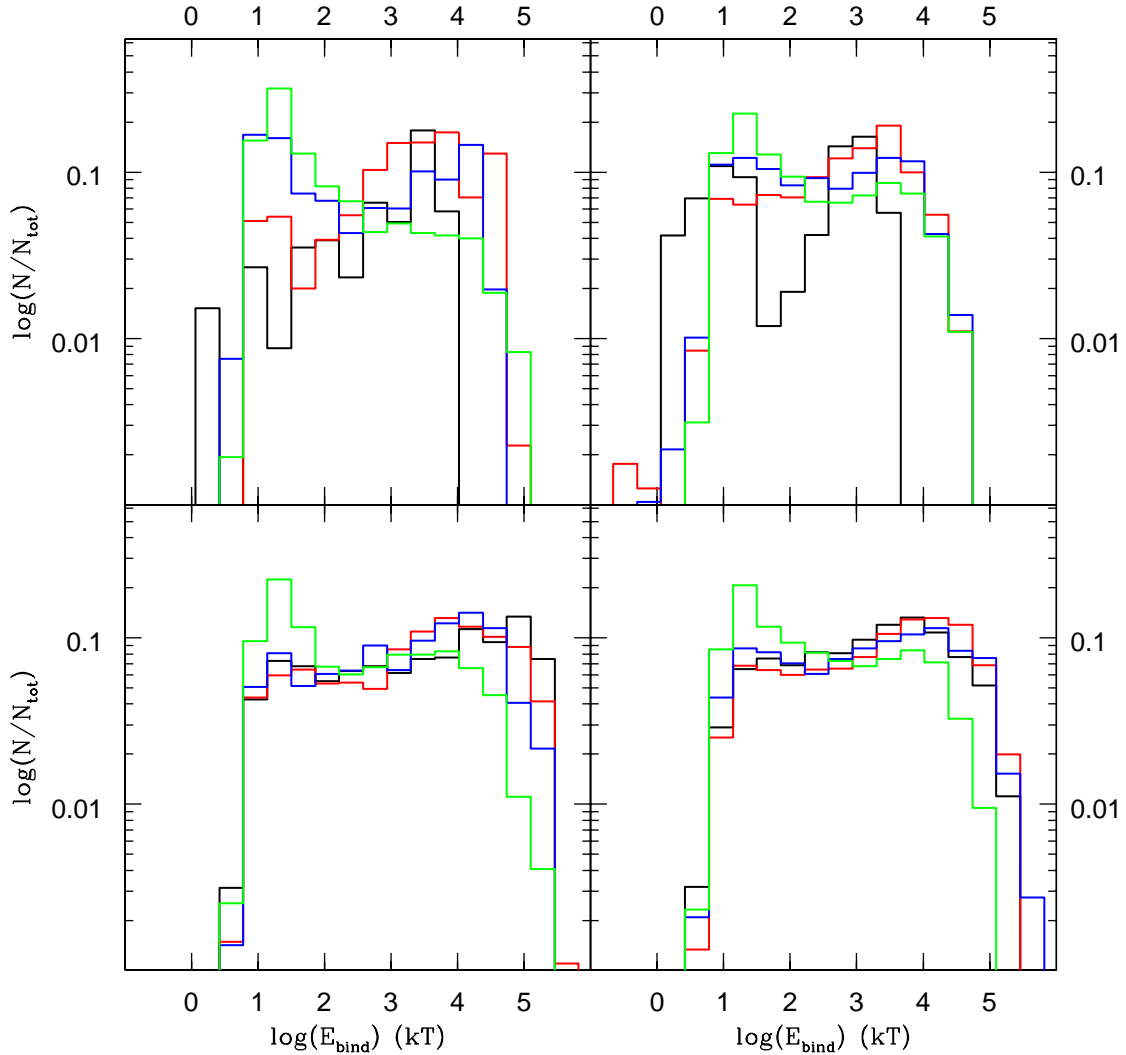


Figure 6.5: Cumulative binding energy distribution of BH-BH binaries up to $1T_H$ binned uniformly in log space. $Z = 0.02$ for the top row and $Z = 0.001$ for the bottom row. $f_b = 0.1$ for the right column and $f_b = 0.5$ for the left column. Concentrations are $r_t/r_h = 21$ (black), $r_t/r_h = 37$ (red), $r_t/r_h = 75$ (blue), and $r_t/r_h = 180$ (green). Energy is in units of kT ($E_{kin} = \frac{3}{2}NkT$) where a hard binary has $|kT| > 1$. Each bin is averaged over the four independent realisations.

and concentrations. Therefore building chirp mass distributions using gravitational wave observations can yield information on the physical and dynamical state of star clusters.

The cumulative distribution of BH-BH binary binding energy (E_{bind}) up to $1T_H$ is given in Figure 6.5. All BH-BH binaries are hard. This is to be expected because soft binaries would be destroyed by the interactions necessary to introduce a BH into the system. There is little variation with the cluster parameters because $k_B T$, the thermal energy of the cluster that is used as the normalisation factor for E_{bind} , scales with cluster mass and

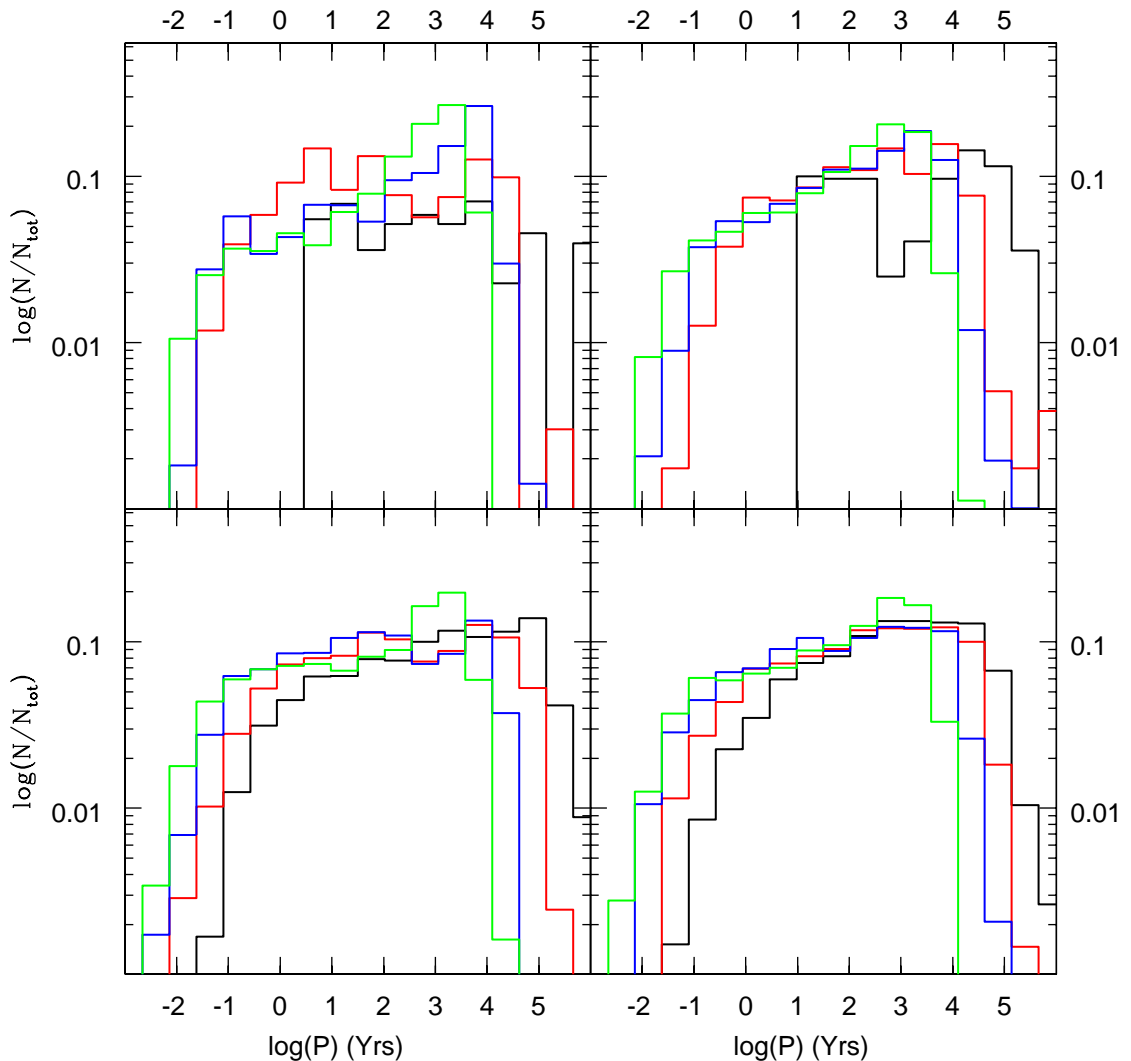


Figure 6.6: Cumulative period distribution of BH-BH binaries up to $1T_H$ binned uniformly in log space. $Z = 0.02$ for the top row and $Z = 0.001$ for the bottom row. $f_b = 0.1$ for the right column and $f_b = 0.5$ for the left column. Concentrations are $r_t/r_h = 21$ (black), $r_t/r_h = 37$ (red), $r_t/r_h = 75$ (blue), and $r_t/r_h = 180$ (green). Each bin is averaged over the four independent realisations.

density. The only exception to this appears to be clusters with $r_t/r_h = 180$. These clusters seem to have an excess of soft binaries. The combination of the larger interaction cross-section for binaries with larger semi-major axes and the larger interaction rate in the cores of very dense clusters may lead to more BHs being exchange into softer binaries. It could also be that the soft binaries in the more concentrated simulations still have a larger binding energy in absolute terms than those in the less concentrated simulations and have a slightly better chance of survival.

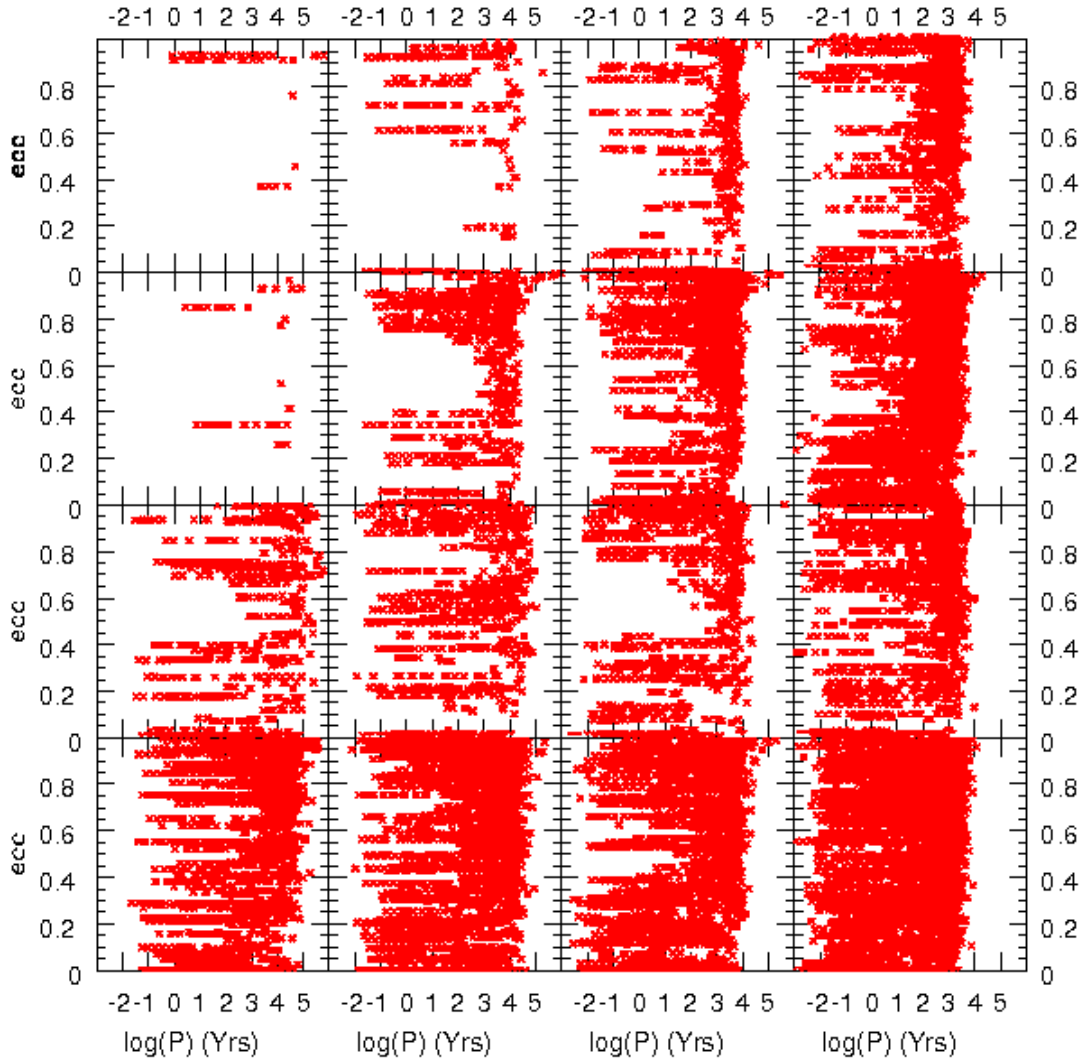


Figure 6.7: The eccentricity as a function of period for all BH-BH binaries at all times in all simulations. From left to right $r_t/r_h = 21$, $r_t/r_h = 37$, $r_t/r_h = 75$, and $r_t/r_h = 180$. From top to bottom $f_b = 0.1$ and $Z = 0.02$, $f_b = 0.5$ and $Z = 0.02$, $f_b = 0.1$ and $Z = 0.001$, and $f_b = 0.5$ and $Z = 0.001$.

In Figure 6.6 I present the cumulative period (P) distribution for the entire populations of BH-BH binaries that have existed up to $1T_H$. There is a large spread in P , ranging from days to $\sim 10^5$ yrs. The period distribution does not depend strongly on the cluster parameters. The 10sol21 and 50sol21 models have no very short-period binaries which could be a product of the low interaction rate combined with the lower interaction cross-section for binaries with small semi-major axes. The statistics for these simulations are rather poor and should not be taken as conclusive. The entire distribution is shifted slightly towards shorter periods in the more highly concentrated simulations. This is partly due to the slightly higher velocity dispersion in these clusters and the consequently higher value of

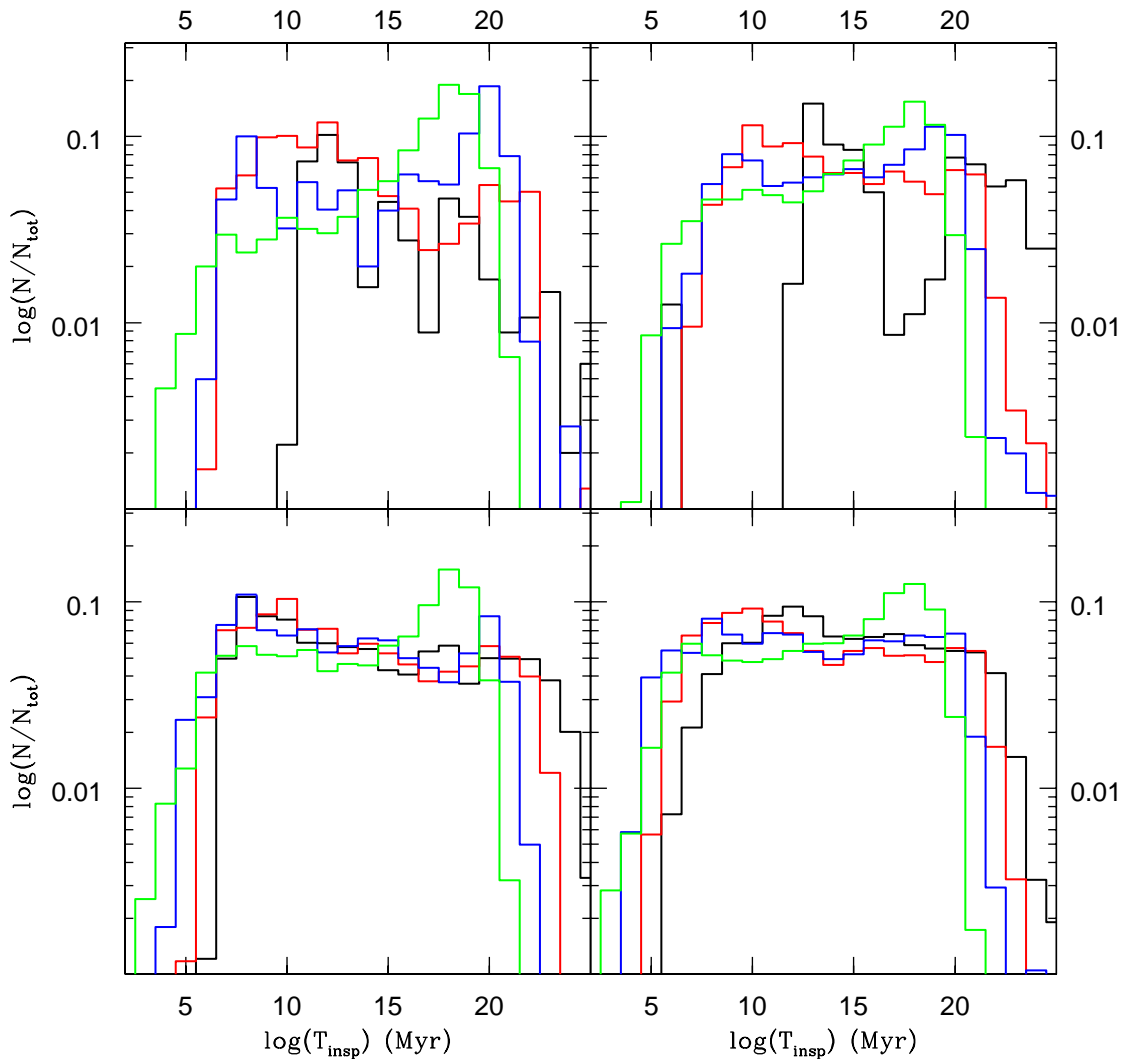


Figure 6.8: Cumulative distribution of BH-BH binary gravitational wave inspiral timescale up to $1T_H$ binned uniformly in log space. $Z = 0.02$ for the top row and $Z = 0.001$ for the bottom row. $f_b = 0.1$ for the right column and $f_b = 0.5$ for the left column. Concentrations are $r_t/r_h = 21$ (black), $r_t/r_h = 37$ (red), $r_t/r_h = 75$ (blue), and $r_t/r_h = 180$ (green). Each bin is averaged over the four independent realisations.

$k_B T$ in physical units. Thus the concentrated cluster binaries must have higher binding energies and shorter periods in physical units. It is also partly due to the larger number of hardening interactions due to the higher interaction rate. Despite the overall shift, the clusters with $r_t/r_h = 180$ show a peak in the period distribution at fairly long periods. This corresponds the peak at low binding energy in Figure 6.5. Overall, however, the period distributions are fairly similar and span approximately the same range for all models.

Although there binaries with periods less than a year present in most simulations, most periods are not short enough to produce a gravitational wave merger within $1T_H$. Using

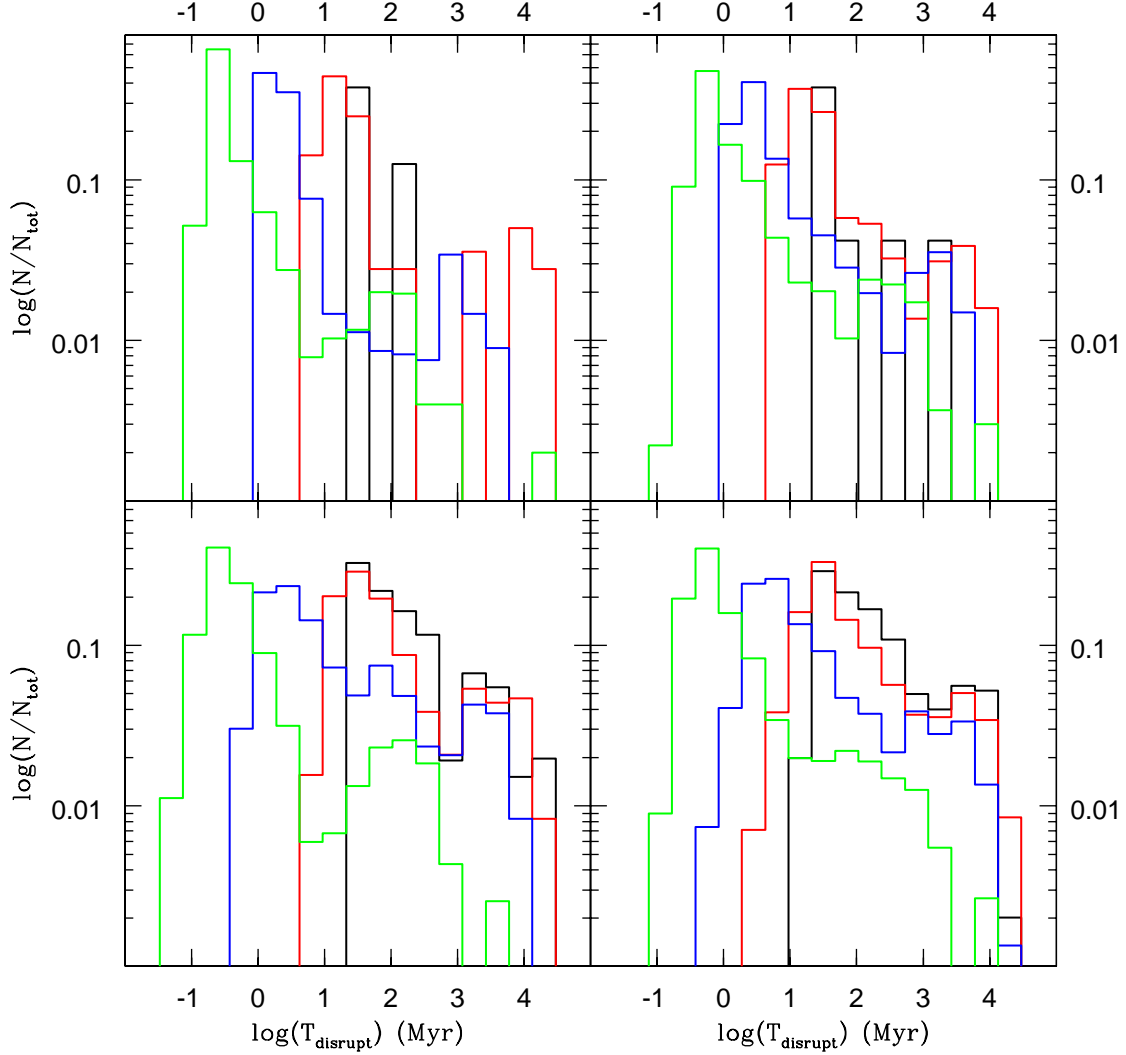


Figure 6.9: Cumulative distribution of BH-BH binary dynamical disruption timescale up to $1T_H$ binned uniformly in log space. $Z = 0.02$ for the top row and $Z = 0.001$ for the bottom row. $f_b = 0.1$ for the right column and $f_b = 0.5$ for the left column. Concentrations are $r_t/r_h = 21$ (black), $r_t/r_h = 37$ (red), $r_t/r_h = 75$ (blue), and $r_t/r_h = 180$ (green). Each bin is averaged over the four independent realisations.

Equation 3.40 I can estimate inspiral timescales, t_{insp} , for a binary by taking:

$$t_{\text{insp}} \approx \frac{a_{\text{in}}}{\dot{a}} \quad (6.1)$$

where a_{in} is the initial semi-major axis of a binary as was done in Table 3.1. For a circular binary with $m_1 = m_2 = 10M_\odot$ and an initial period of $P_{\text{in}} = 1$ day, $t_{\text{insp}} \approx 1$ Gyr. If $P_{\text{in}} = 1$ yr then $t_{\text{insp}} = 10^6$ Gyr. Thus all but the shortest period binaries in the cluster will be unable to merge within $1T_H$. Furthermore, the minimum gravitational wave frequency

for which LISA is sensitive is $\approx 10^{-5}$. From Chapter 3 gravitational for a circular orbit are emitted only in the $n = 2$ harmonic of the orbital frequency. Thus circular binaries must have periods of less than a day to be detected by LISA.

As discussed in Chapter 3 the presence of eccentricity in a binary can vastly improve its prospect for gravitational wave detection. Figure 3.1 shows that the power radiated is strongly enhanced by high eccentricity and Table 3.1 proves that this reduces t_{insp} by a significant factor, enhancing the chance of a relativistic merger. Figure 3.3 shows that eccentric orbits also produce gravitational waves at much higher frequencies, moving longer period binaries into the LISA band. In Figure 6.7 I show the eccentricity of our BH-BH binaries as a function of period. These eccentricities must be treated with care since they are produced randomly by the interaction prescriptions rather than by self-consistent dynamical evolution but they give an idea of what can be expected in real cluster. Figure 6.7 shows that there are a wide range of eccentricities for any given period and particularly for more concentrated simulations short period binaries can have significant eccentricity.

Since some of my binaries are eccentric and since this eccentricity can significantly reduce the inspiral timescale of the binary, I use Equation 6.1 to estimate the inspiral timescale of all BH-BH binaries in my simulations. The result is given in Figure 6.8. It is apparent that even with eccentricity included there are very few binaries with an inspiral timescale of less than $1T_H$ and most are much longer. There is a very slight tendency towards shorter inspiral times for the more concentrated models, reflecting the slightly shorter periods present in these systems, but the peak of the distribution is not shifted $t_{\text{insp}} < T_H$. There are a few BH-BH binaries with $t_{\text{insp}} < 10^5$ Myr and here the dynamics play a destructive role. Figure 6.9 shows the timescale for dynamical disruption or ejection of BH-BH binaries, t_{disrupt} . It is apparent that the average t_{disrupt} for BH-BH binaries is very short, between 1 – 100 Myr in most cases, and is shorter in the more concentrated clusters. There is almost no overlap between the distributions in Figure 6.8 and Figure 6.9 and $t_{\text{insp}} > t_{\text{disrupt}}$ in almost all cases. Indeed in none of my simulations do I find a BH-BH merger. Thus although star clusters produce BH-BH binaries very efficiently they disrupt them very efficiently as well, at least when BH-BH binaries are allowed to interact. Therefore I predict few compact mergers in globular clusters due to gravitational wave radiation. Some of the eccentric, short-period binaries in my simulations may, however, have a chance of appearing in the LISA band and I will consider this possibility in Chapter 8.

Chapter 7

The Escapers

Stars escape from tidally limited clusters due to re-population of the high velocity tail of the velocity distribution by small angle scattering or due to dynamical ejection where a star gains enough kinetic energy from one close interaction in order to exceed the escape velocity of the cluster. Dynamical ejection is particularly likely for hard binaries because the kinetic energy gained by stars in interactions is related to the binding energy of the binary or binaries involved. As I have shown in Chapter 6 the BH-BH binaries in my simulations are hard and thus will be susceptible to dynamical ejection. Ejection is most likely to occur as a result of binary-single interactions, where the binding energy of the binary is increased and the binary centre of mass gains $\Delta E_b/3$ of the change as kinetic energy, or in binary-binary interactions where one binary is disrupted and the centres of mass gain a fraction of the total change in energy, $0.516(E_{b1} + E_{b2})$, distributed according to conservation of momentum (see Chapter 4). BH-NS and NS-NS binaries (such as they exist) will also be affected by this process although less strongly. Hard binaries have short periods and this also opens up the possibility of cluster BH-BHs merging in the galactic field, providing the interesting new perspective that gravitational wave sources in the field may have originated in star clusters.

7.1 Escaper Statistics

In Figure 7.1 I present the binding energy distribution of escaping BH-BH binaries. All binaries are very hard, much harder on average than the binaries remaining in the cluster, and this supports a dynamical ejection scenario. Relaxation interactions are not affected by the binding energy of the binary and thus binaries removed by relaxation should have the same energy distribution as the cluster binaries. Figure 7.1 agrees well with the binding energy distribution of ejected BH-BH binaries found in O’Leary et al. (2006) (their Figure 6). The O’Leary et al. (2006) distribution extends to lower energy than mine but this is probably due to the smaller total number of stars across all my simulations (their simulation set was larger). Their simulations are based on simplified cluster dynamics but include explicit few-body integration for the interactions. This agreement between our approximations increases my confidence that the treatment of processes in the core of our clusters is essentially correct. Since they will no longer be disrupted by interactions, there is a good chance that at least some of these binaries will be able to merge in the galactic field within a Hubble time.

As mentioned this distribution peaks at much higher binding energy than the distribution shown in Figure 6.5 and this helps explain why there are no merger candidates in the

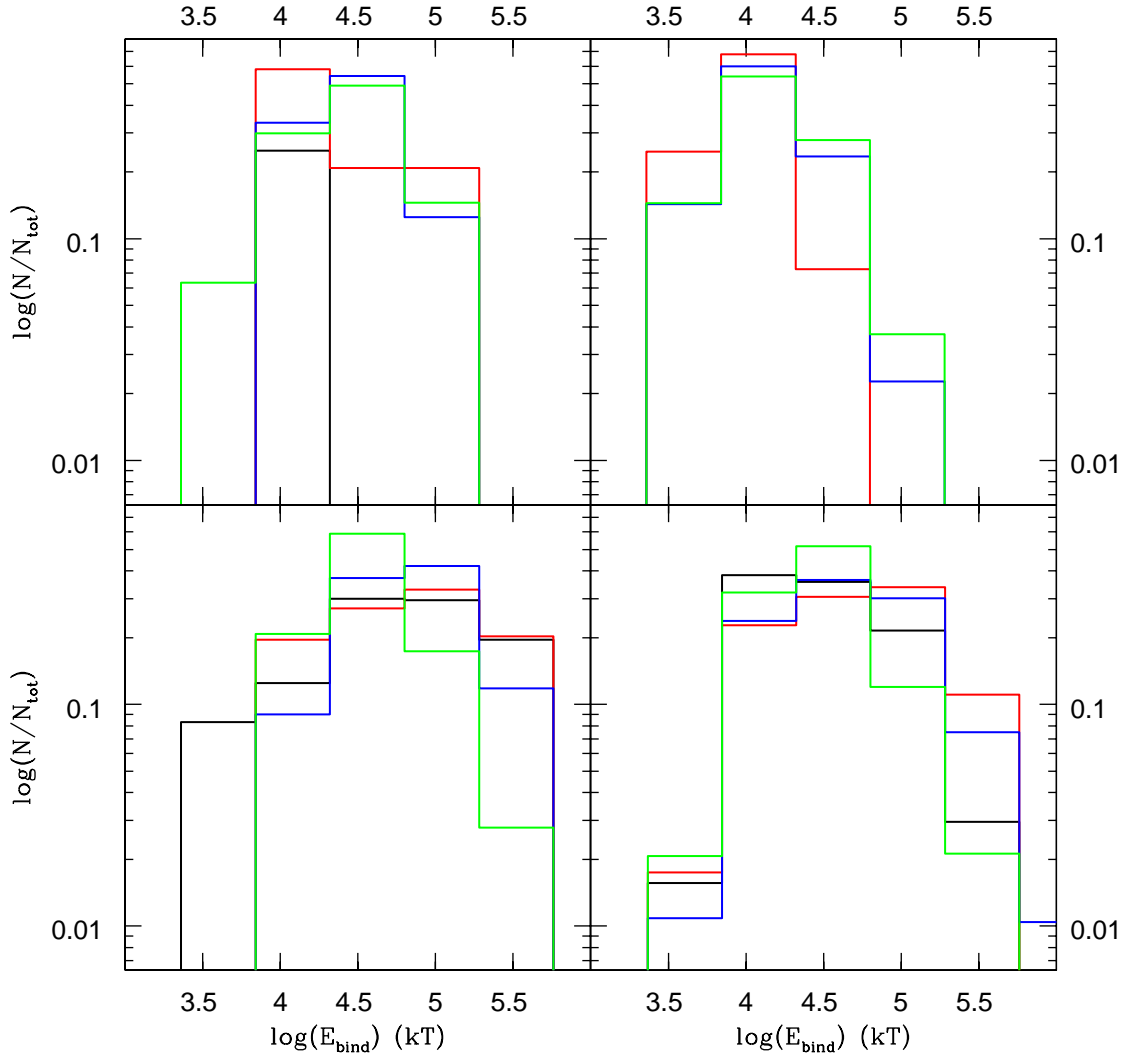


Figure 7.1: The binding energy of BH-BH escapers from the cluster in units of $k_B T$. Top row has $Z = 0.02$, bottom row has $Z = 0.001$. Left column has $f_b = 0.1$, right column has $f_b = 0.5$. Black is for $r_t/r_h = 21$, red for $r_t/r_h = 37$, blue for $r_t/r_h = 75$, and green for $r_t/r_h = 180$. Both axes are plotted in log scale.

clusters themselves. Those very hard binaries that are good candidates for gravitational wave merger will be preferentially ejected and will merge in the galactic field. Therefore clusters themselves may not be strong gravitational wave merger sources but they may still enhance the total detection rate in field mergers.

The total number of escapers is shown in Table 7.1 for all simulations. In this table I have summed rather than averaged the results of the different realisations in order to give better statistics. This also makes sense physically. The escapers will be mixed with both the galactic field binaries and with each other rather than being associated with individual

clusters. Several trends are apparent in Table 7.1: the number of escapers increases with concentration, binary fraction, and decreasing metallicity.

The number of escapers is affected by the concentration primarily because there are more BH-BH binaries in these simulations (see Chapter 6). This is further enhanced by two factors. First the more concentrated clusters will have a higher interaction rate than the less concentrated clusters, increasing the probability for any given binary to experience a dynamical ejection. Second, t_{rh} is shorter in the more concentrated clusters leading to faster dynamical evolution, a higher ejection rate, and more escapers after a Hubble time. As was shown in Chapter 6 these clusters will deplete their BH-BH population faster and thus the escape rate should drop off at later times.

The correlation with f_b is also related to the number of BH-BH binaries and the interaction rate. The clusters with $f_b = 0.5$ have more binaries than those with $f_b = 0.1$ and will have both more escaper candidates and more binary-binary interactions in which they can be ejected.

The correlation with metallicity is due to the different mass range of BHs. As described in Section 4.4 the lower mass-loss rates and greater fallback at low metallicity will create more BHs and thus more candidates to be exchanged into BH-BH binaries. Furthermore these binaries are more massive and will sink to the cluster centre, where interaction rates are highest and ejections most likely, more rapidly than for the high-metallicity simulations. In

BH-BH Escapers				
Simulation	N_E	$N_{Eave} \pm \sigma_{N_E}$	N_M	$N_{Mave} \pm \sigma_{N_M}$
10sol21	1	0 ± 1	0	0 ± 0
10sol37	8	2 ± 1	1	0 ± 1
10sol75	11	3 ± 1	1	0 ± 1
10sol180	23	6 ± 2	9	2 ± 1
50sol21	0	0 ± 0	0	0 ± 0
50sol37	23	6 ± 1	2	1 ± 1
50sol75	51	13 ± 2	6	2 ± 1
50sol180	89	22 ± 4	17	4 ± 2
10low21	14	4 ± 1	1	0 ± 1
10low37	26	6 ± 1	1	0 ± 1
10low75	30	8 ± 2	10	2 ± 2
10low180	42	10 ± 2	22	6 ± 1
50low21	66	16 ± 1	1	0 ± 1
50low37	97	24 ± 5	10	2 ± 1
50low75	93	23 ± 1	26	6 ± 2
50low180	143	36 ± 1	63	16 ± 5

Table 7.1: The number of BH-BH binaries that escape from the simulations after one Hubble time. Column 1 gives the simulation parameters. Column 2 is the sum of all escapers from all four independent realisations of each set of initial conditions. Column 3 gives the average number of escapers per realisation of each simulation \pm the standard deviation across all four realisations. Column 4 gives the total number of mergers summed over all simulations. Column 4 gives the average number of mergers per simulation \pm the standard deviation across all four realisations.

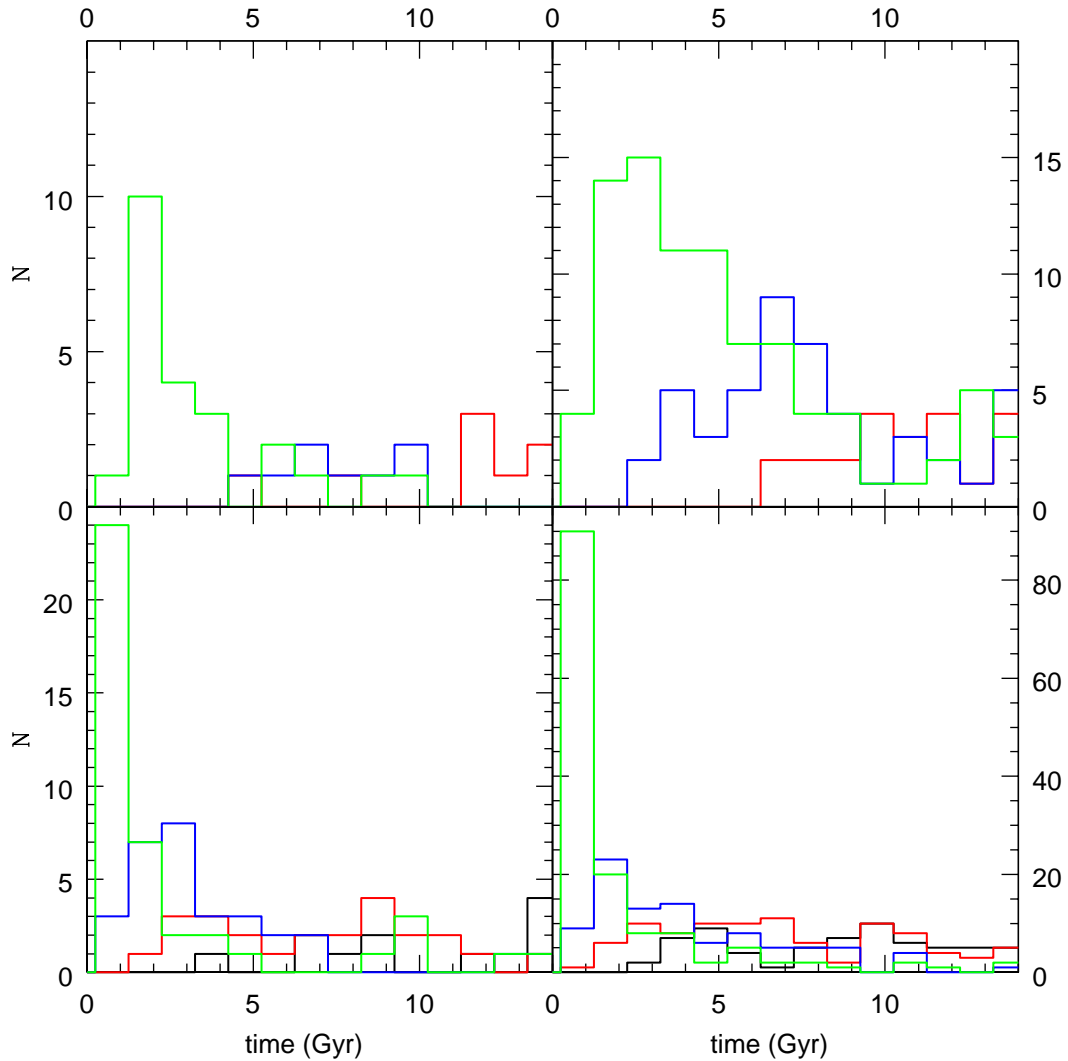


Figure 7.2: The number of BH-BH escapers per Gyr for all simulations. Top row has $Z = 0.02$, bottom row has $Z = 0.001$. Left column has $f_b = 0.1$, right column has $f_b = 0.5$. Black is for $r_t/r_h = 21$, red for $r_t/r_h = 37$, blue for $r_t/r_h = 75$, and green for $r_t/r_h = 180$. Note that the scale on the y-axis for each plot is different.

principle these binaries can also receive a greater recoil velocity since they are more massive and have a higher binding energy for the same orbital separation.

I consider the number of escapers per Gyr in Figure 7.2. The number in each bin is a sum over all realisations of a given model. The trends visible in Table 7.1 are confirmed in Figure 7.2. In particular the binary fraction increases the overall number of escapers but not the shape of the distribution whereas the concentration and metallicity have an effect on the evolution of the number of escapers per Gyr. More concentrated clusters have many escapers early and almost none after $1T_H$. This is simply due to the faster relaxation processes in these clusters. Low-metallicity clusters have an even larger number of escapers

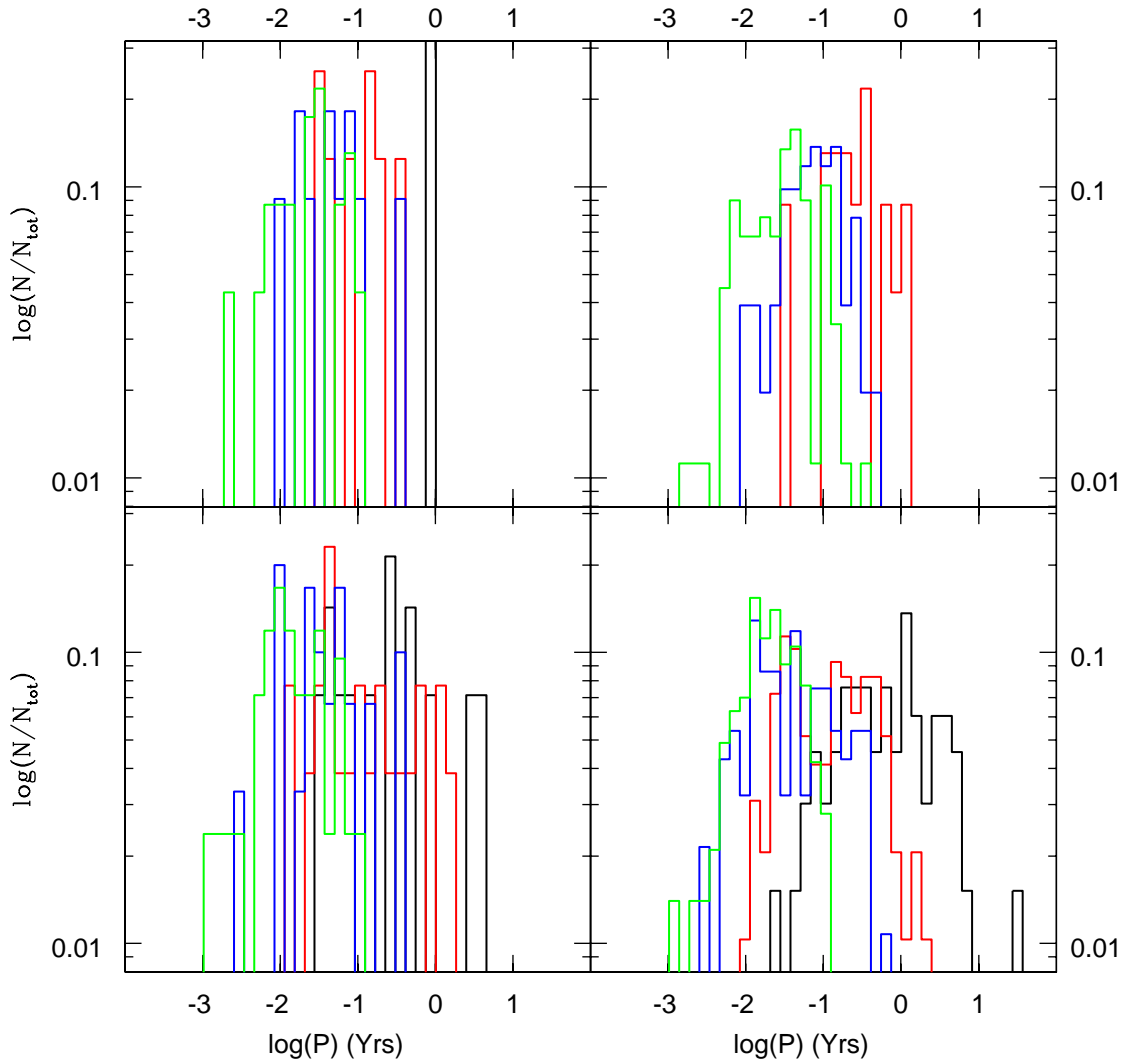


Figure 7.3: The period distribution of escaping BH-BH binaries. Top row has $Z = 0.02$, bottom row has $Z = 0.001$. Left column has $f_b = 0.1$, right column has $f_b = 0.5$. Black is for $r_t/r_h = 21$, red for $r_t/r_h = 37$, blue for $r_t/r_h = 75$, and green for $r_t/r_h = 180$. Both axes are in log scale.

when young due to the additional enhancement from fast mass segregation. The result is that dense, low metallicity clusters will tend to lose many BH-BH binaries while young but few later whereas clusters with lower concentration and higher metallicity maintain a more modest but more constant number of escapers per unit time over their entire lives.

Figure 7.3 gives the period distribution for all BH-BH escapers at the time of escape from the cluster. As to be expected from their high binding energies, the periods for the escapers are short, generally less than a year and some less than a day. The periods tend to be shorter for the high concentration simulations. This is a consequence of the higher value of E_{bind} in physical units in these clusters as discussed in Chapter 6. Recalling the estimates

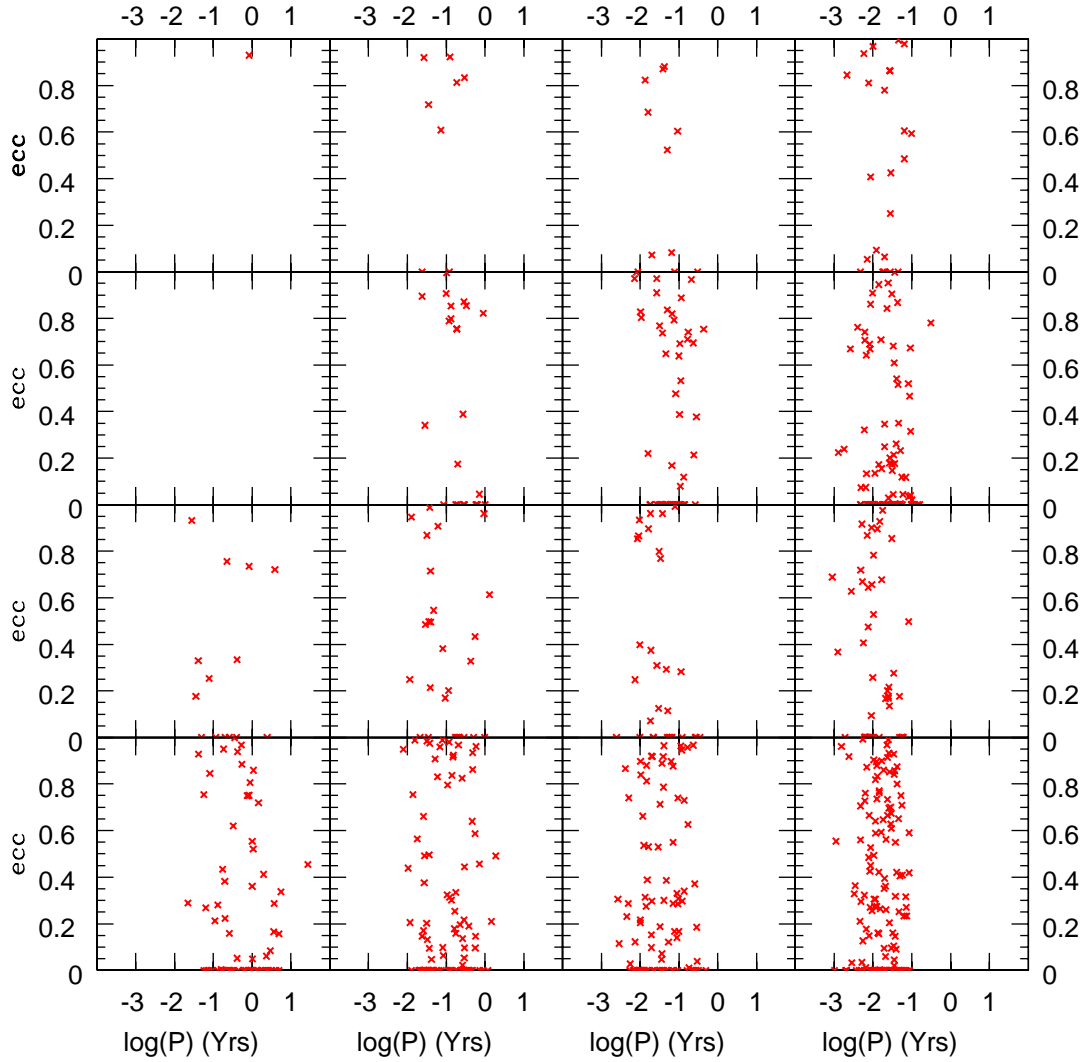


Figure 7.4: The eccentricity of BH-BH binaries as a function of period at the time of escape. Top to bottom: $Z = 0.02$ and $f_b = 0.1$, $Z = 0.02$ and $f_b = 0.5$, $Z = 0.001$ and $f_b = 0.1$, and $Z = 0.001$ and $f_b = 0.5$. Left to right: $r_t/r_h = 21$, $r_t/r_h = 37$, $r_t/r_h = 75$, and $r_t/r_h = 180$. The x-axis is in log scale.

from Chapters 3 and 6 many of these binaries will merge within $1T_H$ due to gravitational radiation. I consider these binaries in more detail later in this chapter.

As mentioned in Chapters 3 and 6 eccentricities can both enhance the number of BH-BH binary mergers over the circular case and move long-period binaries into the LISA band. In Figure 7.4 the eccentricity as a function of period for the BH-BH binaries at their time of escape from the cluster is shown. The eccentricity does not depend on cluster properties because it is a product individual interactions the outcome of which are independent of the global dynamics. There is significant eccentricity present at all periods for all simulations. This is in contrast to expectations (e.g. Willems et al. 2007) that all BH-BH binaries

should be circularised due to gravitational wave radiation. This is a consequence of the fact that dynamical interactions can introduce significant eccentricity into very close binaries (relative changes of up to 30% per interaction are possible (Heggie & Rasio 1996)). These binaries will circularise during the course of their relativistic inspiral but some are already in the LISA band at the time of escape. Again it must be stressed that these eccentricities are not self-consistently obtained. As such they must be treated with caution but should be at least representative of what is possible in globular clusters.

7.2 Mergers due to Gravitational Radiation

Since there are a reasonable number of escapers that may merge within a Hubble time and since they will not be disrupted, it makes sense to follow the orbital evolution of the BH-BH binaries in the galactic field more carefully than in Chapter 6. To do this I calculate the relativistic inspiral of all escapers in the quadrupole approximation using Equations 3.40 and 3.41. I solve this pair of coupled differential equations using a Runge-Kutta 4th order integrator. I choose a timestep such that the change in semi-major axis is never more than 1%. I perform this integration for every escaping compact binary, terminating the integration either when the stars come within 10 Schwarzschild radii ($r_s = 2Gm_{1,2}/c^2$ where $m_{1,2}$ is the mass of the primary or secondary) of each other or when the integration time plus the escape time from the cluster is greater than $1T_H$.

The total number of mergers during $1T_H$ are given in the last two columns of Table 7.1. The general trends are the same as for the escapers, namely more mergers at higher binary fraction, higher concentration, and low metallicity. For the most part the number of mergers is directly correlated with the number of escapers. For the more concentrated cases, however, the number of mergers is enhanced due to the shorter periods. For the low metallicity cases there is also an enhancement in merger number due to the more massive BHs that radiate more strongly and are thus more likely to inspiral and merge within a Hubble time. This accounts for the larger fraction of escapers that merge in the more dense, lower metallicity simulations. It is clear from Table 7.1 that these star clusters are the best prospect for enhancing the number of mergers in the galactic field.

Figure 7.5 presents the number of mergers per Gyr as a function of time. The general trends follow those in Figure 7.2 but with a time delay. This delay is the time taken for the binaries to inspiral in the galactic field after they have escaped from the cluster. For solar metallicity there is an average of only 1–2 mergers per Gyr and these come only from the two clusters with the highest concentrations. The number of mergers per Gyr in the clusters with $r_t/r_h = 180$ is initially high (relative to the other simulations) and drops-off at later times whereas the clusters with $r_t/r_h = 75$ produce no mergers while young but have a comparable number of merger per unit time to the $r_t/r_h = 180$ simulations at late times. For the more metal poor clusters the number of mergers is somewhat higher, especially at early times but except for young clusters with $f_b = 0.5$ does not much exceed 1–2 mergers per Gyr. The $r_t/r_h = 180$ simulations are always dominant at early times but by $1T_H$ the three most concentrated clusters are contributing mergers in roughly similar amounts. Thus for young globular cluster systems binaries from the most concentrated clusters will dominate the merger population while for old globular cluster systems most clusters will contribute mergers.

The delays between escape and merger are presented in Figure 7.6. Plotted is the inspiral timescale in the field vs. the time of escape from the cluster. There are a wide range of

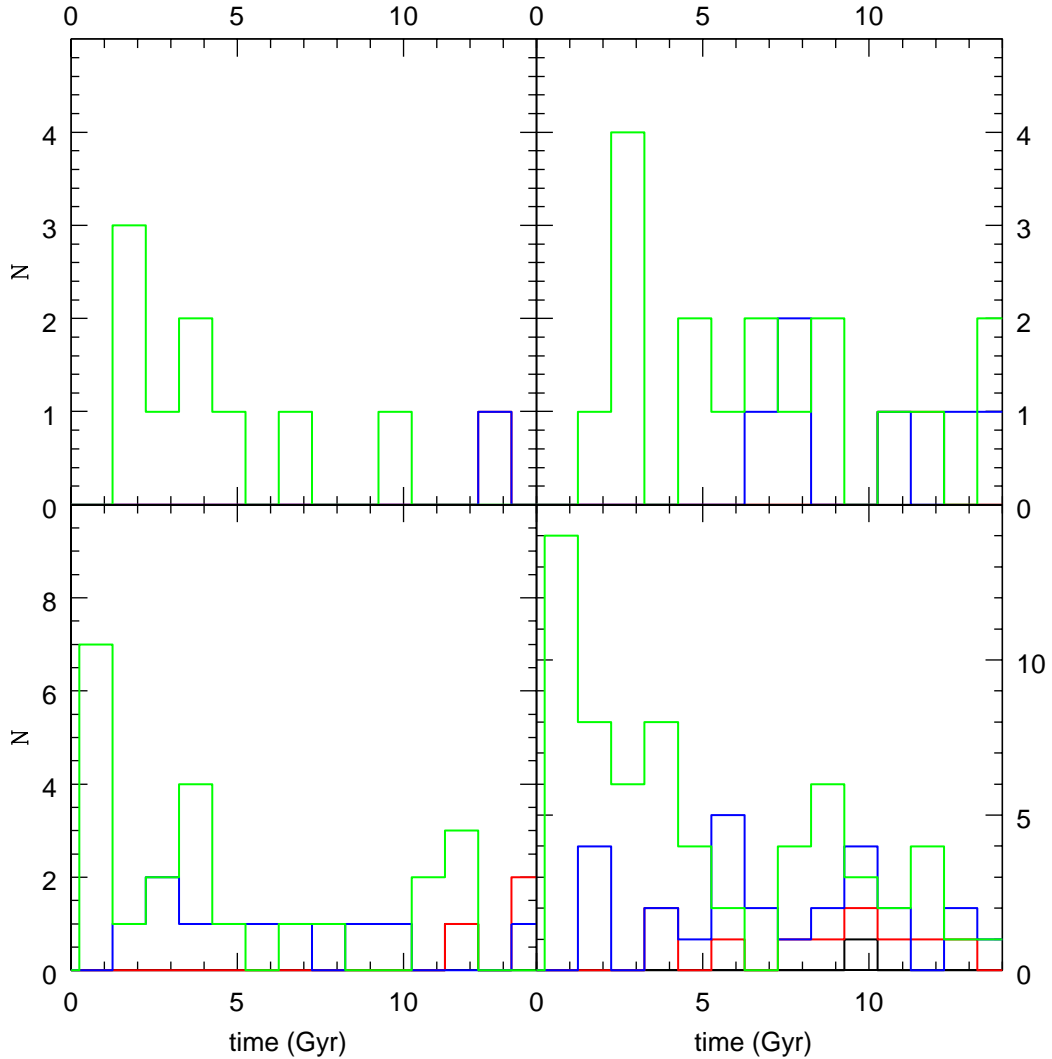


Figure 7.5: The number of escaped BH-BH binaries that merger per Gyr. Top row has $Z = 0.02$, bottom row has $Z = 0.001$. Left column has $f_b = 0.1$, right column has $f_b = 0.5$. Black is for $r_t/r_h = 21$, red for $r_t/r_h = 37$, blue for $r_t/r_h = 75$, and green for $r_t/r_h = 180$. Note that the scale on the y-axis for each plot is different.

inspiral timescales present between ~ 0.1 Myr and ~ 10 Gyr. Low metallicity clusters in particular seem to have shorter inspiral timescales at low concentration, probably due to the more massive BHs, but there is little trend with binary fraction or metallicity at higher concentration. There is no clear trend in inspiral timescale as a function of escape time.

For the concentrated clusters the majority of mergers come from binaries that are ejected early. This is related to the number of escapers, which is much smaller for these clusters at later times. By contrast the lower concentration clusters have escapers at later times that still merge within a Hubble time. From Figure 7.5 it is clear that the dense clusters can still contribute to the merger population after a Hubble time which means that these binaries

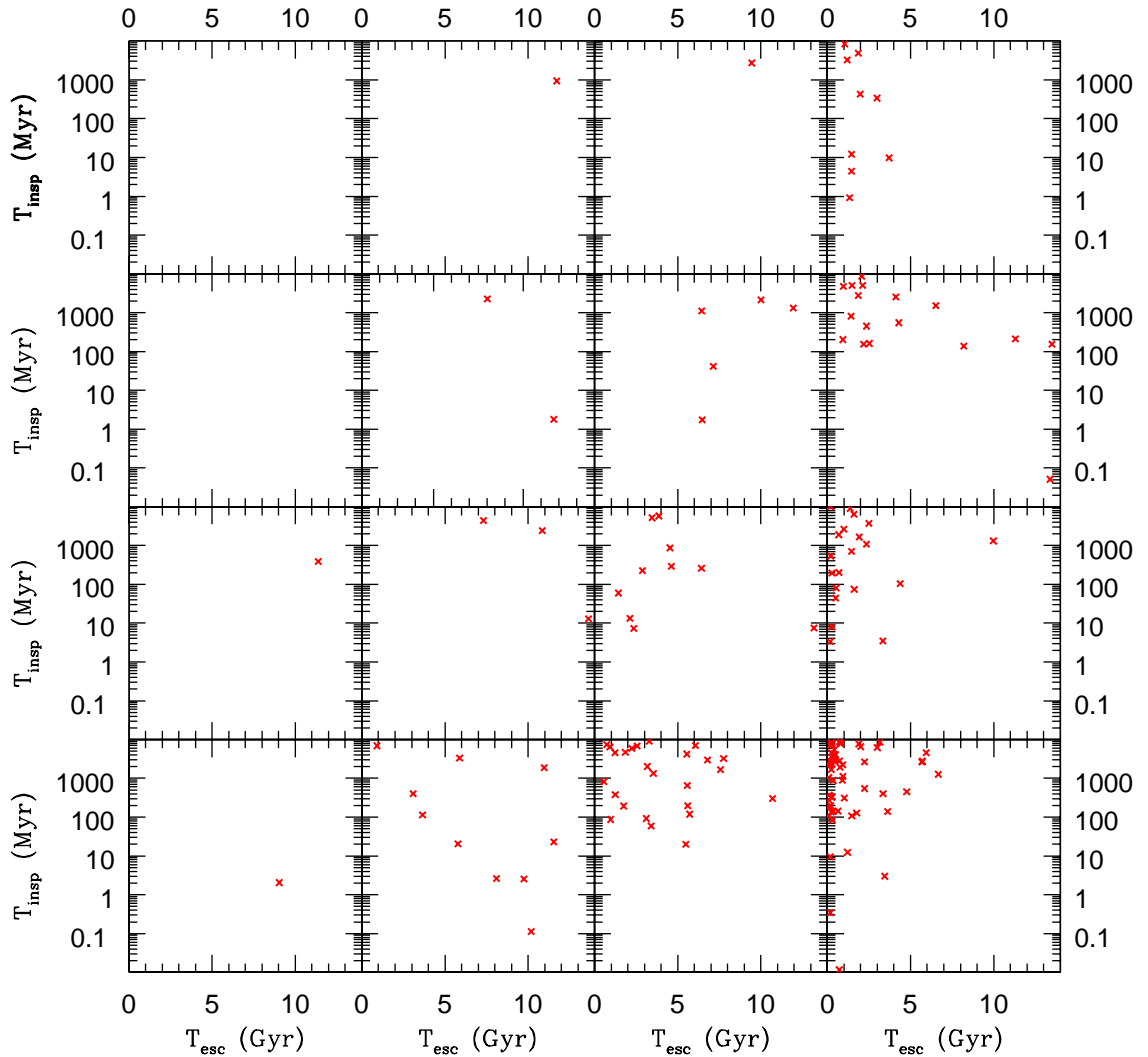


Figure 7.6: The inspiral timescale for escaped BH-BH binaries to merge in the galactic field. Top to bottom: $Z = 0.02$ and $f_b = 0.1$, $Z = 0.02$ and $f_b = 0.5$, $Z = 0.001$ and $f_b = 0.1$, and $Z = 0.001$ and $f_b = 0.5$. Left to right: $r_t/r_h = 21$, $r_t/r_h = 37$, $r_t/r_h = 75$, and $r_t/r_h = 180$. The x-axis is the time the binary escaped from the cluster in Gyrs. The y-axis is the time for the binary to inspiral to merger in $\log(\text{Myr})$. Only binaries that merge within a Hubble time are shown.

must have existed in the galactic field for some time. The mergers from the concentrated clusters will probably die out at some point and the population BH-BH mergers from globular clusters will then be dominated by contributions from the less dense clusters.

The significant time delay between escape and merger means that these mergers cannot be differentiated from mergers of binaries born in the galactic field on the basis of location or dynamics. The chirp mass distribution may, however, provide a way to do so. The chirp masses for the mergers are shown in Figure 7.7. Care must be taken when considering the

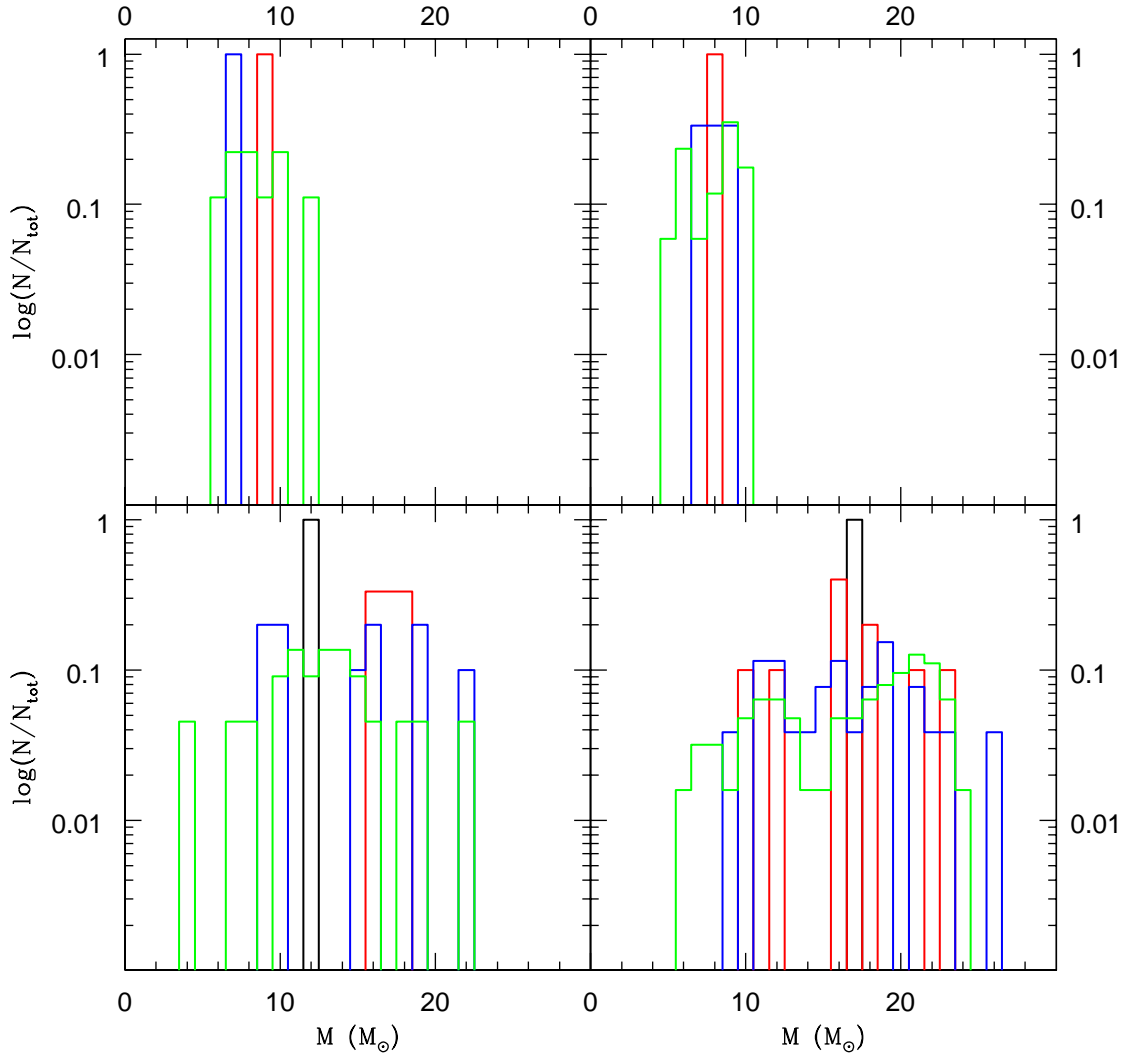


Figure 7.7: The distribution of chirp masses for mergers of ejected BH-BH binaries. Top row has $Z = 0.02$, bottom row has $Z = 0.001$. Left column has $f_b = 0.1$, right column has $f_b = 0.5$. Black is for $r_t/r_h = 21$, red for $r_t/r_h = 37$, blue for $r_t/r_h = 75$, and green for $r_t/r_h = 180$. The y-axis is in log scale.

low-concentration, high metallicity plots since these are based on small number statistics. Nonetheless it is clear that, as for the internal binaries in Chapter 6, the distribution of chirp masses is quite different at different metallicities. For the solar metallicity simulations there is a tight peak at $9\text{--}10 M_\odot$ whereas the distribution at low metallicity is much broader and reaches up to $30 M_\odot$. This is a consequence of the more massive BHs present at low metallicity. This is an interesting result because in principle it provides a way to use gravitational wave observations to distinguish which stellar populations are the major contributor to the BH-BH detection rate. If the distribution looks like the top two panels, then low metallicity globular clusters cannot be important whereas a distribution like the

bottom two panels would indicate there are few BH-BH binaries born in metal rich systems such as the galactic disk.

7.3 Other Species

As well as BH-BH binaries, NS-NS and NS-BH binaries can be detected by gravitational wave detectors and indeed NS-NS binaries are expected to provide the bulk of detections

Number of NS-NS and BH-NS Escapers				
Simulation	N_{NSNS}	N_{NSNSm}	N_{BHNS}	N_{BHNSm}
10sol21	0	0	0	0
10sol37	0	0	0	0
10sol75	0	0	0	0
10sol180	0	0	4	1
50sol21	0	0	0	0
50sol37	0	0	0	0
50sol75	0	0	0	0
50sol180	2	0	0	0
10low21	0	0	0	0
10low37	0	0	0	0
10low75	0	0	0	0
10low180	1	0	0	0
50low21	0	0	0	0
50low37	0	0	0	0
50low75	0	0	1	0
50low180	0	0	0	0

Table 7.2: The number of NS-NS and BH-NS binaries that escape from the cluster and merge in the galactic field within $1T_H$. Column 1 is the initial conditions. Columns 2, 3, 4, and 5 give the number of NS-NS escapers, NS-NS mergers, BH-NS escapers and BH-NS mergers respectively. Numbers are summed over all four independent realisations of each simulation.

Properties of NS-NS and BH-NS Escapers				
Simulation	Type	M_p [M_\odot]	M_s [M_\odot]	T_{esc} Gyr
10sol180	BH-NS	6.908	2.452	9.639
10sol180*	BH-NS	10.087	1.497	9.716
10sol180	BH-NS	8.130	2.581	12.063
10sol180	BH-NS	3.560	2.186	12.965
50sol180	NS-NS	1.434	1.434	0.193
50sol180	NS-NS	1.720	1.389	1.0720
10low180	NS-NS	2.056	1.306	14.023
50low75	BH-NS	9.979	1.836	14.077

Table 7.3: The physical properties of the NS-NS and BH-NS escapers. Column 1 gives the type of binary, Column 2 the primary mass, Column 3 the secondary mass, and Column 4 the time of escaper. The \star indicates the merger. This merger took place when the cluster that produced it was 10.676 Gyr old.

from the galactic field (Belczynski, Benacquista & Bulik 2008; Belczynski et al. 2007). Although few NS-NS or NS-BH binaries exist within my clusters, a few escape from some of my simulations. The number of these escapers are given in Table 7.2. There are very few such objects produced and of these only one merges in a Hubble time. Note that my inspiral calculations in the field include only orbital decay due to gravitational radiation. In principle NSs (unlike BHs) can have tidal oscillations excited in them and this could slightly enhance the inspiral rate. I do not at present have access to a code where both effects are included but since so few NS-NS and NS-BH binaries escape it is unlikely to affect the overall merger rate by very much. The lack of NS-NS and NS-BH binaries is a consequence of both stellar evolution and dynamics. Most processes that lead to NS-NS or NS-BH binaries have a much greater probability of leading to a merger or a disruption during a supernova than to a stable double degenerate system. In order to produce a significant number of these systems, several orders of magnitude more mass in stars are required than are present in my simulations. These species are also unlikely to be created efficiently by the dynamical processes that create BH-BH binaries. Although they are massive compared to the average mass of cluster stars after the first few hundred Myr of stellar evolution, neutron stars are still low-mass compared to black holes. Thus as long as black holes are present in the cluster, they will be preferentially exchanged into binaries at the expense of neutron stars. Thus the efficient creation of BH-BH binaries we find in our simulations does not help increase the NS-NS or NS-BH binary population. This result agrees with the previous findings of Sigurdsson & Phinney (1993) and Sadowski et al. (2008). It is possible that in smaller clusters where the high-mass end of the IMF is less well-sampled or in clusters where the IMF is truncated at the high-mass end there would be proportionately fewer BHs and thus NSs would be more efficiently introduced into binaries by dynamics. Simulations in this direction are an interesting possibility for future work.

The number of NS-NS and BH-NS binaries is too small to make reasonable statistics but I report the individual properties of each binary in Table 7.3. The NS-NS binaries tend to be of equal mass due to the limited mass range of NSs whereas the BH-NS binaries can have mass ratios of up to 4 – 5. Two out of three NS-NS binaries escape while the clusters are young whereas most of the BH-NS binaries escape from older clusters but the numbers are too small to draw any significant conclusions. There is one merger between a black hole and a neutron star and it actually takes place at about the current age of the galactic globular cluster population.

This result is very different to that expected to the galactic field where NS-NS mergers dominate. This is largely because dynamical creation of BH-BH binaries is not possible in the galactic field and because NSs are far more common than BHs due to their lower mass and the power-law shape of the IMF. If many BH-BH mergers are observed in gravitational waves, it would be strong evidence that the BH-BH population of the galactic field is enhanced by globular clusters. This could possibly be used to constrain how many stars in the galactic field have escaped from star clusters and thus what fraction galactic stars were actually formed in star clusters.

Chapter 8

Prospects for Gravitational Wave Detection

My simulations produce potential gravitational wave sources in both the ground-based and space-based regimes. First I will consider the detection of BH-BH mergers by ground-based detectors and then the prospects for LISA to detect the inspiraling BH-BH binaries at larger separation.

8.1 Ground-Based Detectors

The BH-BH mergers my simulations produce may be detectable by LIGO and Virgo in either their current or advanced forms. For a merger to be detected its signal to noise ratio must be above some threshold value in the detector. Follow the work of Bonazzola & Marck (1994) and Bulik, Belczynski & Rudak (2004) I approximate the signal to noise ratio for a compact merger at luminosity distance D_L to be:

$$\frac{S}{N} = \frac{A_{det}}{D_L} [(1+z)M_{chirp}]^{5/6} \quad (8.1)$$

where A_{det} is a scale distance in Mpc and varies depending on the specific detector, and z is the redshift at which the merger takes place. Values of A_{det} have been calculated for current LIGO ($A_{eLIGO} = 100$ Mpc), advanced LIGO ($A_{aLIGO} = 2200$ Mpc) (Flanagan & Hughes 1998), and Virgo ($A_{VIRGO} = 150$ Mpc) (Hello 1998). A more detailed calculation of S/N is complicated by the finite size of the frequency interval available to each detector (Flanagan & Hughes 1998) but Equation 8.1 is accurate to better than 10% for $M_{ch} < 20M_{\odot}$ (Bulik, Belczynski & Rudak 2004) which is true for most of my binaries. Furthermore I do not make detailed models of the formation history of globular clusters or their environment so my estimates will be at best order of magnitude.

$D_L = (1+z)D_{prop}$ where D_{prop} is the proper distance to the merger given by (e.g. Hogg 2000):

$$D_{prop}(z) = \frac{c}{H_0} \int_0^z \frac{dz'}{E(z')} \quad (8.2)$$

where c is the speed of light, H_0 the Hubble constant, and $E(z)$ is a scale factor given by:

$$E(z) = \sqrt{\Omega_M(1+z)^3 + \Omega_K(1+z)^2 + \Omega_\Lambda} \quad (8.3)$$

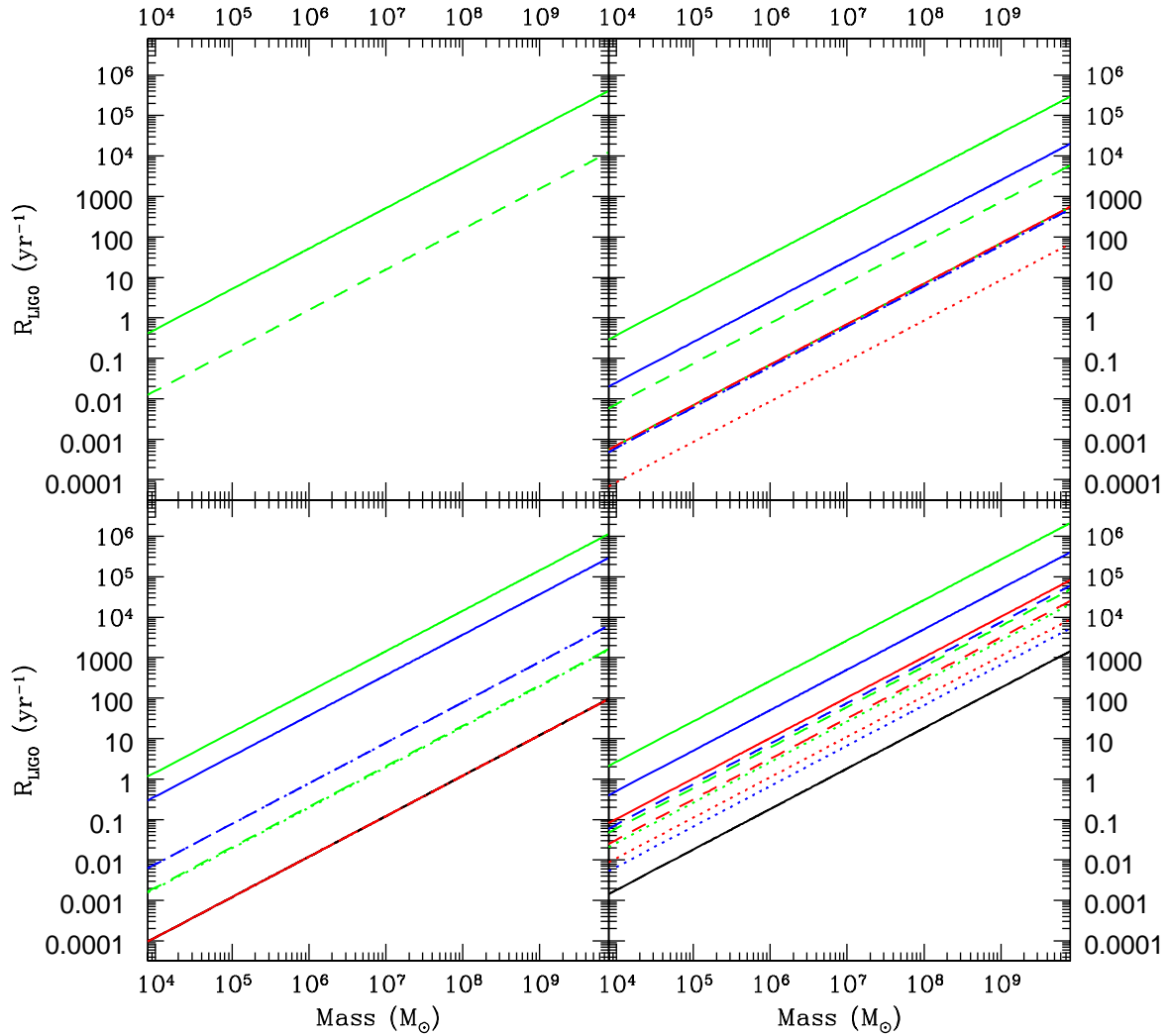


Figure 8.1: The merger detection rate assuming a detection if $S/N > 2$. Top to bottom $Z = 0.02$ and $Z = 0.001$. Left to right $f_b = 0.1$ and $f_b = 0.5$. Black is $r_t/r_h = 21$, red $r_t/r_h = 37$, blue $r_t/r_h = 75$, and green $r_t/r_h = 180$. Solid is for advanced LIGO, dotted for current LIGO, and dashed for Virgo.

where Ω_M is the matter density in the universe, Ω_K is the curvature “density”, and Ω_Λ is the density associated with the cosmological constant. For my calculations I choose values corresponding to the current concordance model of cosmology: $H_o = 72 \text{ kms}^{-1} \text{ Mpc}^{-1}$, $\Omega_M = 0.3$, $\Omega_\Lambda = 0.7$, and $\Omega_K = 0$ (i.e. a flat universe). Thus for a merger at a given redshift, I can calculate M_{chirp} , D_{prop} , and D_L and then use Equation 8.1 to calculate the signal to noise ratio and determine if it can be detected.

In order to calculate a detection rate at the current time I must make an assumption about the formation history of globular clusters. For simplicity I assume a δ -function formation event 12 Gyr in the past (a reasonable estimate for the age of the oldest globular

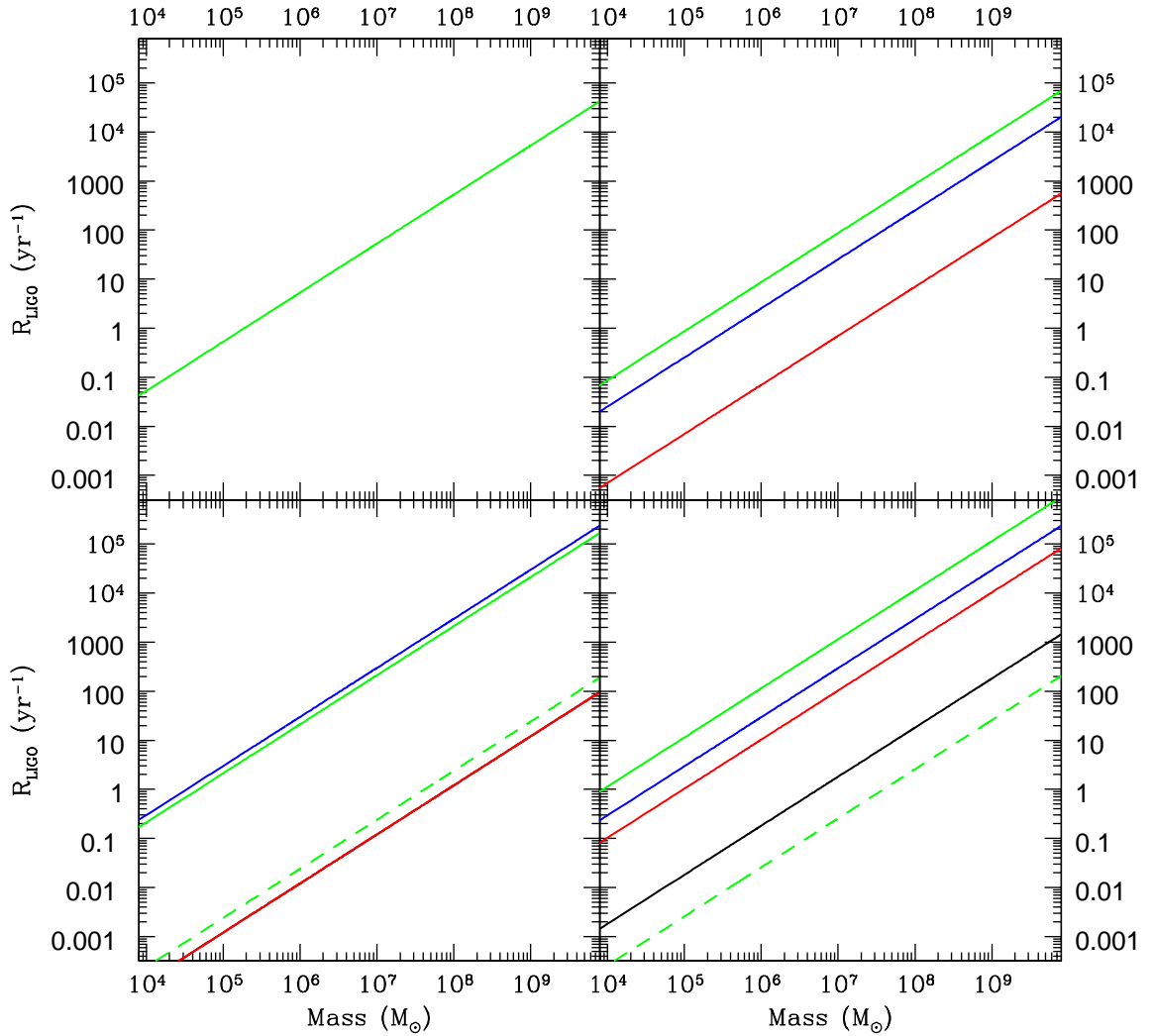


Figure 8.2: The merger detection rate assuming a detection if $S/N > 8$. All panels, colours, and line styles have the same meaning as Figure 8.1.

clusters (Brodie & Strader 2006; Harris 1996). Note that other assumptions can be made and there is plenty of evidence for both younger GCs in the universe (Kundu et al. 2005). Different assumptions about the star cluster formation history can certainly affect the detection rates but I have made the assumption of a single formation event in order to compare my results to earlier work (O’Leary et al. 2006; Sadowski et al. 2008) and have not yet investigated other possibilities. Because my merger rates are in 1 Gyr bins, I divide the time from globular cluster formation until the present time into 12 time bins each with a width $\Delta t = 1$ Gyr. I can calculate a look back time to the edge of each bin by taking $t_{\text{curr}} - T_i$ where t_{curr} is the current age of the universe and T_i is the edge of time bin i . I can calculate the redshift corresponding to a given look back time by inverting the formula

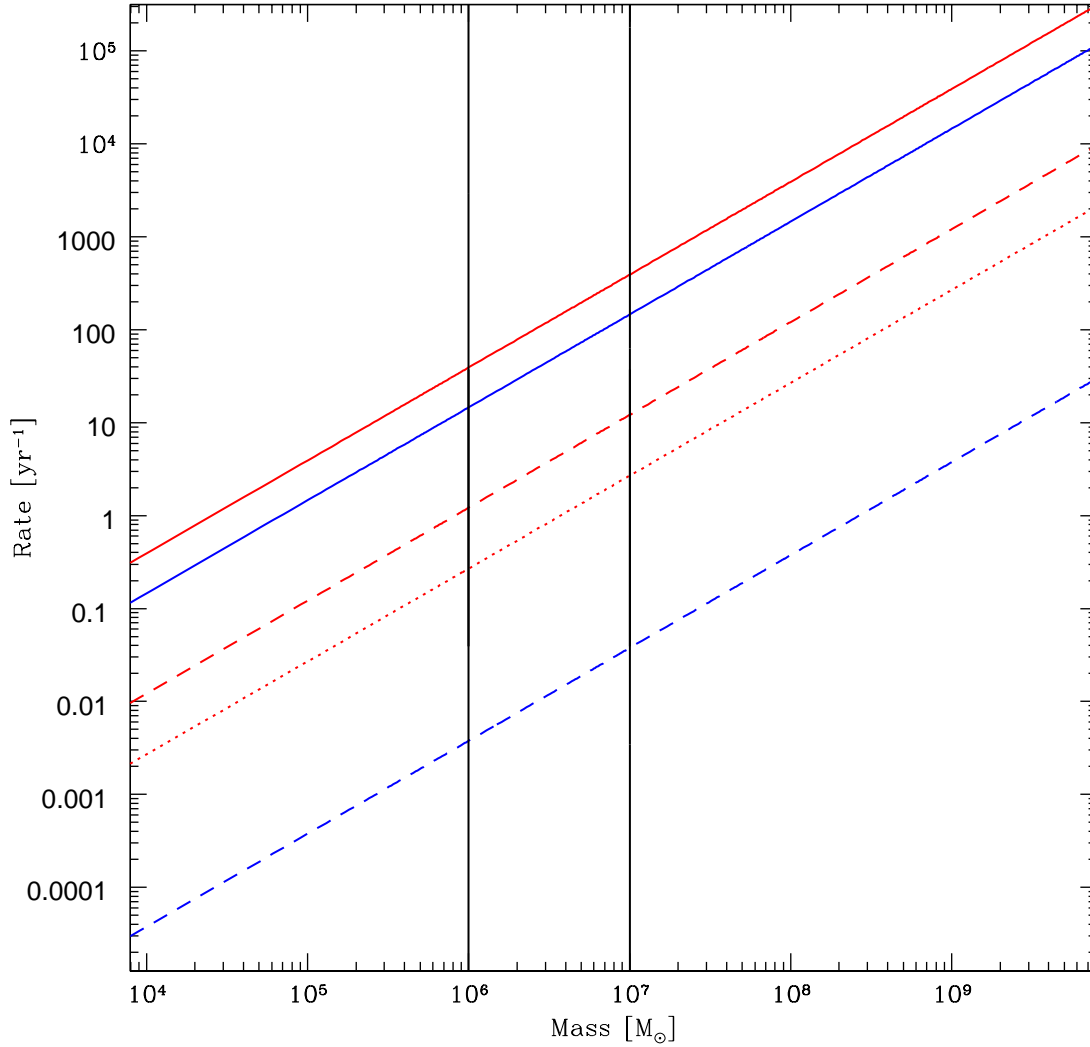


Figure 8.3: The total detection rate per year assuming all simulated types of clusters are present in equal numbers in the universe. Red is for detections at the $S/N > 2$ level and blue for detections at the $S/N > 8$ level. Solid is the detection rate for advanced LIGO, dotted for current LIGO, and dashed for Virgo.

(Hogg 2000):

$$T_L = T_H \int_0^z \frac{dz'}{(1+z')E(z')} \quad (8.4)$$

where for simplicity I take the Hubble time $T_H = 14$ Gyr. Thus I can use Equation 8.4 to calculate the redshift corresponding to the edge of each time bin (z_i) and then use Equation 8.2 to calculate a corresponding proper distance (D_i). I then calculate the number of mergers per time bin using the following procedure: I know when the merger occurred so I can calculate the look back time and assign the merger to its proper time bin, T_i . I then randomly choose a redshift for the merger between z_i and z_{i-1} and use this redshift to

calculate a proper distance to the merger. Finally I use Equation 8.1 to calculate a signal to noise ratio for the merger. If this ratio is above a chosen threshold I count the merger as a detection and increase the number of detections in the corresponding bin, N_i by one. I do this for all mergers from each cluster to get a number of mergers per cluster per time bin. I then normalise this to number of mergers per $10^5 M_\odot$ (all my clusters are a small-number multiple of $10^5 M_\odot$) for ease of comparison.

To calculate the total merger rate for a gravitational wave detector at the current time I sum over the rates in all bins using the formula:

$$R_{\text{det}} = \sum_{i=1}^{12} \frac{N_i}{\Delta t} \frac{4\pi}{3} \rho (D_i^3 - D_{i-1}^3) (1 + z_i)^{-1} \quad (8.5)$$

where ρ is the number of clusters per Mpc and the factor $(1 + z_i)$ is due to time dilation of the cosmological merger rate. For simplicity I use $\rho = 1 \text{ Mpc}^{-3}$ and then scale up the mass to observe the effect of increasing the number or size of clusters.

I have plotted the detection rate for each model in Figures 8.1 and 8.2 for signal to noise thresholds of $S/N > 2$ and (following Bulik, Belczynski & Rudak (2004)) $S/N > 8$ respectively. Each line in Figures 8.1 and 8.2 assume that the cluster population in the universe is composed of only one type of cluster. The x -axis is the mass in clusters per Mpc in solar masses. For the assumption of 1 cluster per Mpc a reasonable values for cluster masses are $10^5 - 10^7 M_\odot$ Brodie & Strader 2006; Harris 1996 and these detection values are probably the most reasonable.

In Figures 8.1 and 8.2 the largest number of detections come from dense clusters. Indeed for some binary fractions and metallicities these are the only clusters that produce detections. This is because dense clusters produce more mergers on the whole and partly because they produce mergers earlier at higher redshift. The high redshift space volume is larger and thus there are more clusters per bin each producing more mergers. This is counterbalanced by the fact that high redshift mergers have a larger luminosity distance and thus, according to Equation 8.1, have a lower value of S/N . From Figure 7.5 it is also clear that some of the less dense clusters do not start producing mergers until after 12 Gyr and thus produce no detections at all. The merger rate also increases with f_b which is simply a consequence of the larger number of mergers in these simulations. Finally the rate increases with decreasing metallicity. This is partly a product of the number of mergers in these simulations but also of their larger chirp masses. From Equation 8.1 the signal to noise ratio increases with chirp mass and thus these binaries can be detected with a higher S/N at greater distances. Therefore low metallicity cluster have a larger detection volume than higher metallicity clusters.

At the $S/N > 2$ level there is the possibility of a detection for the current generation of gravitational wave detectors with a detection rate of $0.1-10 \text{ yr}^{-1}$ in the most optimistic cases in the expected mass range. The probability of detection with advanced LIGO is even better with $10 - 10^2 \text{ yr}^{-1}$. $S/N > 2$ is not, however, a particularly firm detection (Flanagan & Hughes 1998) and the results for the more certain $S/N > 8$ are less promising, at least for the current generation of detectors. Only Virgo will have any detections (due to a slightly better low-frequency performance than LIGO) and this at a rate of only $\sim 0.1 \text{ yr}^{-1}$ for the most optimistic cases. The prospects for advanced LIGO are much more encouraging and will produce $1 - 10^4 \text{ yr}^{-1}$ depending on the type of cluster observed and the assumed mass in clusters.

Figures 8.1 and 8.2 assume the cluster population is composed of one type of cluster only. In Figure 8.3 I have assumed that all types of simulated clusters are present in equal numbers and I have plotted the total detection rate as a function of mass in clusters per Mpc^3 .

The detection rates for $S/N > 2$ are still promising for the current incarnation of Virgo (1-10 detections yr^{-1}) and less so for current LIGO (0.1-1 yr^{-1}). The detection rate for the current generation of detectors at the $S/N > 8$ level is very low ($\sim 0.01 \text{ yr}^{-1}$ at best) and a firm detection would be a truly serendipitous event. The prospects for advanced LIGO are, however, very good with 1-100 yr^{-1} year expected for $10^5 - 10^7 M_\odot$ in clusters per Mpc^3 at the $S/N > 8$ confidence level. This plot is only for mergers coming from clusters but the galactic field is only expected to contribute NS-NS mergers in large numbers (e.g. Belczynski et al. 2007). The cluster mergers themselves are all BH-BH mergers and I predict they will dominate the BH-BH merger rate. This provides a way for the cluster and field mergers to be disentangled.

As previously mentioned, other assumptions can be made for the formation history of globular clusters in the universe and my assumption of a single formation event at 12 Gyr was made primarily to compare with other work (e.g. O’Leary et al. 2006). It is now well-known that there are intermediate-age globular cluster populations in several galaxies (Kundu et al. 2005) and this indicates that the δ -function globular cluster formation history is unlikely to be realistic outside the Milky Way. In some sense my assumption will produce a minimum detection rate because the majority of merges come from young, dense clusters and thus the peak merger rate occurs at high redshift, beyond the reach of the current generation of gravitational wave detectors. Another possible assumption and one that I am currently investigating is a constant cluster formation rate. This assumption will almost certainly increase the detection rate because it produces young, dense clusters at non-cosmological distances and could lead to more promising detection rates even for the current generation of gravitational wave detectors. There is also the possibility of detections from objects such as very massive GCs or dwarf-globular transition objects (Hasegan et al. 2005) but these are, at present, beyond the scope of my work.

8.2 Space-Based Detectors

The space-based gravitational wave detector LISA will be able to detect BH-BH binaries in the Milky Way during their relativistic inspiral but before the merger. My collaborator Matthew Benacquista at the Centre for Gravitational Wave Astronomy at the University of Texas in Brownsville has investigated whether LISA will be able to detect any of the BH-BH binaries produced by my simulations. At present results are only available for the population of binaries that remain within the cluster. The results for the escapers are the subject of future work.

To calculate the LISA detection rate we need to find out which binaries are emitting gravitational waves in the LISA sensitivity band and which of these can be detected at a given signal-to-noise ratio. If the frequency of the harmonic with peak power (see Chapter 3) is in the LISA frequency range then we define the binary to be emitting in the LISA band. The peak harmonic is found by approximating the orbit of the binary as a circular orbit with a radius equal to the periastron of the eccentric orbit, $r = a(1 - e)$ where a is the semi-major axis and e the eccentricity. The circular orbit only emits in one frequency that is then proportional to $(1 - e)^{-3/2}$. This must be modified slightly because the velocity at

periastron is higher for an eccentric binary than for a circular one which leads to a slightly higher gravitational wave frequency. For a parabolic orbit the velocity is enhanced by a factor of $\sqrt{2}$ and thus we approximate the peak harmonic of a binary as:

$$n_{\max} \approx \sqrt{\frac{2}{(1-e)^3}} \quad (8.6)$$

Note that this formula is only approximate and that more detailed considerations taking into account the burst nature of eccentric binaries are possible but not necessary for my basic estimate. Only binaries found in clusters between the ages of 11.5-14 Gyr are considered. This covers the current age distribution of galactic globular clusters (Harris 1996) and LISA is unlikely to be sensitive to stellar-mass binaries beyond the Milky Way.

With these frequency and age restrictions, we find 10 potential LISA sources in my simulations. These are found in 10low37, 10low75, 10sol37, 50low21, 50low37, 50sol37, 50sol75, and 50sol180. All are BH-BH binaries. There is no clear trend in any of the initial parameters and it seems that potential LISA sources can form in most conditions. Only one source, one of the ones in 50sol180, has an eccentricity below 0.9 and is still fairly eccentric ($e = 0.67$). It seems that eccentric BH-BH binaries could be quite common in the LISA band.

In order to estimate the number of sources that can actually be resolved, we calculate the expected signal-to-noise ratio using the equation:

$$(S/N)^2 = 4 \int_0^\infty df \frac{|\bar{h}(f)|^2}{S_n(f)} \quad (8.7)$$

Name	RA			dec			dist (kpc)
	h	m	s	°	'	''	
NGC104	00	24	05.2	-72	04	51	4.5
E3	09	20	59.3	-77	16	57	4.3
NGC3201	10	17	36.8	-46	24	40	5.0
NGC6121	16	23	35.5	-26	31	31	2.2
NGC6218	16	47	14.5	-01	56	52	4.9
NGC6254	16	57	08.9	-04	05	58	4.4
NGC6366	17	27	44.3	-05	04	36	3.6
NGC6397	17	40	41.3	-53	40	25	2.3
NGC6540	18	06	08.6	-27	45	55	3.7
NGC6544	18	07	20.6	-24	59	51	2.7
2MSGC01	18	08	21.8	-19	49	47	3.6
2MSGC02	18	09	36.5	-20	46	44	4.0
Ter12	18	12	15.8	-22	44	31	4.8
NGC6656	18	36	24.2	-23	54	12	3.2
NGC6752	19	10	52.0	-59	59	05	4.0
NGC6838	19	53	46.1	18	46	42	4.0

Table 8.1: Celestial coordinates and distances for the 16 globular clusters within 5 pc of Earth

where $\bar{h}(f)$ is the response of LISA to a gravitational wave and $S_n(f)$ is the power spectral density of LISA noise. $S_n(f)$ includes contributions both from instrument noise and the effect of the foreground WD-WD binary population (an incoherent noise source) described in Ruiter et al. (2007).

To estimate the expected waveforms, $h(t)$, 10 realisations of each binary were placed in each of the 16 globular clusters within 5 kpc of earth. The parameters of these clusters are give in Table 8.1 and are taken from Harris (1996). Each binary has a randomly chosen orientation and cluster position and the resulting waveform is calculated using the harmonic expansion of Pierro et al. (2001) described in Chapter 3. The response of LISA, $\bar{h}(f)$ can then be calculated in the long wavelength limit described in Cutler (1998) and Equation 8.7 used to calculate the signal-to-noise ratio for the specific binary configuration.

Following Belczynski, Benacquista & Bulik (2008) we define a binary to be detectable if $S/N \geq 7$. With this limit two of the 10 potential sources, those in 10low37 and 50sol180, can be resolved. The properties of these binaries are given in Table 8.2. Both are highly eccentric. The higher mass binary from 10low37 can be detected from almost all orientations in all clusters except NGC 3201 and NGC 6121. The lower mass binary from 50sol180 can be detected only at some orientations and only in the clusters NGC 6121 NGC 6397. Two detections are not enough to make firm statistical predictions but it is interesting to note that there is no clear correlation with cluster parameters, indicating that a wide range of clusters have the potential to produce LISA sources. The small number of sources found in my simulations also confirms that LISA detections of stellar mass binaries should be rare, even in star clusters.

Simulation	Age (Gyr)	M_1 M_\odot	M_2 M_\odot	P_{orb} (s)	e
10low37	13.628	14.26	23.89	405976.1	0.947
50sol180	13.385	5.90	5.62	1142952.0	0.997

Table 8.2: Properties of the two potential LISA sources from these simulations.

Chapter 9

Million-Body Simulations

5.0×10^5 stars is fairly small by the standards of globular clusters so in order to constrain the N -dependence of my results I have performed a second set of simulations each containing one million bodies. Realistic million-body simulations have long been considered the goal of stellar dynamics but there are many difficulties in performing such simulations due to the physical complexity of the problem and the computational cost. Heggie & Hut (2003) gives an interesting review of the path to million-body simulations and the many challenges surrounding them. The Monte Carlo code is capable of simulating million-body clusters (Giersz 2006) but simulations take approximately twice as long to run as the simulations with 5×10^5 particles and care must be taken during compiling and running them because the arrays can become very large. At minimum the current code requires 64-bit architecture and several Gigabytes of on-board memory. The datafiles also become very large (several 10s of Gigabytes) and this makes running a complete repetition of all the 500k simulations impractical. I have computed 16 one million-body simulations using similar initial conditions as the 5×10^5 body simulation (hereafter referred to as the 500k simulations). I first describe the initial conditions, then binary population within the cluster, the escapers, and finally the prospects for ground-based gravitational wave detection.

9.1 Initial Conditions

I have chosen initial conditions for my million-body simulations such that both the initial stellar density within the half-mass radius is similar to the 500k simulations. To do this the initial tidal cut-off is expanded to 230 pc while r_t/r_h is kept constant. This gives initial stellar densities within the half-mass radius that are within a factor of two of those in the 500k simulations. Otherwise all initial conditions are identical to the 500k simulations. The initial conditions are given in Table 9.1

In physical units the only changes are total number, total mass, and initial tidal and half-mass radii. In normalised units all most of the cluster quantities (mass densities, velocity dispersion, half-mass radii, etc.) are similar between the 500k and million body simulations. Only the total number N and thus the individual masses, which vary as $1/N$, change. Therefore the relaxation time increases in physical units according to Equation 1.5 to the values given in Table 9.1. The larger values of t_{rh} means that the secular evolution proceeds more slowly in physical units than for the 500k simulations and the million-body clusters will be dynamically younger at a given physical age. This has important consequences for the production of BH-BH binaries. Due to storage space and time constraints I have

so far performed only one realisation of each set of initial conditions rather than the four performed for the 500k models. This makes my statistics noisier than for the 500k case because I cannot average away initial fluctuations. The total stellar mass in each million-body simulation is twice that of the corresponding 500k simulation but I have only 16 simulations as opposed to 64. Thus the total mass of my million-body simulation set is only half that of the total mass of the set of 500k simulations and I produce fewer BH-BHs, escapers, and mergers in absolute terms.

9.2 Population Statistics Within the Clusters

In Table 9.2 I present the number of BHs formed in the cluster due to stellar evolutionary processes both in isolation and in binaries. This table is analogous to Table 6.1 for the 500k clusters. In general the numbers are consistent with simply doubling the BH population in the 500k clusters. This is expected since BHs are produced for the most part by stellar evolutionary rather than stellar dynamical means and the only influence increasing the total number of stars has is to increase the total number of BH progenitors by the same number. There is a slight further enhancement in the number of primordial BH-BH binaries, probably due to better sampling of the high-mass end of the IMF. Just as in the 500k case none of these BH-BH binaries survive the formation process and thus all BH-BH binaries are formed dynamically. Overall increasing N has no effect on the BH fraction in the cluster.

To first order, increasing N should also have little effect on the binary fraction at a given dynamical age. Roughly assuming that a 90° degree deflection leads to the capture of a BH by a binary then the rate of formation of BH-BH binaries, \dot{N}_{BHBH} , should be $\propto n_{\text{bin}} p_{90}^2 v_{\text{rel}}$

Simulation	Initial Conditions				
	f_b	Z	r_t/r_h	$M [M_\odot]$	$t_{rh} [\text{Myr}]$
10sol21	0.1	0.02	21	7.24×10^5	8.8×10^3
10sol37	0.1	0.02	37	7.28×10^5	3.8×10^3
10sol75	0.1	0.02	75	7.22×10^5	1.3×10^3
10sol180	0.1	0.02	180	7.21×10^5	3.5×10^2
10low21	0.1	0.001	21	7.26×10^5	8.8×10^3
10low37	0.1	0.001	37	7.22×10^5	3.8×10^3
10low75	0.1	0.001	75	7.28×10^5	1.3×10^3
10low180	0.1	0.001	180	7.22×10^5	3.5×10^2
50sol21	0.5	0.02	21	1.01×10^6	7.5×10^3
50sol37	0.5	0.02	37	1.02×10^6	3.2×10^3
50sol75	0.5	0.02	75	1.01×10^6	1.1×10^3
50sol180	0.5	0.02	180	1.01×10^6	3.0×10^2
50low21	0.5	0.001	21	1.01×10^6	7.5×10^3
50low37	0.5	0.001	37	1.02×10^6	3.2×10^3
50low75	0.5	0.001	75	1.01×10^6	1.1×10^3
50low180	0.5	0.001	180	1.03×10^6	1.6×10^2

Table 9.1: The initial conditions for the million-body simulations. Column 1 gives the name of the simulation, Column 2 the initial binary fraction, Column 3 the metallicity, Column 4 the ratio of initial tidal to initial half-mass radius, column 5 the initial mass, and column 6 the initial half-mass relaxation time.

where n_{bin} is the number density of binaries, v_{rel} is the dispersion in relative velocities, and p_{90} is the impact parameter for a 90° deflection angle. $p_{90} = Gm_{\text{BH}}/v_{\text{rel}}^2$ where m_{BH} is the average mass of a black hole and thus $\dot{N}_{\text{BHBH}}/m_{\text{BH}} \propto \rho_{\text{BH}}/v_{\text{rel}}^3$ where $\rho_{\text{BH}} = n_{\text{bin}}/m_{\text{BH}}$. Since the right-hand-side of the equation is independent of the total particle, \dot{N}_{BHBH} should be independent of the total particle number as well. When comparing the number of BH-BH binaries formed in the million-body simulation in Table 9.3 with its counterpart for the 500k simulations, Table 6.2 at the same number of half-mass relaxation times the million-body simulations do indeed produce roughly twice as many BH-BH binaries. This means that both sets of simulations produce the same number of BH-BH binaries per unit mass at a given dynamical time as expected. In some cases the number of BH-BH binaries in the million-body simulations appears to be more than doubled, possibly due to the total BH population mass segregating to a sub-system of the same physical radius as in the 500k case (see Figure 9.2). Thus the central density of BHs might be higher in the million-body systems leading to a higher rate of binary formation (but also a higher rate of destruction and ejection). It should be noted however that the simulation-to-simulation scatter for BH-BH binaries is high (see the standard deviations in Table 6.2) and this enhancement could simply be a consequence of random fluctuations. This is consistent with the number of BH-BH binaries simply doubling with the number of stars in the system. The picture after $1T_H$, however, is rather different. Here most million-body simulations have produced fewer BH-BH binaries than their 500k counterparts both per unit mass and often also in absolute number per simulation. Only the very densest, lowest metallicity clusters with the highest binary fractions have produced more BH-BH binaries per cluster and none have significantly

Simulation	Number of Single BHs			
	N_{sBH}	N_{bBH}	N_{BHBH}	N_{surv}
10sol21	2197	417	0	0
10sol37	2307	420	7	0
10sol75	2178	423	9	0
10sol180	2208	420	9	0
10low21	2541	457	6	0
10low37	2561	466	8	3
10low75	2656	482	10	2
10low180	2436	451	13	1
50sol21	3034	2022	22	0
50sol37	2987	1991	28	0
50sol75	2967	1972	23	0
50sol180	3023	1977	23	0
50low21	3394	2305	45	4
50low37	3502	2387	42	3
50low75	3621	2428	52	6
50low180	3615	2324	35	12

Table 9.2: The total number of BHs formed in the million-body simulations. Column 1 gives the simulation, Column 2 the total number of BHs formed, Column 3 the number formed in binaries, Column 4 the number formed in BH-BH binaries, and Column 5 the number of binaries that survived the formation of the BH. No BH-BH binaries survive the process of forming the second BH, all are disrupted.

more per unit mass. This is due to the longer relaxation times in the million-body clusters. Because they are dynamically younger than their 500k counterparts their rate of dynamical interactions in physical time has been lower and they have not been able to form as many BH-BH binaries through dynamical interactions during $1T_H$.

This interpretation is confirmed by Figure 9.1, the number of BH-BH binaries in the clusters per 500 Myr. In comparing this to Figure 6.1 I find that the million-body clusters start producing BH-BH binaries later, have a later peak in BH-BH number, and have more sustained BH-BH production. In particular the number of BH-BH binaries per unit time for the two lowest density clusters is much reduced and they cannot produce as many BH-BH binaries as the 500k simulations over a fixed span of physical time. Dynamical BH-BH production for these simulations is not truncated at $1T_H$ and if they were allowed to evolve further they would probably many more BH-BH binaries. The $r_t/r_h = 75$ clusters produce a high peak in BH-BH production for the two simulations where $f_b = 0.1$. The overall number of BH-BHs produced, however, is not affected and it is not clear if this peak is simply a statistical fluctuation. The numbers per unit time in Figure 9.1 are much noisier than for 500k simulations and this is due to simulation-to-simulation fluctuations that have not been averaged away. The very dense clusters do reach peak BH-BH number per unit time in $1T_H$ and these are the clusters that also have more BH-BH binaries than their 500k counterparts. Thus if dynamical BH-BH production peaks within a Hubble time it

simulation	Number of BH-BH binaries after xt_{rh}			
	$t = 1t_{rh}$	$t = 3t_{rh}$	$t = 10t_{rh}$	$t = 14$ Gyr
10sol21	0,0	-	-	0,2
10sol37	0,0	4,2	-	5,9
10sol75	0,0	3,0	24,9	25,52
10sol180	0,0	2,0	8,20	79,128
10low21	16,6	-	-	19,33
10low37	0,2	62,23	-	64,44
10low75	1,3	40,22	69,42	69,55
10low180	10,4	47,27	91,56	114,124
50sol21	0,0	-	-	2,2
50sol37	0,0	9,4	-	15,57
50sol75	0,0	2,1	42,32	63,146
50sol180	1,0	2,0	30,20	265,342
50low21	59,36	-	-	143,126
50low37	69,15	226,173	-	269,182
50low75	26,7	187,64	419,144	442,176
50low180	13,18	130,95	348,196	659,480

Table 9.3: The number of BH-BH binaries formed in the million-body simulations after the number of relaxation times given at the top of the columns and after $1T_H$ (last column). The first three times are the last full relaxation time before $1T_H$ for the clusters with $r_t/r_h =$, 21, 37, and 180 respectively. The clusters with $r_t/r_h = 180$ are (from top to bottom) 38, 38, 46, and 90 half-mass relaxation times old after $1T_H$. The large dynamical age for the last cluster is due to its rather large mass generated by random sampling of the IMF. The numbers after the comma are the number of BH-BH binaries in the 500k simulations at the same number of half-mass relaxation times averaged over all four realisations.

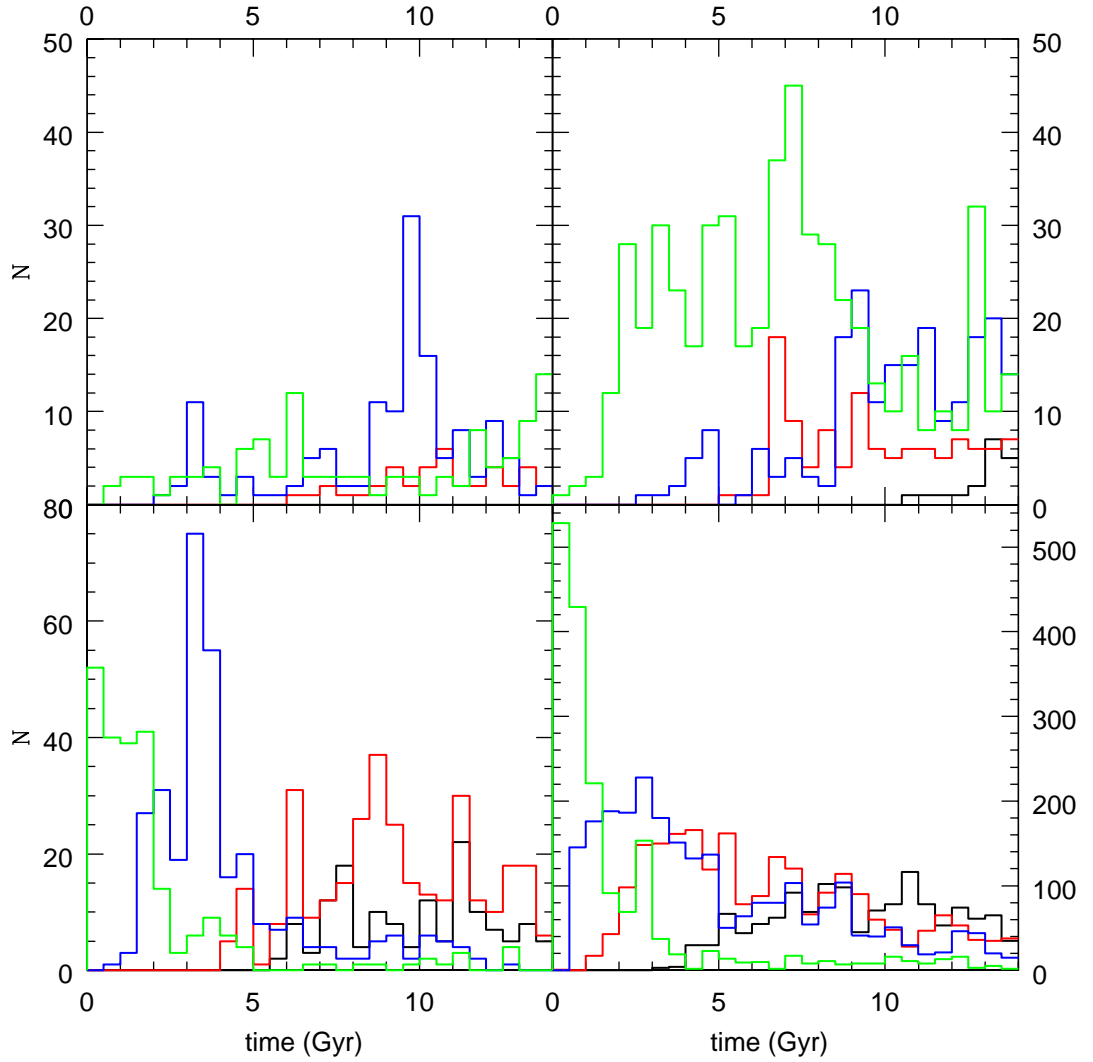


Figure 9.1: The number of BH-BH binaries in each cluster per 500 Myr. Top to bottom $Z = 0.02$ and $Z = 0.001$. Left to right $f_b = 0.1$ and $f_b = 0.5$. Black is for $r_t/r_h = 21$, red for $r_t/r_h = 37$, blue for $r_t/r_h = 75$, and black for $r_t/r_h = 180$.

is possible for the million-body simulations to produce similar numbers of BH-BH binaries per unit mass as their 500k counterparts.

Figure 9.2 presents the evolution of the half-mass radius for the cluster, BH population, and BH-BH population and is analogous to Figure 6.2. The general trends are the same: the BHs sink towards the centre due to mass segregation and BH-BH binaries only start to form once the BH population has contracted sufficiently for interactions to become frequent. The primary difference between the 500k and million-body simulations is the speed at which this process takes place. In the million-body simulations the contraction occurs more slowly and production of BH-BHs does not set in until later. It is worth noting that the half-mass radii for the BHs and the BH-BH binaries seem to approach similar physical values as the

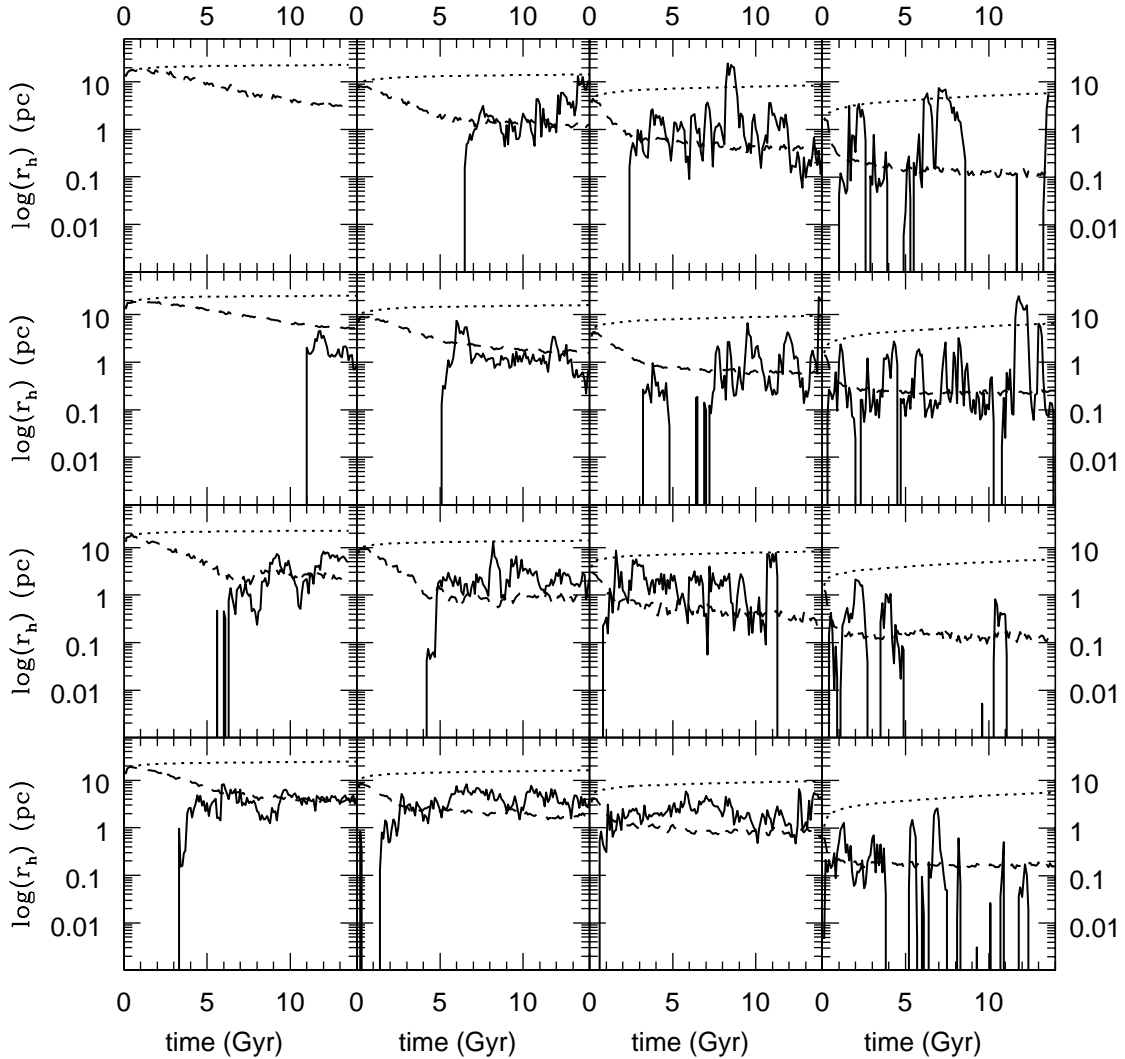


Figure 9.2: The half-mass radii for the system, all BHs, and just BH-BHs for the million-body simulations. Top to bottom $Z = 0.2$ and $f_b = 0.1$, $Z = 0.001$ and $f_b = 0.1$, $Z = 0.02$ and $f_b = 0.5$, and $Z = 0.001$ and $f_b = 0.5$. Left to right $r_t/r_h = 21$, $r_t/r_h = 37$, $r_t/r_h = 75$, and $r_t/r_h = 180$.

500k simulations. This means that the core density of BHs will be higher in the million-body simulations. This could explain the possible enhancement beyond a simple population doubling of BH-BHs at the same number of relaxation times observed in Table 9.3.

The binding energy and period distributions for the million-body clusters are given in Figures 9.3 and 9.4 respectively. There is no significant difference between these distributions and those shown for the 500k simulations in Figures 6.5 and 6.6. Thus it seems that the individual binary parameters are not strongly affected by the total number of stars in the system. This makes sense because the formation, evolution, and disruption of binaries

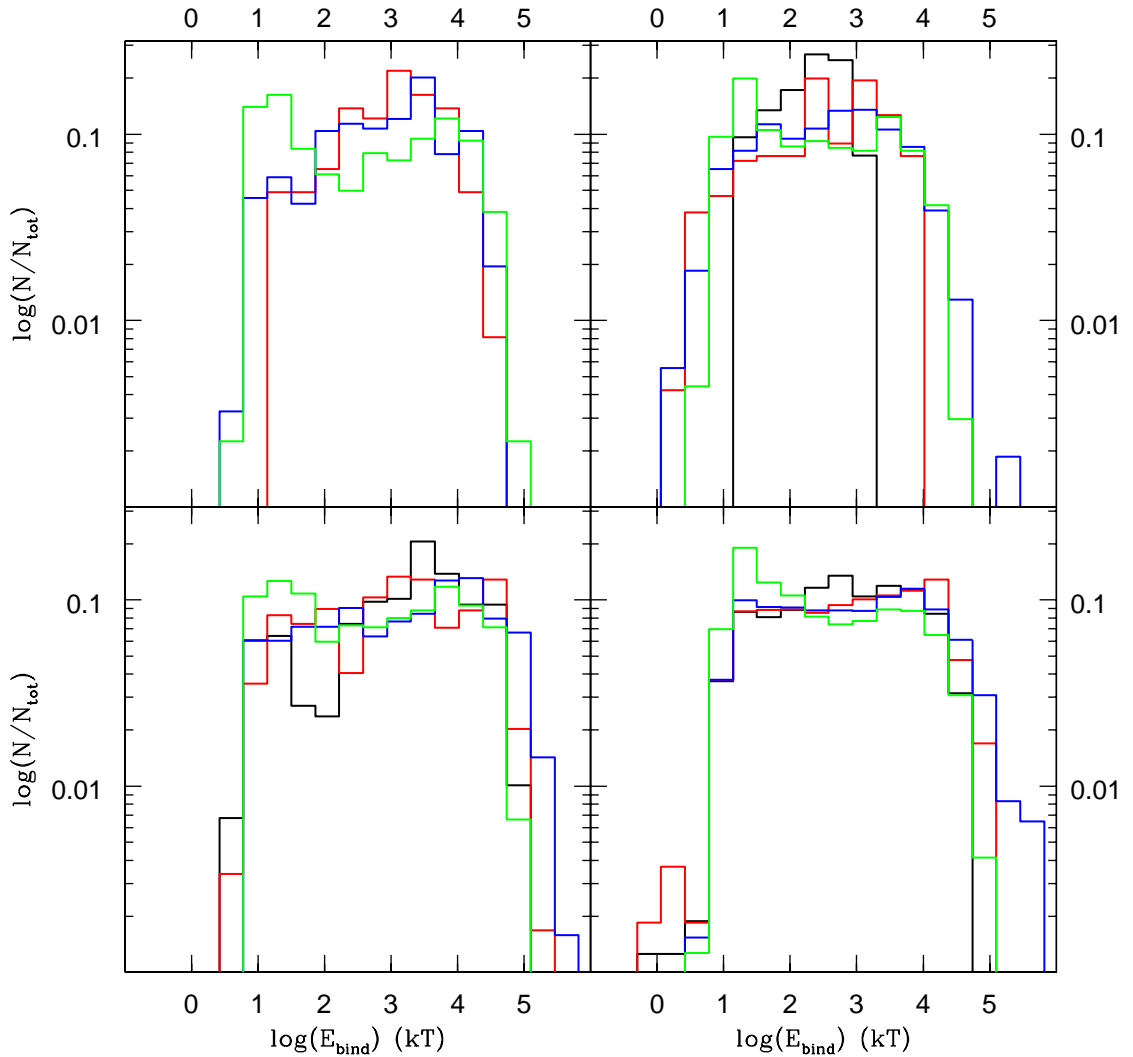


Figure 9.3: The binding energy distribution for the million-body simulations. Top to bottom $Z = 0.02$ and $Z = 0.001$. Left to right $f_b = 0.1$ and $f_b = 0.5$. Black is for $r_t/r_h = 21$, red for $r_t/r_h = 37$, blue for $r_t/r_h = 75$, and green for $r_t/r_h = 180$.

is a local process and the clusters have been normalised such that the initial local properties should be similar.

Finally in Figures 9.5 and 9.6 I present the gravitational wave inspiral and BH-BH binary disruption timescales calculated in the same way as for Figures 6.8 and 6.9 in the 500k case. The distribution of inspiral timescales are essentially identical for the 500k and million-body simulations which is to be expected in light of the similar distribution of orbital parameters found in Figures 9.3 and 9.4. The distribution of disruption timescales are also similar for both sets of simulations, indicating that the binary formation and destruction processes are not strongly affected by the size of the system. There is again little overlap between the inspiral timescales in Figure 9.5 and 9.6, indicating that BH-BH mergers in

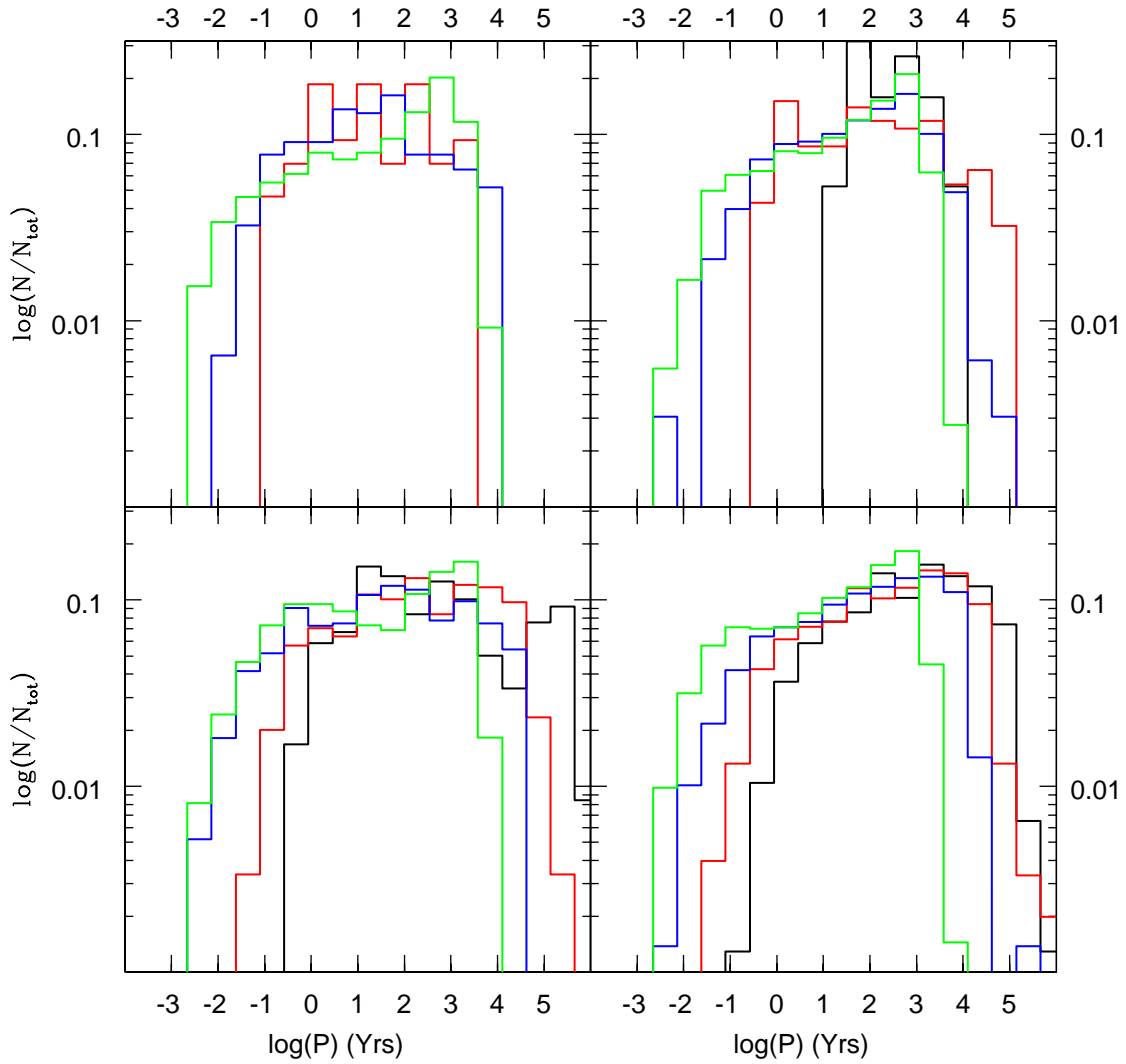


Figure 9.4: The period distribution for the million-body simulations. Top to bottom $Z = 0.02$ and $Z = 0.001$. Left to right $f_b = 0.1$ and $f_b = 0.5$. Black is for $r_t/r_h = 21$, red for $r_t/r_h = 37$, blue for $r_t/r_h = 75$, and green for $r_t/r_h = 180$.

Merger Parameters			
Simulation	T [Myr]	$m_1 [M_\odot]$	$m_2 [M_\odot]$
50low180	2.20×10^2	25.5	13.9
50low180	3.52×10^3	23.4	9.22

Table 9.4: The parameters of the two BH-BH binary mergers that occur within the million-body simulations. Column 1 gives the simulation in which the merger occurred, Column 2 the time at which the merger occurred, Column 3 the mass of the primary, and Column 4 the mass of the secondary.

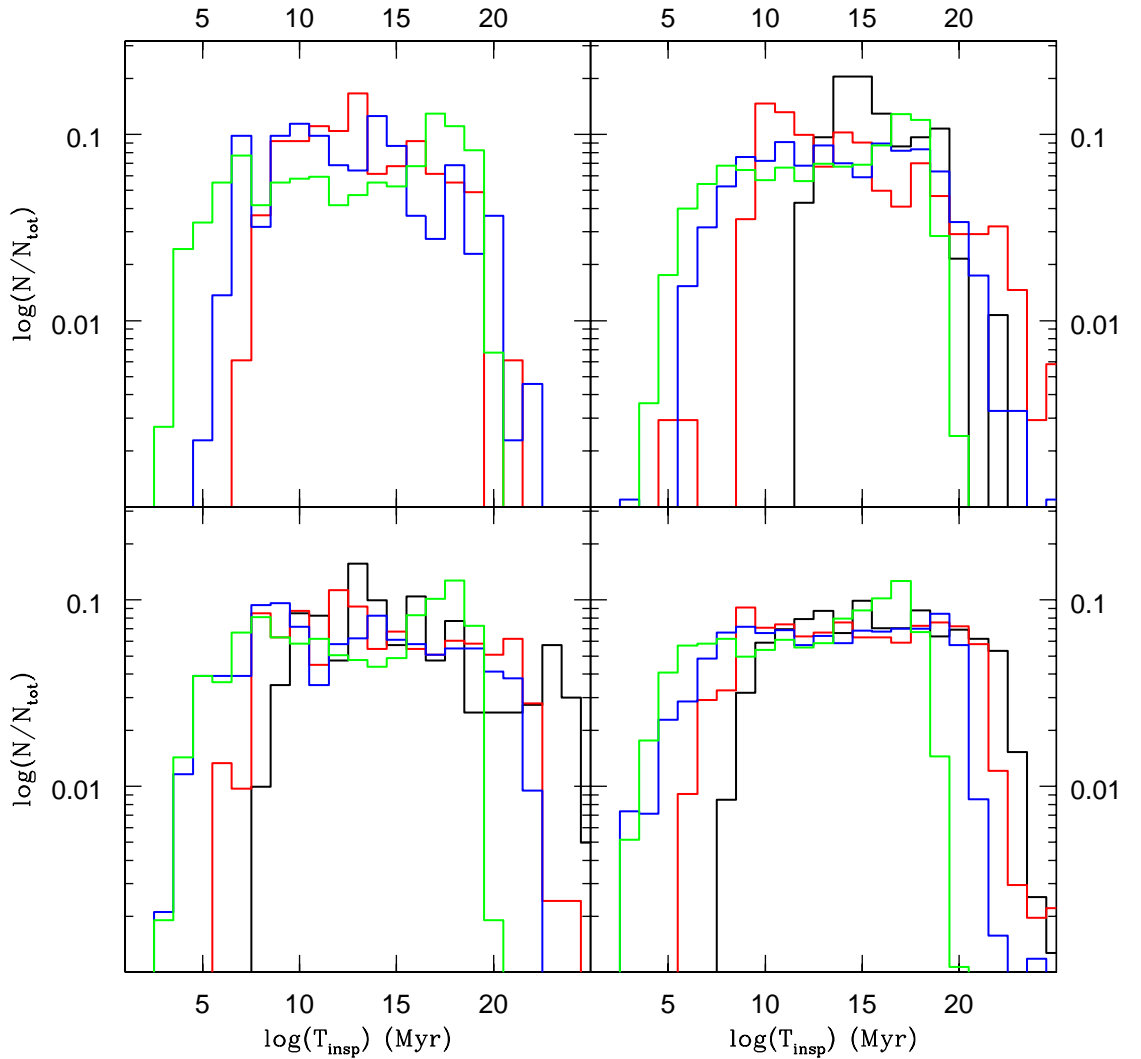


Figure 9.5: The distribution of gravitational wave inspiral timescales for the million-body simulations. Top to bottom $Z = 0.02$ and $Z = 0.001$. Left to right $f_b = 0.1$ and $f_b = 0.5$. Black is for $r_t/r_h = 21$, red for $r_t/r_h = 37$, blue for $r_t/r_h = 75$, and green for $r_t/r_h = 180$.

million-body star clusters should remain rare events. There are two BH-BH mergers within my million-body clusters, both in the model 50low180. The parameters of the mergers are given in Table 9.4. This is in contrast to the 500k simulations where no mergers were found within the clusters. Both binaries are quite massive and will certainly be sources for LIGO and Virgo. Two mergers in one simulation cannot be taken as conclusive evidence of different merger behaviour between the 500k and million-body clusters, especially given the similarity in binary parameters between the two sets of simulations. More simulations of both sets of clusters would need to be run to confirm that these mergers are not simply statistical fluctuations that are equally likely in the 500k clusters.

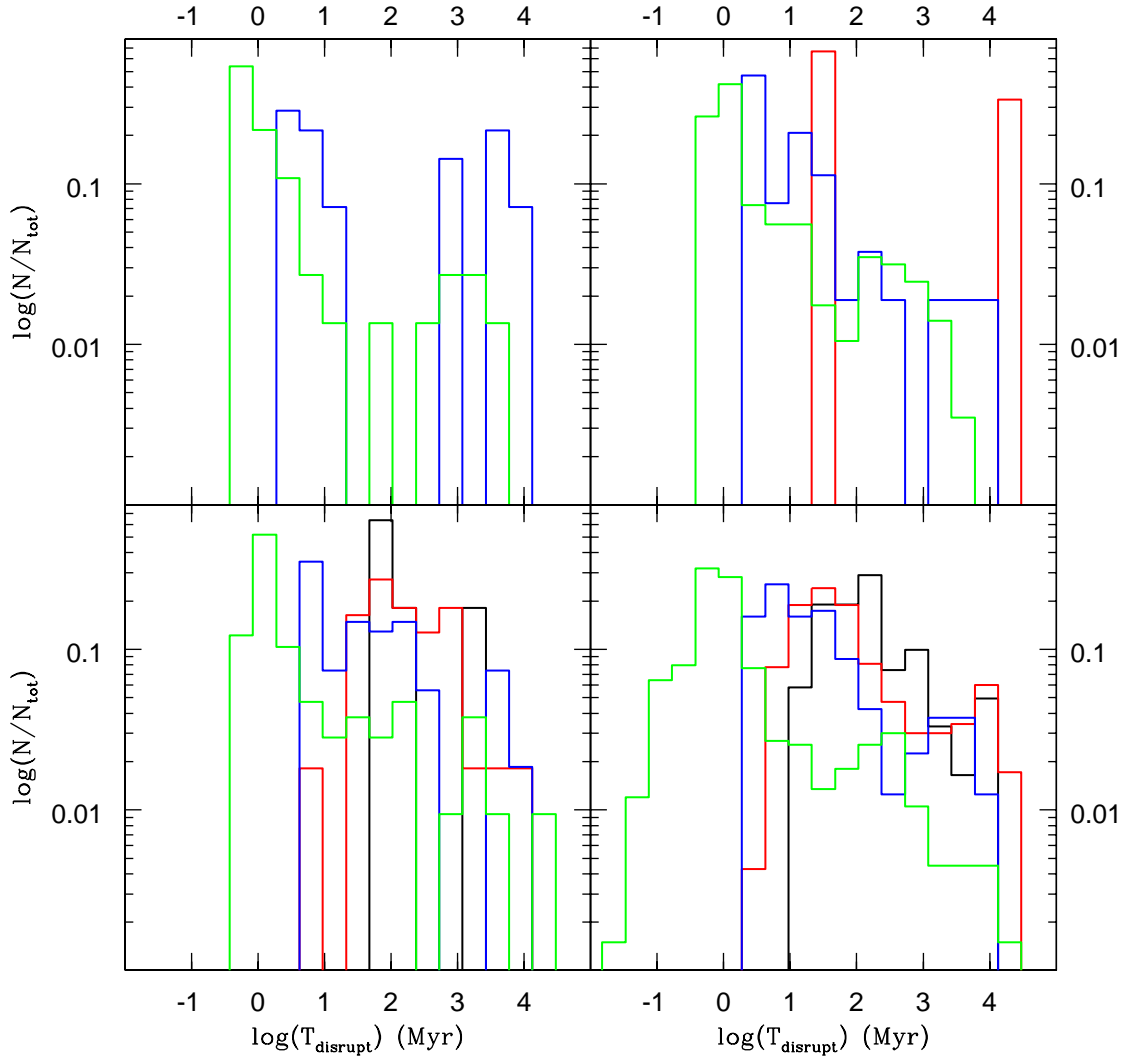


Figure 9.6: The distribution of disruption timescales due to interactions, mergers, or ejections for the BH-BH binaries in the million-body simulations. Top to bottom $Z = 0.02$ and $Z = 0.001$. Left to right $f_b = 0.1$ and $f_b = 0.5$. Black is for $r_t/r_h = 21$, red for $r_t/r_h = 37$, blue for $r_t/r_h = 75$, and green for $r_t/r_h = 180$.

Overall I find that the dynamics of BH-BH production are not strongly affected by doubling the number of stars in the system. All numbers at an equivalent dynamical time are simply doubled as well. The distribution of binary parameters remain essentially identical. The only difference is that the relaxation time of a larger system is longer than for a smaller system and thus the larger system will be less dynamically evolved at the same physical time. Therefore I actually find fewer BH-BH binaries per unit mass at a given physical time for the million-body simulations.

9.3 Escapers

In this section I consider the stars that escape from the million-body simulations and were, in the case of the 500k simulations, the only source of relativistic mergers. The number of escapers for each simulation is given in Table 9.5. Just as for the total number of BH-BHs there are often fewer escapers per unit mass than in the 500k simulations. This is an effect of the slower dynamical evolution in the million-body clusters. The exception is again the high-density clusters where the simulations can produce as many or more escapers after $1T_H$. The low-density clusters do not have time to eject large numbers of BH-BHs whereas the dense clusters have short enough relaxation times to reach peak BH-BH production and ejection within a Hubble time. As for the 500k clusters the merger rate follows the escape rate and the lower density clusters have fewer mergers than their 500k counterparts whereas the high density clusters can have as many or more. NS-NS and BH-NS still have a negligible contribution to the population of compact binary escapers.

The number of escapers, Figure 9.7, mergers of escapers per Gyr, Figure 9.8, confirm this interpretation. In general the escape rate is lower and more constant for the million-body clusters leading to a lower number of escapers and mergers after $1T_H$ for the low density clusters and a higher number for the high density clusters. The merger rate follows the same trends as the escape rate with low-density clusters producing fewer mergers per cluster and per unit mass than their 500k counterparts and the high density clusters producing the same number or slightly more. It is possible that a larger proportion of escapers from the highest density clusters merge for the million-body than in the 500k clusters however there is a fairly large simulation-to-simulation scatter in both escape and merger number for the

Number of Escapers and Mergers				
Simulation	$N_{\text{BHBH,e}}, N_{\text{BHBH,m}}$	$N_{\text{BHNS,e}}, N_{\text{BHNS,m}}$	$N_{\text{NSNS,e}}, N_{\text{NSNS,m}}$	
10sol21	0,0	0,0		0,0
10sol37	1,0	0,0		0,0
10sol75	6,0	0,0		0,0
10sol180	6,4	0,0		0,0
10low21	0,0	0,0		0,0
10low37	4,0	0,0		0,0
10low75	10,7	0,0		0,0
10low180	13,8	0,0		1,0
50sol21	0,0	0,0		0,0
50sol37	1,0	0,0		0,0
50sol75	9,1	0,0		0,0
50sol180	31,10	0,0		0,0
50low21	9,0	0,0		0,0
50low37	38,0	0,0		0,0
50low75	53,12	0,0		0,0
50low180	66,46	0,0		0,0

Table 9.5: The number of BH-BH binaries that escape and merge from the million-body clusters. Column 1 gives the simulation. Column 2 gives numbers for BH-BH binaries, Column 3 BH-NS binaries, and Column 4 NS-NS binaries. In each column the format is escapers,mergers.

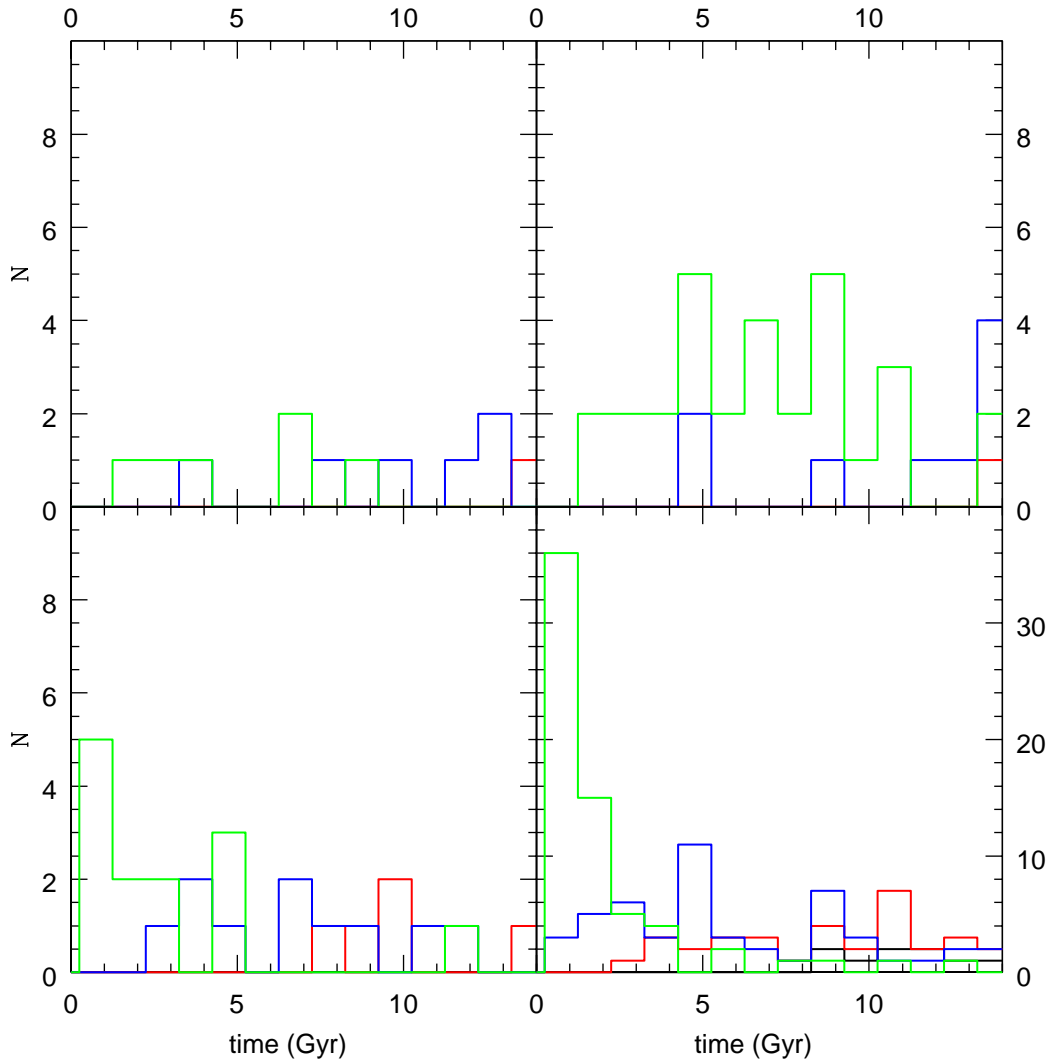


Figure 9.7: The escape rate per Gyr of BH-BH binaries from the million-body simulations. Top to bottom $Z = 0.02$ and $Z = 0.001$. Left to right $f_b = 0.1$ and $f_b = 0.5$. Black is for $r_t/r_h = 21$, red for $r_t/r_h = 37$, blue for $r_t/r_h = 75$, and green for $r_t/r_h = 180$.

500k simulations which could explain the discrepancy in individual cases. More simulations are necessary to determine if this enhancement is statistically significant.

I consider the period distribution at the time of escape and the eccentricities as a function of period in Figures 9.9 and 9.10. In both cases the distributions are essentially identical to those found in Figures 7.3 and 7.4, confirming that there is no significant difference between the parameters of the binaries escaping the 500k and million-body simulations. Finally in Figure 9.11 I present the inspiral timescales for the merging binaries once they have escaped the cluster. There is no apparent difference between these and the inspiral timescales found in Figure 7.6, indicating no difference in merger dynamics between the two sets of simulations. This implies that the apparent enhancement in merger fraction between

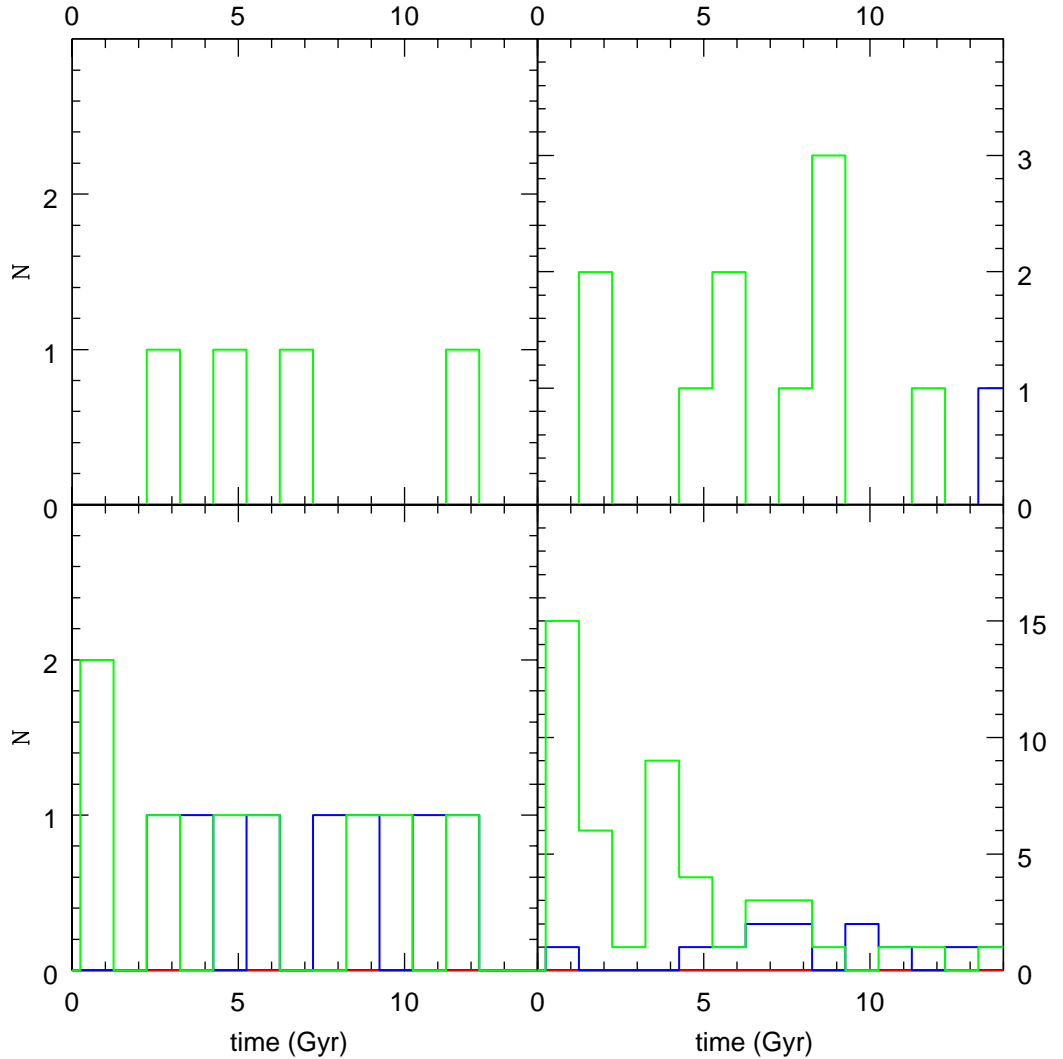


Figure 9.8: The merger rate per Gyr of BH-BH binaries that have escaped from the million-body simulations. Top to bottom $Z = 0.02$ and $Z = 0.001$. Left to right $f_b = 0.1$ and $f_b = 0.5$. Black is for $r_t/r_h = 21$, red for $r_t/r_h = 37$, blue for $r_t/r_h = 75$, and green for $r_t/r_h = 180$.

the dense 500k and million-body simulations is merely a product of statistical fluctuations rather than a systematic effect.

Overall the number of mergers after $1T_H$ for the million-body simulations is reduced for the less-dense clusters because they evolve more slowly and thus have a lower escape rate than their 500k counterparts. The dense clusters have a similar or slightly enhanced number of mergers per unit mass because although they evolve more slowly they still have time to reach peak BH-BH production and are able to produce the same number of BH-BH binaries within $1T_H$.

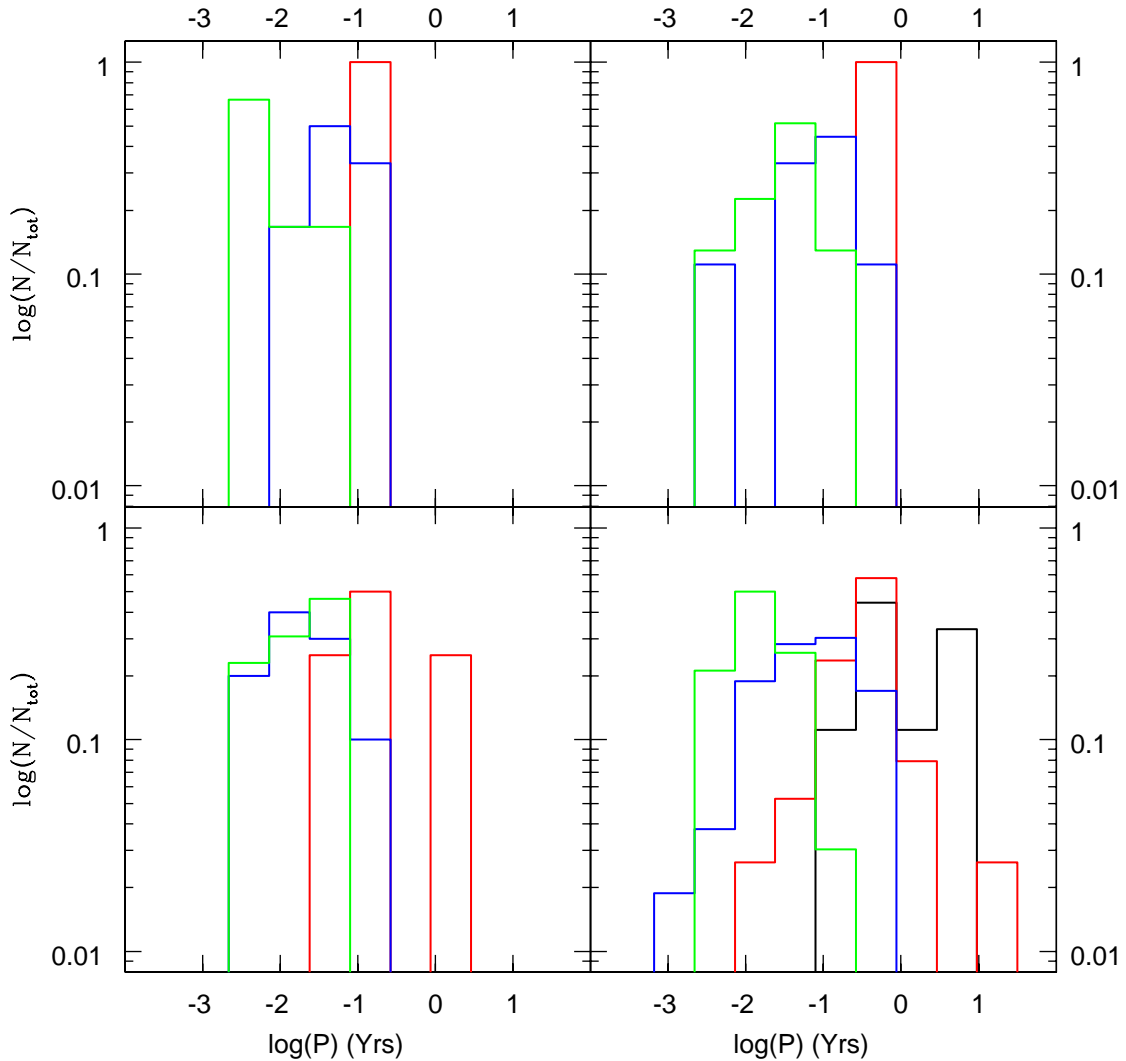


Figure 9.9: The period distribution of BH-BH binaries at the time of escape from the million-body simulations. Top to bottom $Z = 0.02$ and $Z = 0.001$. Left to right $f_b = 0.1$ and $f_b = 0.5$. Black is for $r_t/r_h = 21$, red for $r_t/r_h = 37$, blue for $r_t/r_h = 75$, and green for $r_t/r_h = 180$.

9.4 Detection Rates

Here I consider ground-based detection rates for the million-body clusters. LISA detection rates are not yet completed and will be published at a later date. I use an identical analysis to that in Section 8.1. Figures 9.12 and 9.13 give detection rates as a function of mass assuming the universe is composed only of clusters of a certain type. They should be compared to Figures 8.1 and 8.1 for the 500k clusters. There are no detections for the two lowest density clusters, unlike in the 500k case, but the detection rates for the two highest density clusters are essentially identical to the 500k simulations. This is a consequence

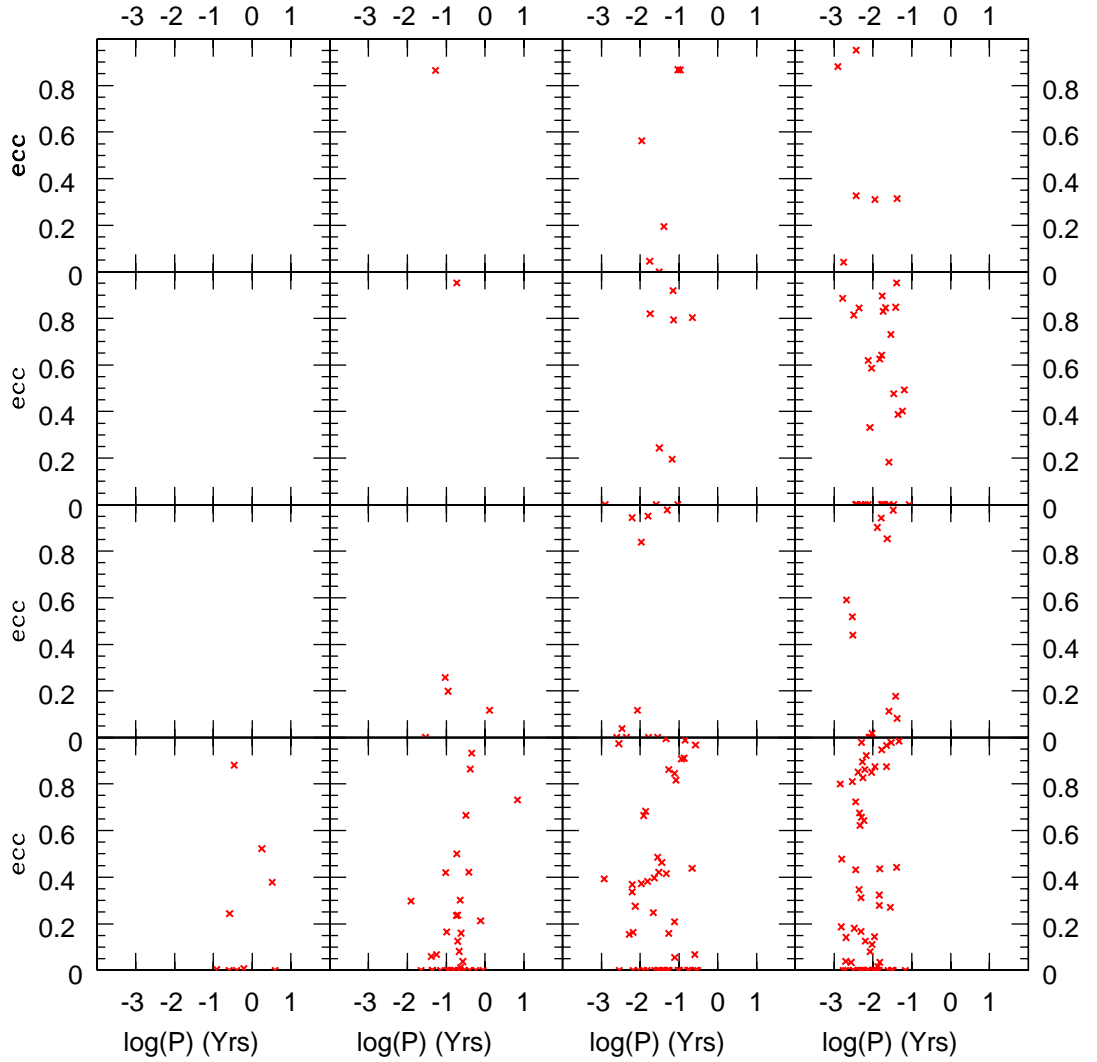


Figure 9.10: The eccentricity as a function of period for BH-BH binaries at the time of escape from the million-body simulations. Top to bottom $Z = 0.2$ and $f_b = 0.1$, $Z = 0.001$ and $f_b = 0.1$, $Z = 0.02$ and $f_b = 0.5$, and $Z = 0.001$ and $f_b = 0.5$. Left to right $r_t/r_h = 21$, $r_t/r_h = 37$, $r_t/r_h = 75$, and $r_t/r_h = 180$.

of the lower number of mergers per unit mass for the low-density clusters and the largely unaffected number of mergers in the high density case. The merger rate per year per unit mass may be slightly enhanced for the dense million-body clusters but the effect is not strong.

The detection rate averaged over all million-body simulations is given in Figure 9.14 using the same assumptions as for Figure 8.3. The global detection rate is virtually identical for both 500k and million-body simulations, despite the reduced number of mergers in the low-density million-body clusters. This is because the detection rate is dominated by the very dense clusters and these detection rates are comparable in both sets of simulations.

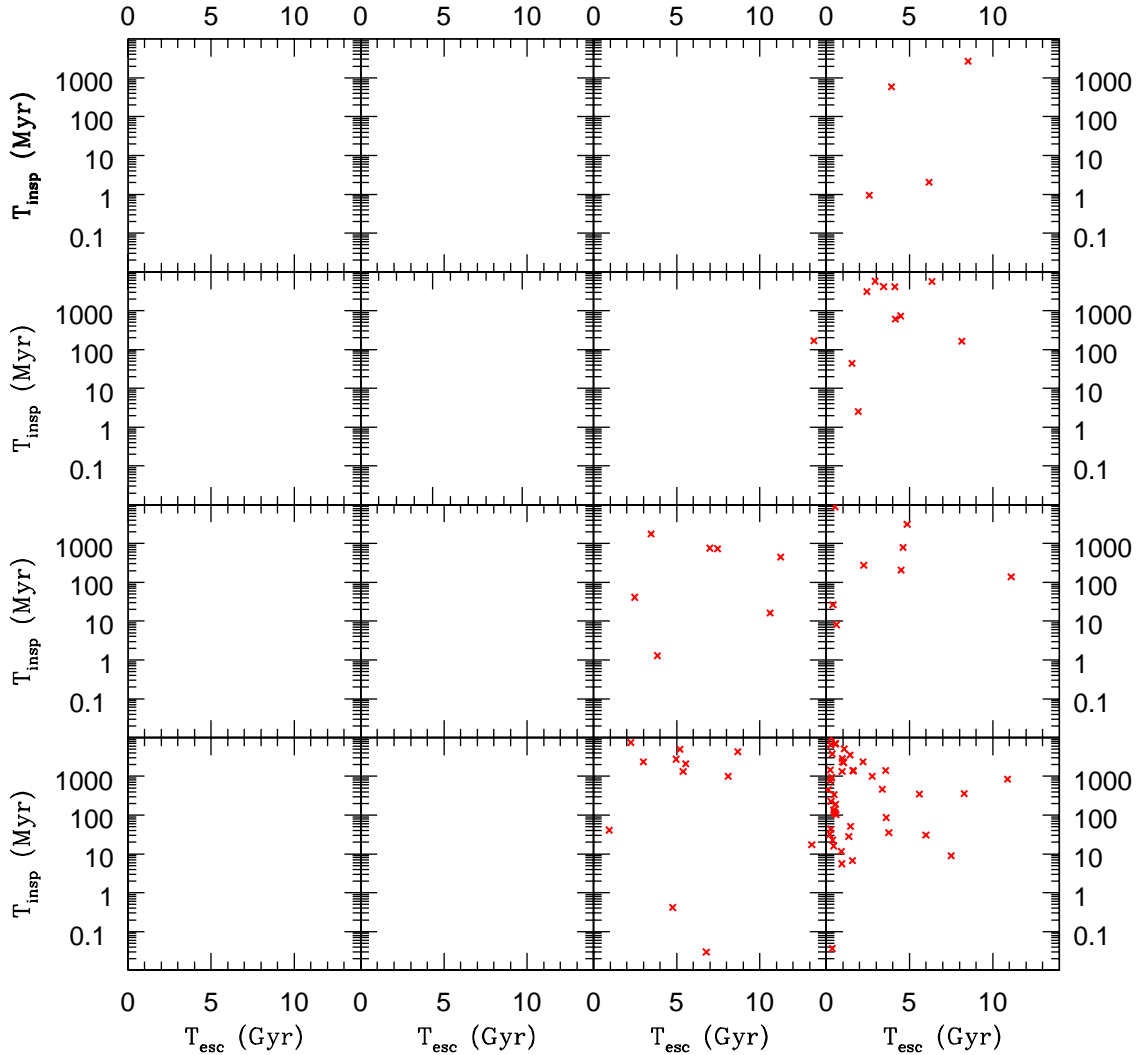


Figure 9.11: The inspiral time for the escaping BH-BH binaries that merge due to gravitational wave radiation within $1T_h$. Top to bottom $Z = 0.2$ and $f_b = 0.1$, $Z = 0.001$ and $f_b = 0.1$, $Z = 0.02$ and $f_b = 0.5$, and $Z = 0.001$ and $f_b = 0.5$. Left to right $r_t/r_h = 21$, $r_t/r_h = 37$, $r_t/r_h = 75$, and $r_t/r_h = 180$.

Therefore both the 500k and million-body simulations predict low detection rates for the current generation of detectors in the $10^5 - 10^7 M_\odot \text{pc}^{-3}$ range but very promising detection rates of $1 - 100 \text{yr}^{-1}$ for the advanced version of LIGO. For detection rates the number of particles used in the simulations does not seem very important and scaling up the 500k models seems adequate.

Finally in Figure 9.15 I give the total number of detections per redshift bin per $10^5 M_\odot \text{yr}^{-1}$ for the two current detectors and in for advanced LIGO in Figure 9.16. Detections for the current generation of ground-based detectors only go out to $z = 1.5$ whereas the majority of detections for advanced LIGO (at $S/N > 8$) will come from $z = 1 - 3$. Thus

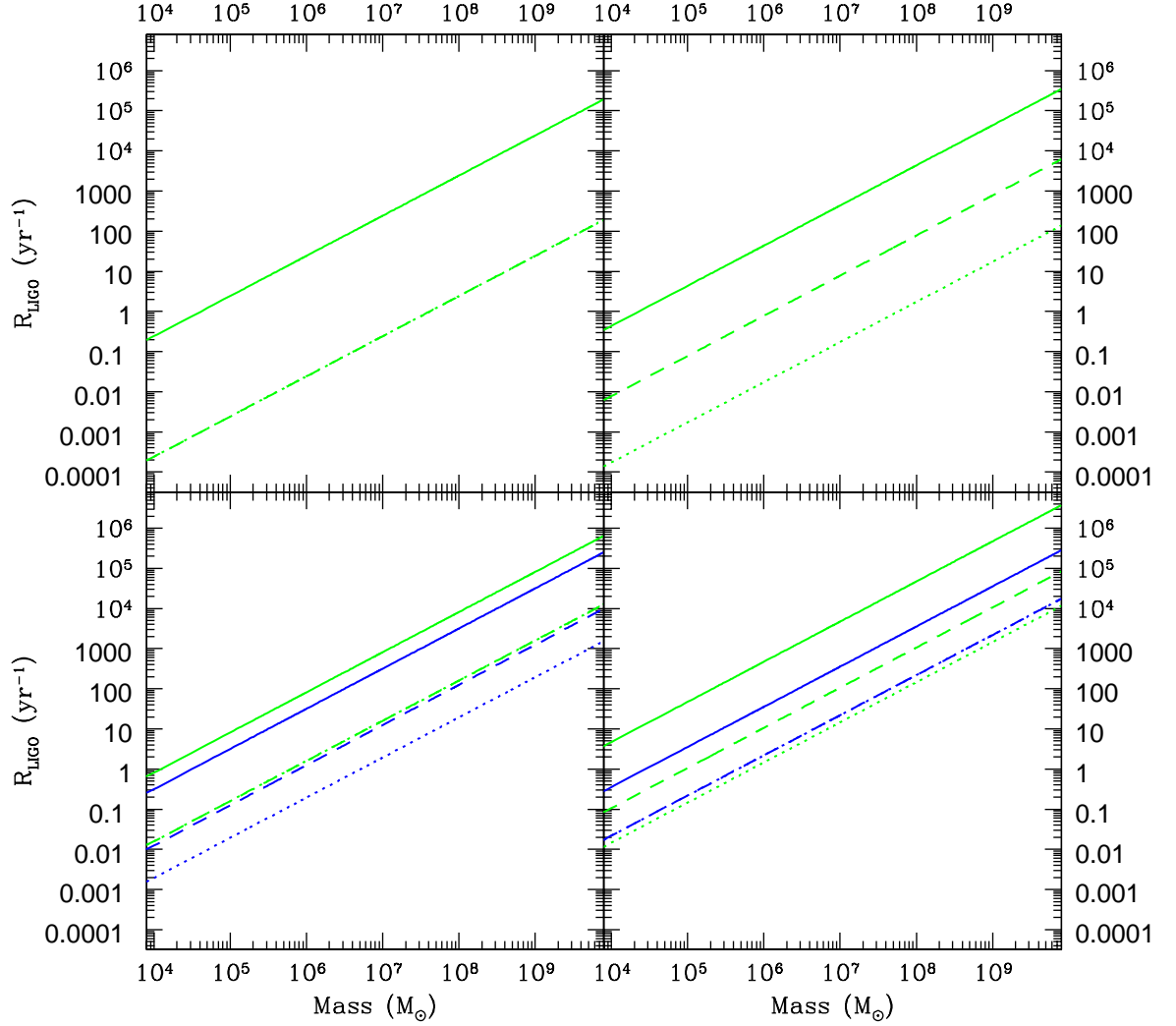


Figure 9.12: The detection rate per year per M_\odot per pc^{-3} with a $S/N > 2$. Top to bottom $Z = 0.02$ and $Z = 0.001$. Left to right $f_b = 0.1$ and $f_b = 0.5$. Black is for $r_t/r_h = 21$, red for $r_t/r_h = 37$, blue for $r_t/r_h = 75$, and green for $r_t/r_h = 180$.

advanced LIGO has a much larger volume in which to detect merger events as well as a greater sensitivity at a given distance than the current generation of ground-based detectors. Furthermore the merger rate for dense clusters peaks at higher z than their low-density counterparts. Thus advanced LIGO detection rates are enhanced both searching a much larger volume and by the larger number of mergers per unit mass and space at high- z . These two properties explain why advanced LIGO will be several orders of magnitude more sensitive than the current generation of detectors and why the high density clusters are so much more important for the merger rate than the low density clusters.

In summary, doubling the number of stars in the simulation increases the relaxation times of the clusters and makes them dynamically younger. This in general reduces the

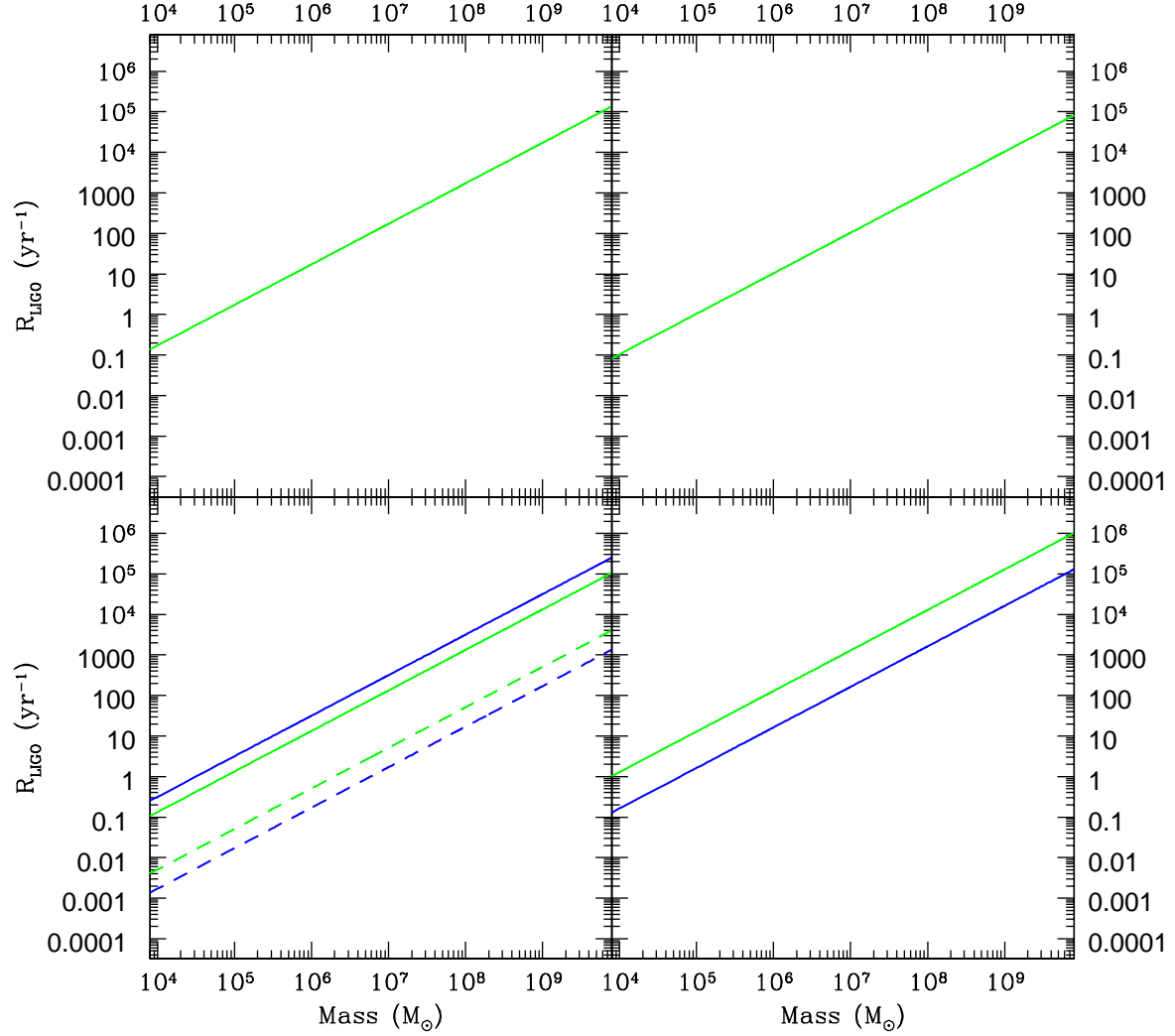


Figure 9.13: The detection rate per year per M_{\odot} per pc^{-3} with a $S/N > 8$. Top to bottom $Z = 0.02$ and $Z = 0.001$. Left to right $f_b = 0.1$ and $f_b = 0.5$. Black is for $r_t/r_h = 21$, red for $r_t/r_h = 37$, blue for $r_t/r_h = 75$, and green for $r_t/r_h = 180$.

number of BH-BH binaries, BH-BH binary escapers, and BH-BH binary mergers at a given physical time. This effect is most noticeable for the low density clusters that do not reach peak BH-BH production within $1T_H$ and is less noticeable or even absent in the high-density clusters which, despite their longer relaxation times still evolve quickly enough to reach peak BH-BH production within $1T_H$. The parameters of the binary population are unaffected both for escapers and mergers. The ground-based detection rate for both types of simulations are comparable because this rate is dominated by higher density clusters that are less affected by the change in relaxation times.

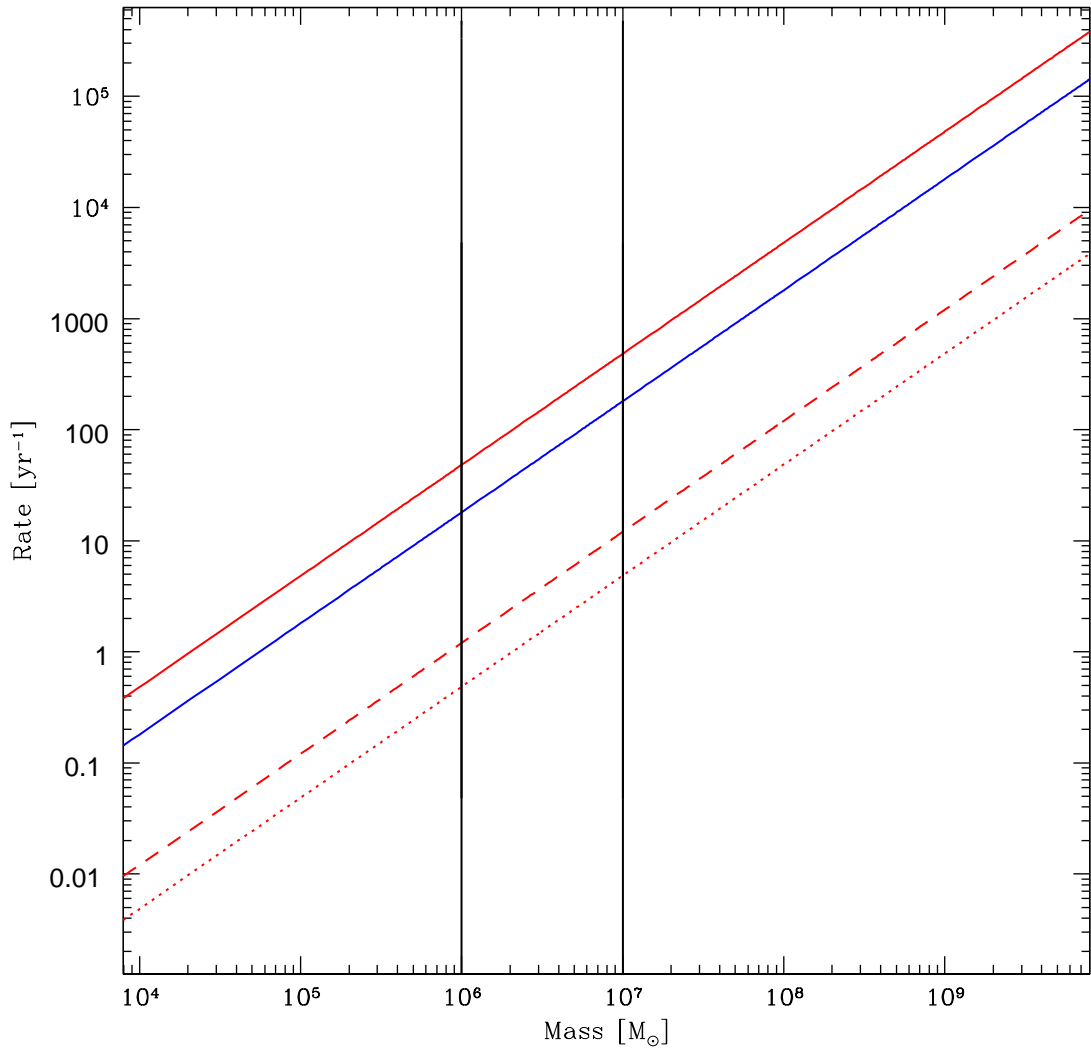


Figure 9.14: The detection rate per year per $M_{\odot} \text{ pc}^{-3}$ for the million-body simulations. Red is for detections at the $S/N > 2$ level and blue for the $S/N > 8$ level. Dotted is for current LIGO, dashed for current VIRGO, and solid for advanced LIGO.

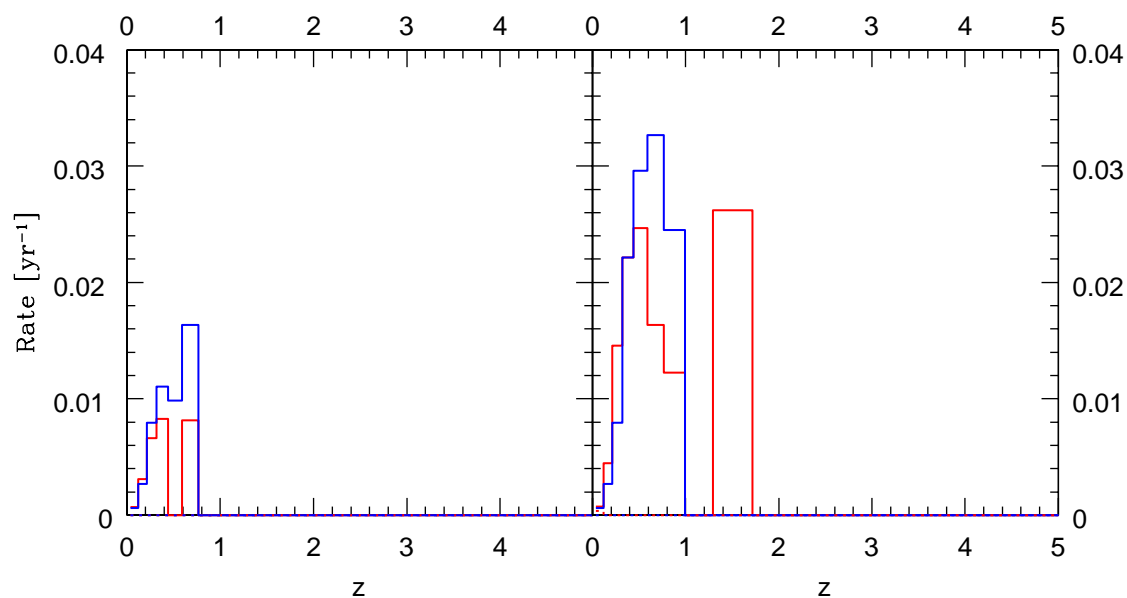


Figure 9.15: The ground-based detection rates for the current generation of gravitational wave detectors $\text{yr}^{-1} 10^5 M_{\odot}^{-1}$ as a function of redshift bin. Red is for 500k simulations, blue for million-body simulations. Solid is for $S/N > 2$, dotted for $S/N > 8$. Left panel is for current LIGO, right panel for Virgo.

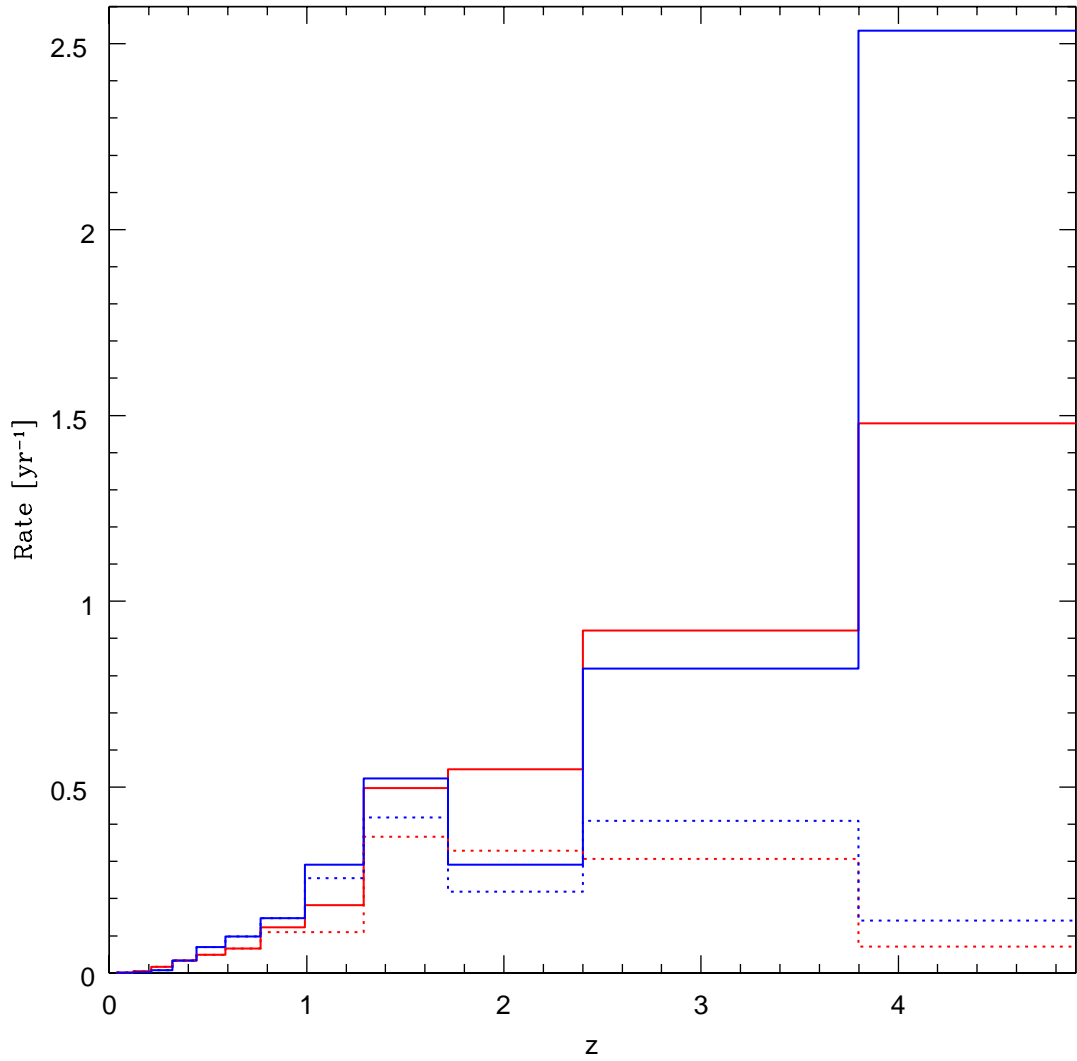


Figure 9.16: The ground-based detection rates for advanced LIGO $\text{yr}^{-1} 10^5 M_{\odot}^{-1}$ as a function of redshift bin. Red is for 500k simulations, blue for million-body simulations. Solid is for $S/N > 2$, dotted for $S/N > 8$.

Chapter 10

Discussion and Outlook

Although there are as yet no detections of gravitational waves I can compare my work to previous theoretical detection rate studies for both the galactic field and cluster population. I will also highlight how my work can be improved and carried further.

10.1 Discussion

As outlined in Sections 1.2 and 2.3 there are several studies of the neutron star and black hole binary merger rate in the galactic field. All generally agree that NS-NS mergers will be the most common source of gravitational waves in the Milky Way but that BH-BH mergers may still dominate the signal because they can be detected at larger distances. This has been called into question by Belczynski et al. (2007) who find that with a modified treatment of common envelope evolution on the Hertzsprung gap the number of BH-BH binaries is significantly reduced and NS-NS mergers should dominate even the advanced LIGO signal. Assuming a space density of 0.01 Milky Way type galaxies per Mpc, Belczynski et al. (2007) find ~ 20 NS-NS mergers, ~ 2 BH-BH mergers, and ~ 1 NS-BH merger per year. By contrast, I find a rate of ~ 10 BH-BH detections per year assuming $10^6 M_\odot$ in clusters per Mpc. Thus although the cluster population does not significantly enhance the total number of detections, it can increase the number of BH-BH detections by a factor of five or more. Thus star clusters are an important source of BH-BH detections and it is necessary to consider them when calculating detection rates.

Sigurdsson & Phinney (1993) already predicted this result. BH-BH binaries are formed rather efficiently in clusters and thus they can provide an enhancement over the field population. This is particularly true if stellar evolutionary processes destroy BH-BH binary progenitors in which case dynamical formation is the only means to produce them. O’Leary et al. (2006) and Sadowski et al. (2008) have confirmed this with numerical simulations but only with unrealistic cluster dynamics. O’Leary et al. (2006) assumed a mass-segregated, self-interacting BH-BH population whereas Sadowski et al. (2008) assume the BHs remain in dynamical equilibrium with the cluster as a whole. My simulations have a complete treatment of star cluster dynamics and can be used to determine which assumption is more accurate.

The assumptions of O’Leary et al. (2006) mean that the binaries are very centrally concentrated and interact strongly with each other. Thus they are liable to disruption or ejection as well as formation. This assumption seems to be confirmed by my simulations.

Considering Figures 6.2 and 9.2 it is clear that the binaries in both the 500k and million-body simulations mass-segregate and do not remain in dynamical equilibrium with the rest of the cluster. The short disruption timescales also indicated that the binaries interact strongly with each other and are almost as liable to be destroyed as to be created. For 5×10^5 to $5 \times 10^6 M_\odot$ in clusters per Mpc^3 , O’Leary et al. (2006) find $\sim 1 - 10$ mergers per year depending on the initial cluster model. This agrees well with the results of my work. O’Leary et al. (2006) also find a time-dependent merger rate with most mergers occurring early in the life of the cluster. O’Leary et al. (2006) also find that as few as 30% or as many as 70% of mergers can take place outside the cluster.

By contrast, the assumptions of Sadowski et al. (2008) means that the BH population is not locally concentrated and thus does not interact strongly with itself. This does not affect the formation of BH-BH binaries because BHs are still be the most massive objects in the system and are still exchanged into any binaries they encounter. Because the BH-BH binaries are massive, however, they have a high binding energy and are unlikely to be destroyed or ejected in encounters with less massive objects. The only other objects massive enough to disrupt BH-BH binaries are other BH-BH binaries. Unlike in my simulations or those of O’Leary et al. (2006) the BH density in Sadowski et al. (2008) is low in all parts of the cluster and therefore the BHs and BH-BH binaries do not interact with each other and are unlikely to be ejected or destroyed. For this reason Sadowski et al. (2008) predict more BH-BH binaries in their clusters and consequently higher detection rates. They 25 – 3000 detections per year for advanced LIGO depending on the density of star clusters in the universe. The merger rate in the Sadowski et al. (2008) simulations is more or less constant at $\sim 2.5 \text{ Gyr}^{-1}$, again in opposition to my work and the results of O’Leary et al. (2006) that indicate a time- and concentration-dependent merger rate. Sadowski et al. (2008) also find that only 10% of mergers take place outside the clusters as opposed to 30-70% for O’Leary et al. (2006) and almost 100% for my simulations. This is again a result of the interaction rate. Fewer encounters with massive objects means that fewer BH-BH binaries will gain an escape velocity due to a single encounter and thus are less likely to be ejected from the system.

My results are much closer to those of O’Leary et al. (2006) than Sadowski et al. (2008). In particular I find a similar number of mergers, a large number of dynamical ejections and consequently a large fraction of mergers outside the cluster, and a time-dependent merger rate. This is because, as is shown in Figures 6.2 and 9.2, a full treatment of dynamics leads to the formation of a strongly interacting, mass segregated subsystem as assumed by O’Leary et al. (2006). It thus seems the O’Leary et al. (2006) assumptions better describe the dynamics of BHs in star clusters than does the two-zone model used by Sadowski et al. (2008) who significantly overestimate the detection rate. This highlights the importance of using proper models for the global dynamics of star clusters when considering individual binary properties, not just accurate few-body dynamics. It is interesting to note that, at least for the BHs, including stellar evolution does make my results significantly different from those of O’Leary et al. (2006). This is not surprising since the black holes are formed early, most within the first 20 Myr, and thus exist before the dynamics starts to play a strong role. Stellar evolution is important, however, for confirming that neutron stars do not contribute significantly to the merger rate and will also be useful when I consider the WDs produced by my simulations.

Although my results are generally consistent with O’Leary et al. (2006) there is one major difference: O’Leary et al. (2006) find a significant number of mergers within the

clusters (never much less than 30% and often more) whereas I find no mergers in the clusters in the 500k simulations and only two in the million-body simulations. Sadowski et al. (2008) find an even higher proportion in the cluster. The discrepancy is probably due to my treatment of few-body encounters. Both O’Leary et al. (2006) and Sadowski et al. (2008) use direct integration to calculate the outcome of few-body encounters and thus can accurately determine the change in binding energy and centre of mass velocity after the encounter. My few-body interactions are drawn from prescriptions and, particularly in the case of binary-binary interactions, only very limited values of energy re-distribution are allowed. It is entirely possible that, while the binding energies of the escapers in my simulations are roughly consistent with the O’Leary et al. (2006) results, the escape velocities are systematically incorrect. Furthermore, the binary-binary prescriptions lead to the disruption of one of the binaries in 88% of interactions. It is possible that this fraction is too large and my simulations disrupt too many BH-BH binaries. This may unrealistically reduce the number of mergers in my simulations. The prescriptions also fail to treat mergers during interactions where very close encounters can occur and further reduces the number of mergers in my simulations. The Monte Carlo code also lacks as good a treatment of general relativity as contained in O’Leary et al. (2006) and Sadowski et al. (2008) who integrate Equations 3.40 and 3.41 explicitly rather than using a timescale criterion. All of these factors will lead me to underestimate cluster merger rates. The way to constrain how important this is would be to include direct few-body integration in my Monte Carlo code.

These results represent the first quantitative estimates of LISA detection rates for BH-BH binaries in star clusters so I can make no comparison with previous studies. I can, however, compare to the galactic field calculations of Belczynski, Benacquista & Bulik (2008). Belczynski, Benacquista & Bulik (2008) have run two sets of simulations, both representing the entire galaxy, one with CE evolution and merger during the Hertzsprung gap phase and one without. They find if CE evolution on the Hertzsprung gap is ignored there are 8831 resolvable binaries in the galaxy, 1563 of which are BH-BH. If CE evolution is taken into account they find 4386 resolvable binaries, only 8 of which are BH-BH. Without CE on the Hertzsprung gap this translates into a total detection rate per unit mass of 1.45×10^{-2} per $10^5 M_{\odot}$ and a BH-BH detection rate of 2.56×10^{-3} per $10^5 M_{\odot}$. For the case with CE on the Hertzsprung gap this yields a total detection rate of 7.19×10^{-3} per $10^5 M_{\odot}$ with a BH-BH detection rate of 1.31×10^{-5} per $10^5 M_{\odot}$. Belczynski, Benacquista & Bulik (2008) use the same detection criterion as I used in Section 8.2. Assuming optimal orientation and keeping in mind that statistics based on two objects are unreliable, I calculate the number of detections for my simulations to be 2.6×10^{-2} per $10^5 M_{\odot}$, all BH-BH. Thus it seems that clusters can provide an enhancement in BH-BH detections in the LISA band as well. The analysis for the escapers is not yet complete but there are many with periods on the order of a day and significant eccentricity that should be visible to LISA. These will be detected as galactic sources and it will be interesting to see if there is any systematic difference that would allow them to be differentiated from the field sources. If they cannot be distinguished this provides problems for one of the predictions of Belczynski, Benacquista & Bulik (2008) namely that the absence of BH-BH detections would be evidence for CE evolution during the Hertzsprung gap whereas detection of them would confirm that no such evolution takes place. My results indicate that the BH-BH population in the LISA band can be enhanced by dynamically formed binaries and thus BH-BH detection cannot be taken as evidence that there is no CE evolution during the Hertzsprung gap.

10.2 Future Directions

There are three ways in which my simulations could be improved in the future, two concerned with the treatment of few-body systems in general and one using a new simulation method. First, I could upgrade the code to include direct integration of few-body interactions. Second, I could implement relativistic integration in the few-body interactions using the Post-Newtonian method. Third, I could supplement my Monte Carlo simulations with direct N-Body simulations. In addition, I can analyse my current simulations for populations other than the NS and BH binary population and thus extend their usefulness beyond gravitational wave detection.

10.2.1 Direct Integration of Few-Body Encounters

It is possible to incorporate direct integration of strong few-body interactions into the Monte Carlo code using an efficient few-body solver. This will improve the accuracy of the few-body encounters and will allow the code to deal with arbitrary initial configurations. It will not, however, help determine the probability of when an interaction will take place. This has been done by the Rasio group (Fregeau & Rasio 2007) using the FEWBODY integrator (Fregeau et al. 2004) and in the hybrid gas-Monte Carlo code of Giersz & Spurzem (2003) using the regularisation schemes of Aarseth & Zare (1974) and Mikkola (1983) for three- and four-body encounters. The Rasio code is not publicly available and still has some stability issues. The hybrid code is available but is still in development and does not include stellar evolution. This is because the hybrid code does not represent single stars individually outside the interactions but rather treats them as a self-gravitating gas. Since there are no individual stellar parameters to follow treatment of stellar evolution must be done for representative stars of similar ensembles to the star cluster of interest. This is a non-trivial problem but progress has been made in this direction (Deiters & Spurzem 2000). A new version of the hybrid code, still without stellar evolution but with the chain regularisation scheme of Mikkola (1997) and Mikkola & Aarseth (1998) is currently in preparation (Giersz & Spurzem 2010). Upgrading the Giersz Monte Carlo code to include regularised integration of binary-single and binary-binary encounters is another obvious step. The code will take longer to run, but, since the Monte Carlo code is so efficient, even a factor of 10 slow-down would still make it an attractive alternative to direct N-body integration.

10.2.2 Relativistic Interactions

If explicit few-body integration can be incorporated into the code then it is possible to supplement the classical integration, at least in two-body encounters, with expressions describing relativistic orbits in the Post-Newtonian (PN) approximation. The PN method consists of taking an expansion of the linearised field equations in powers of v/c where v is the relative velocity in the binary rather than as a quadrupole expansion. This involves matching a near-zone expansion within the binary with a far-zone expansion in the region external to the binary and is developed in detail in Blanchet (2006). It is possible to use this expansion to write the equations of motion for a binary in as a series of corrections to the Newtonian equations of motion:

$$\vec{a} = \vec{a}_N + \frac{v}{c} \vec{a}_1 + \left(\frac{v}{c}\right)^2 \vec{a}_2 + \left(\frac{v}{c}\right)^3 \vec{a}_3 + \left(\frac{v}{c}\right)^4 \vec{a}_4 + \left(\frac{v}{c}\right)^5 \vec{a}_5 \dots \quad (10.1)$$

where \vec{a}_N is the Newtonian acceleration in the binary. Formally Equation 10.1 works only when v/c is small but has actually been found to produce accurate orbits and gravitational waveforms up to the last orbits before the relativistic merger (Baker et al. 2007). This is because each of the terms itself contains several terms with different signs that can cancel out. Thus the factor v/c is only a symbolic measure of the scale of each correction and the corrections can actually be much smaller than v/c when actually calculated. Blanchet (2006) shows that the terms \vec{a}_1 and \vec{a}_3 vanish. Thus \vec{a}_2 and \vec{a}_4 are the leading non-zero terms and are dubbed PN1 and PN2 respectively. These terms affect both the phase of the binary and, through the Runge-Lenz vector, the orientation of the orbit. They are, however, both conservative with respect to the energy of the system. The first non-conservative term is the fifth-order term, dubbed PN2.5, and it can be shown that this term is equivalent to the quadrupole formula in Chapter 3. In the centre of mass reference frame the PN equations can be displayed in the compact form:

$$\vec{a}_{PN} = -\frac{Gm}{r^2} [(1 + \mathcal{A})\vec{n} + \mathcal{B}\vec{v}] \quad (10.2)$$

where, $\vec{x} = \vec{x}_1 - \vec{x}_2$, $r = |\vec{x}|$, $\vec{n} = \vec{x}/r$, $\vec{v} = \vec{v}_1 - \vec{v}_2$, and \mathcal{A} and \mathcal{B} up to the PN2.5 order are given by (Blanchet 2006):

$$\begin{aligned} \mathcal{A} = & \frac{1}{c^2} \left[-\frac{3\dot{r}^2\nu}{2} + v^2 + 3\nu v^2 - \frac{Gm}{r}(4 + 2\nu) \right] \\ & + \frac{1}{c^4} \left[\frac{15\dot{r}^4\nu}{8} - \frac{45\dot{r}^4\nu^2}{8} - \frac{9\dot{r}^2\nu v^2}{2} + 6\dot{r}^2\nu^2 v^2 + 3\nu v^4 - 4\nu^2 v^4 \right. \\ & \left. + \frac{Gm}{r} \left(-2\dot{r}^2 - 25\dot{r}^2\nu - 2\dot{r}^2\nu^2 - \frac{13\nu v^2}{2} + 2\nu^2 v^2 \right) + \frac{G^2 m^2}{r^2} \left(9 + \frac{87\nu}{4} \right) \right] \\ & \frac{1}{c^5} \left[-\frac{24\dot{r}\nu v^2}{5} \frac{Gm}{r} - \frac{136\dot{r}\nu}{15} \frac{G^2 m^2}{r^2} \right] \end{aligned} \quad (10.3)$$

and

$$\begin{aligned} \mathcal{B} = & \frac{1}{c^2} [-4\dot{r} + 2\dot{r}\nu] \\ & \frac{1}{c^4} \left[\frac{9\dot{r}^3\nu}{2} + 3\dot{r}^3\nu^2 - \frac{15\dot{r}\nu v^2}{2} - 2\dot{r}\nu^2 v^2 + \frac{Gm}{r} \left(2\dot{r} + \frac{41\dot{r}\nu}{2} + 4\dot{r}\nu^2 \right) \right] \\ & \frac{1}{c^5} \left[\frac{8\nu v^2}{5} \frac{Gm}{r} + \frac{24\nu}{5} \frac{G^2 m^2}{r^2} \right] \end{aligned} \quad (10.4)$$

where $\nu = m_1 m_2 / (m_1 + m_2)^2$, and $\dot{r} = \vec{n} \cdot \vec{v}$. Expressions for the PN3 and PN3.5 orders are also available and, among other things, address the effect of spin-orbit coupling in binaries. While in principle only valid for binary systems these equations can be used to deal with hierarchical triples provided the scales are sufficiently separated that the PN effects can be calculated for the inner binary alone and then between the inner binary as a centre of mass and the third star.

The stellar dynamics group at the ARI-ZAH at the University of Heidelberg have used the PN method to study the evolution of SMBHs in stellar systems (Berentzen et al. 2009) and have developed a two-body integrator with PN corrections. This integrator uses a 4th-order Hermite scheme to calculate the evolution of a two-body system under the effect of

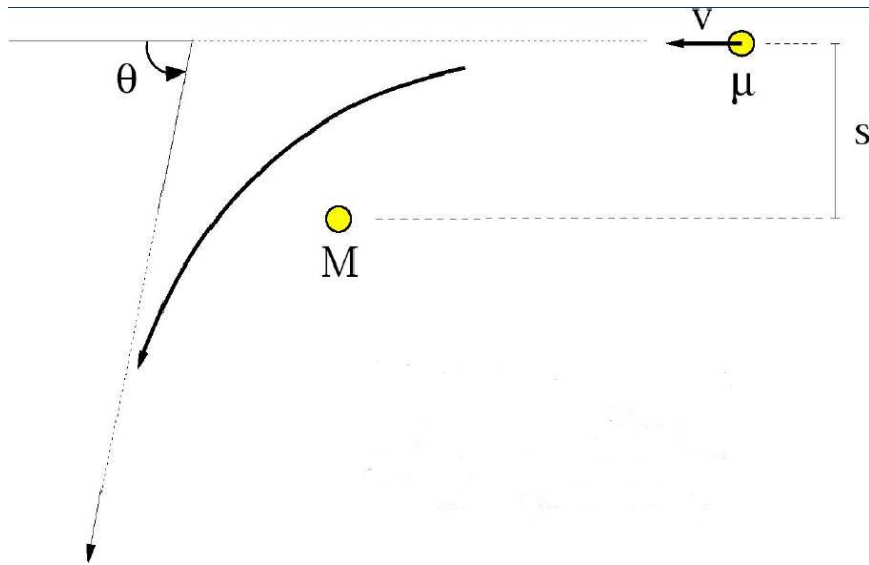


Figure 10.1: The classical set-up for scattering in an attractive central potential. Figure provided by Ingo Berentzen (private communication).

general relativity. I have worked with Ingo Berentzen, the primary developer of the code, to set up and run relativistic black hole-black hole scattering experiments. The geometry of the problem is given in Figure 10.1. The theoretical scattering angle for the purely Newtonian potential is given by the formula:

$$\cot \frac{\Theta}{2} = \frac{2E_0 s}{Gm_1 m_2} \quad (10.5)$$

where Θ is the scattering angle, E_0 the total energy, s the impact parameter at infinity, and $m_{1,2}$ are the masses of the black holes. My relativistic experiments start with a similar set-up and the scattering angles as a function of impact parameter are calculated and compared to both the classical formula and Newtonian two-body integration in Figure 10.2. The black holes are considered to merge if they come within ten Schwarzschild radii of each other.

It is clear that the PN terms have an effect on the scattering angle at smaller impact parameters, first enhancing it and then apparently reducing it. It also seems that when the PN corrections are included, the black holes can merge with a larger impact parameter than in the pure Newtonian case. Both of these effects occur because the PN2.5 term dissipates energy and can result in the black holes becoming bound to each other much like in a classical tidal interaction. The effect of the PN terms on two specific orbits, one that leads to a merger and one that does not, are shown in Figure 10.3.

In the case without the merger, the PN terms almost lead to a capture but not quite. The black holes make a full orbit and the scattering angle is actually $> \pi$ rad. Since I measure the scattering angle by taking the dot product between the initial and final velocity vector, this manifests in as a smaller scattering angle in Figure 10.2. For a smaller impact parameter the PN terms dissipate enough energy that the binary is captured, forms a bound orbit, and merges after some time due to gravitational radiation. This cannot happen for the pure Newtonian case because there are no dissipative forces and the black holes can merge only by direct collision.

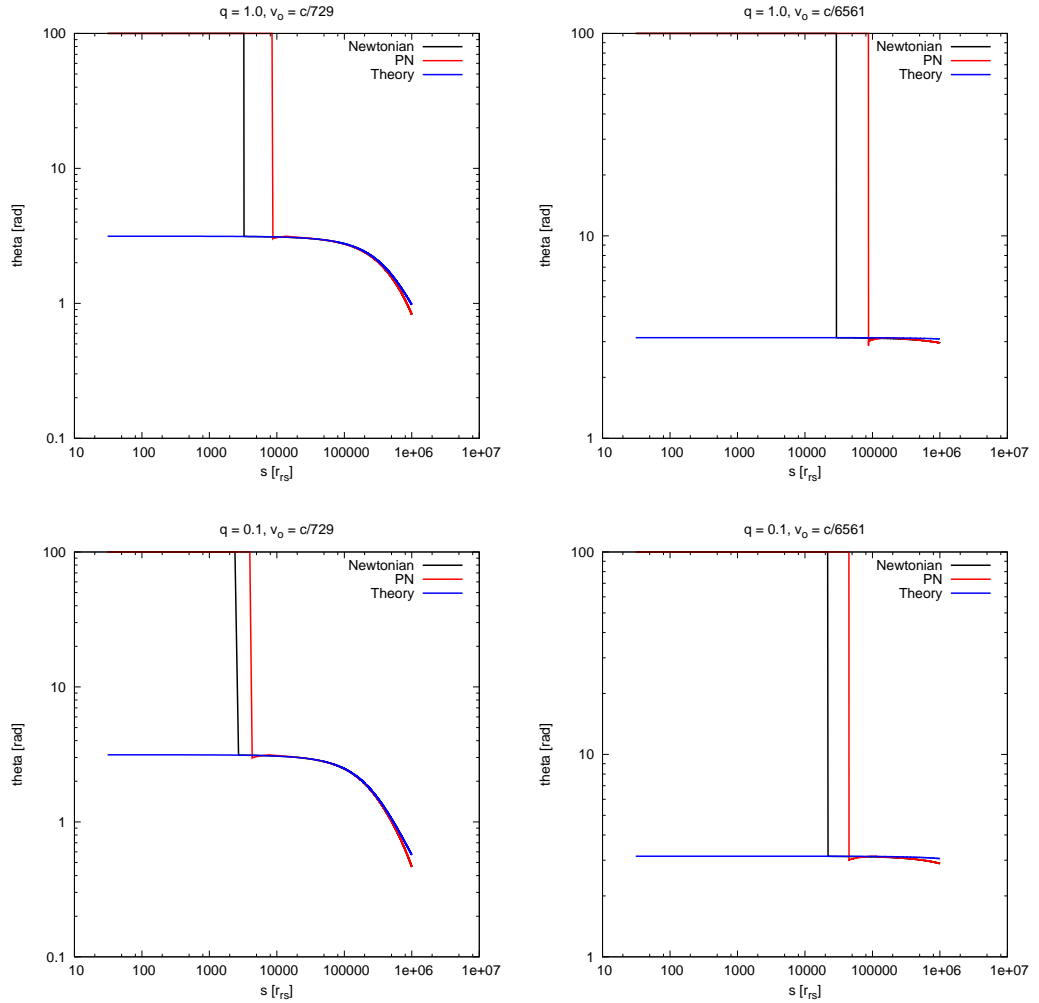


Figure 10.2: The scattering angles for the relativistic experiments. Theory is the prediction of Equation 10.5, Newtonian is the result of numerical integration using only the Newtonian force, and PN is numerical integration including Post-Newtonian corrections. v_0 is the velocity at infinity as a fraction of c and q is the mass ratio. The vertical jump in the numerically calculated properties indicates a merger.

It is obvious that the dynamics are different for small impact parameters in the Newtonian and PN cases. The relativistic captures in particular are very interesting for gravitational wave detection both because they will lead to mergers and because during the very close periastron approaches brought on by the high initial orbital eccentricity they may be burst sources. These scattering experiments were conducted in the context of encounters between SMBHs in galactic centres and units were chosen such that the unit of mass was $10^9 M_\odot$. Thus these results cannot be directly applied to my star cluster simulations. If I assume that the black holes can be captured at the same number of Schwarzschild radii regardless of the physical mass of the black holes then the results for $c/6561 \approx 45 \text{ km s}^{-1}$ (the more reasonable value for the central velocity dispersion in star clusters (Harris 1996)) would yield a maximum impact parameter for capture of $p_{\max} \sim 5 \times 10^5 \text{ km}$ (taken from Figure 10.2). My clusters have ~ 1000 BHs and, assuming they are all concentrated

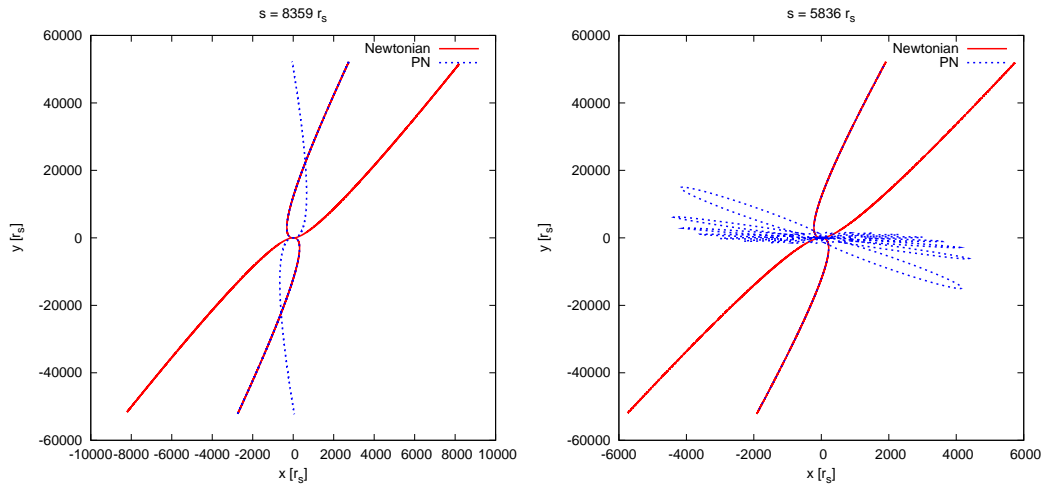


Figure 10.3: Two examples of relativistic two-body orbits, both for $v_\infty = c/729$. The orbit on the left does not lead to a merger for either the Newtonian or the PN orbit whereas the orbit on the right leads to a capture and merger of the PN orbit but not the Newtonian orbit. The effect of the PN terms is clearly visible in both cases.

within the central pc, have a number density of 1000 BH pc^{-3} . Using the maximum impact parameter to calculate a merger cross-section, $\sigma = \pi p_{\text{max}}^2$, this leads to a PN capture rate of $\sim 1.6 \times 10^{-7}$ events per BH per Myr. Assuming that all 1000 BHs can experience tidal capture this produces ~ 1 such event per cluster per Hubble time. This is probably an overestimate since the black hole population is depleted from the cluster over time due to dynamical ejection. Furthermore it is not obvious that the scattering experiments can be scaled in this way since the mass-dependence for the Schwarzschild radius and the PN terms are different and the impact parameter for tidal capture in terms of Schwarzschild radius could well be lower in the stellar mass case. Nonetheless, these experiments point to an interesting possibility for gravitational wave generation and I am currently following-up these galactic-scale simulations with ones scaled to stellar mass black holes.

Relativistic scattering experiments have also been carried out for binary-single encounters in the context of intermediate mass black hole (IMBH) binaries by Gültekin, Miller & Hamilton (2006) and Amaro-Seoane, Miller & Freitag (2009). They use only the PN1 in these experiments as well as a treatment of the radiation reaction due to gravitational waves. They find that although the merger rate between two of the stars in the three-body interaction is not strongly increased in any one encounter, nonetheless the cumulative effect of many encounters is to increase the growth and merger rate of IMBHs by a factor of two. The IMBH inspirals should be strong LISA sources with significant eccentricity. It would be interesting to include PN dynamics in the binary-single interactions in the Monte Carlo code to see if the effect is important for stellar-mass binaries. Thus including relativistic few-body dynamics in the Monte Carlo code is a very interesting possibility for the future.

10.2.3 Direct N-Body Simulations

PN dynamics can also be added to the binary interactions in direct N-body codes. This has been done for NBODY6 (Aarseth 1999) by Kupi, Amaro-Seoane & Spurzem (2006). NBODY6 regularises its binaries according to the principles developed by Kustaanheimo

& Stiefel (1965) and improved by the chain regularisation of Mikkola (1997) and Mikkola & Aarseth (1998). In this scheme the standard Kepler problem can be mapped through quaternion space to a simple harmonic oscillator (Neutsch 1992). External forces can be applied as "perturbations" and since PN is essentially a correction to the Newtonian force, it can be applied in the same way. Perturbations is placed in quotes because, although external forces are applied the same way as a perturbation, they can actually be arbitrarily large without loss of accuracy in the regularisation scheme and are not, formally speaking, perturbations. A parallel version of this code with realistic binary parameters was the focus of an early phase of my project during which I ported the PN corrections calculated by Kupi, Amaro-Seoane & Spurzem (2006) into the parallel version of NBODY6, NBODY6++ (Spurzem 1999). This provides a self-consistent method of treating relativistic binaries in star clusters with full few-body integration.

In practise this approach was complicated by two factors. The first is that the PN approximation is strictly valid only for two-body systems. It is possible to treat hierarchical triples where the scales are well-separated but a democratic treatment of three-body systems is impossible beyond the 1 PN order. This is important in the direct N -body simulations not only for the accurate treatment of three-body systems but also because the PN terms affect the energy of the binary and this must be taken into account in the (Newtonian) global energy conservation of the code. For binaries that start their evolution outside the relativistic regime and enter it later the PN energy can be approximated using a simple dissipative argument and the result applied to the total energy of the cluster. If, however, three stars interact and there is no clear separation of scales, dealing with the energy associated with the PN dynamics becomes difficult. Only one pair can be treated with PN at a time and yet both may be in the relativistic regime. This creates problems reconciling the energy of the relativistic binary with the global Newtonian energy of the cluster and causes (possibly spurious) spikes in the total energy of the cluster. This is shown in Figure 10.4 for one of my sample runs where the effect of the PN terms was enhanced in order to produce more events. It is probably possible to solve this problem, at least in a technical sense, by revising the regularisation criterion to only allow only two of the bodies to be affected by the PN corrections at any one time and, if one of the bodies is swapped for a third one, to find a proper description of the energy generated in the PN interaction and apply it as a correction to the bookkeeping of the overall Newtonian energy. This is an interesting problem to be explored in future work.

The second and more serious problem with this approach is that relativistic interactions and inspirals are rare events. In my most promising Monte Carlo situations I get only 6×10^2 BH-BH binaries per $10^5 - 10^6$ stars and only a few tens of mergers over a Hubble time. Furthermore I require a 50% binary fraction to do so. There are even fewer LISA events. Direct N -body codes are not at present able to reach the size of the Monte Carlo simulations my work is based upon and would thus produce even poorer statistics. They also take much longer to run, particularly with large numbers of binaries, and this renders parameter space studies and multiple realisations of simulations in order to constrain fluctuations impossible. Therefore at present Monte Carlo methods, particularly if direct integration of few-body interactions are included, are a more attractive choice for investigating the BH-BH population in star clusters. Future developments in direct N -body simulations, particularly combining parallel codes such as NBODY6++ with hardware acceleration such as graphical processing units (GPUs) (Spurzem et al. 2009, 2008) will make much larger and faster direct N -body simulations possible. At this point it will certainly be worth re-visiting Post-Newtonian enhanced direct N -body simulations for gravitational wave detection. It is

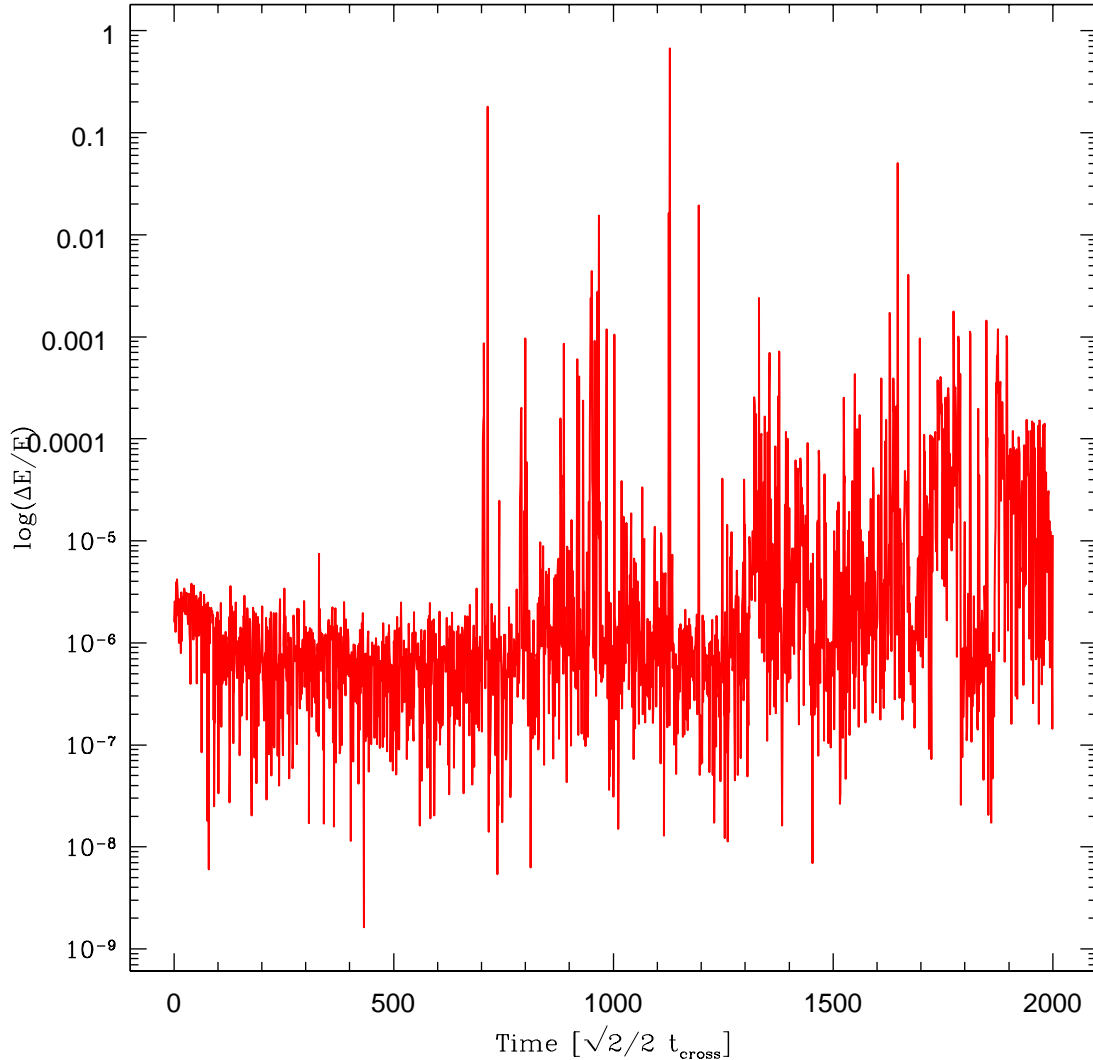


Figure 10.4: The change in energy per timestep for direct N-body simulations including PN corrections for the binaries. Step-to-step energy conservation of 10^{-6} or better is sought in direct N-body simulations. The spikes observed are thought to be due to swapping of PN pairs in three-body encounters that are not yet properly taken into account in the Newtonian energy balance.

worth noting that while direct N-body simulations may not be the most attractive choice for dealing with stellar-mass binaries in star clusters they have been used very successfully to investigate the behaviour of IMBHs and SMBHs in dense stellar environments (Amaro-Seoane, Miller & Freitag 2009; Berentzen et al. 2009). Here PN corrections need only be calculated for one or two massive objects and the timescales of interest are normally Myr rather than the Gyr needed to simulate an old star cluster. Furthermore direct N-body simulations have no symmetry requirements and can treat all of the encounters accurately. Thus in this context direct N-body simulations are the method of choice.

10.2.4 Further Analysis of the Simulations

One possible way to extend the results of my simulations further would be to calculate actual gravitational waveforms for my inspiraling BH-BH binaries. I have explicit binary parameters and I can use the PN code presented in Damour, Gopakumar & Iyer (2004) and Tessmer & Gopakumar (2008) to properly predict the gravitational waves generated at any distance in the far field. This code applies the PN equations of motion to the Kepler equations and develops a quasi-Keplerian prescription for the inspiral, merger, and gravitational wave generation of an isolated binary. This method should be faster than full orbital integration of short-period binaries over Myr-Gyr timescales and produces Post-Newtonian accurate waveforms for binaries with various eccentricities. The accuracy of these waveforms has not yet been fully tested but introduces the possibility of generating templates directly from my simulations that can be used for filter-matching in gravitational wave detectors.

It would also be interesting to extend my work to other kinds of clusters. The cluster population in the Milky Way is old and contains clusters of $10^5 - 10^6$ solar masses. There are, however, other types of clusters in other galaxies. There is evidence for a population of intermediate age globular clusters (Kundu et al. 2005) which would be in a different state of dynamical evolution than the clusters in our galaxy. Young massive clusters in the Milky Way such as the Arches cluster which may be sites of massive star formation (Stolte et al. 2002) may also be interesting candidates from BH and gravitational wave generation. There are also very massive systems such as dwarf-globular transition objects (DGTOs Hasegan et al. 2005) and ultra-compact dwarf galaxies (UCDs Drinkwater et al. 1999) which do not fall clearly into the category of either galaxy or star cluster. The formation history of these objects is not clear but they could result from stripping dwarf galaxies (Bekki et al. 2003) or (for DGTOs) the merger of super star clusters (Fellhauer & Kroupa 2002). There is some knowledge of how to link observations of clusters and cluster systems to their initial conditions (Fleck et al. 2006; Vesperini et al. 2003) and it might be interesting to investigate the BH-BH binary population in these systems using the Monte Carlo code.

Finally, my current simulations are not limited to the neutron star and black hole populations. SSE and BSE treat all aspects of stellar evolution and my simulations represent a full star cluster population synthesis study. The most immediate use I can put this to is to study the WD-WD binaries. These are an important noise source for LISA (Ruiter et al. 2007) and are thus very interesting in the context of gravitational wave detection. This has been studied before but again in the context of a two-zone model (Willems et al. 2007) and a study of the WD-WD population with a full dynamical treatment would be interesting. Future work on this topic is planned with my colleague Matthew Benacquista.

As well as the WD-WD binaries I can produce photometric data such as surface brightness profiles and colour-magnitude diagrams for all of my simulations. SSE and BSE also provide sufficient information to generate spectroscopic data. The methods for such an analysis have been developed in the context of NBODY6 by Borch, Spurzem & Hurley (2006) and Borch, Spurzem & Hurely (2007). Both NBODY6 and the Giersz Monte Carlo code use SSE and BSE to calculate their stellar properties and thus it is, in principle, easy to port these prescriptions into the Monte Carlo code. Therefore my simulations can be used to investigate almost any problem associated with star clusters and produce data that can be compared directly with observations. I hope to make the data from my simulations publicly available for these types of investigations in the near future.

10.3 Conclusions

The focus of my work has been to understand the compact binary population in star clusters and how this contributes to the detection rate for ground- and space-based detectors. This is the first study of clusters as gravitational wave sources that uses a full treatment of both the global cluster dynamics and stellar evolution.

I have been able to confirm several previous results. I have shown, as predicted by Sigurdsson & Phinney (1993), that star clusters are able to produce BH-BH binaries and they are produced at a much higher rate than would be expected from isolated stellar evolution in the galactic field. This work demonstrates that star clusters will strongly enhance the BH-BH detection rate for the next generation of ground-based detectors, confirming the results of O’Leary et al. (2006) and Sadowski et al. (2008), but also shows that there is only a very small possibility for detecting BH-BH mergers with the current generation of ground-based detectors.

I have also found several new results. I have been able to prove that a full treatment of dynamics in star clusters leads to mass-segregation of the BH population and a very high interaction rate between BHs and BH-BH binaries. This matches the assumptions made in O’Leary et al. (2006) and my result agrees well with theirs. This means that the two-zone model of Sadowski et al. (2008) is disfavoured. The simulations also eject many hard binaries and most mergers of binaries originating in clusters will actually occur in the galactic field. This is different from the results of either O’Leary et al. (2006) or Sadowski et al. (2008) although this may be at least partly to do with the more accurate few-body method these authors used. Another result of these simulations is that star clusters may produce BH-BH binaries detectable by the LISA observatory. This has been suggested before for the galactic field (e.g. Belczynski, Benacquista & Bulik 2008) and for WD-WD binaries in clusters (Willems et al. 2007) but not before for been quantitatively studied in star clusters. Two objects in my simulations appear in the LISA band, indicating that such events are possible but rare. This does, however, indicate an enhancement over the rate of such detections per unit mass in the galactic field. Both sources are highly eccentric. The population of escapers has not yet been analysed for LISA but will almost certainly further enhance the detection rate. More simulations are needed in order to produce better statistics.

There are several possibilities for improving my work, the most important of which is incorporating direct integration of strong few-body encounters into the Monte Carlo code. This will have several advantages: more accurate outcomes and energy generation in few-body encounters, the possibility of mergers during interactions, and the ability to include relativistic dynamics in the binary motion allowing the code to resolve relativistic inspirals more accurately and to simulate gravitational wave bursts that could occur due to close hyperbolic encounters.

Finally the simulations can be used to investigate question beyond the BH-BH population. The same data exists for the WD-WD binaries and these are an important source of noise for LISA (e.g. Ruiter et al. 2007). The simulations also represent a full set of cluster populations synthesis models that can be used for photometric and spectroscopic studies. I hope to make these publicly available soon.

In conclusion I find that star clusters are likely to produce gravitational wave sources in both the ground-based and space-based regimes and these should be reliably detected by the next generation of gravitational wave detectors. I conclude that dynamical evolution

in star clusters must be taken into account in order to produce accurate event rates and population statistics for gravitational wave detection.

Bibliography

- Aarseth, S. J., 1999, *Publ. Astron. Soc. Pac.*, 111, 1333
- Aarseth, S. J., and Zare, K., 1974, *Celest. Mech.*, 10, 185
- Abbott, B. et al. (LIGO Scientific Collaboration), 2005, *Phys. Rev. D*, 72, 082001
- Abbott, B. et al. (LIGO Scientific Collaboration), 2006, *Phys. Rev. D*, 73, 062001
- Abramovicie, A., et al., 1992, *Science*, 256, 325
- Amaro-Seoane, P., Miller, M. C., and Freitag, M., 2009, *ApJ*, 692, 50
- Antonov, V. A., 1962, *Vestnik. Leningrad, Univ.* 7, 135
- Bacon, D., Sigurdsson, S. and Davies, M. B., 1996, *MNRAS*, 281, 830
- Baker, J. G., van Meter, J. R., McWilliams, S. T., Centrella, J. and Kelly, B. J., 2007, *Phys. Rev. Lett.*, 99, 181101
- Baumgardt, H., 2001, *MNRAS*, 325, 1323
- Bekki, K., Couch, W. J., Drinkwater, M. J., and Shioya, Y., 2003, *MNRAS*, 344, 399
- Belczynski, K., Benacquista, M. and Bulik, T., 2008, arXiv:0811.1602v1, submitted to *ApJ*
- Belczynski, K., Kalogera, V. and Bulik, T., 2002, *ApJ*, 572, 407
- Belczynski, K., Taam, R. E., Kalogera, V., Rasio, F. A., and Bulik, T., 2007, *ApJ*, 662, 504
- Benacquista, M. J., 2006, *Living Rev. Relativity*, 9, 2
- Benz, W. and Hills, J. G., 1987, *ApJ*, 323, 614
- Berentzen, I., Preto, M., Berczick, P., Merritt, D., and Spurzem, R., 2009, *ApJ*, 695, 455
- Bettwieser, E. and Sugimoto, D., 1984, *MNRAS*, 208, 493
- Binney, J. and Tremaine, S., 1987, *Galactic Dynamics*, Princeton Series in Astrophysics, Princeton University Press, Princeton, NJ, USA
- Blanchet, L., 2006, *Living Rev. Relativity*, 9, 4
- Bonazzola, S., and Marck, J. A., 1994, *Annu. Rev. Nucl. Part. Sci.*, 45, 655
- Borch, A., Spurzem, R., and Hurley, J., 2006, *IAUJD*, 14, 60

- Borch, A., Spurzem, R., and Hurley, J., 2007, arXiv0704.3915v1, Submitted to A&A
- Bradaschia, et al., Nucl. Instr. Meth., A289, 518
- Brodie, J. P., and Strader, J., 2006, ARA&A, 44, 193
- Bulik, T., Belczynski, K., and Rudak, B., 2004, A&A, 415, 407
- Chandrasekhar, S., and von Neumann, J., 1942, ApJ, 95, 489
- Cheng, T., 2005, *Relativity, Gravitation and Cosmology: A Basic Introduction*, Oxford Master Series in Particle Physics, Astrophysics, and Cosmology, Oxford University Press, Oxford, UK
- Cutler, C., Phys. Rev. D., 57, 7089
- Damour, T., Gopakumar, A., and Iyer, B. R., 2004, Phys. Rev. D, 70, 064028
- Danzmann, K., et al., 1992, in *Relativistic Gravity Research*, Proc. 81 WE-Heraeus-Seminar, ed. J. Ehlers and G. Schäfer. Also Lecture Notes in Physics (Berlin, Heidelberg, New York: Springer-Verlag), 410, 184
- Deiters, S. and Spurzem, R., 2000, ASPC, 211, 204
- Drinkwater, M. J., Phillipps, S., Jones, J. B., Gregg, M. D., Parker, Q. A., and Smith, R. M., 1999, ASPC, 170, 128
- Eggleton, P. P., 1983, ApJ, 268, 368
- Ernst, A., Glaschke, P., Fiestas, J., Just, A. and Spurzem, R., 2007, MNRAS, 377, 465
- Ernst, A., Just, A., and Spurzem, R., 2009, arXiv:0906.4459
- Fabian, A. C., Pringle, J. E. and Rees M. J., 1975, MNRAS, 172, 15
- Fellhauer, M., and Kroupa, P., 2002 MNRAS, 330, 642
- Flanagan, É. É., and Hughes, S. A., 1998, Phys. Rev. D, 57, 4535
- Fleck, J.-J., Boily, C. M., Lançon, A., and Deiters, S., 2006, MNRAS, 369, 1392
- Fregeau, J. M., Cheung, P., Portegies Zwart, S., F., and Rasio, F. A., MNRAS, 352, 1
- Fregeau, J. M., and Rasio, F. A., 2007, ApJ, 658, 1047
- Freitag, M. and Benz, W., 2002, A&A, 394, 345
- Fryer, C. L., Woosley, S. E., and Hartmann, D. H., 1999, ApJ, 526, 152
- Gao, B., Goodman, J., Cohn, H. and Murphy, B., 1991, ApJ, 370, 567
- Giersz, M., 1998, MNRAS, 298, 1239
- Giersz, M., 2001, MNRAS, 324, 218
- Giersz, M., 2006, MNRAS, 371, 484

- Giersz, M. and Heggie, D. C., 1994, MNRAS, 268, 257
- Giersz, M. and Heggie, D. C., 2008, MNRAS, 389, 1858
- Giersz, M. and Heggie, D. C., 2009, MNRAS, 395, 1173
- Giersz, M., Heggie, D. C. and Hurley, J. R., 2008, MNRAS, 388, 429
- Giersz, M. and Spurzem, R., 2000, MNRAS, 317, 581
- Giersz, M., and Spurzem, R., 2003, MNRAS, 343, 781
- Giersz, M. and Spurzem, R., 2010, in preparation
- Goodman, J., 1987, ApJ, 313, 576
- Goodman, J. and Hut, P., 1993, ApJ, 403, 271
- Gültekin, K., Miller, M. C., and Hamilton, D. P., 2004, ApJ, 616, 221
- Gültekin, K., Miller, M. C., and Hamilton, P. H., 2006, ApJ, 640, 156
- Hachisu, I., Nakada, Y., Nomoto, K. and Sugimoto, D., 1978, Pr. Th. Phys., 60, 393
- Hansen, B. M. S. and Phinney, E. S., 1997, MNRAS, 291, 569
- Harris, W. E., 1996, AJ, 112, 1487
- Harris, W. E., Whitmore, B. C., Karakla, D., Okoń, W., Baum, W. A., and Hanes, D. A., 2006, ApJ, 636, 90
- Hasegan, M., Jordán, A., Côte, P., Djorgovski, G., McLaughlin, D. E., Blakeslee, J. P., Mei, S., West, M. J., Peng, E. W., Ferrarese, L., Milosavljević, M., Tonry, J. L., and Merritt, D., 2005, ApJ, 627, 203
- Heggie, D. C., 1975, MNRAS, 173, 729
- Heggie, D. C. and Giersz, M., 2009, MNRAS, 397, 46
- Heggie, D. C. and Hut P., 2003, *The Gravitational Million-Body Problem: A Multidisciplinary Approach to Star Cluster Dynamics*, Cambridge University Press, Cambridge, UK
- Heggie, D. C., Hut, P. and McMillan, S. L. W., 1996, ApJ, 467, 359
- Heggie, D. C., Portegies Zwart, S., and Hurley, J. R., 2006, New Astron., 12, 20
- Heggie, D. C., and Rasio, F. A., 1996, MNRAS, 282, 1064
- Hello, P., 1998, in Proc. Second Workshop on Gravitational Wave Data Analysis, (Paris: Éditions Frontières), 87
- Hénon, M., 1971, Ap&SS, 13, 284
- Hénon, M., 1971, Ap&SS, 14, 151
- Hénon, M., 1975, IAUS, 69, 133

- Hilditch, R. W., 2001, *An Introduction to Close Binary Stars*, Cambridge University Press, Cambridge, UK
- Hills, J. G., and Fullerton, L. W., 1980, *AJ*, 85, 1281
- Hjellming, M. S. and Webbink, R. F., 1987, *ApJ*, 318, 794
- Hogg, D. W., 2000, arXiv:astro-ph/9905116v4
- Hughes, S. A., 2006, Laser Interferometer Space Antenna: 6th International LISA Symposium, 873, 13
- Hughes, S. A., 2009, ArXiv:0903.4877v1, Invited review to appear in Annual Reviews of Astronomy and Astrophysics
- Hurley, J. R., Pols, O. R. and Tout, C. A., 2000, *MNRAS*, 315, 543
- Hurley, J. R., Tout, C. A. and Pols, O. R., 2002, *MNRAS*, 329, 897
- Hut, P., 1985, *IAUS*, 113, 231
- Hut, P. and Bahcall, J. N., 1983, *ApJ*, 268, 319
- Ivanova, N., Heinke, C. O., Rasio, F. A., Taam, R. E., Belczynski, K., and Fregeau, J. M., 2006, *MNRAS*, 372, 1043
- Ivanova, N., Heinke, C.O., Rasio, F.A., Belczynski, K. and Fregeau, J.M., 2008, *MNRAS*, 386, 553
- Kalogera, V., Narayan, R., Spergel, D. N., and Taylor, J. H., 2001, *ApJ*, 556, 340
- Khalisi, E., Amaro-Seoane, P. and Spurzem, R., 2007, *MNRAS*, 374, 703
- Kippenhahn, R. and Weigrert, A., 1967, *Z. Astrophys*, 65, 251
- Kozai, Y., 1962, *AJ*, 67, 591
- Kroupa, P., 1995, *MNRAS*, 277, 1507
- Kroupa, P., Tout, C.A. and Gilmore, G., 1993, *MNRAS*, 251, 293
- Kundu, A., Zepf, S. E., Hempel, M., Morton, D., Ashman, K. M., Maccarone, T. J., Kissler-Patig, M., Puzia, T. H., and Vesperini, E., 2005, *ApJ*, 634, 41
- Kupi, G., Amaro-Seoane, P., and Spurtzem, R., 2006, *MNRAS*, 371, 45
- Kustaanheimo, P., and Stiefel, E., 1965, *J. Reine Angew. Math.* 218, 204
- Larson, R. B., 1970, *MNRAS*, 147, 323
- Lee, H. M. and Ostriker, J. P., 1986, *ApJ*, 310, 176
- Lee, H. M. and Ostriker, J. P., 1987, *ApJ*, 322, 123
- Lorimer, D., 2005, *Living Rev. Relativity*, 8, 7
- Lynden-Bell, D. and Eggleton, P. P., 1980, *MNRAS*, 191, 438

- Lynden-Bell, D. and Wood, R., 1968, MNRAS, 138, 495
- Lyne, A. G. and Lorimer, D. R., 1994, Nature, 369, 127
- Maggiore, M., 2008, *Gravitational Waves Volume 1: Theory and Experiments*, Oxford University Press, Oxford, UK
- McMillan, S. L. W., McDermott, P. N., and Taam, R. E., 1987, ApJ, 318, 261
- Mikkola, S., 1983, MNRAS, 205, 733
- Mikkola, S., 1984, MNRAS, 207, 115
- Mikkola, S., 1984b, MNRAS, 208, 75
- Mikkola, S., 1997, CeMDA, 68, 87
- Mikkola, S. and Aarseth, S. J., 1998, New Astron., 3, 309
- Miller, R. H., 1964, ApJ, 140, 250
- Narayan, R., Piran, T., and Semi, A., 1991, ApJ, 379, L17
- Neusch, W., 1992, *Celestial mechanics: An introduction to classical and contemporary methods*, B. I. Wissenschaftsverlag, Germany
- O'Leary, R.M., Rasio, F.A., Fegeau, J.M., Ivanova, N. and O'Shaughnessy, R., 2006, ApJ, 637, 937
- Padmanabhan, T., 2000, *Theoretical Astrophysics, Volume I, Astrophysical Processes*, Cambridge University Press, Cambridge, UK.
- Peters, P. C. and Mathews, J., 1963, Phys. Rev., 131, 435
- Peters, P. C., 1964, Phys. Rev., 136, 1224
- Pfhal, E., Rappaport, S. and Podsiadlowski, P., 2002 ApJ, 573, 283
- Pierro, V., Pinto, I. M., Spallicci, A. D., Laserra, E. and Recano, F., 2001, MNRAS, 325, 358
- Plummer, H. C., MNRAS 71, 460
- Portegies Zwart, S. F., Makino, J., McMillan, S. L. W. and Hut, P., 1999, A&A, 348, 117
- Portegies Zwart, S.F and McMillan, S.L.W., 2000, ApJ, 528, 17
- Portegies Zwart, S. F., and Yungelson, L. R., 1998, A&A, 332, 173
- Press, W. H. and Teukolsky, S. A., 1977, ApJ, 213, 183
- Ruiter, A. J., Belczynski, K., Benacquista, M., Larson, S. L., and Williams, G., 2007, arXiv:0705.3272v2
- Ray, A., Kembhavi, A. K., and Antia, H. M., 1987, A&A, 184, 164

- Sadowski, A., Belczynski, K., Bulik, T., Ivanova, I., Rasio, F.A. and O'Shaughnessy, R., 2008, *ApJ*, 676, 1162
- Salpeter, E. E., 1955, *ApJ*, 121, 161
- Shara, M .M. and Hurley, J. R., 2002, *ApJ*, 570, 830
- Sigurdsson, S., and Phinney, E. S., 1993, *ApJ*, 415, 631
- Sills, A., Karakas, A. and Lattanzio, J., 2009, *ApJ*, 692, 1411
- Spitzer, L., 1969, *ApJ*, 158, 139
- Spitzer, L., 1975, *IAUS*, 69, 3
- Spitzer, L., 1987, *Dynamical Evolution of Globular Clusters*, Princeton University Press, Princeton, NJ, USA
- Spurzem, R., 1999, *J. Comp. Appl. Maths.*, 109, 407
- Spurzem, R. and Aarseth, S. J., 1996, *MNRAS*, 282, 19
- Spurzem, R., Berczik, P., Marcus, G., Kugel, A., Lienhart, G., Berentzen, I., Männer, R., Klessen, R., Banerjee, R., 2009, *Accelerating astrophysical simulations with programmable hardware (FPGA and GPU)*, Computer Science – Research and Development, Springer Verlag, 23, 231
- Spurzem, R., Berentzen, I., Berczik, P., Merritt, D., Amaro-Seoane, P., Harfst, S., Gualandris, A., 2008, *Parallelization, Special Hardware and Post-Newtonian Dynamics in Direct N-Body Simulations*, Lecture Notes in Physics, Berlin Springer Verlag, 760, 377
- Spurzem, R., Giersz, M., Takahashi, K. and Ernst, A., 2005, *MNRAS*, 364, 948
- Stodólkiewicz, J. S., 1982, *Acta Astronomica*, 32, 63
- Stodólkiewicz, J. S., 1986, *Acta Astronomica*, 36, 19
- Stolte, A., Grebel, E. K., Brandner, W. F. and Figer, D. F., 2002, *A&A*, 394, 459
- Takahashi, K. and Portegies Zwart, S. F., 1998, *ApJ*, 503, 49
- Tessmer, M., and Gopakumar, A., 2008, *Phys. Rev. D*, 78, 084029
- Thorne, K. S., 1987, *300 Years of Gravitation*, ed. S. W. Hawking and W. Israel,, Cambridge University Press, Cambridge, UK, 330-458
- Tsubono, K., 1995, in *First Edoardo Amaldi Conference on Gravitational Wave Experiments*, 112
- Vesperini, E., Zepf, S. E., Kundu, A., and Ashman, K. M., 2003, *ApJ*, 593, 760
- Watters, W. A., Joshi, K. J. and Rasio, F. A., 2000, *ApJ*, 539, 331
- Willems, B., Kalogera, V., Vecchio A., Ivanova, N., Rasio, F. A., Fregeau, J. M., and Belczynski, K., 2007, *ApJ*, 665, 59

Acknowledgements

I would like to thank my supervisor, Rainer Spurzem for his help during this project and particularly for the many conference and travel opportunities he provided me. I would also like to thank my main collaborators Matthew Benacquista and Mirek Giersz. Matt first alerted me to the vast amount of useful data the Monte Carlo simulations were producing and showed me that LISA detections could be generated from stellar-mass sources. Mirek has been very helpful in upgrading the Monte Carlo code at my request, answering my many questions, and helping to diagnose endless problems with my early simulations.

I would like to acknowledge the International Max-Planck Research School for providing funding for my Ph.D. and both the German D-Grid initiative and Astrogrid-D through which I obtained the computing time necessary for my simulations at the HLRS supercomputer in Stuttgart as part of bwgrid.

I would like to thank the stellar dynamics working group at the ARI for providing a positive working environment and many fruitful discussions. In particular I want to thank Ingo Berentzen for helping me better understand Post-Newtonian Dynamics and Peter Berczik for providing that special Ukrainian elixir that our group has come to know and love.

I would also like to thank the star formation group at the ITA. They have been great friends to me and have provided a social environment that has kept me happy and sane during my time in Heidelberg. I would not have made it through without the long nights at Maxbar and Sonderbar, thanks guys!

Finally I would like to thank Jose Fiestas from the ARI and Simon Glover from the ITA for reading this thesis and suggesting several improvements and Oliver Porth from the MPIA for providing a German translation of the abstract.

